
Electronic Thesis and Dissertation Repository

12-12-2018 3:30 PM

Investigation of Flow Disturbances and Multi-Directional Wall Shear Stress in the Stenosed Carotid Artery Bifurcation Using Particle Image Velocimetry

Amanda L. DiCarlo, *The University of Western Ontario*

Supervisor: Dr. Tamie Poepping, *The University of Western Ontario*

A thesis submitted in partial fulfillment of the requirements for the Doctor of Philosophy degree in Physics

© Amanda L. DiCarlo 2018

Follow this and additional works at: <https://ir.lib.uwo.ca/etd>



Part of the [Biophysics Commons](#), and the [Fluid Dynamics Commons](#)

Recommended Citation

DiCarlo, Amanda L., "Investigation of Flow Disturbances and Multi-Directional Wall Shear Stress in the Stenosed Carotid Artery Bifurcation Using Particle Image Velocimetry" (2018). *Electronic Thesis and Dissertation Repository*. 5924.

<https://ir.lib.uwo.ca/etd/5924>

This Dissertation/Thesis is brought to you for free and open access by Scholarship@Western. It has been accepted for inclusion in Electronic Thesis and Dissertation Repository by an authorized administrator of Scholarship@Western. For more information, please contact wlsadmin@uwo.ca.

Abstract

Hemodynamics and shear forces are associated with pathological changes in the vascular wall and its function, resulting in the focal development of atherosclerosis. Flow complexities that develop in the presence of established plaques create environments favorable to thrombosis formation and potentially plaque rupture leading to stroke. The carotid artery bifurcation is a common site of atherosclerosis development. Recently, the multi-directional nature of shear stress acting on the endothelial layer has been highlighted as a risk factor for atherogenesis, emphasizing the need for accurate measurements of shear stress magnitude as well as direction. In the absence of comprehensive patient specific datasets numerical simulations of hemodynamics are limited by modeling assumptions. The objective of this thesis was to investigate the relative contributions of various factors - including geometry, rheology, pulsatility, and compliance – towards the development of disturbed flow and multi-directional wall shear stress (WSS) parameters related to the development of atherosclerosis

An experimental stereoscopic particle image velocimetry (PIV) system was used to measure instantaneous full-field velocity in idealized asymmetrically stenosed carotid artery bifurcation models, enabling the extraction of bulk flow features and turbulence intensity (TI). The velocity data was combined with wall location information segmented from micro computed tomography (CT) to obtain phase-averaged maps of WSS magnitude and direction. A comparison between Newtonian and non-Newtonian blood-analogue fluids demonstrated that the conventional Newtonian viscosity assumption underestimates WSS magnitude while overestimating TI. Studies incorporating varying waveform pulsatility demonstrated that the levels of TI and oscillatory shear index (OSI) depend on the waveform amplitude in addition to the degree of vessel constriction. Local compliance resulted in a dampening of disturbed flow due to volumetric capacity of the upstream vessel, however wall tracking had a negligible effect on WSS prediction. While the degree of stenosis severity was found to have a dominant effect on local hemodynamics, comparable relative differences in metrics of flow and WSS disturbances were found due to viscosity model, waveform pulsatility and local vessel compliance.

Keywords

Atherosclerosis, carotid artery, wall shear stress, oscillatory shear index, transverse wall shear stress, turbulence intensity, particle image velocimetry, non-Newtonian fluid, pulsatility index, compliance

Co-Authorship Statement

Chapter 2 presents material from an article entitled “Study of the effect of stenosis severity and non-Newtonian viscosity on multidirectional wall shear stress and flow disturbances in the carotid artery using particle image velocimetry” which has been submitted to *Medical Engineering and Physics*. This article was co-authored by Amanda L. DiCarlo, David W. Holdsworth, and Tamie L. Poepping. Dr. Cameron Hopkins is acknowledged for assisting with the collection of rheometer data for the non-Newtonian fluid sample. A. DiCarlo performed all of the PIV experiments, analyzed the data, and wrote the manuscript. D. W. Holdsworth and T. L. Poepping reviewed the results and manuscript prior to submission.

A version of Chapter 3, titled “Effects of waveform pulsatility on shear stress and flow disturbances in carotid artery models using particle image velocimetry” is being prepared for submission to the *Journal of Biomechanics*, co-authored by Amanda L. DiCarlo, David W. Holdsworth, and Tamie L. Poepping. A. DiCarlo performed the experiments, analyzed the data, and wrote the manuscript, and all authors will review the results and manuscript prior to submission.

A version of Chapter 4, “Modeling the Effects of vascular stiffening: An in vitro study of carotid artery hemodynamics using particle image velocimetry” is being prepared for submission to the *Journal of Biomechanics* with co-authors Amanda L. DiCarlo, Chris Norley, Steve Pollman, David W. Holdsworth, and Tamie L. Poepping. A. DiCarlo performed the PIV experiments, analyzed the data, and wrote the manuscript draft. C. Norley and S. Pollman assisted with dynamic CT data collection and reconstruction. All authors will review the results and manuscript prior to submission.

Acknowledgments

First and foremost, I must thank my supervisor, Dr. Tamie L. Poepping, for giving me the opportunity from which I have learned a lot, and for her continuous encouragement, optimism, and patience.

I am very thankful to Dr. David W. Holdsworth, for his kindness and generosity, and contributing his wealth of knowledge and ideas towards the work in this thesis.

Thanks to my advisory committee, Dr. Blaine Chronik and Dr. Eugene Wong, for all of their guidance and advice.

I would like to acknowledge Hristo Nikolov for the phantom fabrication, Chris Norley and Steve Pollman for assistance with the dynamic CT data collection and reconstruction, Jaques Milner for help with vascular modeling, Frank Van Sas and Brian Dalrymple for their machining expertise and Doug Hie for help with electronics. Without their expertise, this work would not have been possible.

I would like to thank my former colleagues: Dr. Sarah Kefayati for passing on her PIV knowledge, Dr. Bushra Hussain for her helpful discussions and advice, and Onaizah Onaizah for her friendship and spending many late nights in the lab with me.

Last and most importantly, I must thank my parents, Jesse and Denise, and my sister, Melissa, for their love and support throughout my Ph.D. and always.

Table of Contents

Abstract	i
Co-Authorship Statement.....	iii
Acknowledgments.....	iv
Table of Contents	v
List of Tables	ix
List of Figures	x
List of Symbols and Abbreviations.....	xvii
Chapter 1	1
1 Introduction	1
1.1 Stroke, Atherosclerosis and the Carotid Artery	1
1.2 The role of hemodynamics in the development of atherosclerosis and thrombosis.....	3
1.2.1 Low and Oscillatory Shear Stress Hypothesis	4
1.2.2 The response of the Vessel Endothelium to Pathological Shear Stress	5
1.2.3 Multidirectional Shear Stress	7
1.2.4 Disturbed Flow and Platelet interactions	9
1.2.5 High Shear Stress and Plaque Vulnerability	11
1.3 Fluid Mechanics.....	12
1.3.1 The Stress Tensor.....	12
1.3.2 The Navier-Stokes Equations	15
1.3.3 Wall Shear Stress Calculation from Measured Data.....	16
1.3.4 Wall Shear Stress Metrics.....	18
1.3.5 Turbulence Intensity	19
1.4 Measuring and Modeling Hemodynamics	20

1.4.1	In-vivo Measurements	20
1.4.2	Numerical Modeling	23
1.4.3	Physical Modeling: Particle Image Velocimetry	24
1.5	Factors Impacting Hemodynamics.....	28
1.5.1	Geometry.....	28
1.5.2	Rheology	29
1.5.3	Pulsatility	30
1.5.4	Compliance	32
1.6	Research Objectives and Outline	34
1.7	References	36
Chapter 2	53
2	Study of the effect of stenosis severity and non-Newtonian viscosity on multidirectional wall shear stress and flow disturbances in the carotid artery using particle image velocimetry	53
2.1	Introduction.....	53
2.2	Methods.....	56
2.2.1	Flow set-up.....	56
2.2.2	Blood analogue fluids	58
2.2.3	PIV data acquisition and velocity vector processing	59
2.2.4	Computed tomography imaging	60
2.2.5	Data analysis	60
2.3	Results.....	65
2.3.1	Velocity and turbulence intensity	65
2.3.2	Wall shear stress and shear metrics.....	71
2.4	Discussion	78
2.5	References	82

Chapter 3	90
3 Effects of waveform pulsatility on shear stress and flow disturbances in carotid artery models using particle image velocimetry	90
3.1 Introduction.....	90
3.2 Methods.....	92
3.3 Results.....	98
3.4 Discussion.....	107
3.5 References.....	110
Chapter 4	114
4 Modeling the Effects of vascular stiffening: An in vitro study of carotid artery hemodynamics using particle image velocimetry	114
4.1 Introduction.....	114
4.2 Methods.....	115
4.2.1 Experimental Flow Set-up	115
4.2.2 PIV Experiments	117
4.2.3 Micro Computed Tomography Experiments	120
4.2.4 Data Postprocessing	122
4.3 Results.....	125
4.4 Discussion.....	134
4.5 Conclusion	137
4.6 References.....	137
Chapter 5	142
5 Summary and Future Work.....	142
5.1 Research Summary and Conclusions.....	142
5.1.1 Summary of Chapter 2	142
5.1.2 Summary of Chapter 3	143

5.1.3	Summary of Chapter 4	144
5.1.4	Quantitative Comparison of Results	145
5.2	Future Directions	149
5.2.1	Further PIV Studies.....	149
5.2.2	Microfluidics and “Lab-on-a-chip” studies.....	153
5.3	References	154
	Appendix A.....	157
	Supplementary Figures to Chapter 2.....	157
	Appendix B	162
	Supplementary Data to Chapter 3	162
	30% stenosed model.....	162
	70% stenosed model.....	165
	Curriculum Vitae	167

List of Tables

Table 2.1: Blood analogue fluid formulations	58
Table 2.2: Turbulence intensity parameters. Absolute max TI is the maximum single site TI value found within the ROI, indicated by the boxed area in Fig. 6. Maximum TI refers to the peak ROI averaged TI value (at t = 180 - 200 ms) and cycle-averaged TI refers to the temporal and spatial mean over the ROI. Errors indicate the maximum differences incurred from shifting the ROI ± 4 mm axially.....	73
Table 2.3: Wall shear stress parameters. Absolute max. WSS refers to the maximum single site WSS value. Remaining values are mean of the parameter over the specified vessel branch with standard deviation in parenthesis.	73
Table 3.1: Waveform properties for the 50% stenosed model. The pulsatility and resistive index were calculated from both flow and velocity waveforms, indicated by Q and U respectively. Reynolds numbers (Re) were calculated from velocity at the narrowest stenosis diameter.	97
Table 4.1: Mechanical properties of carotid artery phantoms	122
Table 5.1: Overall comparison of hemodynamics parameters across all models. a) Overview of flow components applied for each model. b) Absolute values of hemodynamic parameters. c) Percent difference in hemodynamic parameters relative to the reference model.....	147
Table B.1: Waveform properties for the 30% stenosed model. The pulsatility and resistive index were calculated from both flow and velocity waveforms, indicated by Q and U respectively. Reynolds numbers (Re) were calculated from velocity at the narrowest stenosis diameter.	162

List of Figures

Figure 1.1: (a) A shear stress applied to an elastic material is related to the deformation by the elastic modulus, G . (b) In a simple shear flow, the shear stress on the fluid is related to the rate of deformation. (c) The elements of the stress tensor in three dimensions acting on a fluid element at point P 13

Figure 2.1: Experimental set-up including flow circuit and PIV components (left). Family of carotid artery bifurcation geometries with progressing degrees of eccentric stenosis (right). Dashed contour line indicates the boundary of the normal, disease-free geometry. CCA: common carotid artery, ICA: internal carotid artery, ECA: external carotid artery 56

Figure 2.2: (a) Flow waveforms measured at the CCA inlet for each experimental PIV dataset (phase averaged from 15 cardiac cycles). Dashed lines represent the mean flow-rate in each case (6.1 ± 0.2 mL/s averaged across all models). (b) Experimental fluid viscosity versus shear rate. Blood data is taken from recent literature. Solid line shows Cross model fit to non-Newtonian blood analogue fluid viscosity measurements. Dashed line indicates constant viscosity of Newtonian blood analogue fluid.57

Figure 2.3: Central plane phase-averaged velocity magnitude at peak systole ($t = 180$ ms). Note that each row of models has an individual color bar. Contour lines correspond to the highest contour level in each row. Recirculation regions are indicated in white on panel c. Slices S1-S5 on panels a, d, and F indicate cross-sections where velocity profiles are extracted for each geometry.66

Figure 2.4: Phase-averaged centerline-projected velocity profiles at peak systole. Profiles are extracted from the central plane ICA at slices S1-S5 spaced 6 mm apart along the centerline indicated in Fig. 3.67

Figure 2.5: Temporal phase-averaged centerline-projected velocity profiles for the 50% eccentric geometry, extracted from the central plane ICA at slices S1 (bottom row) and S5 (top row) indicated in Fig. 3. Sparse error bars representing standard deviation are shown for the profiles corresponding to peak systole and diastole.68

Figure 2.6: Central plane maps of turbulence intensity magnitude in the ICA, shown at the time point of peak ROI-averaged TI, as indicated in each panel. A transverse slice is shown for each model at the center of the ROI, which is indicated by the boxed area.....70

Figure 2.7: ROI-averaged TI versus cardiac cycle time for all models.71

Figure 2.8: Contours of TAWSS. Each model is shown in two orientations, exposing the inner and outer walls of the ICA on the left and right, respectively. Note that each row of models has an individual color bar. Contour lines correspond to the highest contour level in each row.72

Figure 2.9: Contours of OSI overlaid with a sparse sample of unit vectors representing the direction only of the mean WSS vector. Each model is shown in two orientations, exposing the inner and outer walls of the ICA on the left and right, respectively. Insets provide enlarged views from points P1 through P5 whose locations are indicated in panels c-f depicting three key contributors to OSI: flow impingement on wall (P1, P3, P5), flow streams merging along wall (P3, P4), and wall-adjacent vortical flow (P2).76

Figure 2.10: Contours of transWSS. Each model is shown in two orientations, exposing the inner and outer walls of the ICA on the left and right, respectively. Each row of models has an individual color bar and contour lines correspond to the highest contour level in each row.77

Figure 2.11: Surface area exposure as a function of stenosis severity and compared for Newtonian (black) and non-Newtonian (blue) fluids. Values are ICA SA exposed to: TAWSS below, OSI above, and transWSS above the respective thresholds. Thresholds defined as the 20th, 80th and 80th percentile values, respectively, of the parameter on the 50% N-fluid ICA surface. Whiskers represent ICA SA coverage when the +/- 5 percentile thresholds are applied.78

Figure 3.1: a) Phantom geometry with 50% eccentric stenosis. Dashed lines indicate the boundaries of 30% and 70% stenosed geometries. CCA: common carotid artery, ICA: internal carotid artery, ECA: external carotid artery; b) Photo of the experimental setup. Arrows indicate flow direction from and to pump; c) Schematic diagram of flow circuit

(not to scale) including compliant (C) and resistive (R) elements. Direction of flow indicated by arrows.93

Figure 3.2: Volumetric flow, pressure, and velocity waveforms for the three cases of high, intermediate, and low pulsatility index (PI) for the 50% stenosed model. Flow and pressure waveforms were measured via electromagnetic flowmeters and pressure transducer at the inlets and outlets of the phantom at locations indicated in Figure 3.1c. Velocity waveforms were extracted from PIV data at sections S1, S3 and S4 shown in Figure 3.1a for CCA, ICA, and ECA respectively.....95

Figure 3.3: Phase-averaged velocity magnitude at peak systole for a 50% stenosed model with high (a,d), intermediate (b,e), and low (c,f) PI waveforms applied. A volumetric representation with transverse slices at 6 mm increments is shown in the top row (a-c); central-plane maps are shown in the bottom row (d-f). Contour lines indicate the highest contour level reached: 1.9, 1.5, and 1.2 m/s for the high, intermediate, and low PI cases, respectively.99

Figure 3.4: Turbulence intensity maps at the time point of maximum ICA-averaged TI in the 50% stenosed model with high (a,d), intermediate (b,e), and low (c,f) PI waveforms applied. A volumetric representation with transverse slices at 6 mm increments is shown in the top row (a-c); central-plane maps are shown in the bottom row (d-f).100

Figure 3.5: ICA-averaged TI versus cardiac cycle phase for the three inlet waveforms applied in the 50% stenosed model, calculated from central-plane TI maps. The dotted blue line indicates the time of peak systole, for phase reference.....101

Figure 3.6: Trends in ICA-averaged TI for 30, 50, and 70% stenosed models and three inlet waveforms. a) Peak ICA-averaged TI as a function of ICA velocity waveform PI (coloured) and CCA velocity waveform PI (grey markers + dashed line). b) Peak ICA-averaged TI versus peak stenosis velocity measured at section S2 indicated in Figure 3.1a. c) Cycle mean ICA-averaged TI versus cycle mean stenosis velocity measured at section S2. For comparison, ICA-averaged TI in a 50% stenosed geometry with constant CCA-inlet flow rates of 6, 8, and 10 mL/s are also shown (crosses). $St = Stenosis$102

Figure 3.7: Contours of WSS magnitude for the 50% stenosed model and the high (left column), intermediate (middle) and low (right) PI waveforms. Two orientations are shown in each frame, displaying the inner ICA wall on the left and outer ICA wall on the right. (a-c) at peak systole ($t = 180$ ms); (d-f) at second flow peak ($t = 350$ ms); (g-i) mid diastole ($t = 830$ ms). Note different individual contour levels implemented for each row. 103

Figure 3.8: Time-averaged shear metrics for the 50% stenosed model with high (a,e), intermediate (b,f) and low (c,g) PI waveforms. Two orientations are shown in each frame, displaying the inner (left) and outer (right) walls of the ICA. (Top row, a-c) Contour maps of TAWSS. (Bottom row, d-f) Contour maps of OSI overlaid with a sparse sample of unit vectors indicating the direction of the mean WSS vector. 105

Figure 3.9: Relative ICA surface area exposed to a) TAWSS below the 20th percentile threshold and b) OSI above the 80th percentile threshold. Threshold values calculated from parameter distributions for the 50% stenosed model with high PI waveform. Error bars indicate the area exposed when +/- 5 percentile thresholds were applied. SA exposed to *both* low TAWSS and high OSI is indicated by blue shading. 106

Figure 3.10: TAWSS (a,b) and OSI (c,d) magnitude profiles extracted along the inner (left column) and outer (right column) walls of the ICA along the plane of symmetry. 106

Figure 3.11: Correlation between surface area exposed to high OSI (OSI_{80}) and waveform descriptors. a) OSI_{80} vs CCA velocity waveform PI (filled markers, solid line) and vs ICA velocity waveform PI (open markers, dashed line). b) OSI_{80} vs CCA velocity waveform RI (closed markers, solid line) and vs ICA velocity waveform RI (open markers, dashed line). c) OSI_{80} (black) and peak ICA-averaged TI (blue) vs peak stenosis velocity. 107

Figure 4.1: a) Thin-walled and block phantom models. b) Photo of the experimental setup. R and C indicate downstream resistive and compliant elements, respectively. 117

Figure 4.2: Flow (top row, a-b), pressure (middle, c-d) and velocity (bottom, e-f) waveforms measured at the CCA inlet and ICA outlet for block (blue) and thin-walled (red) phantom models. Grey dotted vertical lines indicate time points of peak flow ($t = 180$ ms) peak pressure (approximately $t = 290$ ms) and mid-diastole ($t = 830$ ms). 119

Figure 4.3: a) CCA diameter vs static pressure for the block (blue, diamond) and thin-walled (red, square) phantom models. CCA diameter vs dynamic pressure over the cardiac cycle for the thin-walled phantom (grey, circle) displays a hysteresis, with lower distension when pressure is increasing. b) CCA diameter vs cardiac cycle phase for the thin-walled phantom, plotted against CCA inlet pressure, for reference. 121

Figure 4.4: Phase-averaged velocity vector maps superimposed on contours of phase-averaged velocity magnitude at time points of peak flow (top row, a-b), peak pressure (middle, c-d) and diastole (bottom, e-f). Note different individual color bars for each row. Slices S1 and S2 on panels e-f indicate cross-sections where velocity profiles were extracted. 126

Figure 4.5: Temporal phase-averaged centerline-projected velocity profiles extracted from the central plane ICA at slices S1 (bottom row) and S2 (top row) indicated in Figure 4.4e-f. Sparse error bars represent standard deviation over 15 collected cardiac cycles. 127

Figure 4.6: Temporal evolution of central plane turbulence intensity in the ICA branch spanning time points from before peak systole through flow deceleration, as indicated. 128

Figure 4.7: ICA-averaged turbulence intensity vs cardiac cycle phase for the block (blue, diamond) and thin-walled (red, square) phantom models, extracted from central plane TI maps. A scaled CCA inlet flow-rate waveform is shown in the background for reference. 129

Figure 4.8: Time-averaged WSS metrics calculated for block (left) and thin-walled (middle) phantoms with static CT surfaces, and thin-walled phantom applying dynamic CT surfaces (right). Two orientations are shown in each frame, displaying the inner and outer walls of the ICA. (Top row, a-c) Contour maps of TAWSS. (middle row, d-f) Contour maps of OSI overlaid with a sparse sample of unit vectors indicating the direction of the mean WSS vector. (Bottom row, g-i) Contour maps of transWSS. 130

Figure 4.9: Axial profiles of TAWSS (a,b), OSI (c,d) and transWSS (e,f) magnitude extracted along the inner (left column) and outer (right column) walls of the ICA, at lines L1 and L2 indicated in Figure 4.8i. 132

Figure 4.10: Axial-projected WSS magnitude vs cardiac cycle phase at specific points indicated by P1-P4 in Figure 4.9c. a) Outer wall stenosis throat; b) Inner wall mid-jet; c) Outer wall jet impingement; d) Inner wall high OSI region.	133
Figure 4.11: Relative ICA surface area exposure to TAWSS below the 20 th percentile threshold and OSI, transWSS and TAWSS above the 80 th percentile threshold. Threshold values were calculated from parameter distributions for the block phantom model. Error bars represent threshold sensitivity, indicating the area exposed for +/- 5 percentile thresholds.	134
Figure A.1: Central-plane instantaneous ensemble-averaged velocity maps for the 50% eccentric geometry (a, d) followed by corresponding maps of uncertainty in the velocity propagated from measurement errors only (b, e) and uncertainty propagated from combined measurement errors and flow fluctuations (c, f). The time point of peak systole is shown in the top row (a-c) and diastole in the bottom row (d-f).....	157
Figure A.2: Contours of instantaneous WSS at peak systole. Each model is shown in two orientations, exposing the inner and outer walls of the ICA on the left and right, respectively. Note that each row of models has an individual color bar.	158
Figure A.3: Contours of instantaneous WSS magnitude at peak systole for the 50% eccentric geometry along with corresponding maps of WSS uncertainty estimated from simulations.	159
Figure A.4: Contours of instantaneous WSS magnitude at diastole for the 50% eccentric geometry along with corresponding maps of WSS uncertainty estimated from simulations.	160
Figure A.5: Contours of transWSS normalized by the site-specific TAWSS. Each model is shown in two orientations, exposing the inner and outer walls of the ICA on the left and right, respectively.....	161
Figure B.1: Volumetric flow, pressure, and velocity waveforms for the three cases of high, intermediate, and low pulsatility index (PI) for the 30% stenosed model. Flow and pressure	

waveforms were measured via electromagnetic flowmeters and pressure transducer at the inlets and outlets of the phantom at locations. Velocity waveforms were extracted from PIV data at sections S1, S3 and S4 shown in Figure 3.1a for the CCA, ICA, and ECA respectively.163

Figure B.2: ICA-averaged TI versus cardiac cycle phase for the three inlet waveforms applied in the 30% stenosed model, calculated from central-plane TI maps. The dotted blue line indicates the time of peak systole, for phase reference..... 164

List of Symbols and Abbreviations

Symbols

C	compliance
CC	cross-sectional compliance
d	distensibility coefficient
E_{inc}	incremental elastic modulus
E_p	Peterson's elastic modulus
G	Young's modulus
Re	Reynolds number
T	cardiac cycle period
\vec{t}	traction vector
U_i	phase-averaged velocity component in the i^{th} direction
u_i	instantaneous velocity component in the i^{th} direction
u_i'	velocity fluctuation component in the i^{th} direction
γ	shear strain
$\dot{\gamma}$	strain rate
η	dynamic viscosity
ρ	density
σ	stress tensor
σ_{ij}	stress component on i -plane in j -direction
τ	shear stress
ω	vorticity

Abbreviations

2D	two-dimensional
2D2C	two-dimensional two-component
2D3C	two-dimensional three-component
3D	three-dimensional
3D3C	three-dimensional three-component
4D	time-varying three-dimensional
CCA	common carotid artery
CCD	charge-coupled device
CFD	computational fluid dynamics
CMOS	complementary metal oxide semiconductor
CT	computed tomography
DOSI	directional oscillatory shear index
DUS	Doppler ultrasound
EC	endothelial cell
ECA	external carotid artery
ECST	European Carotid Surgery Trial
eNOS	endothelial nitric oxide synthase
FFT	fast Fourier transform

FSI	fluid-structure interaction
ICA	internal carotid artery
ICAM1	intercellular adhesion molecule 1
ICA-TI	ICA-averaged turbulence intensity
ICH	intracerebral hemorrhage
KIF2	kruppel-like factor 2
LDA	laser doppler anemometry
LDL	low-density lipoprotein
LDV	laser doppler velocimetry
MCP1	monocyte chemotactic protein 1
MFD	microfluidic device
MR	magnetic resonance
MRI	magnetic resonance imaging
NASCET	North American Symptomatic Carotid Endarterectomy Trial
NF- κ B	nuclear factor κ B
N-fluid	Newtonian fluid
nN-fluid	non-Newtonian fluid
NO	nitric oxide
OSI	oscillatory shear index
OSI ₈₀	surface area coverage of OSI above 80 th percentile threshold
PC-MRI	phase-contrast magnetic resonance imaging
PDMS	polydimethylsiloxane
PECAM1	platelet endothelial cell-adhesion molecule-1
PI	pulsatility index
PTV	particle tracking velocimetry
RBC	red blood cell
RI	resistive index
ROI	region of interest
RSS	Reynolds shear stress
SAH	subarachnoid hemorrhage
SMC	smooth muscle cell
SS	shear stress
TAWSS	time-averaged wall shear stress
TAWSS ₂₀	surface area coverage of TAWSS below 20 th percentile threshold
TAWSS ₈₀	surface area coverage of TAWSS above 80 th percentile threshold
TI	turbulence intensity
\overline{TI}	ROI-averaged TI
TKE	turbulent kinetic energy
transWSS	transverse wall shear stress
transWSS ₈₀	surface area coverage of transWSS above 80 th percentile threshold
US	ultrasound
VCAM1	vascular cellular adhesion molecule 1
VE-cadherin	vascular-endothelial cadherin
VMTK	Vascular Modeling Toolkit
WSS	wall shear stress

Chapter 1

1 Introduction

1.1 Stroke, Atherosclerosis and the Carotid Artery

Stroke is a medical condition defined by the World Health Organization (WHO) as “rapidly developing clinical signs of focal (at times global) disturbance of cerebral function, lasting more than 24 hours or leading to death with no apparent cause other than of vascular origin” [1]. A stroke occurs when cerebral blood flow is compromised resulting in the death of brain cells due to lack of oxygen and subsequently, persisting brain injury and neurological deficit. The most common type of stroke is ischemic (87%), characterized by cerebral infarction due to thrombosis or embolism, followed by intracerebral hemorrhage (ICH, 10%) and subarachnoid hemorrhage (SAH, 3%).

Globally, stroke is the second leading cause of death behind ischemic heart disease (compromised blood supply to the heart due to coronary artery blockage), with 5.9 million deaths annually due to stroke, and the third leading cause of disability [2]. In a 2010 assessment of the global impact of stroke, there were an estimated 16.9 million incident strokes and 33 million stroke survivors worldwide [2]. In the United States, stroke is the fifth leading cause of mortality, with 795,000 people experiencing a new or recurrent stroke each year [3]. In Canada, stroke is the third leading cause of death [4] and there are an estimated 62,000 strokes each year [5]. The economic burden of stroke is also substantial, with the estimated total of direct (drugs, hospital costs, and physicians) and indirect (loss of productivity due to injury, illness, and mortality) costs of stroke reaching \$40 billion in the United States in 2015 [3] and approximately \$3.6 billion dollars in Canada in 2000 [6]. The prevalence of and mortality from stroke is expected to rise in the coming years due to population growth and aging [2].

There are several known risk factors for stroke of which some are non-modifiable such as age, gender, and ethnicity. Other common modifiable risk factors include hypertension

(high blood pressure), diabetes mellitus, heart disease (including heart rhythm disorders), hyperlipidemia (high cholesterol), smoking and tobacco use, alcohol consumption, physical inactivity, unhealthy diet/nutrition, obesity, sleep disordered breathing, environmental factors such as pollution, stress and depression [3; 7-9]. The risk for new or recurring stroke can be mitigated by lifestyle changes to improve modifiable risk factors as well as surgical or drug therapies, and a focus on prevention strategies and effective treatment and monitoring will be necessary to alleviate the burden of stroke [10-13].

Atherosclerosis is one of the primary causes of ischemic stroke. Atherosclerosis is characterized by a thickening or hardening of the arteries and the development of lesions, or plaques - composed of lipids, fibrous tissue and inflammatory cells - within the artery wall [14]. Atherogenesis, the initiation of the atherosclerotic process, begins early in life when the endothelial cell layer comprising the inner lining of the artery becomes damaged, and progresses with age. Over time, the gradual buildup of plaque results in the narrowing of the artery lumen, or a stenosis. Atherosclerotic plaques become problematic when they rupture or erode, causing the blockage of arteries (ischemia) by either 1.) thrombosis – the local occlusion of the vessel at the site of plaque due to a blood clot or 2.) thrombo- or athero-embolism – thrombotic material or eroded plaque components, respectively, break off and travel downstream to block narrower peripheral arteries.

Atherosclerosis shares many of the same risk factors as stroke, including hypertension and hyperlipidemia, smoking, diabetes, age, gender, race, etc. [15], emphasizing the link between them. Despite these systemic risk factors affecting the entire body uniformly, the early development of atherosclerotic lesions is highly focal and non-uniform, selectively occurring mainly at branches and bifurcations (i.e. carotid, coronary or femoral artery bifurcations), bends and curvatures (i.e. aortic arch). The affinity for plaques to develop in specific geometrical configurations suggests that local mechanical factors, such wall shear stress (WSS) imparted by local blood flow, potentiate atherogenesis [16]. Many studies have shown that hemodynamics play a key role in both the localization and the vulnerability of plaques, stimulating endothelial dysfunction and atherogenesis [17]. The

complex relationship between hemodynamics and the development and progression of atherosclerosis is discussed further in Section 1.2.

The carotid artery bifurcation is particularly vulnerable to atherosclerosis. The carotid arteries are the major arteries supplying blood to the brain, head, and face. The common carotid artery (CCA) originates either from the aortic arch (left common carotid artery) or the brachiocephalic artery (right common carotid artery). Both the left and right CCA bifurcate (split) within the neck region into the internal carotid artery (ICA) - supplying blood to the brain - and the external carotid artery (ECA) – supplying blood to the head exterior and face. The disruption of plaque at the carotid bifurcation can potentially result in dire clinical consequences – a stroke or cerebrovascular event – and poses a significant risk [16]. Carotid artery disease is responsible for about 15% of ischemic strokes [18]. Therefore, the carotid artery remains the focus of a body of research to determine the link between hemodynamics and regions vulnerable to atherogenesis and atherosclerotic complications.

1.2 The role of hemodynamics in the development of atherosclerosis and thrombosis

The well-established systemic risk factors for atherosclerosis, outlined in Section 1.1, influence the entire vascular tree uniformly. However, atherosclerosis is a geometrically focal disease, with the distribution of atherosclerotic lesions developing preferentially at regions of flow complexity such as at curvatures or bifurcations, suggesting that hemodynamic forces play a critical role in the process of atherogenesis.

Wall shear stress (WSS), explained in detail in Section 1.3, is the frictional force exerted by blood on the vessel wall due to its viscosity. Blood flow may be laminar, meaning that the fluid flows in parallel layers as commonly found in straight vessel segments, in which WSS will be highly uniform in magnitude and direction. Alternatively, disturbed flow refers to flow which is non-uniform in nature, including vortices, recirculation, etc., in

which WSS is typically low in magnitude and may be oscillating or reversing in direction over time. The two regimes are associated with very different pathological outcomes.

This section describes how various aspects of the hemodynamic environment impact the pathology of atherosclerosis.

1.2.1 Low and Oscillatory Shear Stress Hypothesis

The theory linking the initiation of atherosclerosis with regions of low magnitude WSS was first proposed by Caro et al. [19], contradicting earlier work by Fry et al. [20] which suggested severely elevated shear stress caused endothelial dysfunction. Caro et al. [19] found that regions with elevated shear stress such as those seen at the flow divider of branching vessel geometries were spared from disease.

Early studies of flow and atherosclerosis made use of experimental techniques such as laser doppler anemometry (LDA) and flow imaging, typically under steady inlet flow conditions, in post-mortem vascular specimens obtained at autopsy, [19; 21; 22] or in simplified glass models [23]. Flow patterns in healthy models of the carotid bifurcation were characterized by elevated wall shear stress at the proximal ICA on the flow divider wall while the proximal carotid bulb region, opposite the flow divider was exposed to low and reversing flow behavior. Zarins et al. [21] found that the proximal and mid carotid sinus regions displayed the most marked intimal layer thickening while the CCA and ECA branches and the distal ICA showed little to no intimal change.

Pulsatile flow visualization experiments were performed by Ku and Giddens in glass models of the human carotid bifurcation using hydrogen bubble techniques [24]. They observed that pulsatile flow creates a continually changing region of flow separation, turbulent disturbances during systolic deceleration, and WSS vectors that change in magnitude and direction over time. In a follow up study, Ku et al. [25] used laser doppler velocimetry (LDV) to quantitatively measure velocity and WSS in a glass carotid bifurcation model under physiological pulsatile flow and compared the results to the distribution of intimal plaques in human carotid bifurcation specimens obtained at autopsy.

They proposed the oscillatory shear index (OSI) to describe the cyclic variation in the WSS vector during pulsatile flow and quantify the deviation of the WSS vector from its predominant direction. In the carotid bifurcation geometry, OSI was highest in the proximal ICA and mid carotid sinus opposite the flow divider, and low but non-zero at the side wall of the proximal ICA. Intimal thickness was found to be inversely correlated with maximum WSS and average WSS and significantly correlated with OSI.

The OSI parameter was redefined to apply to a general three dimensional (3D) case in a later study of the coronary bifurcation [26] and the updated definition has been widely used to quantify oscillatory shear stress behavior. In general, sites with low magnitude of shear stress tend to coincide with those experiencing shear stress oscillations, thus the low and oscillatory shear stress hypotheses have merged into one.

Modern studies of hemodynamics and atherosclerosis use various medical imaging techniques including doppler ultrasound (DUS), computed tomography (CT) for vessel geometry imaging, magnetic resonance imaging (MRI), numerical simulations or some combination thereof. These will be discussed further in Section 1.4.

1.2.2 The response of the Vessel Endothelium to Pathological Shear Stress

Endothelial cells (ECs) have many functions, including the transport of molecules from blood to tissue, the regulation of vascular tone, vasoconstriction and vasodilation and regulation of blood pressure, the adhesion of leukocytes to the wall, as well as inflammatory responses. ECs form the interface between flowing blood and tissue, and regional differences in blood flow locally modulate endothelial gene expression. ECs contain mechanoreceptors which sense changes in blood flow and transfer these mechanical stimuli into biochemical responses, a process known as mechanotransduction. There are multiple mechanisms of mechanotransduction, including but not limited to ion channels, integrins and the cytoskeleton, G proteins and G-protein-coupled receptors, junction proteins such as platelet/endothelial cell-adhesion molecule-1 (PECAM1), adhesion molecules such as vascular-endothelial cadherin (VE-cadherin) and various

growth factors. Many researchers have examined the process of mechanotransduction and the various pathways involved and the reader is directed to the following for a more exhaustive review: Berk 2008 [27], Chatzizisis et al. 2007 [28], Chien 2003 [29], Chien 2008 [30], Davies 1995 [31], Davies 2009 [32], Hahn and Schwartz 2009 [33], Li et al. 2005 [34], Orr et al. 2006 [35], Malek et al. 1999 [36], Resnick et al. 2000 [37], Tarbell et al 2014 [38].

The two distinct flow environments characterized by either high magnitude, laminar flow or low magnitude, disturbed flow impact the endothelium in contradictory ways, suppressing or inducing the expression of relevant genes and changing the morphology and function of ECs resulting in either an atheroprotective or atheroprone phenotype, respectively.

Endothelial cells respond to increased flow (shear stress, SS) by relaxation of surrounding smooth muscle cells via the release of nitric oxide (NO) activated by endothelial nitric oxide synthase (eNOS) and prostacyclin, responsible for regulating vascular tone and anti-inflammatory responses. Physiological shear stress (on the order $\sim 1.5\text{-}2$ Pa) promotes the elongation and alignment of ECs in the direction of flow [36]. In these regions, ECs develop long well-organized parallel actin stress fibers and F-actin filaments [39; 40]. The amount of EC elongation is typically proportional to the magnitude and duration of the applied shear stress [40; 41]. In regions of high laminar shear there is also a decrease in EC turnover, suppression of inflammatory mediators, activation of antioxidant pathways that decrease levels of reactive oxygen species, and increased levels of the transcription factor kruppel-like factor 2 (KLF-2), which has been linked to the expression of atheroprotective genes [33].

In contrast, when the flow is disturbed and the shear stress is low, endothelial cells fail to align in the flow direction, exhibit higher rates of proliferation and apoptosis and higher permeability to solutes [33; 34; 42]. In these regions there is also an increase in the adhesion receptors intercellular adhesion molecule 1 (ICAM1) and vascular cell adhesion molecule 1 (VCAM1), and chemokines such as monocyte chemoattractant protein 1 (MCP1) [33]. These

components work to recruit leukocytes to the vessel wall and maintain inflammation. Chiu et al. observed that endothelial cells located at the reattachment point of a vertical step flow chamber, where shear tends to be oscillatory, exhibited a more rounded morphology with short actin filaments and increased DNA synthesis suggesting enhanced cell turnover [39]. High rates of endothelial cell turnover expose the underlying intima, (which may contain collagen, tissue factor, and other procoagulant and proinflammatory mediators) and are associated with an increase in permeability of macromolecules such as low-density lipoprotein (LDL) cholesterol across cell junctions, leading to focal accumulation of lipids [27; 30].

1.2.3 Multidirectional Shear Stress

The low and oscillatory shear stress hypothesis for atherogenesis is generally accepted, however, more recently efforts have been made to distinguish between different types of shear oscillations, namely between uniaxial forward and reverse shear stress and truly multidirectional disturbed shear stress.

Peiffer et al. [43] conducted a systematic review of studies which had used computational modeling and in-vivo vessel geometries to correlate computed WSS patterns with lesion development. They found a wide variation in measurement techniques, methods to assess disease, as well as data reduction and statistical analysis. While many of the reviewed studies claimed to support the low/oscillatory shear hypothesis, among the most robust studies conducting point-by-point comparison all of them failed to find a significant correlation between low WSS magnitude or OSI and wall thickness [44-48]. However, it is noted that measuring wall thickness alone does not isolate intimal thickening specifically due to the presence of atherosclerosis. Moreover, two of the studies did observe early plaque formation at low and oscillatory shear stress regions upon visual inspection only [44; 46].

The above discrepancies prompted the question of whether traditional metrics used to assess the low and oscillatory nature of shear stress, such as TAWSS and OSI, failed to

capture some physiologically relevant features of the flow. Peiffer et al. proposed a new metric, the transverse wall shear stress (transWSS), which calculates the cumulative amount of wall shear stress directed normal to the direction of the mean WSS vector over the cardiac cycle for a specific location. [49] In subsequent in-vitro animal studies, it was shown qualitatively that the transWSS correlated better with lesion frequency than did the conventional metrics of TAWSS or OSI [49; 50]. However, one limitation of the new metric is that it becomes ambiguous when the mean WSS vector is not well defined.

The impact of flow direction on ECs was investigated in vitro by Wang et al. [51] using a custom flow system allowing the orientation of the applied stress with respect to EC alignment to be manipulated [52]. ECs that were pre-aligned exhibited increased phosphorylation of eNOS for a 180 degree change in direction of applied stress, and maximum nuclear factor κ B (NF- κ B) activation for a 90 degree change. However, if the cells were not pre-aligned, no significant changes were observed, indicating that the orientation/angle of applied stress relative to the cytoskeletal axis of the cell is critical and that cross-flow, rather than simply uniaxial changes in direction, leads to an atheroprone phenotype. It should be noted though, that applied flow was laminar and ECs were exposed to the same flow conditions over long periods. No investigation of pulsatile flow effects or cyclic variation in direction of applied stress over short time periods was investigated.

The impact of cyclic bi-directional shear stress on ECs was examined by Chakraborty et al. [53] using an orbital shaker, capable of producing uniaxial shear stress at the periphery of the cell dish with bi-axial oscillating shear at the dish center. Computational simulations were used to calculate the shear stress distribution within the dish. A new parameter, the directional oscillatory shear index (DOSI) was applied to quantify the relative magnitude of shear stress oscillations in two principal directions. (DOSI ranges from 1 for uniaxial oscillatory shear stress to zero for equal shear stress oscillations in both directions.) Near the center of the dish where DOSI was low, an increase in cell proliferation was observed as well as random cell orientation. Cell alignment with the dominant tangential direction of flow and elongation increased with increasing radial location. In a following study [54]

it was shown that DOSI impacted the expression of pro-atherogenic genes, whereas shear stress magnitude alone did not.

1.2.4 Disturbed Flow and Platelet interactions

In the presence of established plaques, flow complexity increases substantially. In particular, following a stenosis or constriction in vessel diameter distinct flow patterns are observed, including flow acceleration through the stenosis resulting in a high velocity jet, flow separation and recirculation into the expansion region, vortex shedding and downstream flow disturbances as well as strong spatial velocity gradients in the region between the core jet flow and the adjacent recirculation. In addition, flow pulsatility introduces temporal velocity and shear gradients associated with flow acceleration and deceleration over the cardiac cycle. These complexities contribute to platelet activation, adhesion and aggregation and subsequently thrombus formation.

Elevated shear rates experienced within the stenosis contribute to platelet activation. Holme et al. [55] found that shear stress on the order of 30 Pa, such as those experienced within moderate to severe stenosis, activated platelets and caused microparticle formation while exposure to common physiological shear rates did not. Sudden accelerations in shear also promote the development of platelet membrane tethers [56]. In-vitro studies of blood in a rotational viscometer have found that in very severe cases, at extremely high levels of shear stress (1500 dynes/cm²), hemolysis (rupture) of red blood cells may occur [57].

In the post-stenotic expansion region, flow deceleration and recirculation promote longer residence times and increased collision rates and increased discoid platelet aggregation is observed [56]. Low shear rates observed in these regions also favor the adhesion of platelets at the vascular wall [58]. Vortex shedding typically occurs in the region between the core jet flow and the adjacent recirculation. In the study of an 84% area reduction axisymmetric stenosis, Bluestein et al. [59] found that at low Reynolds number (Re , see Section 1.3.5), the amount of platelet deposition peaked at the jet reattachment point. Conversely for high Re cases (>1000) maximum platelet deposition, was higher in

magnitude and occurred very close to the stenosis throat, corresponding with an upstream shift in the vortex formation region. Platelets potentially activated by exposure to high shear and subsequently entrapped in vortices could potentially lead to the formation of free emboli [60].

Turbulence, characterized by random and irregular fluctuations in fluid motion and flow velocities, can occur downstream of stenoses and increases with inlet velocity magnitude and stenosis severity. In vitro studies measuring thrombus formation on artificial surfaces found that significantly more platelet aggregates were produced under turbulent compared to laminar conditions [61; 62]. In addition, a linear relationship was observed between both 1.) turbulence intensity, and 2.) the size and number of platelet aggregates with inlet Re , suggesting that the weight of thrombi produced is related to the level of flow disturbances [62]. Bluestein et al. [58] concluded that differences in downstream platelet aggregation could be attributed to unsteady flow development as a result of increasing Re . In addition, stenosis asymmetry has been shown to influence the intensity of downstream flow fluctuations [63-65].

Finally, strong temporal flow acceleration and deceleration experienced under more physiological pulsatile flow conditions creates strong temporal shear gradients that enhance platelet aggregation. Nesbitt et al. [56] observed that platelets aggregated during the flow deceleration phase of the cardiac cycle and disaggregated during the flow acceleration of the following cycle, and that the size of aggregates was dependent upon the magnitude of shear gradients. For moderate to high stenosis and appropriate inlet flow conditions, transition to turbulence occurs just prior to peak systole and substantial velocity fluctuations occur near the reattachment point during the deceleration portion of the flow cycle [63]. More platelet aggregation was observed under pulsed exposure to shear stress compared to continuous exposure for the same cumulative exposure time to stress [66] emphasizing the role of temporal shear and velocity gradients in platelet interactions and thrombosis [58].

1.2.5 High Shear Stress and Plaque Vulnerability

While the focal development of atherosclerosis is typically associated with low magnitude, oscillatory wall shear stress, cardiovascular events are often the result of rupture of vulnerable plaques. Both tensile stress within the plaque itself and fluid shear stress exert potentially risky forces which could lead to rupture, ulceration, thrombosis, and embolism. Although high shear stress is thought to be atheroprotective to the healthy endothelium in regions without plaques, high shear stresses are implicated in thinning of the plaque fibrous cap and the spatial variations in plaque susceptibility to rupture.

Determining the exact cause of plaque vulnerability and rupture proves difficult because the instances of pre- and post-rupture imaging are rare. Nevertheless, there is still a great interest in determining the effect of wall shear stress on the development of plaques, plaque structure and their vulnerability to rupture [67].

In an isolated longitudinal case study, Groen et al. [68] found that at 11 month follow-up, an ulcer had developed in the plaque where numerical simulation in the baseline geometry predicted the highest WSS. Lovett et al. [69] compared the sites of plaque ulceration in carotid plaques from angiograms of carotid stenosis as well as pathologically and found that plaque ulceration was more likely to occur upstream of the point of maximum stenosis. Additionally, the proportion of patients with proximal ulceration increased with stenosis severity whereas the number with distal ulceration was not affected, suggesting that increased WSS with increased stenosis impacts upstream ulcerations. In a study comparing the smooth muscle cell (SMC) and macrophage content of carotid artery plaques, Dirksen et al. [70] showed that the proximal side of the plaque (upstream of the narrowest lumen diameter) had significantly more macrophages compared to SMCs, where plaques dominated by SMCs are considered stable, and the macrophage areas were much larger in the upstream shoulder of the plaque. Moreover, the majority of ruptured plaques had occurred proximal to the stenosis.

Some studies have suggested that the 3D mechanical stresses, as opposed to fluid shear stresses are most important when determining plaque vulnerability. Leach et al. [71] found that the WSS at the site of plaque rupture was actually at a minimum and instead the rupture site coincided with the maximum tensile stress caused by systemic pressure. While Teng et al. [72] concluded that critical stresses were more important in determining plaque vulnerability, they still measured 76% higher shear stress in rupture group.

1.3 Fluid Mechanics

This section gives an overview of the physical concepts of fluid motion necessary to calculate important hemodynamic parameters such as wall shear stress and turbulence intensity. For brevity, equations are shown for incompressible Newtonian fluids only, and rigorous derivations are not provided. (See Section 1.5.2 for a brief introduction to non-Newtonian fluids.)

1.3.1 The Stress Tensor

A stress is a physical quantity that expresses the force per unit area in a continuous material which neighbouring fluid elements exert on one another due to deformation, or strain. It is equal to the force per unit area acting on an infinitesimal boundary or surface element. When the stress is applied perpendicular to the surface it is referred to as a normal stress and when it is parallel, or tangential, to the surface it is referred to as a shear stress. In elastic solids, the applied stress is linearly related to the deformation (strain) of the material, and the proportionality constant is the elastic modulus, denoted G for shear stress/strain (Figure 1.1a).

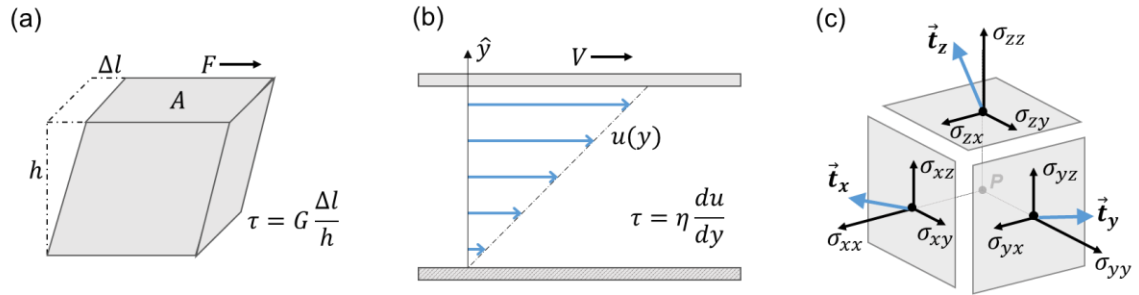


Figure 1.1: (a) A shear stress applied to an elastic material is related to the deformation by the elastic modulus, G . (b) In a simple shear flow, the shear stress on the fluid is related to the rate of deformation. (c) The elements of the stress tensor in three dimensions acting on a fluid element at point P .

A fluid, however, deforms continuously and irreversibly when a stress is applied, and the stress is related to the *rate* of deformation. Consider the simple shear flow in Figure 1.1b, with fluid between parallel plates, the top plate moving at some speed V with respect to the bottom which is stationary. The fluid near the plates obeys the no-slip condition: fluid in contact with a solid boundary will have zero velocity with respect to the boundary. The layers of fluid adjacent to the top plate will also begin to flow, and once equilibrium is reached, will also have velocity V . A linear flow profile develops between the plates, and the force per unit area, or stress on the fluid layers is proportional to the velocity gradient or the strain rate:

$$\tau = \eta \frac{\partial u}{\partial y} = \eta \frac{\partial \gamma}{\partial t} = \eta \dot{\gamma} \quad (1.1)$$

where τ is the stress, u is the horizontal velocity, y is the vertical distance, γ is the strain, $\dot{\gamma}$ is the strain rate (time derivative of strain) and η is the viscosity which describes the resistance of a particular fluid to flow. Equation 1.1 is known as Newton's law of viscosity.

Consider now the three-dimensional case, depicted in Figure 1.1c, describing the stress acting at a point P within the fluid. Three orthogonal reference planes oriented in the directions of the coordinate axes are depicted. The coordinate stress, σ_{ij} , denotes the

component of stress acting on the i -plane in the j -direction. The coordinate stresses are elements of the stress tensor, $\boldsymbol{\sigma}$, at point P:

$$\boldsymbol{\sigma} = \begin{pmatrix} \sigma_{xx} & \sigma_{xy} & \sigma_{xz} \\ \sigma_{yx} & \sigma_{yy} & \sigma_{yz} \\ \sigma_{zx} & \sigma_{zy} & \sigma_{zz} \end{pmatrix} \quad (1.2)$$

The diagonal elements of the stress tensor ($\sigma_{ij}, i = j$) represent the normal stresses, and the remaining elements ($\sigma_{ij}, i \neq j$) represent shear stresses. The stress tensor is symmetric, therefore

$$\sigma_{ij} = \sigma_{ji} \quad (1.3)$$

The stress vector, \mathbf{t}_x , acting on the x-plane is the usual sum of components in the x, y, and z directions, as shown.

$$\mathbf{t}_x = \sigma_{xx}\hat{\mathbf{x}} + \sigma_{xy}\hat{\mathbf{y}} + \sigma_{xz}\hat{\mathbf{z}} \quad (1.4)$$

For an arbitrarily oriented surface located at point P with unit normal vector $\hat{\mathbf{n}}$ the stress (or traction) vector on that surface is given by the dot product of the surface normal and the stress tensor at that point:

$$\mathbf{t}_n = \hat{\mathbf{n}} \cdot \boldsymbol{\sigma} \quad (1.5)$$

The total stress tensor can be written as

$$\boldsymbol{\sigma} = -p\mathbf{I} + \boldsymbol{\tau} \quad (1.6)$$

where p is the pressure, \mathbf{I} is the identity tensor and $\boldsymbol{\tau}$ is the viscous (or deviatoric) stress tensor. The pressure is isotropic (acts equally in all directions) and only acts normally to the surface thereby only affecting the normal stress components. In the case where the fluid is at rest, the total stress tensor is equal to the pressure. The viscous stress tensor, which contains the shear stresses, results from the deformation of the fluid. It is related to the motion of the fluid by

$$\boldsymbol{\tau} = \eta \dot{\boldsymbol{\gamma}} = \eta(\nabla \mathbf{u} + (\nabla \mathbf{u})^T) \quad (1.7)$$

where η is the viscosity of the fluid, $\dot{\boldsymbol{\gamma}}$ is the rate-of-strain tensor representing the symmetric part of the velocity gradient, and \mathbf{u} is the velocity vector. Equation 1.7 is a *constitutive equation* (for an incompressible Newtonian fluid) which specifies the response of the fluid to flow or deformation. Using index notation we can write the viscous stress tensor as

$$\tau_{ij} = \eta \left(\frac{\partial u_i}{\partial x_j} + \frac{\partial u_j}{\partial x_i} \right) \quad (1.8)$$

For completeness, the antisymmetric part of the velocity gradient is the vorticity tensor

$$\boldsymbol{\omega} = (\nabla \mathbf{u} - (\nabla \mathbf{u})^T) = \nabla \times \mathbf{u} \quad (1.9)$$

and combining them gives the velocity gradient, or deformation tensor:

$$\nabla \mathbf{u} = \frac{\partial u_j}{\partial x_i} = \frac{1}{2}(\dot{\boldsymbol{\gamma}} + \boldsymbol{\omega}) \quad (1.10)$$

The vorticity represents a pure rotation of the fluid, in which the individual distances between particles does not change and thus it does not contribute to the viscous stress tensor.

1.3.2 The Navier-Stokes Equations

The motion of a fluid is governed by two laws, the conservation of mass, and the conservation of momentum. The general conservation of mass equation is given by

$$\frac{\partial \rho}{\partial t} + \nabla \cdot (\rho \mathbf{u}) = 0 \quad (1.11)$$

where ρ is the fluid density. However, for an incompressible fluid, the density is constant in time and space and the equation reduces to

$$\nabla \cdot \mathbf{u} = 0 \quad (1.12)$$

The conservation of momentum equation is Newton's second law of motion, which states that the change in momentum must be equal to the sum of the applied forces. Both external body forces, such as gravity or magnetic field, and internal surface forces, such as viscous stresses, act within a fluid. In its general form, the conservation of momentum equation is

$$\rho \frac{\partial \mathbf{u}}{\partial t} + \rho \mathbf{u} \cdot \nabla \mathbf{u} = \nabla \cdot \boldsymbol{\sigma} + \mathbf{f} \quad (1.13)$$

where $\boldsymbol{\sigma}$ is the stress tensor and \mathbf{f} represents body forces on the fluid. Using the constitutive equation in 1.7 for an incompressible Newtonian fluid as well as 1.12 gives

$$\rho \frac{\partial \mathbf{u}}{\partial t} + \rho \mathbf{u} \cdot \nabla \mathbf{u} = -\nabla p - \eta \nabla^2 \mathbf{u} + \mathbf{f} \quad (1.14)$$

Equations 1.12 and 1.14 are the incompressible Navier-Stokes equations for a Newtonian fluid. They represent a closed set of equations that can be solved analytically in some cases or numerically, such as in computational fluid dynamics (CFD) simulations.

1.3.3 Wall Shear Stress Calculation from Measured Data

This section describes the method used to obtain the wall shear stress for the purposes of this thesis. The 3D three-component (3D3C) velocity data is acquired using particle image velocimetry (See Section 1.4.3) and the reconstructed vessel surface is obtained via segmentation from micro-CT scans. Thus, we have volumetric velocity data arranged in a Cartesian grid, as well as locations and normal vectors corresponding to the nodes of a coarse tetrahedral surface mesh representing the vessel wall.

If the 3D velocity components, as well as the fluid viscosity, are known at every point within the measurement volume, then the components of the stress tensor may be calculated at any location using Equation 1.8. To calculate the WSS at a point on the vessel surface, we can apply Equation 1.5, and take the dot product of the inward normal to the

surface and the stress tensor at that point. The challenge comes in calculating the local velocity gradients at the wall from discrete data. Here, a method is used that is similar to those applied for WSS calculation based on phase-contrast magnetic resonance imaging (PC-MRI) in which both anatomical and flow information are available [73-76].

The expanded components of the viscous stress tensor are:

$$\boldsymbol{\tau} = \eta \begin{pmatrix} \tau_{11} & \tau_{12} & \tau_{13} \\ \tau_{21} & \tau_{22} & \tau_{23} \\ \tau_{31} & \tau_{32} & \tau_{33} \end{pmatrix} = \eta \begin{pmatrix} 2 \frac{\partial u_x}{\partial x} & \frac{\partial u_x}{\partial y} + \frac{\partial u_y}{\partial x} & \frac{\partial u_x}{\partial z} + \frac{\partial u_z}{\partial x} \\ \frac{\partial u_y}{\partial x} + \frac{\partial u_x}{\partial y} & 2 \frac{\partial u_y}{\partial y} & \frac{\partial u_y}{\partial z} + \frac{\partial u_z}{\partial y} \\ \frac{\partial u_z}{\partial x} + \frac{\partial u_x}{\partial z} & \frac{\partial u_z}{\partial y} + \frac{\partial u_y}{\partial z} & 2 \frac{\partial u_z}{\partial z} \end{pmatrix} \quad (1.15)$$

The surface points as well as their normal vectors are oriented arbitrarily with respect to the velocity data. The calculation of the traction vector $\mathbf{t} = \hat{\mathbf{n}} \cdot \boldsymbol{\tau}$ is simplified if the normal vector is directed along one of the coordinate axis. In addition, we also assume no flow through the vessel wall such that $\hat{\mathbf{n}} \cdot \mathbf{u} = 0$ at the wall location. Then if $\hat{\mathbf{n}} = (0,0,1)$ is directed in the positive z-direction, the traction vector reduces to [74]

$$\mathbf{t} = \eta \left(\frac{\partial u_x}{\partial z}, \frac{\partial u_y}{\partial z}, 0 \right) \quad (1.16)$$

According to Equation 1.16, we need only calculate the velocity gradient along the inward normal of the components of velocity parallel to the surface.

The WSS calculation was performed at each wall point individually via the following steps:

- 1.) The 3D velocity components were interpolated at four evenly spaced query points along the inward normal from the measured velocity data.
- 2.) a coordinate transformation (a rotation with respect to the wall point) is applied to the interpolated velocity data points such that the normal direction corresponds to the new z' -axis.
- 3.) The velocity gradients are determined in the rotated frame. For each component, a cubic spline fit was applied to the four velocity data values plus the wall location assigned zero velocity and the derivative

of the fit at the wall was calculated. 4.) The traction vector was calculated as in Equation 1.16 and then an inverse rotation was applied to return to the original reference frame.

The advantages of this method are 1.) the wall location information from CT is used, thus no assumptions must be made about the location of the wall with respect to the PIV grid and 2.) it allows the WSS vector to be obtained, containing both magnitude and direction, allowing additional shear stress metrics to be calculated.

1.3.4 Wall Shear Stress Metrics

The following time-integrated WSS metrics are studied in this thesis:

Time-averaged WSS (TAWSS) – the average magnitude of the WSS at a single location over the cardiac cycle with period T .

$$\text{TAWSS} = \frac{1}{T} \int_0^T |\boldsymbol{\tau}_w| dt \quad (1.17)$$

Oscillatory Shear Index (OSI) – In its original formulation, the OSI was used to describe “the cyclic departure of the wall shear stress vector from its predominant direction” [25; 26]. It compares the magnitude of the time-averaged WSS *vector* with the TAWSS. The OSI is dimensionless and ranges from 0-0.5, with 0 corresponding to no oscillations and 0.5 corresponding to purely oscillatory WSS.

$$\text{OSI} = \frac{1}{2} \left[1 - \left(\frac{|\int_0^T \boldsymbol{\tau}_w dt|}{\int_0^T |\boldsymbol{\tau}_w| dt} \right) \right] = \frac{1}{2} \left[1 - \left(\frac{|\boldsymbol{\tau}_{\text{mean}}|}{\text{TAWSS}} \right) \right] \quad (1.18)$$

Transverse Wall Shear Stress (transWSS) – the time average of WSS components perpendicular to the direction of the time-averaged WSS vector [49]. The transWSS value ranges from 0 to the TAWSS. A normalized transWSS can also be obtained by dividing transWSS by the local TAWSS value.

$$\text{transWSS} = \frac{1}{T} \int_0^T \left| \boldsymbol{\tau}_w \cdot \left(\mathbf{n} \times \frac{\int_0^T \boldsymbol{\tau}_w dt}{\left| \int_0^T \boldsymbol{\tau}_w dt \right|} \right) \right| dt \quad (1.19)$$

1.3.5 Turbulence Intensity

Flow may be described as either laminar or turbulent. Laminar flow (from the Latin, “lamina”, meaning layer) describes well-organized flow where fluid particles slide across one another in parallel layers. Conversely, turbulent flow is characterized by irregular and chaotic changes in pressure and velocity in both space and time. Turbulence is also associated with high local values of vorticity, the presence of vortical structures and eddies, and increased diffusivity and mixing. Turbulence is a dissipative process and kinetic energy is transferred from large eddies down to small eddies via the cascade process where it is transformed into thermal energy.

The Reynolds number is a dimensionless parameter often used to predict flow behaviour, or the transition from laminar to turbulent regime, for a specific type of flow. It is defined as the ratio of inertial to viscous forces in the flow and calculated as

$$Re = \frac{\rho u L}{\eta} \quad (1.20)$$

where ρ is the fluid density, u is the characteristic velocity, L is the characteristic length scale for the flow, and η is the fluid viscosity. Laminar flows are highly affected by viscous forces, while turbulence arise more readily at lower viscosities and high velocities. For flow in a vessel or pipe, the characteristic length scale is the diameter of the vessel and the critical Reynolds number, where the laminar to turbulent transition takes place, is approximately 2300 [77]. However, many factors influence when the transition will take place, including smoothness of the vessel wall and the shape of the entrance region. Many studies have focused on determining the critical Re for common biological flows such as pulsatile flow in tubes [78-80].

The instantaneous velocity at any time point can be written as the sum of the mean velocity, U_i , and a fluctuating turbulent component, denoted u_i' . This formulation is known as a Reynolds' decomposition [81]:

$$u_i = U_i + u_i' \quad (1.21)$$

where $i = x, y, z$ specifies the velocity component. Turbulence may be quantified from measured data using statistical quantities. In this case, we use the turbulence intensity (TI) metric defined as follows. The mean velocity in the case of pulsatile flow refers to the phase average:

$$U_i(t) = \frac{1}{N} \sum_{n=0}^{N-1} u_i(t + nT) \quad (1.22)$$

where T refers to the period of the pulsatile cycle and N is the number of cardiac cycles averaged. Then each turbulence intensity (TI) component is calculated as the rms of corresponding velocity fluctuations

$$TI_i(t) = \sqrt{\frac{\sum_{n=1}^N u_i'(t, n)u_i'(t, n)}{N - 1}} \quad (1.23)$$

and the total turbulence intensity metric at a specific phase is

$$TI(t) = \sqrt{(TI_x(t))^2 + (TI_y(t))^2 + (TI_z(t))^2} \quad (1.24)$$

1.4 Measuring and Modeling Hemodynamics

1.4.1 In-vivo Measurements

The two main techniques for measuring hemodynamics in-vivo are doppler ultrasound (DUS) and phase-contrast magnetic resonance imaging (PC-MRI). Both ultrasound and

MRI are non-invasive imaging techniques which can also be used to derive anatomical information. They are described briefly below.

1.4.1.1 Doppler Ultrasound

Ultrasound imaging is a pulse-echo technique which uses the transmission and reception of high frequency sound waves within tissue. Reflections arise due to acoustic impedance mismatch between different tissue structures which can be located along the beam path based on the timing of the reflected pulse and the average speed of sound. DUS is based on the principle of the Doppler effect – estimating the velocity of a moving target (ie. blood) based on a shift in frequency of the echo pulse. Conventional DUS measures the frequency shift along the beam direction, and the angle of the beam with respect to the suspected flow direction must be known to obtain accurate results.

Extensions of the basic DUS principle have allowed for more complex flow information to be derived. Cross-beam techniques utilizing multiple transmitters and receivers allow two- and three-component velocity vectors to be measured [82; 83]. Pulsed wave spectral DUS applies short bursts of transmitted pulses and can be used to obtain a sonogram of the distribution of velocities within a sample volume. Spectral doppler techniques have been applied in-vivo to estimate turbulence based on spectral broadening [84]. In multi-gate DUS, several doppler spectra are collected from offset sample volumes or ‘gates’ along the beam direction, allowing both velocity profiles and localized wall shear rate to be obtained [85]. Colour DUS, which combines conventional US and DUS to provide composite images of colour encoded blood velocity maps and vessel anatomy, has been applied to measure flow patterns in the carotid artery [86; 87]. Finally, the application of cross-correlation techniques - typically used in PIV processing - to the natural speckle patterns of red blood cell “scatterers” in consecutive US images has allowed velocity vector maps to be obtained. This technique is sometimes referred to as echo PIV and its feasibility has been demonstrated in the carotid artery [88; 89].

Advances in processing power and parallel acquisition systems have allowed for ultrafast, high frame-rate US, in which large areas are insonated at once via spherical or plane-wave transmission [90; 91]. The temporal resolution of high-frame rate systems is on the order 1 kHz. Combined with cross-correlation post-processing algorithms, these techniques allow for 4D (time-varying 3D) velocity vector data to be obtained. The in-vitro and in-vivo feasibility of ultrafast US for flow imaging, as well as localized WSS measurement, within carotid arteries has been demonstrated [92-94]. Given the ability to capture 3D flow on short time scales, and the added ability of US to measure anatomical information, ultrasfast techniques show promise for the future of in-vivo flow imaging and possible 3D-WSS measurement [94].

1.4.1.2 Phase-Contrast Magnetic Resonance Imaging

Magnetic Resonance Imaging (MRI), very basically, is an anatomical imaging technique which measures the response of materials exposed to magnetic fields to construct an image. Velocity measurement using phase contrast MRI (PC-MRI) is accomplished based on the principle that magnetic resonance (MR) phase is related to velocity of moving blood [95]. During an MRI acquisition, the proton spins within a voxel acquire both magnitude and phase information. Under a magnetic gradient, phase accumulation occurs due to stationary and moving spins as well as a background phase offset due to field inhomogeneity. A bipolar gradient applied in the velocity encoding direction allows the phase accumulations due to static spins and background to be removed, and the resulting phase difference is directly proportional to the velocity of fluid in the voxel [95; 96].

4D flow MRI is an extension of the above technique, with velocity encoding in all three directions for a series of time-resolved volumetric image acquisitions, resulting in time-resolved 3D three-component velocity data. The feasibility of 4D-flow MRI techniques for blood flow quantification have been demonstrated both in-vitro and in-vivo [97; 98]. In-vivo quantification of WSS has been achieved by combining 4D flow MRI with MR angiography to derive lumen boundary information. Frydrychowicz [99; 100] measured segmental WSS in-vivo in the ascending aorta. Markl et al. [101] applied the technique to

map WSS and OSI in normal and stenosed carotid arteries. Dyverfeldt et al. developed a method using 4D flow MRI to quantify turbulence by measuring the standard deviation of the distribution of spin velocities within an MRI voxel, and validated the method in-vitro and in-vivo for aortic and cardiac flow imaging [102; 103].

Although MRI offers the ability to measure both anatomical as well as flow information, there are some limitations. To achieve sufficient spatial resolution, multiple gated acquisitions of many cardiac cycles must be collected over a long period of time (~20 minutes), limiting its clinical feasibility [95]. In addition, temporal resolution is low compared to DUS or optical techniques.

1.4.2 Numerical Modeling

Numerical modeling is a valuable tool for fluid dynamic study, as it is both time- and cost-effective in relation to other experimental techniques, and readily accessible. CFD, at its most basic level, involves solving the coupled partial differential equations of fluid motion (Navier-Stokes equations), over a discretized set of points within the flow domain, with the appropriate boundary and initial conditions applied. Numerical simulations may be readily applied to measure both steady-state and pulsatile time-resolved 3D velocity data. CFD is inherently able to calculate WSS, and thus the investigation of multi-directional WSS parameters like OSI and transWSS which require both magnitude and direction of the WSS vector over time, has been dominated by numerical studies.

Magnetic resonance (MR) or computed tomography (CT) angiography and 3D-US are clinical imaging techniques capable of providing structural information about the anatomy of blood vessels for purpose of CFD. The 3D greyscale images must then undergo image segmentation to obtain an accurate rendering of the vessel geometry which will define the boundary of the fluid domain [104]. Boundary conditions, usually pressure or flow waveforms or velocity profiles at the inlets/outlets of the fluid domain, may be obtained using 4D flow MRI or DUS. However, oftentimes assumed or idealized boundary

conditions (averaged across many individuals from cohort studies) are applied in the absence of patient-specific flow information.

Numerical modeling of hemodynamics is complicated by the arising flow complexities, for instance at stenosis with increasing Reynolds number, which may cause localized turbulence or transitional flow behavior. Solving the equations of motion with incorporated turbulence becomes difficult due to added unknown stresses arising in the Reynolds stress term (closure problem). Several different turbulence models have been applied to study transitional flows in simple stenosis geometries or stenosed carotid bifurcations [105-109].

Fluid-structure interaction (FSI) is a multiphysics modeling technique coupling the equations of fluid motion with structural mechanics describing the deformation of the boundary, allowing compliance effects to be considered. FSI models of stenosis have demonstrated that severe stenoses constrict wall motion resulting in higher downstream velocities and localized WSS [110]. Applications of FSI to study fluid shear stress as well as principle mechanical stresses on atherosclerotic plaques have been explored, with implications for the risk of plaque rupture [111; 112].

Validation of numerical predictions is required if the technique is to be applied as a clinical evaluation tool. While PC-MRI has been used to validate CFD predictions both in-vivo and in-vitro, [113; 114] PC-MRI suffers from its own limitations (described in Section 1.4.1.2). Particle image velocimetry (PIV), described below, is a “gold-standard” experimental technique used for full-field velocity vector characterization in-vitro, and due to its high temporal and spatial resolution, is a useful validation tool for both simulations and in-vivo flow measurements.

1.4.3 Physical Modeling: Particle Image Velocimetry

PIV is an optical flow visualization method which utilizes high-speed imaging of tracer particles in conjunction with sophisticated post-processing software to quantify fluid velocity. The PIV technique emerged in the late 1980s and early 1990s and has been steadily gaining popularity since. It can provide high spatial resolution ($10^3 - 10^5$ points)

for rapidly evolving flows to allow the computation of vorticity, rate of strain and turbulence, and has become a standard and invaluable measurement tool in fluid mechanics.

In PIV, the fluid displacement is inferred from the movement of tracer particles, selected to be sufficiently small and light so that they follow the motion of the fluid with high accuracy without impeding the flow. The basic experimental set-up consists of a light source, typically a double-pulsed laser equipped with sheet optics to form a thin light sheet, and a single digital camera oriented normal to the light sheet plane. The particles are illuminated (at least twice) by successive laser pulses separated by a known time interval Δt , and the camera records and stores the images in separate frames. The images are then processed by subdividing each camera frame into small interrogation windows. The local displacement of tracers is determined for each interrogation window by spatial cross-correlation of the two frames, which is typically facilitated/accelerated by fast Fourier transform (FFT) based algorithms. The correlation peak gives an estimate of the in-plane particle displacement within each window and the velocity ($\Delta x/\Delta t$) is assigned to the center of the interrogation window. Sub-pixel accuracy is achieved by fitting a Gaussian or similar function to the correlation peak. A velocity vector is obtained for each interrogation window in the image, thus building a two-dimensional two-component (2D2C) instantaneous velocity vector field. Overlap of the interrogation windows may be applied to reduce the spacing between vectors, obtaining a denser vector map.

The temporal evolution of velocity fields over time can be evaluated by collecting double-pulsed PIV image pairs in rapid succession. Temporal resolution of time resolved PIV is determined by the capabilities of the light source and cameras used. Most cameras typically used in PIV applications have either charge-coupled device (CCD) or complementary metal oxide semiconductor (CMOS) sensors. Modern CMOS sensors are capable of achieving recording rates up to 5kHz at 1024 x 1024 pixel resolution. The most commonly used laser for PIV is the Neodymium-YAG (Nd:YAG) laser at 532 nm. Modern Nd:YAG lasers for PIV applications are capable of repetition rates on the order of 10 kHz [115].

Stereoscopic PIV is an extension of the basic method described above, and the primary experimental measurement technique used in this thesis. The use of two cameras arranged at different viewing angles allows three components of velocity to be recovered. Comparison of the projections of a velocity vector obtained in the two image planes allows the in-plane and out-of-plane components to be separated. For perspective viewing purposes, Scheimpflug adapters are used to tilt the camera lens with respect to the sensor, such that the image plane, lens plane, and object plane intersect at a common point as per the Scheimpflug criterion. A-priori calibration using a multi-level calibration target with markers at known vertical spacing is extremely important for obtaining reliable measurements. In addition, a self-calibration procedure may also be implemented, accounting for small discrepancies in alignment by comparing de-warped images from the two cameras at the same time point [116]. The result is a two-dimensional three-component (2D3C) velocity map. However, by collecting data over several incrementally offset planes, a full three-dimensional three-component (3D3C) velocity field can be constructed.

Additional extensions of the basic PIV method include tomographic PIV and microscopic PIV. In tomographic PIV, the entire flow volume is illuminated, and tracer particles are imaged via multiple cameras (typically 4-6) at multiple viewing angles simultaneously. Complex reconstruction techniques allow the instantaneous 3D3C velocity field to be calculated from a single acquisition (instead of via multiple acquisitions at several planes) [117]. In microscopic PIV, the combined use of a light source and CCD camera in conjunction with a microscope permit velocity measurement at microscopic length scales. The flow experiments are carried out in microfabricated fluidic devices. Finally, with advancements in particle tracking velocimetry (PTV) algorithms, they can now be applied to images with medium to high particle density, allowing single particle velocities to be mapped from conventional PIV images.

PIV is an attractive option for studying hemodynamics in-vitro, due to its combined high temporal and spatial resolution. In addition, the similarity between PIV and CFD datasets make it well-suited as a validation tool. A vast number of vascular PIV studies may be

found in the literature however only a limited number have specifically investigated carotid artery bifurcation models. They are summarized briefly below.

Conventional 2D2C PIV was applied by Bale-Glickman et al. [118] to study flow patterns in atherosclerotic carotid artery flow phantoms constructed from patient specific geometries with 70% and >70% stenosis. Under steady inlet flow conditions, they measured in-plane velocity and vorticity and demonstrated complex flow features downstream of stenosis. Vetel et al. [119] used multi-plane stereoscopic PIV to measure 3D3C velocity and also observed vorticity and flow complexity in a complex carotid bifurcation model. Cheung et al. [120] used experimental 2D2C PIV to validate numerical simulations of flow in a stenosed carotid bifurcation model and found good agreement between measured and predicted flow features. Kabinejadian et al. [121] used PIV to evaluate the efficiency of a covered carotid artery stent design in-vitro.

Two wall shear stress studies of idealized healthy carotid bifurcation models were conducted. In the first, Buchmann et al. [122] applied an interfacial PIV technique to calculate the in-plane WSS from 2D2C PIV images in idealized and physiological realistic healthy (non-stenosed) carotid bifurcation phantoms under steady inlet conditions. In the second, Buchmann et al. [123] compared 3D3C results from multi-plane stereoscopic PIV and tomographic PIV experiments in a healthy patient-specific carotid artery model under steady inlet flow. In this study, principle shear stress was calculated from second order regression to the velocity data, a method similarly applied to measure WSS from PIV data in coronary models [124]. The shear stress was then interpolated onto a surface mesh reconstructed from CT scans of the phantom model to obtain 3D WSS magnitude maps.

Previous stereoscopic PIV experiments conducted using the same carotid artery models studied in this thesis investigated the effects of stenosis severity, plaque eccentricity, and ulceration on flow patterns, turbulence, and wall shear stress magnitude [65; 125; 126]. Wall shear stress was obtained at the vessel wall by applying a spatial first-order central differencing scheme and calculating the principle shear stresses. The wall location for this calculation was assumed based on the location of the last resolvable velocity vector. While

this method allowed for comparison across models, it provided a conservative estimate of WSS magnitude without calculating direction. Additional assumptions of Newtonian viscosity and rigid walls were also applied and only one inlet waveform condition was investigated.

To date, no studies have used PIV to calculate full 3D maps of OSI or transWSS encompassing both wall shear stress magnitude *and direction*.

1.5 Factors Impacting Hemodynamics

1.5.1 Geometry

As explained in Section 1.2, the development of plaques in association with atherosclerosis is a complicated process, occurring over time and impacted by both hemodynamic and biological factors. Established plaques then impart changes on the local flow and WSS, which affects the subsequent progression of local disease. Consequently, a large body of work has focused on measuring and modeling hemodynamics in progressively stenosed vessels [23; 127; 128]. In previous in-vitro DUS and PIV experiments, increasing stenosis severity, plaque asymmetry and the presence of ulcerations have been found to increase the level of flow disturbances in idealized carotid geometries [65; 126; 129-131]. To the same end, Harloff et al. [132] found a significant reduction between pre- and post-endarterectomy measurements of ICA WSS and OSI using 4D flow MRI. These studies confirm the otherwise intuitive significance of vessel morphology changes, either due to disease progression or intervention, on hemodynamics.

In the context of patient specific CFD studies, the accuracy of geometry reconstruction from in vivo imaging modalities is a concern. For physical models (PIV and optical techniques), this concern translates to fidelity of fabricated flow phantoms to the parent geometry they were derived from [133]. Moore et al. [134] compared the WSS calculated in 3D models reconstructed from MR images of an idealized carotid artery phantom. Average WSS errors of 15% were attributed to the reconstruction method alone, although spatial distribution of WSS was consistent. Thomas et al. found average variability of 37%

in computed WSS between geometries reconstructed from subsequent imaging sessions in the same subject. Several comparison studies have concluded that accurate geometry reconstruction is the dominant factor when it comes to patient specific modeling [135; 136].

1.5.2 Rheology

Recall Equation 1.7, indicating the shear stress for a Newtonian fluid is linearly related to the strain rate with a viscosity that is constant for a particular temperature. A non-Newtonian fluid, instead has a viscosity which is dependent on shear rate:

$$\boldsymbol{\tau} = \eta(\dot{\boldsymbol{\gamma}})\dot{\boldsymbol{\gamma}} \quad (1.25)$$

Blood is a specific type of non-Newtonian fluid, known as a shear-thinning fluid, meaning that it becomes less viscous as the applied shear force increases.

Blood is composed of erythrocytes (red blood cells, RBC), leukocytes (white blood cells) and platelets suspended in plasma, consisting of water, proteins including fibrinogen, mineral ions and additional organic substances. RBCs make up more than 99% of the cellular elements and contribute largely to the shear thinning behavior of whole blood. RBCs are highly deformable, transforming from a biconcave discoid shape into an ellipsoid at high shear rates to facilitate alignment with flow streamlines, resulting in decreased viscosity. At low shear rates, discoid platelets aggregate into long structures resembling stacks of coins known as rouleaux, contributing to increased viscosity [137].

Viscosity of blood increases with hematocrit – the volume fraction of red blood cells in whole blood. Normal hematocrit of human blood is in the range of 40-45%. Higher hematocrit also increases the shear rate dependence of viscosity due to increased RBC aggregation. Enhanced plasma and whole blood viscosity have been observed with age due to impaired deformability of RBCs and increased concentration of plasma fibrinogen, a protein which strongly promotes RBC aggregate formation [137].

Measurements of the viscosity of whole blood are challenging due to sedimentation and coagulation of *ex vivo* samples. Several studies observed shear-thinning behavior, with a large variation of viscosities at low shear rates between subjects, and a steady viscosity approaching 4 cP at high shear rates [138-141].

The non-Newtonian formulation of blood adopted in Chapter 2 of this thesis is the Cross model. It describes a non-Newtonian fluid with no yield stress, with a Newtonian viscosity plateau for low shear rates, η_0 and a second one at high shear rates, η_∞ . The viscosity is given by:

$$\eta(\dot{\gamma}) = \eta_\infty + \frac{\eta_0 - \eta_\infty}{1 + a\dot{\gamma}^{1-q}} \quad (1.26)$$

Some studies have suggested that blood exhibits a yield stress, a critical stress which must be exceeded before it can flow, and that it can also display slight viscoelasticity [142]. Both viscoelasticity and yield stress behavior are not considered in the cross model or in the work in Chapter 2.

Given the link between viscosity and hemodynamics, numerical and physical models of vascular flows often incorporate non-Newtonian viscosity. Overall effects of shear thinning on hemodynamics include increased WSS [143-145], reduced recirculation lengths [146; 147] and dampening of turbulence [148; 149] compared to a Newtonian model. Some studies found that the effects of shear thinning on hemodynamics were small and suggest that a Newtonian assumption is reasonable in large arteries [136; 150]. However, comparisons between non-Newtonian model types showed that the differences can depend on the model applied, and that the significance of non-Newtonian effects can vary based on the geometry observed [136; 151].

1.5.3 Pulsatility

Pulsatility is an intrinsic property of the cardiovascular system. When the heart contracts during *systole*, blood is rapidly ejected into the aorta and large arteries during which the proximal arteries expand to accommodate the increased volume. During *diastole*, the heart

relaxes, and elastic recoil in the large arteries forces the blood into the peripheral circulation. Pulsatility implies variation of the amplitude of the flow-rate waveform over the cardiac cycle.

Two dimensionless parameters are used in vivo to quantify the pulsatility of measured flow (or velocity) waveforms:

Pulsatility Index (PI) [152]

$$PI = \frac{\Phi_{MAX} - \Phi_{MIN}}{\Phi_{MEAN}} \quad (1.27)$$

Resistive Index (RI)

$$RI = \frac{\Phi_{MAX} - \Phi_{MIN}}{\Phi_{MAX}} \quad (1.28)$$

Where Φ refers to either the flow rate or the velocity depending on measurement techniques.

Pulsatility can vary significantly across patient groups and can vary in individuals over long time scales (due to development of atherosclerosis and vessel stiffening) or short time scales (due to changes in blood pressure, cognitive engagement, or exercise) [153; 154]. Increased carotid flow pulsatility was correlated with an increased incidence of stroke [155] and PI was significantly elevated in subjects with diabetes or previous cerebral infarction compared to controls [156]. Many studies have attempted to characterize the shape of the flow waveform in both the CCA and the ICA [157-161]. The highest values of CCA PI were found to be greater than 3 in studies of young healthy adults [157; 161], while other studies quoted values of 1.5-1.9 over various age ranges [158; 162; 163] although a clear age dependence has not been confirmed. A dampening of PI is observed along the arterial tree [161] and lower PI values of approximately 1-1.5 are typically found in the ICA [158; 162; 163].

Waveform PI is intricately connected to both vascular stiffness and resistance. The dampening effect of large arteries prevents the transmission of pulsatility into the microcirculation. Increases in cerebral pulsatility, which may cause microvascular damage, have been associated with increased large artery stiffness [164-166]. In addition both PI and RI were found to be correlated with peripheral resistance [167; 168]. An overall decrease in downstream compliance was shown to result in reduced carotid PI in a lumped parameter model of carotid artery blood flow [169].

Regardless of the in-vivo manifestation, the large variation in flow waveform shapes suggests that more careful consideration of chosen boundary conditions may be needed for accurate patient-specific flow modeling. CFD studies of aneurysm geometries found differences in WSS and OSI of up to 30% between patient specific and idealized inlet waveforms [170]. Xiang et al. [171] found that TAWSS was similar across waveform shapes with the same mean inlet flow rate, but that OSI was correlated with waveform PI. In addition, there is still some debate as to whether steady state simulations can accurately predict hemodynamics, without considering pulsatility at all. Friedman compared steady and pulsatile simulations in a branched arterial model and found that the presence of high shear, low shear and separation, were all increased with flow pulsatility.

1.5.4 Compliance

Compliance is an inherent property of arteries. The intima, media and adventitia (layers of the vessel wall) contain collagen, elastin, and vascular smooth muscle cells (SMCs). Collagen is much stiffer than elastin, and elasticity of the large arteries is due to high ratios of elastin to collagen within their walls. As lipids accumulate in the intima during atherogenesis, the cellular structure of the artery becomes compromised, and an increase in arterial stiffness occurs due to the degradation of elastin fibers [172; 173]. Vessel wall stiffness may also be actively modulated by changes in SMC tone.

Recall that the relationship between stress and strain for an elastic material is determined by Hooke's law, and proportionality constant known as the elastic modulus. However, the

stress-strain curve for arterial walls is not linear, with an increase in stiffness at higher distending pressures or high levels of strain due to the recruitment of less elastic collagen. Therefore, the *incremental elastic modulus*, E_{inc} , measured from the slope of the stress-strain curve, is used to represent the local elastic modulus for a given pressure.

Arterial compliance is defined as a change in volume for a given change in pressure

$$C = \frac{\Delta V}{\Delta P} \quad (1.29)$$

However, it is challenging to measure volume changes directly in vivo. Therefore, measures of cross-sectional compliance or distensibility are often used. Cross sectional compliance is defined here as a change in area for a given change in pressure:

$$CC = \frac{\Delta A}{\Delta P} = \frac{\pi D_S^2 - D_D^2}{4 \Delta P} \quad (1.30)$$

The distensibility is defined here as the relative change in diameter for a corresponding change in pressure:

$$d = \frac{\Delta D/D}{\Delta P} = \frac{D_S - D_D}{D_D \Delta P} \quad (1.31)$$

Clinically, changes in diameter and pressure are measured over the cardiac cycle, thus the ‘S’ and ‘D’ subscripts refer to systole and diastole respectively. The definitions in Equations 1.30 and 1.31 assume that a change in volume is due to a radial distension and ignores effects of axial elongation. In addition, 1.31 assumes a circular vessel cross-section. The pressure-strain elastic modulus, developed by Peterson et al. and also known as Peterson’s elastic modulus [174], describes the mechanical properties of arteries based on the change in pressure for a given fractional change in diameter:

$$E_P = \frac{\Delta P}{\Delta D/D} = \frac{D_D \Delta P}{D_S - D_D} = \frac{1}{d} \quad (1.32)$$

It is important to note that CC, d and E_p are not strictly measurements of the stiffness of the arterial wall material and are also influenced by the vessel geometry. Therefore, two arteries with identical vessel wall properties can have very different compliance based on the size of the vessel and the wall thickness. The pressure-strain modulus can be related to the incremental elastic modulus by: $E_{inc} = E_p D / 2h$.

Increased carotid artery stiffness is associated with the development of plaques [172] and large artery stiffness is also an independent predictor of cerebrovascular events/stroke [175; 176]. Vascular stiffness increases with age [177-181] and also in association with cardiovascular risk factors such as hypertension, diabetes, smoking, hypercholesterolemia and kidney disease [176; 182].

Recently, more attention has been drawn towards the impact of compliance on hemodynamic predictions with FSI simulations becoming more common. Many studies have conducted comparisons of rigid (CFD) and compliant (FSI) simulations in simplified and complex arterial geometries [183]. However the necessity of including compliance has not been determined conclusively, with some results suggesting that a rigid wall assumption is adequate [184], and others reporting large differences due to compliance [185]. Likewise, the development of compliant phantoms for in vitro PIV experiments has allowed vessel elasticity to be observed in-vitro [133; 186-188]. However, the only matched model studies of rigid and flexible phantoms that have been conducted were in simplified geometries and did not consider bulk flow disturbances or OSI [189].

1.6 Research Objectives and Outline

Hemodynamics, including bulk flow disturbances as well as temporal fluctuations in the WSS, play an important role in the development and progression of atherosclerosis and the risk for cerebrovascular events. Although WSS is essential to the pathology of atherogenesis, its measurement in vivo is difficult and often suffers from inaccuracies. Moreover, clinical studies are somewhat limited because it is difficult to account for the

inherent variability across the study population making it difficult to distinguish which factors are contributing and assess the level of risk.

Due to accessibility and improvements in computational resources, numerical simulations such as CFD and FSI are the most common method of quantifying hemodynamics. However, some skepticism is aimed towards computational methods due to the number of assumptions often applied in practice and limitations due to the lack of comprehensive patient-specific data sets available (containing both flow and anatomical information). The large variation of conditions applied and solver methods available makes it difficult to make comparisons between computational studies, especially when patient-specific geometries are employed. Some numerical and experimental studies have attempted to gage the relative importance of various combinations of parameters in hemodynamic modeling [136; 190]. To date, no controlled study (numerical or physical) has provided a cumulative assessment of the relative contributions of various model assumptions towards the prediction of hemodynamics.

The overall objective of this thesis was to investigate the relative contributions of various factors - including geometry, rheology, pulsatility, and compliance - on disturbed flow and multi-directional WSS parameters related to the development of atherosclerosis to 1.) Provide a big picture look at the hemodynamic impact of physiological in-vivo changes (structure, elasticity, hematocrit, etc) contributing to the interpretation and guidance of clinical risk assessment and 2.) Provide insight on the level of uncertainties that may be attributed to modeling assumptions (rigid walls, Newtonian viscosity, assumed boundary conditions, etc) and their relative importance.

The above objective was investigated experimentally in vitro for idealized carotid artery bifurcation geometries using an experimental stereoscopic PIV system in conjunction with high accuracy wall location information derived from micro computed tomography scans. A wall shear stress calculation method was applied to evaluate both WSS magnitude *and* direction, further allowing parameters like OSI and transWSS, reflecting temporal WSS variation/disturbances, to be derived. The high temporal and spatial resolution of the PIV

technique also enables the calculation of turbulence intensity, reflecting bulk flow fluctuations, for comparison.

Physical components of the in-vitro flow setup were manipulated to impose differences in the four factors of interest, and the effects were isolated and assessed individually in the remaining chapters. In Chapter 2, we investigated the impact of viscosity model on flow and shear stress by implementing a physiological shear thinning blood-mimicking fluid. Experiments were completed for rigid carotid artery phantoms with increasing ICA stenosis from 30% - 70%, thus the effect of changes in geometry due to progressive plaque development were also observed. This chapter includes an estimation of the errors in the WSS calculation due to both the propagation of velocity uncertainties and misalignments of the CT and PIV datasets. Chapter 3 focused on the effect of waveform shape, specifically pulsatility, for a single 50% stenosed rigid geometry and Newtonian blood mimicking fluid. In Chapter 4, the method was extended to measure the effect of local compliance on hemodynamics using a thin-walled phantom and the importance of wall tracking was evaluated by implementing a dynamic computed tomography technique. Finally, the results will be summarized in Chapter 5 where a comprehensive comparison of the relative differences in hemodynamic parameters due to the above factors will be presented.

1.7 References

- [1] Hatano, S., 1976. Experience from a multicenter stroke register - preliminary-report. *Bulletin of the World Health Organization* 54:541-553.
- [2] Feigin, V.L., Forouzanfar, M.H., Krishnamurthi, R., *et al.*, 2014. Global and regional burden of stroke during 1990-2010: Findings from the global burden of disease study 2010. *Lancet* 383:245-255.
- [3] Benjamin, E.J., Virani, S.S., Callaway, C.W., *et al.*, 2018. Heart disease and stroke statistics-2018 update a report from the american heart association. *Circulation* 137:E67-E492.
- [4] Statistics Canada (2016). *Leading causes of death, total population, by age group*. Available online at <https://www150.statcan.gc.ca/t1/tb11/en/tv.action?pid=1310039401>

- [5] Heart and stroke foundation of canada (2018). *Lives Disrupted: The Impact of Stroke on Women*. Available online at <https://www.heartandstroke.ca/-/media/pdf-files/canada/stroke-report/strokereport2018.ashx?la=en>
- [6] Public health agency of canada (2011). *Tracking Heart Disease and Stroke in Canada – Stroke Highlights 2011*. Available online at <https://www.canada.ca/en/public-health/services/chronic-diseases/cardiovascular-disease/tracking-heart-disease-stroke-canada-stroke-highlights-2011.html>
- [7] Sacco, R.L., 2001. Newer risk factors for stroke. *Neurology* 57:S31-S34.
- [8] 1989. Special report from the world-health-organization - stroke - 1989 - recommendations on stroke prevention, diagnosis, and therapy. *Stroke* 20:1407-1431.
- [9] Hankey, G.J., 2017. Stroke. *Lancet* 389:641-654.
- [10] Bailey, R.R., 2018. Lifestyle modification for secondary stroke prevention. *American Journal of Lifestyle Medicine* 12:140-147.
- [11] Rothwell, P.M., Algra, A., Amarenco, P., 2011. Medical treatment in acute and long-term secondary prevention after transient ischaemic attack and ischaemic stroke. *Lancet* 377:1681-1692.
- [12] Swanepoel, A.C., Pretorius, E., 2015. Prevention and follow-up in thromboembolic ischemic stroke: Do we need to think out of the box? *Thrombosis Research* 136:1067-1073.
- [13] Strong, K., Mathers, C., Bonita, R., 2007. Preventing stroke: Saving lives around the world. *Lancet Neurol* 6:182-187.
- [14] Gallego, J., Martinez Vila, E., Munoz, R., 2007. Patients at high risk for ischemic stroke: Identification and actions. *Cerebrovasc Dis* 24 Suppl 1:49-63.
- [15] Banerjee, C., Chimowitz, M.I., 2017. Stroke caused by atherosclerosis of the major intracranial arteries. *Circulation Research* 120:502-513.
- [16] Glagov, S., Zarins, C., Giddens, D.P., *et al.*, 1988. Hemodynamics and atherosclerosis - insights and perspectives gained from studies of human arteries. *Archives of Pathology & Laboratory Medicine* 112:1018-1031.
- [17] Gimbrone, M.A., Garcia-Cardena, G., 2013. Vascular endothelium, hemodynamics, and the pathobiology of atherosclerosis. *Cardiovascular Pathology* 22:9-15.

- [18] Chaturvedi, S., Bhattacharya, P., 2014. Large artery atherosclerosis: Carotid stenosis, vertebral artery disease, and intracranial atherosclerosis. *Continuum (Minneapolis)* 20:323-334.
- [19] Caro, C.G., Fitzgibbon, J.M., Schroter, R.C., 1971. Atheroma and arterial wall shear - observation, correlation and proposal of a shear dependent mass transfer mechanism for atherogenesis. *Proceedings of the Royal Society Series B-Biological Sciences* 177:109-14.
- [20] Fry, D.L., 1968. Acute vascular endothelial changes associated with increased blood velocity gradients. *Circulation Research* 22:165-197.
- [21] Zarins, C.K., Giddens, D.P., Bharadvaj, B.K., *et al.*, 1983. Carotid bifurcation atherosclerosis quantitative correlation of plaque localization with flow velocity profiles and wall shear-stress. *Circulation Research* 53:502-514.
- [22] Motomiya, M., Karino, T., 1984. Flow patterns in the human carotid-artery bifurcation. *Stroke* 15:50-56.
- [23] Gijzen, F.J.H., Palmen, D.E.M., vanderBeek, M.H.E., *et al.*, 1996. Analysis of the axial flow field in stenosed carotid artery bifurcation models - In vivo experiments. *Journal of Biomechanics* 29:1483-1489.
- [24] Ku, D.N., Giddens, D.P., 1983. Pulsatile flow in a model carotid bifurcation. *Arteriosclerosis* 3:31-39.
- [25] Ku, D.N., Giddens, D.P., Zarins, C.K., *et al.*, 1985. Pulsatile flow and atherosclerosis in the human carotid bifurcation - positive correlation between plaque location and low and oscillating shear-stress. *Arteriosclerosis* 5:293-302.
- [26] He, X.J., Ku, D.N., 1996. Pulsatile flow in the human left coronary artery bifurcation: Average conditions. *Journal of Biomechanical Engineering-Transactions of the Asme* 118:74-82.
- [27] Berk, B.C., 2008. Atheroprotective signaling mechanisms activated by steady laminar flow in endothelial cells. *Circulation* 117:1082-1089.
- [28] Chatzizisis, Y.S., Coskun, A.U., Jonas, M., *et al.*, 2007. Role of endothelial shear stress in the natural history of coronary atherosclerosis and vascular remodeling - molecular, cellular, and vascular behavior. *Journal of the American College of Cardiology* 49:2379-2393.
- [29] Chien, S., 2003. Molecular and mechanical bases of focal lipid accumulation in arterial wall. *Progress in Biophysics & Molecular Biology* 83:131-151.

- [30] Chien, S., 2008. Effects of disturbed flow on endothelial cells. *Annals of Biomedical Engineering* 36:554-562.
- [31] Davies, P.F., 1995. Flow-mediated endothelial mechanotransduction. *Physiological Reviews* 75:519-560.
- [32] Davies, P.F., 2009. Hemodynamic shear stress and the endothelium in cardiovascular pathophysiology. *Nature Clinical Practice Cardiovascular Medicine* 6:16-26.
- [33] Hahn, C., Schwartz, M.A., 2009. Mechanotransduction in vascular physiology and atherogenesis. *Nature Reviews Molecular Cell Biology* 10:53-62.
- [34] Li, Y.S.J., Haga, J.H., Chien, S., 2005. Molecular basis of the effects of shear stress on vascular endothelial cells. *Journal of Biomechanics* 38:1949-1971.
- [35] Orr, A.W., Helmke, B.P., Blackman, B.R., *et al.*, 2006. Mechanisms of mechanotransduction. *Developmental Cell* 10:11-20.
- [36] Malek, A.M., Alper, S.L., Izumo, S., 1999. Hemodynamic shear stress and its role in atherosclerosis. *Jama-Journal of the American Medical Association* 282:2035-2042.
- [37] Resnick, N., Yahav, H., Schubert, S., *et al.*, 2000. Signalling pathways in vascular endothelium activated by shear stress: Relevance to atherosclerosis. *Current Opinion in Lipidology* 11:167-177.
- [38] Tarbell, J.M., Shi, Z.D., Dunn, J., *et al.*, 2014. Fluid mechanics, arterial disease, and gene expression. *Annual Review of Fluid Mechanics* 46:591-614.
- [39] Chiu, J.J., Wang, D.L., Chien, S., *et al.*, 1998. Effects of disturbed flow on endothelial cells. *Journal of Biomechanical Engineering-Transactions of the Asme* 120:2-8.
- [40] Galbraith, C.G., Skalak, R., Chien, S., 1998. Shear stress induces spatial reorganization of the endothelial cell cytoskeleton. *Cell Motility and the Cytoskeleton* 40:317-330.
- [41] Levesque, M.J., Nerem, R.M., 1985. The elongation and orientation of cultured endothelial-cells in response to shear-stress. *Journal of Biomechanical Engineering-Transactions of the Asme* 107:341-347.
- [42] Brooks, A.R., Lelkes, P.I., Rubanyi, G.M., 2004. Gene expression profiling of vascular endothelial cells exposed to fluid mechanical forces: Relevance for focal susceptibility to atherosclerosis. *Endothelium-Journal of Endothelial Cell Research* 11:45-57.

- [43] Peiffer, V., Sherwin, S.J., Weinberg, P.D., 2013. Does low and oscillatory wall shear stress correlate spatially with early atherosclerosis? A systematic review. *Cardiovascular Research* 99:242-250.
- [44] Steinman, D.A., Thomas, J.B., Ladak, H.M., *et al.*, 2002. Reconstruction of carotid bifurcation hemodynamics and wall thickness using computational fluid dynamics and mri. *Magnetic Resonance in Medicine* 47:149-159.
- [45] Augst, A.D., Ariff, B., Thom, S., *et al.*, 2007. Analysis of complex flow and the relationship between blood pressure, wall shear stress, and intima-media thickness in the human carotid artery. *American Journal of Physiology-Heart and Circulatory Physiology* 293:H1031-H1037.
- [46] Gijssen, F.J.H., Wentzel, J.J., Thury, A., *et al.*, 2007. A new imaging technique to study 3-d plaque and shear stress distribution in human coronar arter bifurcations in vivo. *Journal of Biomechanics* 40:2349-2357.
- [47] Wentzel, J.J., Gijssen, F.J.H., Schuurbiens, J.C.H., *et al.*, 2005. Geometry guided data averaging enables the interpretation of shear stress related plaque development in human coronary arteries. *Journal of Biomechanics* 38:1551-1555.
- [48] Joshi, A.K., Leask, R.L., Myers, J.G., *et al.*, 2004. Intimal thickness is not associated with wall shear stress patterns in the human right coronary artery. *Arteriosclerosis Thrombosis and Vascular Biology* 24:2408-2413.
- [49] Peiffer, V., Sherwin, S.J., Weinberg, P.D., 2013. Computation in the rabbit aorta of a new metric - the transverse wall shear stress - to quantify the multidirectional character of disturbed blood flow. *Journal of Biomechanics* 46:2651-2658.
- [50] Mohamied, Y., Rowland, E.M., Bailey, E.L., *et al.*, 2015. Change of direction in the biomechanics of atherosclerosis. *Annals of Biomedical Engineering* 43:16-25.
- [51] Wang, C., Baker, B.M., Chen, C.S., *et al.*, 2013. Endothelial cell sensing of flow direction. *Arteriosclerosis Thrombosis and Vascular Biology* 33:2130-2136.
- [52] Wang, C., Lu, H., Schwartz, M.A., 2012. A novel in vitro flow system for changing flow direction on endothelial cells. *Journal of Biomechanics* 45:1212-1218.
- [53] Chakraborty, A., Chakraborty, S., Jala, V.R., *et al.*, 2012. Effects of biaxial oscillatory shear stress on endothelial cell proliferation and morphology. *Biotechnology and Bioengineering* 109:695-707.
- [54] Chakraborty, A., Chakraborty, S., Jala, V.R., *et al.*, 2016. Impact of bi-axial shear on atherogenic gene expression by endothelial cells (vol 44, pg 3032, 2016). *Annals of Biomedical Engineering* 44:3046-3046.

- [55] Holme, P.A., Orvim, U., Hamers, M., *et al.*, 1997. Shear-induced platelet activation and platelet microparticle formation at blood flow conditions as in arteries with a severe stenosis. *Arteriosclerosis Thrombosis and Vascular Biology* 17:646-653.
- [56] Nesbitt, W.S., Westein, E., Tovar-Lopez, F.J., *et al.*, 2009. A shear gradient-dependent platelet aggregation mechanism drives thrombus formation. *Nature Medicine* 15:665-U146.
- [57] Leverett, L.B., Lynch, E.C., Alfrey, C.P., *et al.*, 1972. Red blood-cell damage by shear-stress. *Biophysical Journal* 12:257-&.
- [58] Bluestein, D., Niu, L.J., Schoepfoerster, R.T., *et al.*, 1997. Fluid mechanics of arterial stenosis: Relationship to the development of mural thrombus. *Annals of Biomedical Engineering* 25:344-356.
- [59] Bluestein, D., Gutierrez, C., Londono, M., *et al.*, 1999. Vortex shedding in steady flow through a model of an arterial stenosis and its relevance to mural platelet deposition. *Annals of Biomedical Engineering* 27:763-773.
- [60] Bluestein, D., Rambod, E., Gharib, M., 2000. Vortex shedding as a mechanism for free emboli formation in mechanical heart valves. *Journal of Biomechanical Engineering-Transactions of the Asme* 122:125-134.
- [61] Smith, R.L., Stein, P.D., Coalson, J., *et al.*, 1972. Thrombus production by turbulence. *Journal of Applied Physiology* 32:261-+.
- [62] Stein, P.D., Sabbah, H.N., 1974. Measured turbulence and its effect on thrombus formation. *Circulation Research* 35:608-614.
- [63] Ojha, M., Cobbold, R.S.C., Johnston, K.W., *et al.*, 1989. Pulsatile flow through constricted tubes - an experimental investigation using photochromic tracer methods. *Journal of Fluid Mechanics* 203:173-197.
- [64] Loree, H.M., Kamm, R.D., Atkinson, C.M., *et al.*, 1991. Turbulent pressure-fluctuations on surface of model vascular stenoses. *American Journal of Physiology* 261:H644-H650.
- [65] Kefayati, S., Holdsworth, D.W., Poepping, T.L., 2014. Turbulence intensity measurements using particle image velocimetry in diseased carotid artery models: Effect of stenosis severity, plaque eccentricity, and ulceration. *Journal of Biomechanics* 47:253-263.
- [66] Suter, S.P., Nowak, M.D., Joist, J.H., *et al.*, 1988. A programmable, computer-controlled cone plate viscometer for the application of pulsatile shear-stress to platelet suspensions. *Biorheology* 25:449-459.

- [67] Eshtehardi, P., Brown, A.J., Bhargava, A., *et al.*, 2017. High wall shear stress and high-risk plaque: An emerging concept. *International Journal of Cardiovascular Imaging* 33:1089-1099.
- [68] Groen, H.C., Gijzen, F.J.H., van der Lugt, A., *et al.*, 2007. Plaque rupture in the carotid artery is localized at the high shear stress region - a case report. *Stroke* 38:2379-2381.
- [69] Lovett, J.K., Rothwell, P.M., 2003. Site of carotid plaque ulceration in relation to direction of blood flow: An angiographic and pathological study. *Cerebrovascular Diseases* 16:369-375.
- [70] Dirksen, M.T., van der Wal, A.C., van den Berg, F.M., *et al.*, 1998. Distribution of inflammatory cells in atherosclerotic plaques relates to the direction of flow. *Circulation* 98:2000-2003.
- [71] Leach, J.R., Rayz, V.L., Soares, B., *et al.*, 2010. Carotid atheroma rupture observed in vivo and fsi-predicted stress distribution based on pre-rupture imaging. *Annals of Biomedical Engineering* 38:2748-2765.
- [72] Teng, Z.Z., Canton, G., Yuan, C., *et al.*, 2010. 3d critical plaque wall stress is a better predictor of carotid plaque rupture sites than flow shear stress: An in vivo mri-based 3d fsi study. *Journal of Biomechanical Engineering-Transactions of the Asme* 132:9.
- [73] van Ooij, P., Potters, W.V., Nederveen, A.J., *et al.*, 2015. A methodology to detect abnormal relative wall shear stress on the full surface of the thoracic aorta using four-dimensional flow mri. *Magnetic Resonance in Medicine* 73:1216-1227.
- [74] Potters, W.V., van Ooij, P., Marquering, H., *et al.*, 2015. Volumetric arterial wall shear stress calculation based on cine phase contrast mri. *Journal of Magnetic Resonance Imaging* 41:505-516.
- [75] Isoda, H., Ohkura, Y., Kosugi, T., *et al.*, 2010. Comparison of hemodynamics of intracranial aneurysms between mr fluid dynamics using 3d cine phase-contrast mri and mr-based computational fluid dynamics. *Neuroradiology* 52:913-920.
- [76] Cheng, C.P., Parker, D., Taylor, C.A., 2002. Quantification of wall shear stress in large blood vessels using lagrangian interpolation functions with cine phase-contrast magnetic resonance imaging. *Annals of Biomedical Engineering* 30:1020-1032.
- [77] Fung, Y.C., 1984. *Biodynamics: Circulation*. Springer-Verlag, New York.

- [78] Stettler, J.C., Hussain, A., 1986. On transition of the pulsatile pipe-flow. *Journal of Fluid Mechanics* 170:169-197.
- [79] Trip, R., Kuik, D.J., Westerweel, J., *et al.*, 2012. An experimental study of transitional pulsatile pipe flow. *Physics of Fluids* 24:17.
- [80] Brindise, M.C., Vlachos, P.P., 2018. Pulsatile pipe flow transition: Flow waveform effects. *Physics of Fluids* 30:13.
- [81] Reynolds, W.C., Hussain, A.K.M., 1972. Mechanics of an organized wave in turbulent shear-flow .3. Theoretical models and comparisons with experiments. *Journal of Fluid Mechanics* 54:263-&.
- [82] Dunmire, B., Beach, K.W., Labs, K.H., *et al.*, 2000. Cross-beam vector doppler ultrasound for angle-independent velocity measurements. *Ultrasound in Medicine and Biology* 26:1213-1235.
- [83] Hussain, B., Yiu, B.Y.S., Yu, A.C.H., *et al.*, 2016. Investigation of crossbeam multi-receiver configurations for accurate 3-d vector doppler velocity estimation. *Ieee Transactions on Ultrasonics Ferroelectrics and Frequency Control* 63:1786-1798.
- [84] Thorne, M.L., Rankin, R.N., Steinman, D.A., *et al.*, 2010. In vivo doppler ultrasound quantification of turbulence intensity using a high-pass frequency filter method. *Ultrasound in Medicine and Biology* 36:761-771.
- [85] Brands, P.J., Hoeks, A.P.G., Hofstra, L., *et al.*, 1995. A noninvasive method to estimate wall shear rate using ultrasound. *Ultrasound in Medicine and Biology* 21:171-185.
- [86] Evans, D.H., Jensen, J.A., Nielsen, M.B., 2011. Ultrasonic colour doppler imaging. *Interface Focus* 1:490-502.
- [87] Polak, J.F., O'leary, D.H., Quist, W.C., *et al.*, 1990. Pulsed and color doppler analysis of normal carotid bifurcation flow dynamics using an invitro model. *Angiology* 41:241-247.
- [88] Zhang, F.X., Lanning, C., Mazzaro, L., *et al.*, 2011. In vitro and preliminary in vivo validation of echo particle image velocimetry in carotid vascular imaging. *Ultrasound in Medicine and Biology* 37:450-464.
- [89] Gates, P.E., Gurung, A., Mazzaro, L., *et al.*, 2018. Measurement of wall shear stress exerted by flowing blood in the human carotid artery: Ultrasound doppler velocimetry and echo particle image velocimetry. *Ultrasound in Medicine and Biology* 44:1392-1401.

- [90] Jensen, J.A., Nikolov, S.I., Yu, A.C.H., *et al.*, 2016. Ultrasound vector flow imaging-part ii: Parallel systems. *Ieee Transactions on Ultrasonics Ferroelectrics and Frequency Control* 63:1722-1732.
- [91] Hansen, K.L., Moller-Sorensen, H., Kjaergaard, J., *et al.*, 2016. Analysis of systolic backflow and secondary helical blood flow in the ascending aorta using vector flow imaging. *Ultrasound in Medicine and Biology* 42:899-908.
- [92] Udesen, J., Gran, F., Hansen, K.L., *et al.*, 2008. High frame-rate blood vector velocity imaging using plane waves: Simulations and preliminary experiments. *Ieee Transactions on Ultrasonics Ferroelectrics and Frequency Control* 55:1729-1743.
- [93] Gurung, A., Gates, P.E., Mazzaro, L., *et al.*, 2017. Echo particle image velocimetry for estimation of carotid artery wall shear stress: Repeatability, reproducibility and comparison with phase-contrast magnetic resonance imaging. *Ultrasound in Medicine and Biology* 43:1618-1627.
- [94] Correia, M., Provost, J., Tanter, M., *et al.*, 2016. 4d ultrafast ultrasound flow imaging: In vivo quantification of arterial volumetric flow rate in a single heartbeat. *Physics in Medicine and Biology* 61:14.
- [95] Markl, M., Frydrychowicz, A., Kozerke, S., *et al.*, 2012. 4d flow mri. *Journal of Magnetic Resonance Imaging* 36:1015-1036.
- [96] Ha, H., Kim, G.B., Kweon, J., *et al.*, 2016. Hemodynamic measurement using four-dimensional phase-contrast mri: Quantification of hemodynamic parameters and clinical applications. *Korean Journal of Radiology* 17:445-462.
- [97] Stalder, A.F., Russe, M.F., Frydrychowicz, A., *et al.*, 2008. Quantitative 2d and 3d phase contrast mri: Optimized analysis of blood flow and vessel wall parameters. *Magnetic Resonance in Medicine* 60:1218-1231.
- [98] Harloff, A., Albrecht, F., Spreer, J., *et al.*, 2009. 3d blood flow characteristics in the carotid artery bifurcation assessed by flow-sensitive 4d mri at 3t. *Magnetic Resonance in Medicine* 61:65-74.
- [99] Frydrychowicz, A., Berger, A., Russe, M.F., *et al.*, 2008. Time-resolved magnetic resonance angiography and flow-sensitive 4-dimensional magnetic resonance imaging at 3 tesla for blood flow and wall shear stress analysis. *Journal of Thoracic and Cardiovascular Surgery* 136:400-407.
- [100] Frydrychowicz, A., Stalder, A.F., Russe, M.F., *et al.*, 2009. Three-dimensional analysis of segmental wall shear stress in the aorta by flow-sensitive four-dimensional-mri. *Journal of Magnetic Resonance Imaging* 30:77-84.

- [101] Markl, M., Wegent, F., Zech, T., *et al.*, 2010. In vivo wall shear stress distribution in the carotid artery effect of bifurcation geometry, internal carotid artery stenosis, and recanalization therapy. *Circulation-Cardiovascular Imaging* 3:647-655.
- [102] Dyverfeldt, P., Sigfridsson, A., Kvitting, J.P.E., *et al.*, 2006. Quantification of intravoxel velocity standard deviation and turbulence intensity by generalizing phase-contrast mri. *Magnetic Resonance in Medicine* 56:850-858.
- [103] Dyverfeldt, P., Kvitting, J.P.E., Sigfridsson, A., *et al.*, 2008. Assessment of fluctuating velocities in disturbed cardiovascular blood flow: In vivo feasibility of generalized phase-contrast mri. *Journal of Magnetic Resonance Imaging* 28:655-663.
- [104] Antiga, L., Piccinelli, M., Botti, L., *et al.*, 2008. An image-based modeling framework for patient-specific computational hemodynamics. *Medical & Biological Engineering & Computing* 46:1097-1112.
- [105] Fischer, P.F., Loth, F., Lee, S.E., *et al.*, 2007. Simulation of high-reynolds number vascular flows. *Computer Methods in Applied Mechanics and Engineering* 196:3049-3060.
- [106] Lee, S.E., Lee, S.W., Fischer, P.F., *et al.*, 2008. Direct numerical simulation of transitional flow in a stenosed carotid bifurcation. *Journal of Biomechanics* 41:2551-2561.
- [107] Ghalichi, F., Deng, X.Y., De Champlain, A., *et al.*, 1998. Low reynolds number turbulence modeling of blood flow in arterial stenoses. *Biorheology* 35:281-294.
- [108] Mittal, R., Simmons, S.P., Udaykumar, H.S., 2001. Application of large-eddy simulation to the study of pulsatile flow in a modeled arterial stenosis. *Journal of Biomechanical Engineering-Transactions of the Asme* 123:325-332.
- [109] Rayz, V.L., Berger, S.A., Saloner, D., 2007. Transitional flows in arterial fluid dynamics. *Computer Methods in Applied Mechanics and Engineering* 196:3043-3048.
- [110] Li, M.X., Beech-Brandt, J.J., John, L.R., *et al.*, 2007. Numerical analysis of pulsatile blood flow and vessel wall mechanics in different degrees of stenoses. *Journal of Biomechanics* 40:3715-3724.
- [111] Cilla, M., Borrás, I., Pena, E., *et al.*, 2015. A parametric model for analysing atherosclerotic arteries: On the fsi coupling. *International Communications in Heat and Mass Transfer* 67:29-38.

- [112] Tang, D.L., Teng, Z.Z., Canton, G., *et al.*, 2009. Sites of rupture in human atherosclerotic carotid plaques are associated with high structural stresses an in vivo mri-based 3d fluid-structure interaction study. *Stroke* 40:3258-3263.
- [113] Long, Q., Xu, X.Y., Ramnarine, K.V., *et al.*, 2001. Numerical investigation of physiologically realistic pulsatile flow through arterial stenosis. *Journal of Biomechanics* 34:1229-1242.
- [114] Botnar, R., Rappitsch, G., Scheidegger, M.B., *et al.*, 2000. Hemodynamics in the carotid artery bifurcation: A comparison between numerical simulations and in vitro mri measurements. *Journal of Biomechanics* 33:137-144.
- [115] Westerweel, J., Elsinga, G.E., Adrian, R.J., 2013. Particle image velocimetry for complex and turbulent flows. *Annual Review of Fluid Mechanics* 45:409-436.
- [116] Wieneke, B., 2005. Stereo-piv using self-calibration on particle images. *Experiments in Fluids* 39:267-280.
- [117] Elsinga, G.E., Scarano, F., Wieneke, B., *et al.*, 2006. Tomographic particle image velocimetry. *Experiments in Fluids* 41:933-947.
- [118] Bale-Glickman, J., Selby, K., Saloner, D., *et al.*, 2003. Experimental flow studies in exact-replica phantoms of atherosclerotic carotid bifurcations under steady input conditions. *Journal of Biomechanical Engineering-Transactions of the Asme* 125:38-48.
- [119] Vetel, J., Garon, A., Pelletier, D., 2009. Lagrangian coherent structures in the human carotid artery bifurcation. *Experiments in Fluids* 46:1067-1079.
- [120] Cheung, S.C.P., Wong, K.K.L., Yeoh, G.H., *et al.*, 2010. Experimental and numerical study on the hemodynamics of stenosed carotid bifurcation. *Australasian Physical & Engineering Sciences in Medicine* 33:319-328.
- [121] Kabinejadian, F., Cui, F.S., Zhang, Z., *et al.*, 2013. A novel carotid covered stent design: In vitro evaluation of performance and influence on the blood flow regime at the carotid artery bifurcation. *Annals of Biomedical Engineering* 41:1990-2002.
- [122] Buchmann, N., Jermy, M., Nguyen, C., 2009. Experimental investigation of carotid artery haemodynamics in an anatomically realistic model. *International Journal of Experimental and Computational Biomechanics* 1:172-192.
- [123] Buchmann, N.A., Atkinson, C., Jeremy, M.C., *et al.*, 2011. Tomographic particle image velocimetry investigation of the flow in a modeled human carotid artery bifurcation. *Experiments in Fluids* 50:1131-1151.

- [124] Brunette, J., Mongrain, R., Laurier, J., *et al.*, 2008. 3d flow study in a mildly stenotic coronary artery phantom using a whole volume piv method. *Medical Engineering & Physics* 30:1193-1200.
- [125] Kefayati, S., Poepping, T.L., 2013. Transitional flow analysis in the carotid artery bifurcation by proper orthogonal decomposition and particle image velocimetry. *Medical Engineering & Physics* 35:898-909.
- [126] Kefayati, S., Milner, J.S., Holdsworth, D.W., *et al.*, 2014. In vitro shear stress measurements using particle image velocimetry in a family of carotid artery models: Effect of stenosis severity, plaque eccentricity, and ulceration. *Plos One* 9:19.
- [127] Lorthois, S., Lagree, P.Y., Marc-Vergnes, J.P., *et al.*, 2000. Maximal wall shear stress in arterial stenoses: Application to the internal carotid arteries. *Journal of Biomechanical Engineering-Transactions of the Asme* 122:661-666.
- [128] Stroud, J.S., Berger, S.A., Saloner, D., 2000. Influence of stenosis morphology on flow through severely stenotic vessels: Implications for plaque rupture. *Journal of Biomechanics* 33:443-455.
- [129] Poepping, T.L., Rankin, R.N., Holdsworth, D.W., 2010. Flow patterns in carotid bifurcation models using pulsed doppler ultrasound: Effect of concentric vs. Eccentric stenosis on turbulence and recirculation. *Ultrasound in Medicine and Biology* 36:1125-1134.
- [130] Wong, E.Y., Nikolov, H.N., Rankin, R.N., *et al.*, 2013. Evaluation of distal turbulence intensity for the detection of both plaque ulceration and stenosis grade in the carotid bifurcation using clinical doppler ultrasound. *European Radiology* 23:1720-1728.
- [131] Wong, E.Y., Nikolov, H.N., Thorne, M.L., *et al.*, 2009. Clinical doppler ultrasound for the assessment of plaque ulceration in the stenosed carotid bifurcation by detection of distal turbulence intensity: A matched model study. *European Radiology* 19:2739-2749.
- [132] Harloff, A., Berg, S., Barker, A.J., *et al.*, 2013. Wall shear stress distribution at the carotid bifurcation: Influence of eversion carotid endarterectomy. *European Radiology* 23:3361-3369.
- [133] Geoghegan, P.H., Buchmann, N.A., Spence, C.J.T., *et al.*, 2012. Fabrication of rigid and flexible refractive-index-matched flow phantoms for flow visualisation and optical flow measurements. *Experiments in Fluids* 52:1331-1347.

- [134] Moore, J.A., Steinman, D.A., Holdsworth, D.W., *et al.*, 1999. Accuracy of computational hemodynamics in complex arterial geometries reconstructed from magnetic resonance imaging. *Annals of Biomedical Engineering* 27:32-41.
- [135] Thomas, J.B., Milner, J.S., Rutt, B.K., *et al.*, 2003. Reproducibility of image-based computational fluid dynamics models of the human carotid bifurcation. *Annals of Biomedical Engineering* 31:132-141.
- [136] Morbiducci, U., Gallo, D., Massai, D., *et al.*, 2011. On the importance of blood rheology for bulk flow in hemodynamic models of the carotid bifurcation. *Journal of Biomechanics* 44:2427-2438.
- [137] Simmonds, M.J., Meiselman, H.J., Baskurt, O.K., 2013. Blood rheology and aging. *Journal of Geriatric Cardiology* 10:291-301.
- [138] Antonova, N., Zvetkova, E., Ivanov, I., *et al.*, 2008. Hemorheological changes and characteristic parameters derived from whole blood viscometry in chronic heroin addicts. *Clinical Hemorheology and Microcirculation* 39:53-61.
- [139] Bor-Kucukatay, M., Keskin, A., Akdam, H., *et al.*, 2008. Effect of thrombocytapheresis on blood rheology in healthy donors: Role of nitric oxide. *Transfusion and Apheresis Science* 39:101-108.
- [140] Carrera, L.I., Etchepare, R., D'Arrigo, M., *et al.*, 2008. Hemorheologic changes in type 2 diabetic patients with microangiopathic skin lesions. A linear discriminant categorizing analysis. *Journal of Diabetes and Its Complications* 22:132-136.
- [141] Galduroz, J.C.F., Antunes, H.K., Santos, R.F., 2007. Gender- and age-related variations in blood viscosity in normal volunteers: A study of the effects of extract of *allium sativum* and *ginkgo biloba*. *Phytomedicine* 14:447-451.
- [142] Merrill, E.W., 1969. Rheology of blood. *Physiol Rev* 49:863-888.
- [143] Cavazzuti, M., Atherton, M.A., Collins, M.W., *et al.*, 2011. Non-newtonian and flow pulsatility effects in simulation models of a stented intracranial aneurysm. *Proceedings of the Institution of Mechanical Engineers Part H-Journal of Engineering in Medicine* 225:597-609.
- [144] Jeong, W.W., Rhee, K., 2009. Effects of surface geometry and non-newtonian viscosity on the flow field in arterial stenoses. *Journal of Mechanical Science and Technology* 23:2424-2433.
- [145] Huh, H.K., Ha, H., Lee, S.J., 2015. Effect of non-newtonian viscosity on the fluid-dynamic characteristics in stenotic vessels. *Experiments in Fluids* 56:12.

- [146] Razavi, A., Shirani, E., Sadeghi, M.R., 2011. Numerical simulation of blood pulsatile flow in a stenosed carotid artery using different rheological models. *Journal of Biomechanics* 44:2021-2030.
- [147] Choi, H.W., Barakat, A.I., 2005. Numerical study of the impact of non-newtonian blood behavior on flow over a two-dimensional backward facing step. *Biorheology* 42:493-509.
- [148] Molla, M.M., Paul, M.C., 2012. Les of non-newtonian physiological blood flow in a model of arterial stenosis. *Medical Engineering & Physics* 34:1079-1087.
- [149] Walker, A.M., Johnston, C.R., Rival, D.E., 2014. On the characterization of a non-newtonian blood analog and its response to pulsatile flow downstream of a simplified stenosis. *Annals of Biomedical Engineering* 42:97-109.
- [150] Johnston, B.M., Johnston, P.R., Corney, S., *et al.*, 2006. Non-newtonian blood flow in human right coronary arteries: Transient simulations. *Journal of Biomechanics* 39:1116-1128.
- [151] Fisher, C., Rossmann, J.S., 2009. Effect of non-newtonian behavior on hemodynamics of cerebral aneurysms. *Journal of Biomechanical Engineering-Transactions of the Asme* 131:9.
- [152] Gosling, R.G., Dunbar, G., King, D.H., *et al.*, 1971. The quantitative analysis of occlusive peripheral arterial disease by a non-intrusive ultrasonic technique. *Angiology* 22:52-55.
- [153] Heffernan, K.S., Spartano, N.L., Augustine, J.A., *et al.*, 2015. Carotid artery stiffness and hemodynamic pulsatility during cognitive engagement in healthy adults: A pilot investigation. *American Journal of Hypertension* 28:615-622.
- [154] Babcock, M.C., Lefferts, W.K., Hughes, W.E., *et al.*, 2015. Acute effect of high-intensity cycling exercise on carotid artery hemodynamic pulsatility. *European Journal of Applied Physiology* 115:1037-1045.
- [155] Chuang, S.Y., Cheng, H.M., Bai, C.H., *et al.*, 2016. Blood pressure, carotid flow pulsatility, and the risk of stroke a community-based study. *Stroke* 47:2262-2268.
- [156] Nakatou, T., Nakata, K., Nakamura, A., *et al.*, 2004. Carotid haemodynamic parameters as risk factors for cerebral infarction in type 2 diabetic patients. *Diabetic Medicine* 21:223-229.
- [157] Holdsworth, D.W., Norley, C.J.D., Frayne, R., *et al.*, 1999. Characterization of common carotid artery blood-flow waveforms in normal human subjects. *Physiological Measurement* 20:219-240.

- [158] Hoi, Y., Wasserman, B.A., Xie, Y.Y.J., *et al.*, 2010. Characterization of volumetric flow rate waveforms at the carotid bifurcations of older adults. *Physiological Measurement* 31:291-302.
- [159] Marshall, I., Papathanasopoulou, P., Wartolowska, K., 2004. Carotid flow rates and flow division at the bifurcation in healthy volunteers. *Physiological Measurement* 25:691-697.
- [160] Ford, M.D., Alperin, N., Lee, S.H., *et al.*, 2005. Characterization of volumetric flow rate waveforms in the normal internal carotid and vertebral arteries. *Physiological Measurement* 26:477-488.
- [161] Gwilliam, M.N., Hoggard, N., Capener, D., *et al.*, 2009. Mr derived volumetric flow rate waveforms at locations within the common carotid, internal carotid, and basilar arteries. *Journal of Cerebral Blood Flow and Metabolism* 29:1975-1982.
- [162] Schoning, M., Walter, J., Scheel, P., 1994. Estimation of cerebral blood-flow through color duplex sonography of the carotid and vertebral arteries in healthy-adults. *Stroke* 25:17-22.
- [163] Scheel, P., Ruge, C., Schoning, M., 2000. Flow velocity and flow volume measurements in the extracranial carotid and vertebral arteries in healthy adults: Reference data and the effects of age. *Ultrasound in Medicine and Biology* 26:1261-1266.
- [164] Tarumi, T., Khan, M.A., Liu, J., *et al.*, 2014. Cerebral hemodynamics in normal aging: Central artery stiffness, wave reflection, and pressure pulsatility. *Journal of Cerebral Blood Flow and Metabolism* 34:971-978.
- [165] Mitchell, G.F., Parise, H., Benjamin, E.J., *et al.*, 2004. Changes in arterial stiffness and wave reflection with advancing age in healthy men and women - the framingham heart study. *Hypertension* 43:1239-1245.
- [166] Robertson, A.D., Tessmer, C.F., Hughson, R.L., 2010. Association between arterial stiffness and cerebrovascular resistance in the elderly. *Journal of Human Hypertension* 24:190-196.
- [167] Legarth, J., Nolsoe, C., 1990. Doppler blood velocity wave-forms and the relation to peripheral resistance in the brachial-artery. *Journal of Ultrasound in Medicine* 9:449-453.
- [168] Legarth, J., Thorup, E., 1989. Characteristics of doppler blood-velocity waveforms in a cardiovascular invitro model .2. The influence of peripheral resistance, perfusion-pressure and blood-flow. *Scandinavian Journal of Clinical & Laboratory Investigation* 49:459-464.

- [169] Onaizah, O., Poepping, T.L., Zamir, M., 2017. A model of blood supply to the brain via the carotid arteries: Effects of obstructive vs. Sclerotic changes. *Medical Engineering & Physics* 49:121-130.
- [170] Karmonik, C., Yen, C., Diaz, O., *et al.*, 2010. Temporal variations of wall shear stress parameters in intracranial aneurysms-importance of patient-specific inflow waveforms for cfd calculations. *Acta Neurochirurgica* 152:1391-1398.
- [171] Xiang, J., Siddiqui, A.H., Meng, H., 2014. The effect of inlet waveforms on computational hemodynamics of patient-specific intracranial aneurysms. *Journal of Biomechanics* 47:3882-3890.
- [172] Boesen, M.E., Singh, D., Menon, B.K., *et al.*, 2015. A systematic literature review of the effect of carotid atherosclerosis on local vessel stiffness and elasticity. *Atherosclerosis* 243:211-222.
- [173] Oliver, J.J., Webb, D.J., 2003. Noninvasive assessment of arterial stiffness and risk of atherosclerotic events. *Arteriosclerosis Thrombosis and Vascular Biology* 23:554-566.
- [174] Peterson, L.H., Jensen, R.E., Parnell, J., 1960. Mechanical properties of arteries in vivo. *Circulation Research* 8:622-639.
- [175] Sugioka, K., Sciacca, R.R., Hozumi, T., *et al.*, 2002. Impact of aortic stiffness on the risk of ischemic stroke in elder patients. *Journal of the American College of Cardiology* 39:196A-196A.
- [176] Chirinos, J.A., 2012. Arterial stiffness: Basic concepts and measurement techniques. *Journal of Cardiovascular Translational Research* 5:243-255.
- [177] Hansen, F., Mangell, P., Sonesson, B., *et al.*, 1995. Diameter and compliance in the human common carotid-artery - variations with age and sex. *Ultrasound in Medicine and Biology* 21:1-9.
- [178] Lanne, T., Hansen, F., Mangell, P., *et al.*, 1994. Differences in mechanical-properties of the common carotid-artery and abdominal-aorta in healthy-males. *Journal of Vascular Surgery* 20:218-225.
- [179] Riley, W.A., Barnes, R.W., Evans, G.W., *et al.*, 1992. Ultrasonic measurement of the elastic-modulus of the common carotid-artery - the atherosclerosis risk in communities (aric) study. *Stroke* 23:952-956.
- [180] Laurent, S., Caviezel, B., Beck, L., *et al.*, 1994. Carotid-artery distensibility and distending pressure in hypertensive humans. *Hypertension* 23:878-883.

- [181] Schmidt-Trucksass, A., Grathwohl, D., Schmid, A., *et al.*, 1999. Structural, functional, and hemodynamic changes of the common carotid artery with age in male subjects. *Arteriosclerosis Thrombosis and Vascular Biology* 19:1091-1097.
- [182] Cheng, K.S., Baker, C.R., Hamilton, G., *et al.*, 2002. Arterial elastic properties and cardiovascular risk/event. *European Journal of Vascular and Endovascular Surgery* 24:383-397.
- [183] Torii, R., Wood, N.B., Hadjiloizou, N., *et al.*, 2009. Fluid-structure interaction analysis of a patient-specific right coronary artery with physiological velocity and pressure waveforms. *Communications in Numerical Methods in Engineering* 25:565-580.
- [184] Chiastra, C., Migliavacca, F., Martinez, M.A., *et al.*, 2014. On the necessity of modelling fluid-structure interaction for stented coronary arteries. *Journal of the Mechanical Behavior of Biomedical Materials* 34:217-230.
- [185] Malve, M., Garcia, A., Ohayon, J., *et al.*, 2012. Unsteady blood flow and mass transfer of a human left coronary artery bifurcation: Fsi vs. Cfd. *International Communications in Heat and Mass Transfer* 39:745-751.
- [186] Pielhop, K., Klaas, M., Schroder, W., 2012. Analysis of the unsteady flow in an elastic stenotic vessel. *European Journal of Mechanics B-Fluids* 35:102-110.
- [187] Pielhop, K., Klaas, M., Schroder, W., 2015. Experimental analysis of the fluid-structure interaction in finite-length straight elastic vessels. *European Journal of Mechanics B-Fluids* 50:71-88.
- [188] Burgmann, S., Grosse, S., Schroder, W., *et al.*, 2009. A refractive index-matched facility for fluid-structure interaction studies of pulsatile and oscillating flow in elastic vessels of adjustable compliance. *Experiments in Fluids* 47:865-881.
- [189] Geoghegan, P.H., Jermy, M.C., Nobes, D.S., 2017. A piv comparison of the flow field and wall shear stress in rigid and compliant models of healthy carotid arteries. *Journal of Mechanics in Medicine and Biology* 17:16.
- [190] Khan, M.O., Chnafa, C., Gallo, D., *et al.*, 2017. On the quantification and visualization of transient periodic instabilities in pulsatile flows. *Journal of Biomechanics* 52:179-182.

Chapter 2

2 Study of the effect of stenosis severity and non-Newtonian viscosity on multidirectional wall shear stress and flow disturbances in the carotid artery using particle image velocimetry

2.1 Introduction

Atherosclerosis - a thickening and hardening of blood vessels due to endothelial dysfunction and plaque build-up - is one of the main risk factors for ischemic stroke and often develops at regions of complex flow patterns such as bifurcations. The focal development of atherosclerosis at particular sites in the arterial tree suggests that hemodynamic forces impact the initiation and progression of vascular disease. Specifically, in the carotid bifurcation, intimal thickening is greater at the outer wall of the carotid bulb opposite the flow divider, where low magnitude flow recirculation occurs [1]. Atherosclerosis has been shown to preferentially develop in regions of low and oscillatory shear stress [2-4] whereas regions with non-disturbed flow and steady, moderate to high shear levels exhibit atheroprotective genes. Furthermore, high WSS, often found at the proximal side of existing plaques, may be linked to plaque vulnerability. More recently, endothelial cell sensing of flow and shear directionality have been shown to play a key role in endothelial cell pro-inflammatory responses [5-7].

Local variation in wall shear stress is often quantified in numerical and experimental studies using the oscillatory shear index (OSI), a metric first proposed by Ku et al. [8] to account for changes in the direction of the cycle-averaged shear stress vector under pulsatile flow. However, recent work failing to find definitive evidence for the low and/or oscillatory shear hypothesis [9; 10] prompted the development of new metrics to quantify specifically the multi-directionality of wall shear stress in arterial flows [6; 7; 11; 12]. The traditional OSI parameter becomes ambiguous in distinguishing between uniaxially reversing shear and truly multidirectional shear stress. Peiffer et al. [7] proposed the transverse wall shear stress (transWSS) metric to capture the flow multi-directionality and showed a qualitative

association between transWSS modeled using CFD and regions of lipid deposition in the rabbit aorta. Additional shear metrics incorporating projections of the WSS along axial and orthogonal-to-axial directions [11; 12] as well as normalization of the instantaneous transWSS components [13] have also been explored.

For a complete three-dimensional analysis of WSS magnitude and direction, it is a requirement to have both three-dimensional, three-component velocity vector data, as well as accurate three-dimensional wall-location information. This requirement is inherently met for numerical simulations but is more challenging to implement experimentally. In vivo hemodynamic studies are completed using either Doppler ultrasound or phase-contrast magnetic resonance imaging (PC-MRI). The ability to calculate full three-dimensional maps of wall shear stress from PC-MRI has been demonstrated, employing interpolation of the velocity field along the inward normal of a segmented vessel surface [14-18]. The use of MRI benefits from being able to capture both velocity data and vessel geometry in the same reference frame, eliminating registration steps, and also allowing patient-specific studies that correlate shear metrics directly with plaque localization [19; 20]. However, MRI wall-shear estimates are limited by poor temporal and spatial resolution and highly influenced by errors in wall segmentation and thus also the estimated wall position. In addition, errors in WSS derived from MRI increase with shear magnitude, making MRI techniques less suitable in regions with high shear such as at a stenosis [21; 22].

Particle image velocimetry (PIV) is a well-established technique for mapping velocity fields in vitro, and it has commonly been used to calculate WSS from 2D and 3D studies of various arterial geometries [23-25]. Buchmann et al. [26] used stereoscopic and tomographic PIV in combination with a computed tomography scan of the phantom vessel to compute 3D WSS magnitude over the vessel surface in a carotid artery model under steady inlet flow (i.e. non-pulsatile). However, their method only allowed the magnitude of the WSS to be calculated, thus any further investigation of directional shear metrics was not conducted. Previously, Kefayati et al. [27] used a similar method to calculate wall-shear magnitude in vessels of varying plaque stenosis severity and eccentricity under pulsatile

flow with a Newtonian viscosity blood-analogue to assess spatial and temporal variations in velocities and WSS, but variation in shear direction was not explored.

Traditionally, experimental and numerical models of blood flow have assumed blood to be a Newtonian fluid with constant viscosity giving a linear stress-strain relationship, where the viscosity is approximated using the high-shear rate viscosity limit. However, blood viscosity characterization has shown that aggregation of red blood cells into long structures known as rouleaux causes the viscosity to increase in low-shear regions, and a shear-thinning behaviour is observed. Approximating blood to be a Newtonian fluid may be acceptable at high shear rates in large arteries but may cause WSS measurements to be inaccurate in regions of low shear, as observed in the post-stenotic recirculation and regions of destabilized flow. Therefore, it is beneficial to determine the effect of a Newtonian blood approximation when estimating local multidirectional shear patterns. Previous numerical studies have shown that a non-Newtonian viscosity model leads to flattened velocity profiles and longer recirculation zones compared to Newtonian, and that a Newtonian viscosity assumption underestimates WSS in low-shear stress regions due to the absence of shear-thinning behaviour [28-30].

The objective of the present study is to utilize a multi-plane stereoscopic PIV system to obtain three-dimensional, three-component velocity vector fields and subsequently combine the dataset with geometry data segmented from micro-computed tomography images to calculate multi-directional WSS. Additionally, a shear-thinning blood analogue fluid was developed, with viscosity fit to a cross model [31], and results compared to a typical Newtonian blood-analogue fluid. Measurements were carried out in idealized carotid bifurcation models with varying stenosis of the internal carotid artery and under pulsatile flow conditions. The differences between modeling blood as either a Newtonian or non-Newtonian fluid when investigating disturbed flow, WSS, OSI and transWSS are presented in stenosed models displaying a broad range of physiological flow disturbances.

2.2 Methods

2.2.1 Flow set-up

Flow measurements were carried out in transparent, life-sized, PIV-compatible carotid bifurcation phantoms fabricated in polydimethylsiloxane (PDMS) using a lost-core casting technique [32] as employed in previous US and PIV studies [27; 33-35]. Three idealized carotid geometries previously described by Smith et al. [36] and shown in Figure 2.1 were investigated, with common carotid artery (CCA) diameter of 8 mm (ICA diameter = 5.5 mm, ECA diameter = 4.6 mm) and eccentric stenosis of the internal carotid artery (ICA) of 30%, 50%, and 70% based on NASCET criteria [37].

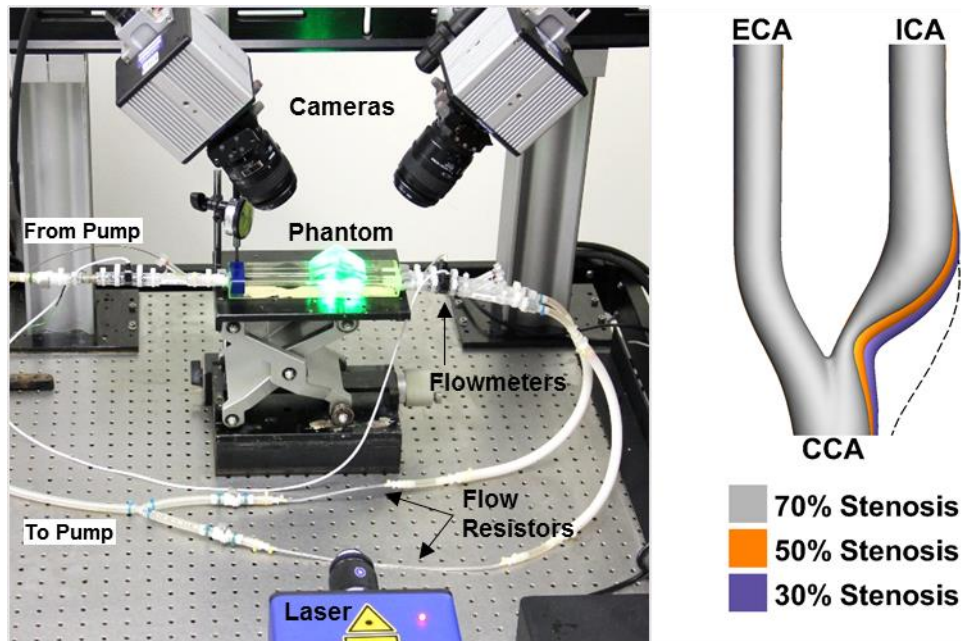


Figure 2.1: Experimental set-up including flow circuit and PIV components (left). Family of carotid artery bifurcation geometries with progressing degrees of eccentric stenosis (right). Dashed contour line indicates the boundary of the normal, disease-free geometry. CCA: common carotid artery, ICA: internal carotid artery, ECA: external carotid artery

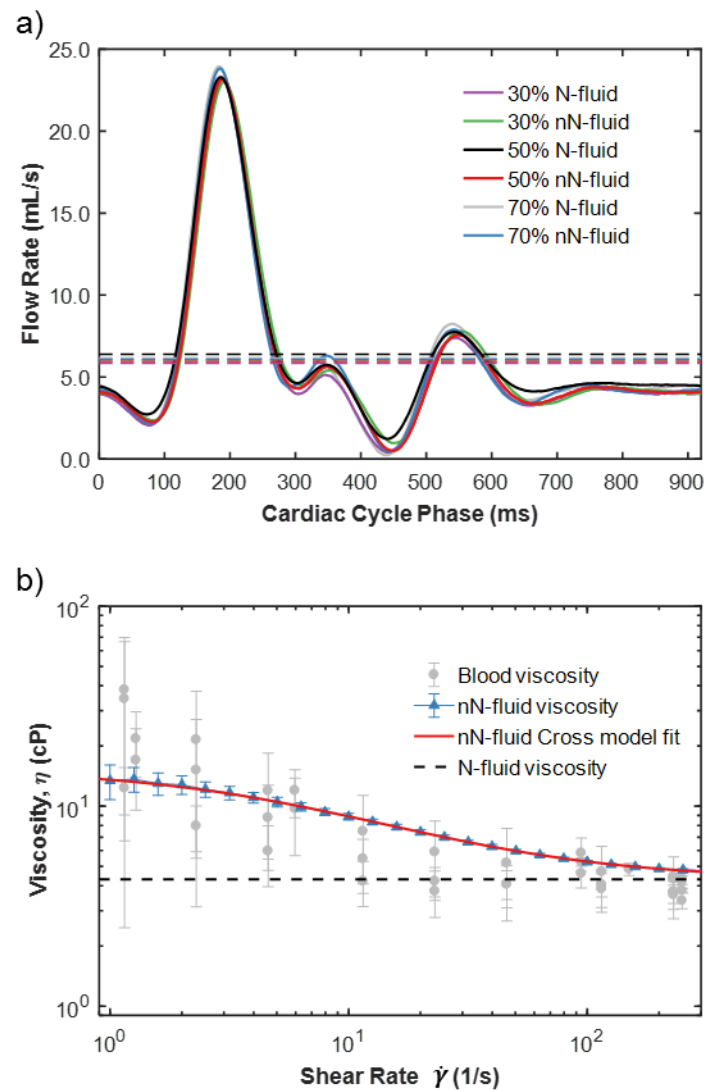


Figure 2.2: (a) Flow waveforms measured at the CCA inlet for each experimental PIV dataset (phase averaged from 15 cardiac cycles). Dashed lines represent the mean flow-rate in each case (6.1 ± 0.2 mL/s averaged across all models). (b) Experimental fluid viscosity versus shear rate. Blood data is taken from recent literature [40-45]. Solid line shows Cross model fit to non-Newtonian blood analogue fluid viscosity measurements. Dashed line indicates constant viscosity of Newtonian blood analogue fluid.

A computer-controlled positive-displacement pump (CompuFlow 1000, Shelley Medical Imaging Technologies, London ON Canada) was used to generate physiological pulsatile flow. An idealized carotid artery waveform based on in-vivo US measurements in young adults was applied at the CCA inlet [38]. Downstream flow resistors composed of small-diameter tubing create a physiologically realistic ICA:ECA flow division of 60:40 [33]. Flow and pressure waveforms were monitored at the phantom inlets and outlets using inline electromagnetic flowmeters (Model 501D, Carolina Medical Electronics, East Bend NC, USA) and a catheter-based pressure transducer (Model SPR-350S, Millar Inc., Houston, TX, USA). The measured CCA-inlet flow waveforms for all phantoms and blood analogue fluids are shown in Figure 2.2a.

2.2.2 Blood analogue fluids

Two custom blood-analogue fluids were utilized, as previously optimized for use in PIV experiments with PDMS phantoms [31; 39]. The first, previously applied in PIV experiments [27; 34; 35] is a Newtonian fluid (N-fluid) composed of water, glycerol and sodium iodide with a viscosity of 4.31 cP matching the high shear-rate viscosity range of human blood. The second includes the addition of xanthan gum to produce a non-Newtonian fluid (nN-fluid) whose composition is based on a best-match to blood viscosity data from a collection of ex vivo studies [40-45], as previously described [31]. The fluid formulations are given in Table 2.1.

Table 2.1: Blood analogue fluid formulations

Blood Analogue Fluid	N-fluid	nN-fluid
Water (% w/w)	47.4	51.9
Glycerol (% w/w)	36.9	22.2
NaI (%w/w)	15.7	25.9
Xanthan Gum (% w/w)		0.0019

The shear-dependent viscosity of the working fluid was measured using a couette-cell rheometer (MCR 302, Anton-Paar, Montreal QC, Canada) and a Cross model fit was applied for shear rates $> 1 \text{ s}^{-1}$ using non-linear least squares regression for use in WSS calculations. The Cross model of viscosity is given by

$$\eta(\dot{\gamma}) = \eta_{\infty} + \frac{\eta_0 - \eta_{\infty}}{1 + a\dot{\gamma}^{1-q}} \quad (2.1)$$

where η_0 and η_{∞} refer to the viscosities as $\dot{\gamma}$ approaches zero and infinity, respectively, and a and q are constants determining the degree and rate of shear thinning. The measured viscosity data for the nN-fluid and the Cross model fit are shown in Figure 2.2b along with the literature blood data [40-45].

2.2.3 PIV data acquisition and velocity vector processing

The PIV image data were acquired using a commercial stereoscopic PIV system as shown in Figure 2.1a. (LaVision Inc., Ypsilanti MI, USA). Double-frame images were acquired at 100 Hz (10 ms resolution) for 870 ms of the total 920 ms cardiac cycle, leaving 50 ms to prepare for the next pump synchronization pulse. The interframe time, dt , ranged from 100-250 μs , depending on the peak systolic velocity expected for a given stenosed model. Volumetric data were assembled by translating the phantom vertically in increments of 0.5 mm to collect 15 2D slices.

PIV data were processed (DaVis 7.2, LaVision Inc.) using a fast-Fourier-transform based cross-correlation algorithm with decreasing window size from 64x64 pixels to 16x16 pixels and 50% window overlap. For final passes, a Gaussian-window weighting and a high-accuracy Whittaker reconstruction was applied. This resulted in an in-plane vector spacing of approximately 0.3 mm across all models. Velocity maps were post-processed using a median filter to remove spurious vectors and one pass with a 3x3 smoothing kernel, and then stacked together to construct the 3D three-component velocity dataset.

2.2.4 Computed tomography imaging

A segmentation of the phantom geometry for WSS estimation was derived from computed tomography scans obtained using a volumetric cone-beam micro-CT scanner (Locus Ultra, General Electric Healthcare, London, ON, Canada). Surface data were obtained from the reconstructed CT images using a level-set segmentation method in the Vascular Modeling Toolkit (VMTK) [46]. Subsequent smoothing and remeshing steps were applied to achieve a coarse surface mesh of triangular elements with a mean edge length of $0.41 \pm 0.06 \mu\text{m}$ across all models. The segmented lumen surface for each phantom was then registered to the respective volumetric PIV data using an iterative closest-point algorithm (VMTK) to the outermost velocity vectors nearest the wall. The registered vessel surface was cropped to include 8 mm proximal and 32 mm distal to the bifurcation apex for WSS calculation, resulting in a mean of 18000 ± 500 surface elements per model.

2.2.5 Data analysis

2.2.5.1 Wall shear stress

The formula for the Cauchy stress tensor is

$$\boldsymbol{\sigma} = -p\mathbf{I} + \boldsymbol{\tau} \quad (2.2)$$

where p is the pressure, \mathbf{I} is the identity matrix and $\boldsymbol{\tau}$ is the deviatoric stress tensor representing the viscous stresses. For an incompressible, Newtonian fluid the deviatoric stress tensor $\boldsymbol{\tau}$ is given by

$$\boldsymbol{\tau} = \eta\dot{\boldsymbol{\gamma}} = \eta(\nabla\mathbf{u} + (\nabla\mathbf{u})^T) \quad (2.3)$$

where $\dot{\boldsymbol{\gamma}}$ is the symmetric rate-of-strain tensor. The deviatoric stress tensor for a Newtonian fluid becomes, using tensor notation,

$$\tau_{ij} = \eta \left(\frac{\partial u_i}{\partial x_j} + \frac{\partial u_j}{\partial x_i} \right) \quad (2.4)$$

The traction vector at a specific surface point is given by the dot product of the stress tensor with the surface inward normal vector, \mathbf{N} :

$$\mathbf{t} = \mathbf{N} \cdot \boldsymbol{\tau} \quad (2.5)$$

Finally, the component of the traction vector tangential to the vessel wall is denoted the wall shear stress vector.

$$\boldsymbol{\tau}_w = \mathbf{t} - (\mathbf{t} \cdot \mathbf{N})\mathbf{N} \quad (2.6)$$

In the case of a shear-thinning fluid, the viscosity is dependent on the local magnitude of the shear rate, as described by the Cross model in Equation 2.1. The deviatoric stress tensor formulation becomes

$$\boldsymbol{\tau} = \eta(\dot{\gamma})\dot{\boldsymbol{\gamma}} \quad (2.7)$$

The magnitude of the shear rate may be calculated from the second invariant of the rate-of-strain tensor as

$$\dot{\gamma} = \sqrt{\frac{1}{2} \text{tr}(\dot{\boldsymbol{\gamma}}^2)} = \sqrt{\frac{1}{2} \dot{\boldsymbol{\gamma}} : \dot{\boldsymbol{\gamma}}} \quad (2.8)$$

From each surface point, the first three points, spaced 0.3 mm apart along the inward normal, were obtained at which the surrounding velocity data were interpolated using cubic polynomials in a 6x6x6 vector neighbourhood, and the null velocity was assigned at the wall point. The wall shear calculation was facilitated by a rotation of the coordinate system to align the wall normal direction with the z-axis, consistent with magnetic resonance imaging studies of WSS [14; 21; 47]. The interpolated velocities were rotated into the new coordinate system, where the reduced deformation tensor derivatives were calculated. The transformed velocities were fit with a shape-preserving piecewise cubic polynomial, and the derivative of the fit at the wall location for each component was taken as the local shear rate in transformed coordinates. The WSS vector was taken as the local in-plane traction

vector found from Equation. 2.6, and an inverse transformation was applied to obtain the WSS in real coordinates.

2.2.5.2 Calculation of wall shear parameters

Standard WSS parameters were derived for comparison across vessel geometries and viscosity models. The cycle average of the *magnitude* of the WSS vector, denoted time-averaged WSS (TAWSS), is defined as

$$\text{TAWSS} = \frac{1}{T} \int_0^T |\boldsymbol{\tau}_w| dt \quad (2.9)$$

Where T is the cardiac cycle period. The oscillatory shear index (OSI) is defined as

$$\text{OSI} = \frac{1}{2} \left[1 - \left(\frac{|\int_0^T \boldsymbol{\tau}_w dt|}{\int_0^T |\boldsymbol{\tau}_w| dt} \right) \right] = \frac{1}{2} \left[1 - \left(\frac{|\boldsymbol{\tau}_{\text{mean}}|}{\text{TAWSS}} \right) \right] \quad (2.10)$$

where the mean WSS vector is

$$\boldsymbol{\tau}_{\text{mean}} = \frac{1}{T} \int_0^T \boldsymbol{\tau}_w dt \quad (2.11)$$

The transverse wall shear stress, defined by Peiffer et al. [7] as the time average of the component of WSS acting perpendicular to the direction of the mean WSS vector, is calculated as

$$\text{transWSS} = \frac{1}{T} \int_0^T \left| \boldsymbol{\tau}_w \cdot \left(\hat{\mathbf{n}} \times \frac{\int_0^T \boldsymbol{\tau}_w dt}{|\int_0^T \boldsymbol{\tau}_w dt|} \right) \right| \quad (2.12)$$

Where $\hat{\mathbf{n}}$ is the wall normal vector. To quantify the spatial extent of cycle-averaged WSS parameters, a thresholding method was used, similar to that applied by others [48-50]. In this case, the 50% eccentric stenosis geometry with N-fluid is chosen as a reference from which threshold levels are calculated corresponding to the 20th percentile of the distribution

for low TAWSS and the 80th percentile of the distribution of OSI and transWSS; this results in the following thresholds: TAWSS₂₀ = 0.69 Pa, OSI₈₀ = 0.18, transWSS₈₀ = 0.51 Pa. The surface area exposure to levels of the time-averaged parameters below the 20th percentile or exceeding the 80th percentile thresholds was calculated.

2.2.5.3 Turbulence intensity

Reynolds numbers were estimated from the mean axial velocity across central plane profiles and the corresponding vessel diameter as $Re = \rho VD/\mu$. Peak and cycle-mean Reynolds numbers in the CCA (averaged across all models) were 1502 and 523, respectively. For comparison, peak and cycle-mean Reynolds numbers calculated within the narrowest stenosis diameter were 1266 and 416 for the 30% model, 1611 and 533 for the 50% model, and 1786 and 724 in the 70% model.

The turbulence intensity (TI) metric was previously used to quantify disturbed flow in models of varying stenosis severity, plaque eccentricity and plaque ulceration using both ultrasound and PIV [35; 51; 52]. Turbulence intensity is calculated based on the Reynold's decomposition method as

$$u'_i(t, n) = u_i(t, n) - U_i(t) \quad (2.13)$$

$$TI_i(t) = \sqrt{\frac{\sum_{n=1}^N u'_i(t, n)u'_i(t, n)}{N - 1}}, i = x, y, z \quad (2.14)$$

$$TI(t) = \sqrt{(TI_x(t))^2 + (TI_y(t))^2 + (TI_z(t))^2} \quad (2.15)$$

where u' is the velocity fluctuation, and U is the phase-averaged velocity for each component. The chosen number of cardiac cycles used in the TI estimation was N=15, shown previously to be the minimum number of sequential cycles required for statistical convergence of the TI value [35].

To compare the evolution of turbulence intensity over time, TI values were averaged over a downstream region of interest (ROI) extending wall-to-wall and approximately one CCA diameter (8 mm) axially. The ROI location was selected as the region where ROI-averaged TI (denoted $\overline{\text{TI}}$) reached a maximum, and only central-plane values were included in the mean calculation. Uncertainties in $\overline{\text{TI}}$ were reported as the absolute maximum difference in $\overline{\text{TI}}$ incurred when the ROI was shifted by ± 4 mm, reflecting the sensitivity to the selection of the ROI location.

2.2.5.4 Uncertainty analysis

PIV uncertainties were analyzed using commercial software (DaVis 8.4, LaVision Inc.) which utilizes the correlation statistics method [53]. Uncertainties were calculated for the 50% stenosed model with Newtonian fluid at peak systole ($t = 180$ ms) and at diastole for comparison ($t = 830$ ms). Uncertainties in the WSS are influenced by several factors, including velocity uncertainty and errors in the segmentation and registration of the CT surface. Given the complexity of the WSS calculation method, a Monte Carlo approach was taken to provide an estimate of the WSS uncertainty propagated from the spatial distribution of velocity errors and random 3D misalignments of the CT surface and velocity data. The WSS calculation was iterated 1000 times. The distribution of resulting velocity magnitude at each location was normal with mean equal to the measured velocity and standard deviation equal to the local uncertainty in velocity magnitude. Thus, vectors were limited to their original direction and only varied in magnitude. For each iteration, the registered CT surface was shifted up to one voxel (154 μm) in a random direction uniformly distributed on the unit sphere. The standard deviation of the resulting WSS distribution at each surface point was used to estimate WSS uncertainty.

2.3 Results

2.3.1 Velocity and turbulence intensity

Figure 2.3 shows the phase-averaged velocity magnitude in the central-plane slice ($z = 0$ mm) for the time point corresponding to peak systole ($t = 180$ ms). A high-velocity jet extends from the stenosis throat along the inner wall, eventually crossing through the lumen and impinging at the outer ICA wall before separating into two recirculation zones, indicated on Figure 2.3c. Flow in the CCA and ECA is generally well organized and approximately laminar. Comparable maximum jet velocities were reached for N-fluid compared to nN-fluid with decreases of 6.9%, 0.02% and 0.56% in the absolute maximum velocities reached in the 30%, 50% and 70% geometries, respectively. The spatial coverage of velocities greater than the maximum scale limit was larger for the N-fluid as indicated by the black contours, and this effect was more pronounced for the 30% stenosed case.

Central-plane phase-averaged velocity profiles in the ICA are shown for N-fluid and nN-fluid in Figure 2.4, displaying the centerline-projected velocity at peak systole for axial locations beginning in the recirculation zone and spaced 6 mm along the centerline, as indicated in the right panels of Figure 2.3 for each geometry. Velocity profiles for nN-fluid models appear blunted compared to N-fluid models. For S1 and S2, a slight deflection of the jet toward the flow-divider wall is evident for nN-fluid models, contributing to a steeper gradient and thus higher WSS at the inner wall. The temporal variation in velocity profiles is shown in Figure 2.5 for the 50% stenosed model. At S1, blunted jet-velocity profiles for the nN-fluid persist throughout the cardiac cycle including a shift of the maximum velocity towards the flow divider wall and slightly more flow reversal in the recirculation region (negative velocities at radial distance > 1 mm). In the downstream region at S5, greater variation between N-fluid and nN-fluid profiles can be observed, reflective of the disturbed flow environment in this region.

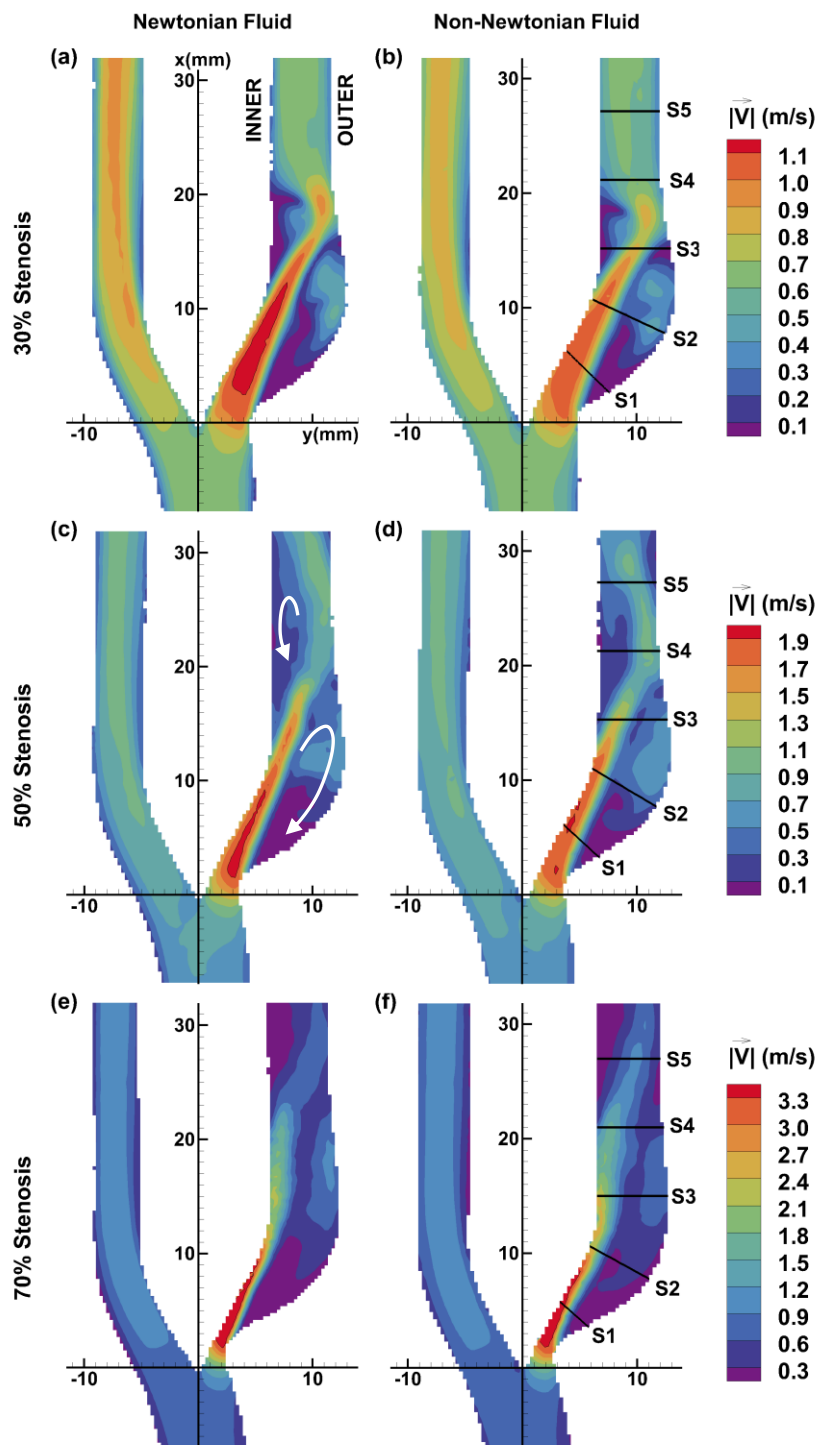


Figure 2.3: Central plane phase-averaged velocity magnitude at peak systole ($t = 180$ ms). Note that each row of models has an individual color bar. Contour lines correspond to the highest contour level in each row. Recirculation regions are indicated in white on panel c. Slices S1-S5 on panels a, d, and F indicate cross-sections where velocity profiles are extracted for each geometry.

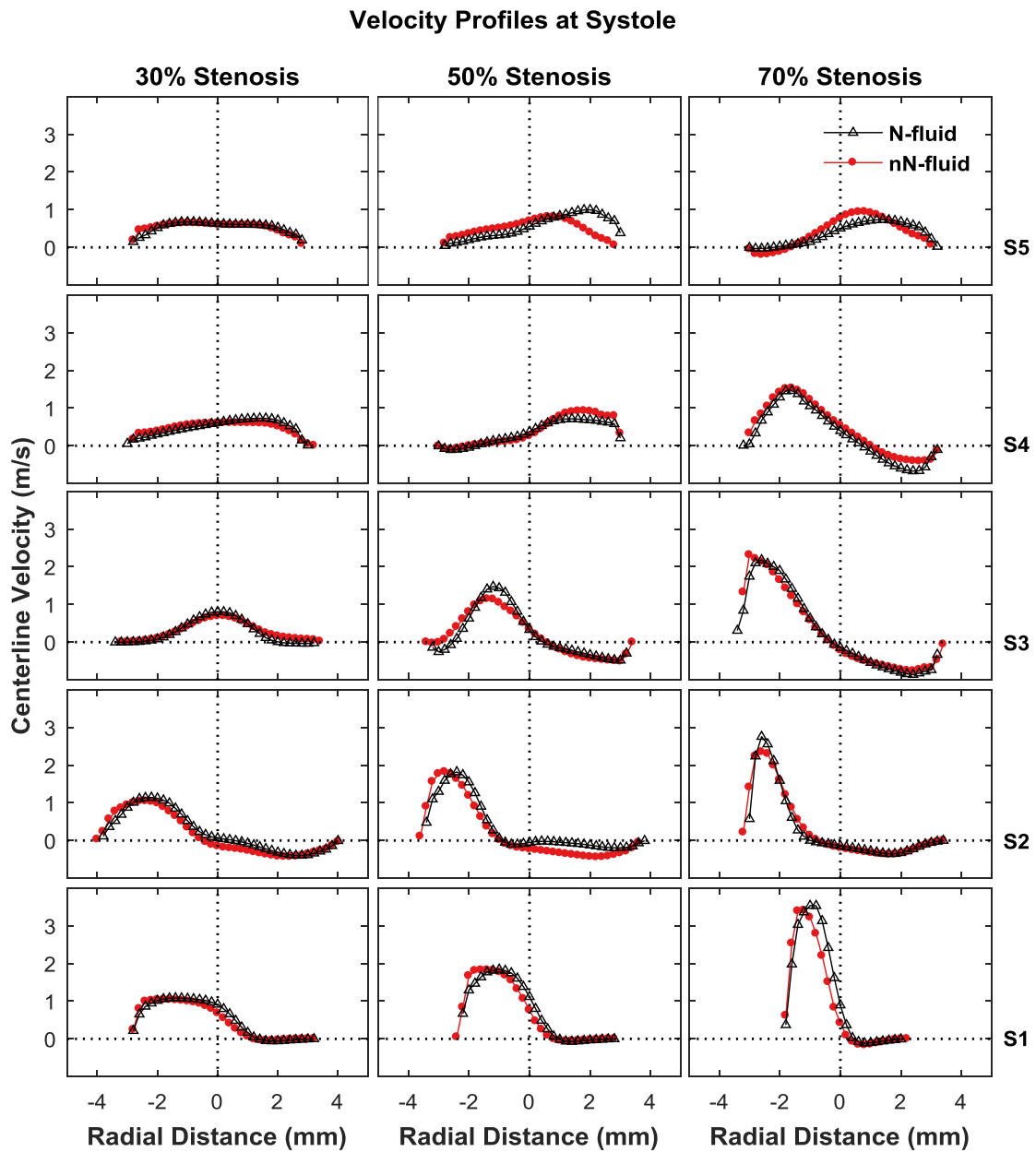


Figure 2.4: Phase-averaged centerline-projected velocity profiles at peak systole. Profiles are extracted from the central plane ICA at slices S1-S5 spaced 6 mm apart along the centerline indicated in Fig. 3.

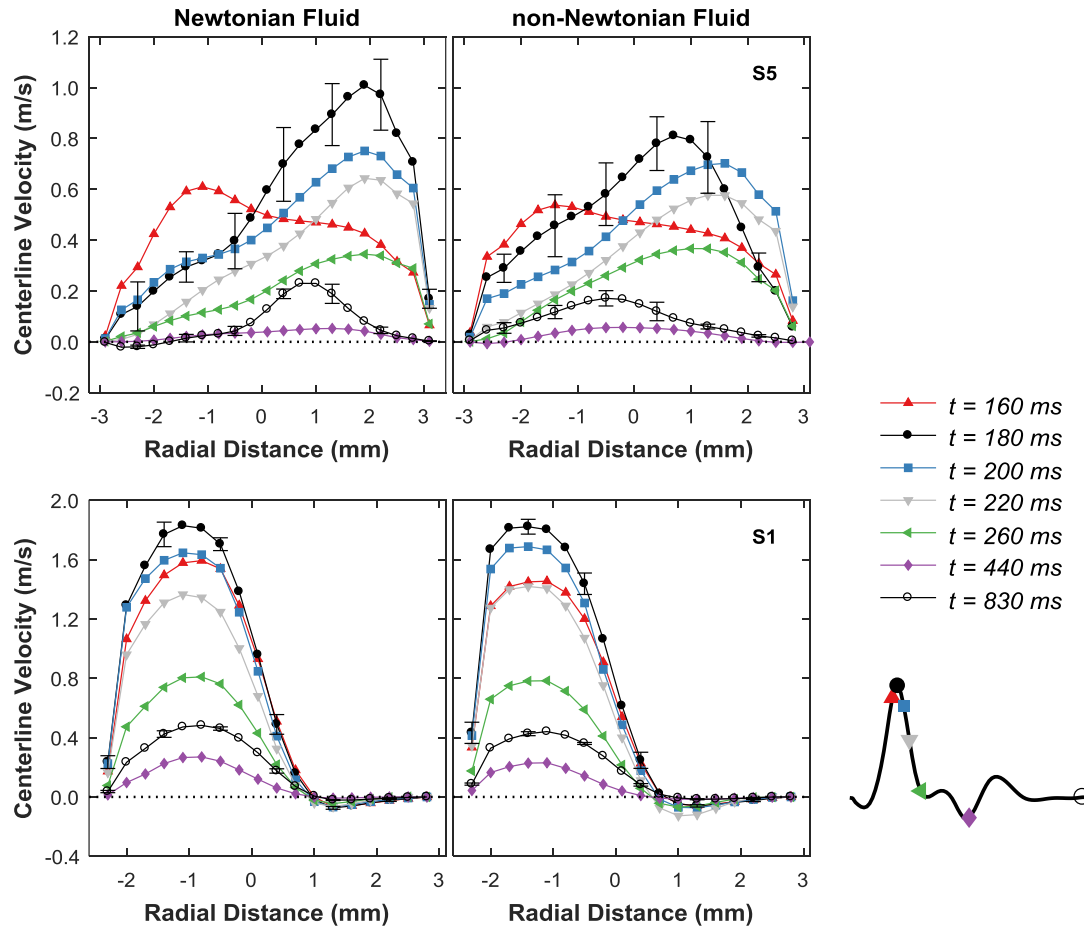


Figure 2.5: Temporal phase-averaged centerline-projected velocity profiles for the 50% eccentric geometry, extracted from the central plane ICA at slices S1 (bottom row) and S5 (top row) indicated in Fig. 3. Sparse error bars representing standard deviation are shown for the profiles corresponding to peak systole and diastole.

Figure 2.6 shows central-plane TI maps in the ICA for the time point of maximum $\overline{\text{TI}}$ for each model ($t = 180\text{-}200$ ms), which occurs in the deceleration portion of the cardiac cycle just after peak systole. The disturbed flow region extends from the inner wall across the lumen where the jet detaches and expands into the downstream ICA. A transverse slice is also shown at the center of the selected ROI, from which patterns are approximately symmetric about the central plane. Evolution of $\overline{\text{TI}}$ over time is illustrated in Figure 2.7, with the selected ROIs indicated by rectangular boxes in Figure 2.6. TI values are summarized in Table 2.2. The peak $\overline{\text{TI}}$ as well as the absolute single-site maximum TI values decreased for the nN-fluid compared to the N-fluid for 30% and 50% stenosis but increased for the 70% case. Although the peak $\overline{\text{TI}}$ reached in the 70% stenosed model is higher for the nN-fluid compared to N-fluid, we see that high $\overline{\text{TI}}$ values are sustained for a longer time frame for the N-fluid (Figure 2.7) resulting in a larger cycle-averaged $\overline{\text{TI}}$ than the nN-fluid (Table 2.2).

Central plane ensemble averaged velocity uncertainties are shown in Figure A.1. The error in the ensemble average contains both the measurement errors and contributions due to velocity fluctuations. [54; 55] The highest errors are found at locations with high shear gradients, such as at the boundaries of the high-velocity jet, propagated from the instantaneous velocity uncertainties. The contribution from flow fluctuations increases the uncertainties in the downstream ICA region due to the disturbed flow, as reflected by the TI metric. At peak systole in the 50% stenosed model with Newtonian fluid, maximum uncertainties in the ensemble averaged velocity propagated from instantaneous velocity errors were approximately 0.09 m/s. When contributions from flow fluctuations were included, the maximum increased to 0.23 m/s and the overall average uncertainty was 0.06 m/s. The maximum and average overall uncertainties at diastole were 0.08 m/s and 0.03 m/s respectively.

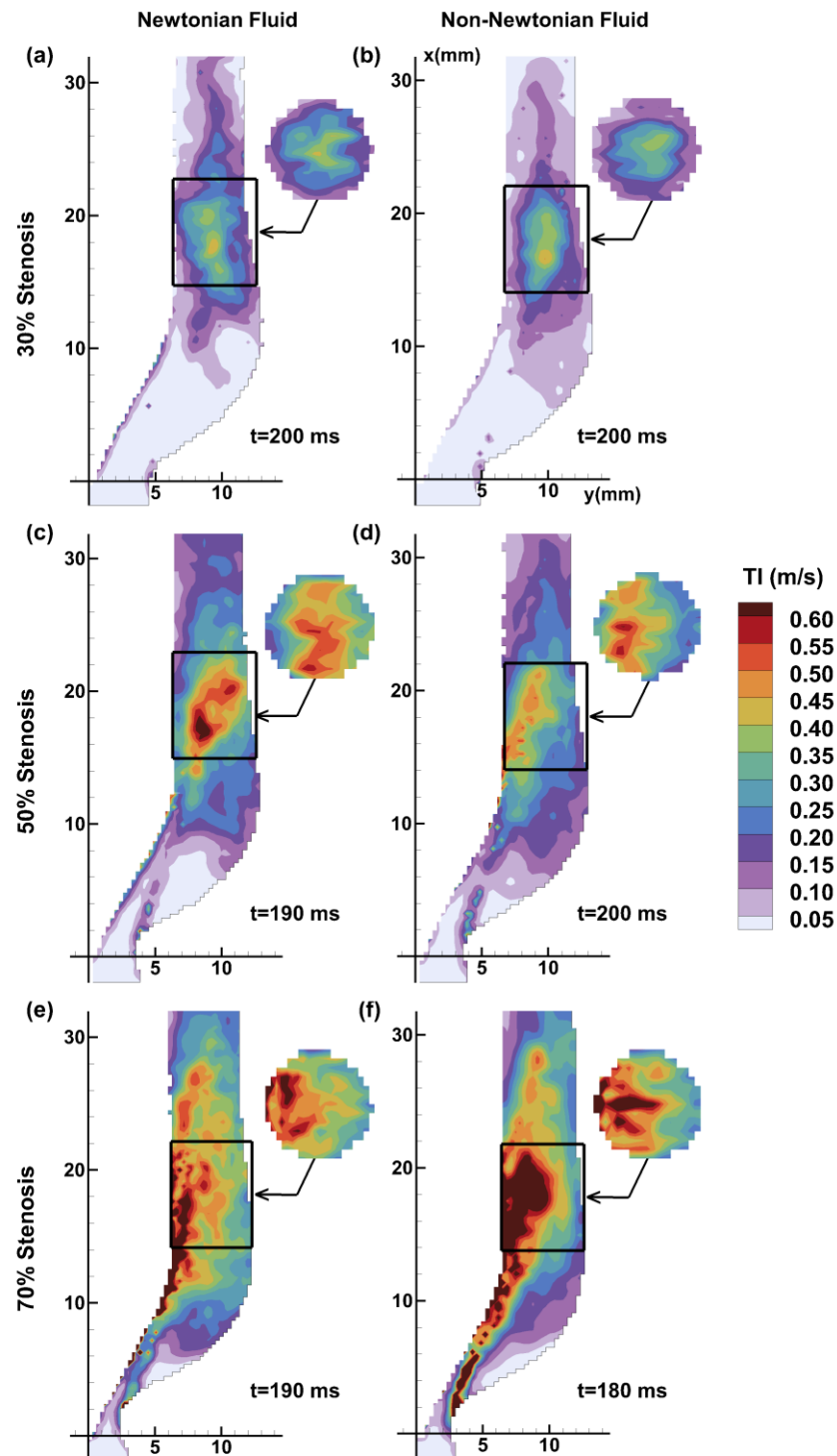


Figure 2.6: Central plane maps of turbulence intensity magnitude in the ICA, shown at the time point of peak ROI-averaged TI, as indicated in each panel. A transverse slice is shown for each model at the center of the ROI, which is indicated by the boxed area.

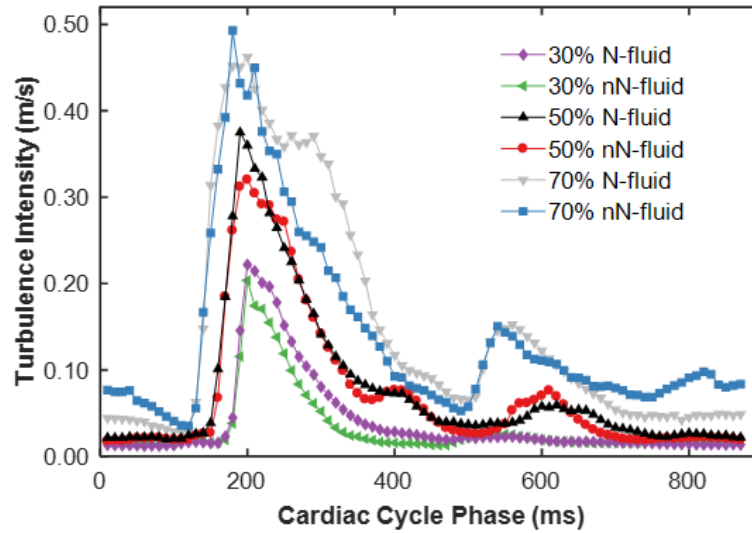


Figure 2.7: ROI-averaged TI versus cardiac cycle time for all models.

2.3.2 Wall shear stress and shear metrics

Figure 2.8 shows the TAWSS for all phantoms. For 3D visualization purposes, the vessel is shown in two orientations exposing the inner and outer walls of the ICA on the left and right, respectively. The outer wall region, along the large recirculation zone, from the stenosis throat to the jet impingement site contains the lowest shear rates. A region of elevated TAWSS occurs at the stenosis throat and continues distally along the inner wall of the ICA adjacent to the high-velocity jet. Instantaneous wall shear stress maps (not shown) showed qualitatively similar patterns. Absolute maximum WSS values (Table 2.3), occurring at peak systole for all models, were 22.9 %, 9.6%, and 2.2% higher for the nN-fluid compared to N-fluid counterparts. N-fluid consistently underestimated WSS compared to nN-fluid when averages were taken over each of the vessel branches. WSS maps at peak systole are shown in Figure A.2.

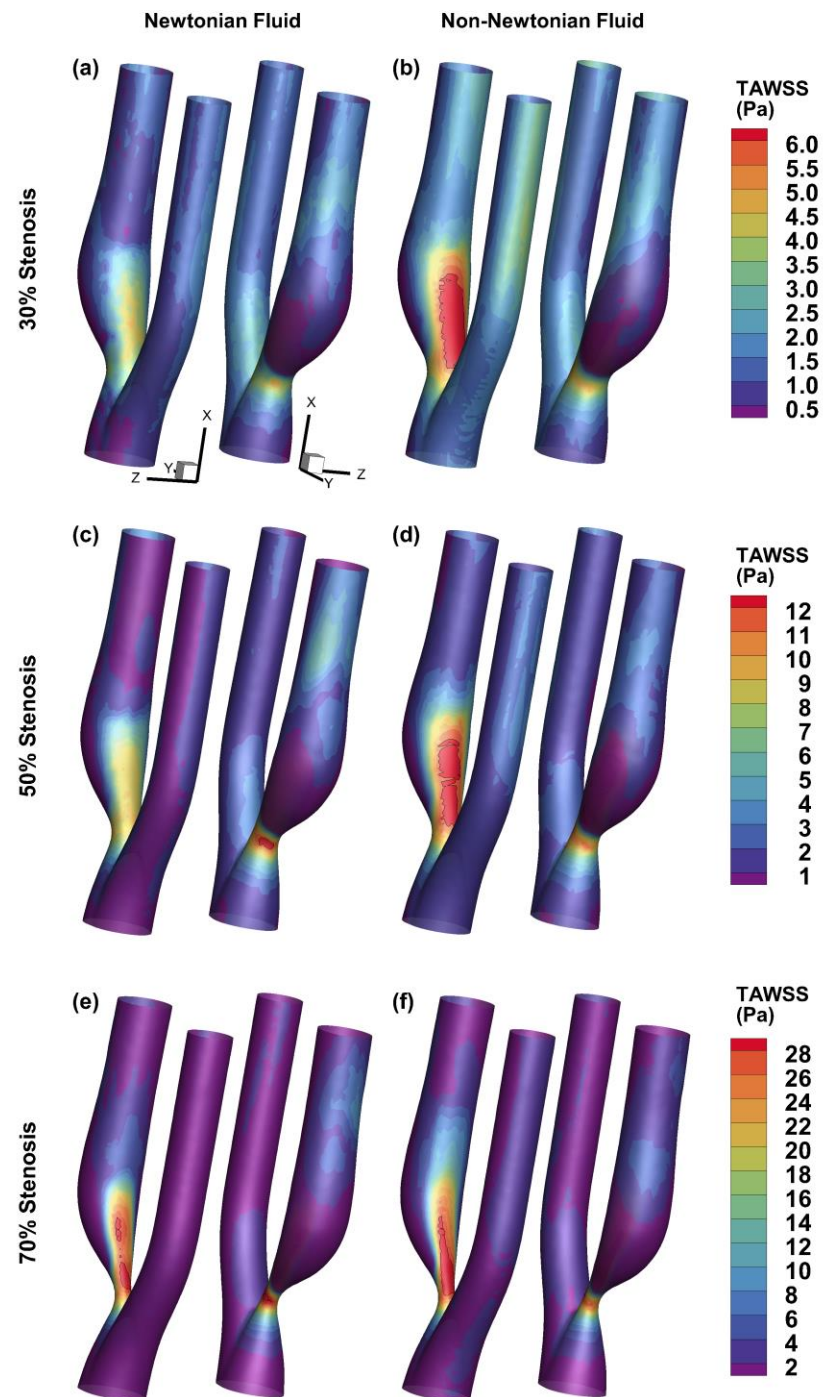


Figure 2.8: Contours of TAWSS. Each model is shown in two orientations, exposing the inner and outer walls of the ICA on the left and right, respectively. Note that each row of models has an individual color bar. Contour lines correspond to the highest contour level in each row.

Table 2.2: Turbulence intensity parameters. Absolute max TI is the maximum single site TI value found within the ROI, indicated by the boxed area in Fig. 6. Maximum $\overline{\text{TI}}$ refers to the peak ROI averaged TI value (at $t = 180 - 200$ ms) and cycle-averaged $\overline{\text{TI}}$ refers to the temporal and spatial mean over the ROI. Errors indicate the maximum differences incurred from shifting the ROI ± 4 mm axially.

Geometry	30% Stenosis		50% Stenosis		70% Stenosis	
	N-fluid	nN-fluid	N-fluid	nN-fluid	N-fluid	nN-fluid
Absolute max. TI (m/s)	0.502	0.453	0.695	0.653	1.293	1.379
Maximum $\overline{\text{TI}}$ (m/s)	0.222 ± 0.054	0.204 ± 0.052	0.375 ± 0.064	0.320 ± 0.050	0.462 ± 0.041	0.493 ± 0.073
Cycle-averaged $\overline{\text{TI}}$ (m/s)	0.039 ± 0.006	0.033 ± 0.006	0.078 ± 0.012	0.073 ± 0.017	0.148 ± 0.036	0.140 ± 0.032

Table 2.3: Wall shear stress parameters. Absolute max. WSS refers to the maximum single site WSS value. Remaining values are mean of the parameter over the specified vessel branch with standard deviation in parenthesis.

Geometry	30% Stenosis		50% Stenosis		70% Stenosis	
	N-fluid	nN-fluid	N-fluid	nN-fluid	N-fluid	nN-fluid
Absolute max. WSS (Pa)	20.75	25.49	41.92	45.94	88.24	90.22
Absolute max. TAWSS (Pa)	5.03	7.09	13.21	13.79	31.67	31.66
TAWSS – CCA (Pa)	0.73 (0.29)	1.03 (0.35)	0.96(0.31)	1.29 (0.31)	1.12 (0.26)	1.53 (0.39)
TAWSS – ICA (Pa)	1.30 (0.99)	1.93 (1.55)	2.43 (2.45)	2.84 (3.05)	4.18 (6.12)	4.57 (6.28)
TAWSS – ECA (Pa)	1.29 (0.49)	1.77 (0.64)	1.42 (0.61)	1.87(0.58)	1.50 (0.52)	2.00 (0.51)
OSI – ICA	0.09 (0.11)	0.08 (0.12)	0.09 (0.11)	0.08 (0.10)	0.10 (0.11)	0.08 (0.09)
transWSS – ICA (Pa)	0.22 (0.15)	0.30 (0.20)	0.35 (0.25)	0.45 (0.34)	0.53 (0.51)	0.68 (0.62)

WSS uncertainty maps for the 50% stenosed model with N-fluid at peak systole are shown in Figure A.3. Errors due to velocity fluctuations were not included in the WSS uncertainty maps shown, reflecting the propagation of only PIV measurement errors. Errors propagated from the registration step are dominant to errors propagated from uncertainty in velocity data. The average percentage error in WSS magnitude over all points was 14%, however point-by-point relative errors vary considerably at systole due to the high dynamic range of velocities. For the highest WSS values (top 10%) the mean WSS and error was 26 ± 1 Pa. For the lowest WSS values (bottom 10%) the mean WSS and error was 1.0 ± 0.2 Pa. When flow fluctuations are included in the uncertainty propagation, the average error in WSS magnitude increases by approximately 10%. WSS uncertainty maps at diastole are shown in Figure A.4 in which absolute error values are lower, but WSS values are also much lower, resulting in a higher average relative error of 30%.

Figure 2.9 shows maps of the OSI computed from Equation 2.10 overlaid with a sparse sample of unit vectors representing the direction only of the temporal mean WSS vector, τ_{mean} (Eq. 11). Elevated OSI demarcates regions of flow impingement and recirculation, occurring in a ring pattern at the outer ICA wall and at the distal inner ICA wall. Insets in Figure 2.9 emphasize that elevated OSI tends to occur at, 1) sites of flow impingement and subsequent divergence of the mean WSS vector as in P1, P3 and P5 at the distal edge of recirculation zones, 2) sites where oppositely directed flow meet as in P4 where the jet flow meets with that from the distal recirculation and also P3 where flow streams along the front and back of the ICA merge at the plane of symmetry, and 3) where a vortex occurs adjacent to the wall as in P2. Models with nN-fluid experience reduced OSI at the downstream inner ICA wall compared to N-fluid but slight increase in OSI levels and surface coverage in the outer ICA wall region

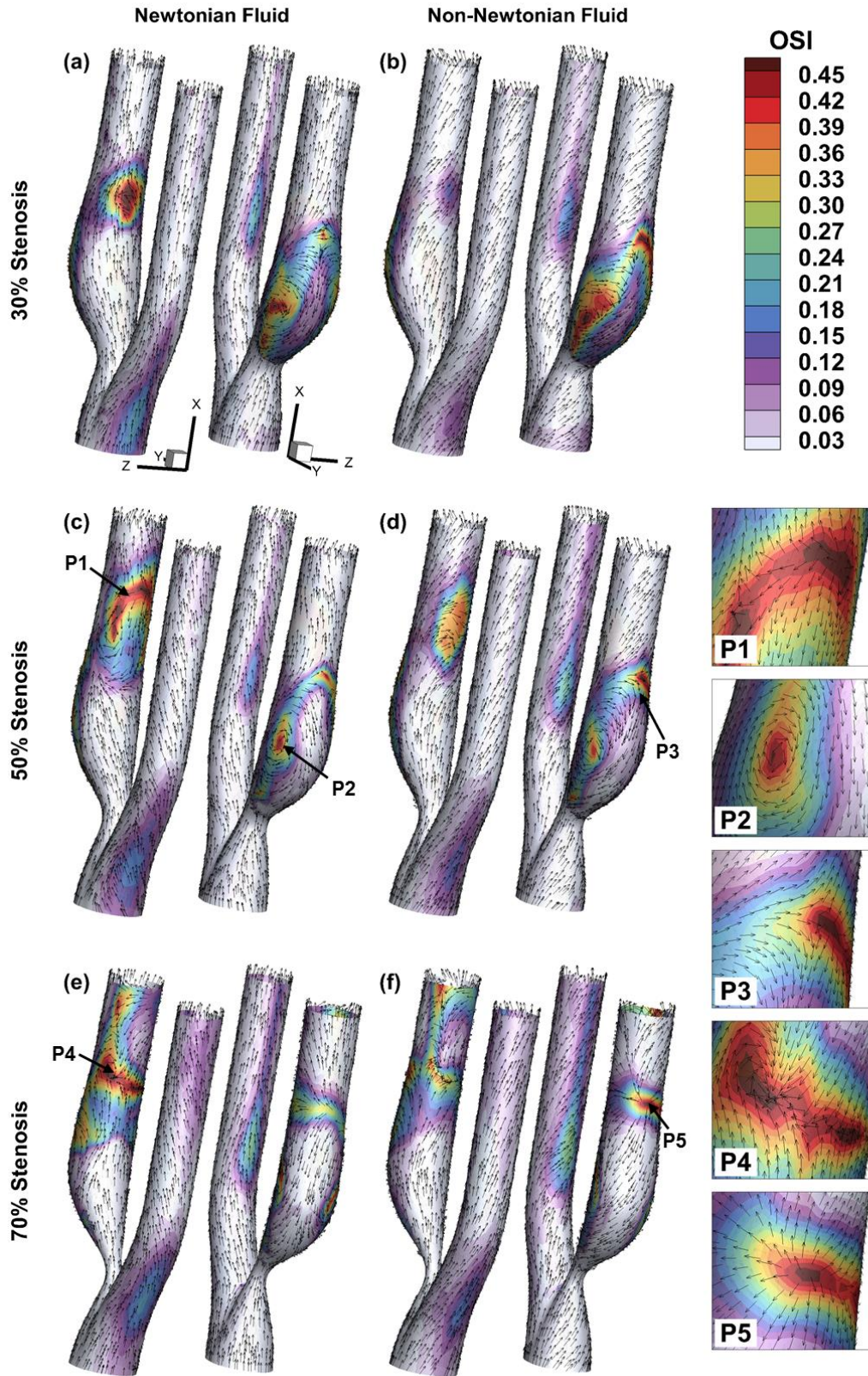


Figure 2.9: Contours of OSI overlaid with a sparse sample of unit vectors representing the direction only of the mean WSS vector. Each model is shown in two orientations, exposing the inner and outer walls of the ICA on the left and right, respectively. Insets provide enlarged views from points P1 through P5 whose locations are indicated in panels c-f depicting three key contributors to OSI: flow impingement on wall (P1, P3, P5), flow streams merging along wall (P3, P4), and wall-adjacent vortical flow (P2).

Figure 2.10 shows elevated transWSS regions occur at the inner ICA adjacent to the jet, extending along the distal recirculation zone, and then at the jet impingement location on the outer ICA wall. Like TAWSS, absolute magnitude of transWSS increases with increasing stenosis severity and is noticeably increased for nN-fluid, reflective of the overall higher WSS magnitude for nN-fluid. If the transWSS at each surface point is normalized by the local TAWSS (shown in Figure A.5), the distributions are very similar to OSI maps, suggesting the low magnitude transverse WSS components may be captured with the OSI metric. However, the transWSS metric also includes regions with elevated transverse component due to small directional changes for high-shear flows, evident in the inner-wall region in Figure 2.10f.

Finally, luminal surface exposure to time-averaged shear metrics is summarized in Figure 2.11. Surface area exposed to low shear magnitude, calculated as $TAWSS_{20}$, decreases with stenosis severity. N-fluid assumption leads to consistently underestimated WSS, thus area exposed to low shear is reduced with nN-fluid by 7.5%, 5.8%, and 8.4% compared to N-fluid counterparts. Fraction of surface area exposed to high OSI is comparable (~20% average) for all models (Figure 2.11, center) despite changes in location and pattern with disease progression and fluid type (Figure 2.8). OSI_{80} appears suppressed in nN-fluid models, as is the mean OSI over the ICA (Table 2.3). The surface area exposed to high transWSS increases with increasing stenosis severity with additional increase in nN-fluid models compared to N-fluid, reflective of the area exposed to high shear magnitude in general. Lastly, differences in the surface area exposure between Newtonian and non-Newtonian fluids are most pronounced in the most severely stenosed 70% model, suggesting that the assumption of a Newtonian viscosity model will have the most impact in these cases.

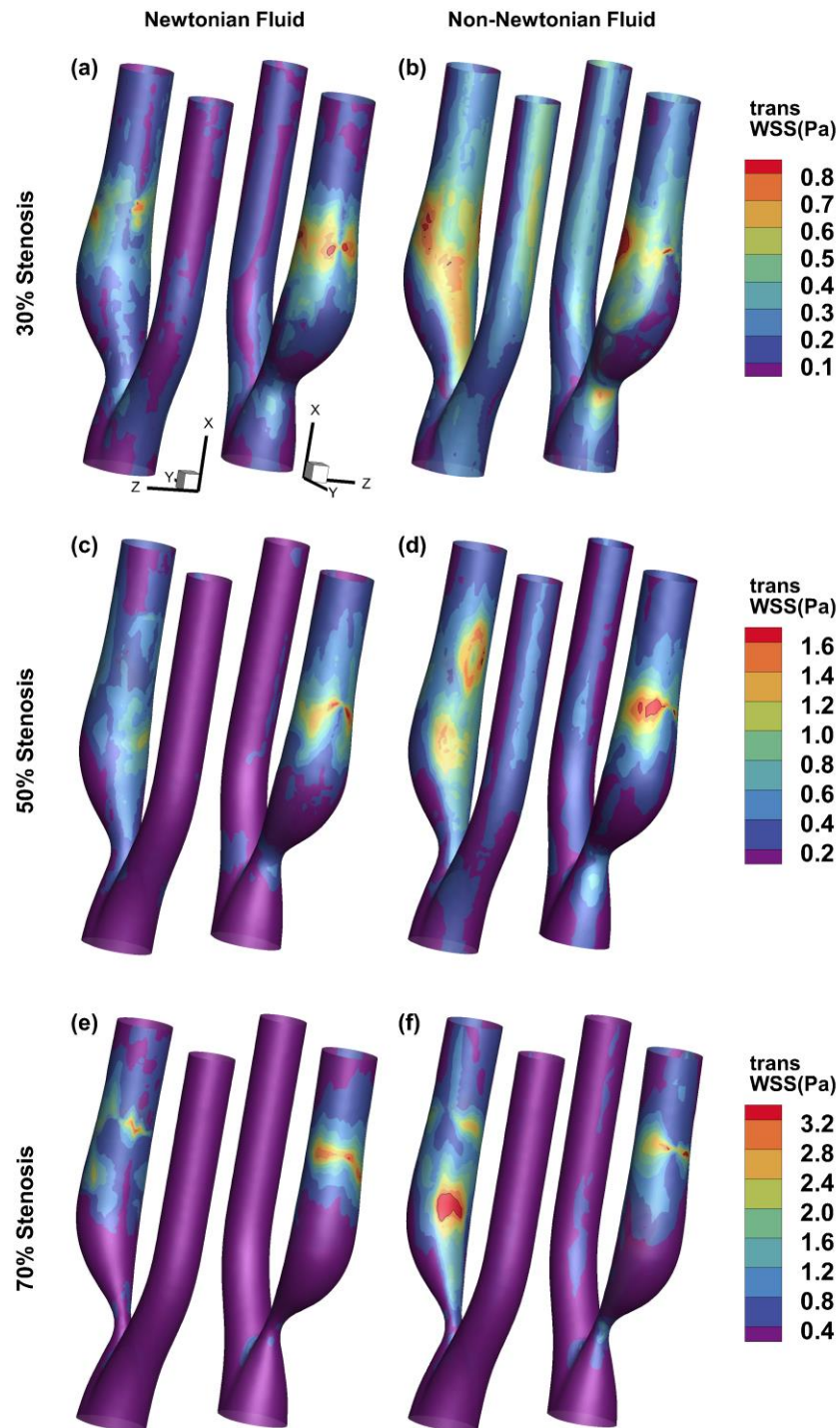


Figure 2.10: Contours of transWSS. Each model is shown in two orientations, exposing the inner and outer walls of the ICA on the left and right, respectively. Each row of models has an individual color bar and contour lines correspond to the highest contour level in each row.

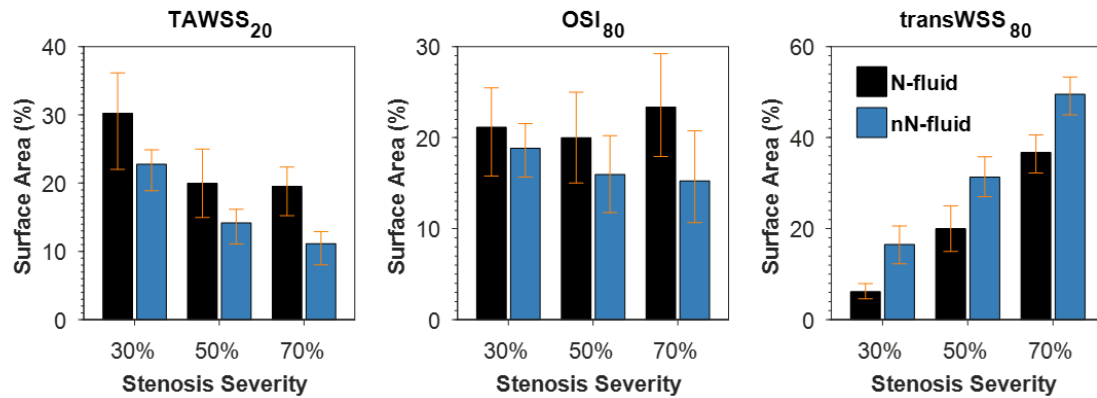


Figure 2.11: Surface area exposure as a function of stenosis severity and compared for Newtonian (black) and non-Newtonian (blue) fluids. Values are ICA SA exposed to: TAWSS below, OSI above, and transWSS above the respective thresholds. Thresholds defined as the 20th, 80th and 80th percentile values, respectively, of the parameter on the 50% N-fluid ICA surface. Whiskers represent ICA SA coverage when the +/- 5 percentile thresholds are applied.

2.4 Discussion

We have presented a method of estimating wall shear stress direction and magnitude in carotid artery models using a combination of PIV and CT and showed detailed maps of disturbed flow and WSS-based predictors with disease progression for varying degrees of eccentric stenosis and different blood analogue fluid types. The results demonstrate that a Newtonian fluid assumption underestimates the WSS magnitude, and thus also overestimates luminal surface exposure to sustained low WSS. The low-shear area decreases with increasing stenosis severity, since higher WSS is sustained with increasing jet velocity through the stenosis. The effect of viscosity model on shear stress patterns has been investigated in several numerical and experimental studies incorporating stenosed tubes or complex vascular geometries. Of these, some report higher WSS in Newtonian models [56; 57] but most report higher WSS for non-Newtonian viscosity models [29; 30; 58-61]. However, others have demonstrated that for a given geometry the WSS measured depends upon the chosen non-Newtonian viscosity model [62-65] and that the effects of viscosity model can vary for different geometries [63]. Moreover, in computational studies

of the carotid bifurcation under various rheological models, the calculation of WSS descriptors and bulk flow metrics were much less sensitive to blood rheology than the geometry reconstruction process [66; 67]. However, we have demonstrated that the impact of rheology on exposure to low and oscillatory shear is more pronounced for higher levels of stenosis, indicating that sensitivity to rheology could change with the progression of vascular disease.

Despite the gaining popularity of OSI as a vascular disease metric, limited studies examine the impact of viscosity on the results of experimental and numerical simulations measuring oscillatory and complex flow. Overall, the N-fluid predicts higher OSI magnitude and surface exposure compared to the nN-fluid. OSI distributions indicate that regions of oscillatory wall shear are mostly governed by the presence and size of flow recirculation zones. High OSI appears due to temporal fluctuations in the sites of flow detachment and re-attachment, which bound regions of continuous flow reversal (recirculation), as shown by Razavi et al. [68] in a simple stenosis model. Other studies in a carotid bifurcation model [30] and in a straight vessel downstream of a wire stent [61] found only one OSI peak for non-Newtonian viscosity models, compared to the two observed for Newtonian when looking along a single dimension. Here we can see that as the second recirculation zone size increases with stenosis severity, an OSI hotspot (single peak axially) at the downstream flow impingement opens into a ring pattern (producing two peaks axially) as seen on the inner ICA wall when progressing from the 30% to 50% stenosis model in Fig. 9a/c. This effect is delayed for the nN-fluid, as a single OSI hotspot is still observed for the 50% stenosis with nN-fluid.

To our knowledge, this is the first study to look at the effects of shear thinning on transverse wall shear stress. The present study demonstrates that the luminal surface area exposed to relatively high transWSS increases with stenosis severity and is underestimated by a Newtonian fluid model due to overall underestimation in WSS. TransWSS was first introduced by Peiffer et al. [7] as a new shear metric inspired by cell studies observing that endothelial cells responded to changes in flow direction perpendicular (transverse) to their

axis of elongation. [5] High transWSS, as originally formulated by Peiffer, can be indicative of either 1) large changes in flow direction, 2) small changes in direction over a long period of time, or 3) small changes in direction of high speed and high shear flow. When the transWSS was normalized here by the site-specific TAWSS, we found that the regions experiencing the highest fractional transWSS were qualitatively similar to the high OSI regions, as shown in supplementary figure A5. However, when transWSS is not normalized, contributions from small side-to-side changes in direction within high speed flow regions, such as at the ICA inner wall jet region, contribute largely to the transWSS. This type of high-speed oscillatory near-wall flow may be more relevant when considering the risk of plaque rupture and thrombosis as stenosis severity increases, as opposed to plaque development often associated with low magnitude shear stress. A limited number of studies have investigated transWSS using numerical simulations. Mohamied et al. [10] found that lesion prevalence correlated more strongly with transWSS than conventional OSI and TAWSS metrics in the rabbit aorta, supporting earlier qualitative observations by Peiffer [7]. Conversely, in a study of healthy human carotid bifurcations, Gallo et al. [69] observed that high transWSS was commonly located at the bifurcation apex, a site where lesions do not frequently occur. Further investigations will be necessary to determine the relevance of transWSS to the pathology of atherosclerosis.

The present study demonstrated that overall nN-fluid resulted in suppression of flow disturbances, in terms of peak value or temporal extent, resulting in a lower cumulative level of turbulence intensity over the cardiac cycle. Only modest differences (0.02-0.06 m/s) in the \overline{TI} metric were observed between viscosity models in matched geometries when compared with increases due to increases in stenosis severity (0.15-0.29 m/s) for a single fluid type. For comparison, previous DUS studies in the same models showed differences of 0.02-0.08 m/s in peak ROI-averaged TI due to ulcerations [51; 52] and previous PIV studies observed differences of 0.05-0.10 m/s in maximum ROI-averaged TI due to plaque eccentricity [27]. Molla and Paul [60] observed that the turbulent kinetic energy (TKE) downstream of a simple 50% stenosis was higher for a Newtonian viscosity model compared to several non-Newtonian models, in line with the present result, and that high

TKE persisted further downstream for nN-fluid models compared to the N-fluid. Walker et al. [61] observed the turbulent Reynold's shear stress (RSS) downstream of a stent to be up to 60% higher for a N-fluid compared to a nN-fluid but found that doubling the flow Reynold's number caused an increase in RSS for both models and additionally increased nN-fluid RSS to match that of the N-fluid. Similar to the effect seen here at higher stenosis, for a higher Reynold's number flow the maximum turbulence intensity is less dependent on the viscosity model.

A limitation of the present study is that the stereoscopic PIV technique requires the stacking of several independent planes of phase-averaged velocity data and a coherent instantaneous volumetric velocity field is not obtained. Thus, instantaneous WSS, and subsequently cycle-to-cycle temporal fluctuations in WSS, cannot be observed. Applying a tomographic PIV technique would overcome this issue, as previously explored by Buchmann et al. [26], but for wall shear magnitude only. The carotid models utilized here do not include physiological compliance. Numerical studies of the combined effect of non-Newtonian viscosity and compliance have shown that they can be interrelated, but in general, compliance has little effect on hemodynamic wall parameters [70]. While the phantoms utilized incorporate an idealized vessel geometry lacking tortuosity or vessel wall roughness, the matched set allows a controlled study of disease progression independent of additional factors.

The wall shear stress estimation can depend on the fitting technique and interpolation spacing applied to the discrete velocity data. Previous studies in the current geometries applied a central differencing scheme to calculate WSS magnitude for N-fluid [27]. While this method allowed a robust comparison between matched geometry models, it provided a conservative underestimate of WSS magnitude. In a study of wall shear rates derived from laser doppler anemometry measurements in a straight tube and different curve-fitting techniques, Fatemi and Rittgers [71] concluded that a third-degree polynomial curve fit with four points provided the most accurate shear-rate estimation for pulsatile flows in a straight tube. However, physiological flows are much more complex and have spatially

varying boundary layer thickness and flow regimes. In the present case, a cubic polynomial curve fit with an interpolation spacing of 0.3 mm approximately equal to the in-plane velocity vector spacing was applied to ensure that interpolated points were within the first non-zero velocity from the wall and to ensure that interpolation points fall in unique and neighbouring voxels where possible. The calculated systolic and time-averaged wall shear stress maps agree well with previous CFD studies for the 30% eccentrically stenosed geometry [72]. In that study, WSS values at peak systole reached 200 dyne/cm² (20 Pa) in the stenosis throat, and TAWSS reached 50 dyne/cm² (5 Pa) at the ICA inner wall and in the throat, similar to the values reported here for the 30% stenosed N-fluid model in Table 3 and Fig. 8a.

In conclusion, we have presented an experimental technique incorporating PIV velocity data and micro-CT geometry reconstruction resulting in both flow and multidirectional wall shear stress parameters in addition to turbulence intensity. We observed decreased TAWSS₂₀, comparable OSI₈₀ and increased transWSS₈₀, as well as increased TI, with increasing stenosis severity. In general, we found that shear stress may be underestimated, and disturbed flow may be exaggerated when shear thinning effects are neglected with the use of a Newtonian fluid model. In addition, higher grades of stenosis exhibited larger differences in measured exposure to low and oscillatory shear between the fluid models. Thus, the importance of rheology may be specific to the level of disease progression, and studies investigating the impact of rheology on hemodynamics should include a range of geometries comprising various levels of flow disturbances.

2.5 References

- [1] Morbiducci, U., Kok, A.M., Kwak, B.R., *et al.*, 2016. Atherosclerosis at arterial bifurcations: Evidence for the role of haemodynamics and geometry. *Thrombosis and Haemostasis* 115:484-492.
- [2] Zarins, C.K., Giddens, D.P., Bharadvaj, B.K., *et al.*, 1983. Carotid bifurcation atherosclerosis quantitative correlation of plaque localization with flow velocity profiles and wall shear-stress. *Circulation Research* 53:502-514.

- [3] Caro, C.G., Fitzgerald, J.M., Schroter, R.C., 1971. Atheroma and arterial wall shear - observation, correlation and proposal of a shear dependent mass transfer mechanism for atherogenesis. *Proceedings of the Royal Society Series B-Biological Sciences* 177:109-+.
- [4] Wentzel, J.J., Chatzizisis, Y.S., Gijzen, F.J.H., *et al.*, 2012. Endothelial shear stress in the evolution of coronary atherosclerotic plaque and vascular remodelling: Current understanding and remaining questions. *Cardiovascular Research* 96:234-243.
- [5] Wang, C., Baker, B.M., Chen, C.S., *et al.*, 2013. Endothelial cell sensing of flow direction. *Arteriosclerosis Thrombosis and Vascular Biology* 33:2130-2136.
- [6] Chakraborty, A., Chakraborty, S., Jala, V.R., *et al.*, 2016. Impact of bi-axial shear on atherogenic gene expression by endothelial cells. *Annals of Biomedical Engineering* 44:3032-3045.
- [7] Peiffer, V., Sherwin, S.J., Weinberg, P.D., 2013. Computation in the rabbit aorta of a new metric - the transverse wall shear stress - to quantify the multidirectional character of disturbed blood flow. *Journal of Biomechanics* 46:2651-2658.
- [8] Ku, D.N., Giddens, D.P., Zarins, C.K., *et al.*, 1985. Pulsatile flow and atherosclerosis in the human carotid bifurcation - positive correlation between plaque location and low and oscillating shear-stress. *Arteriosclerosis* 5:293-302.
- [9] Peiffer, V., Sherwin, S.J., Weinberg, P.D., 2013. Does low and oscillatory wall shear stress correlate spatially with early atherosclerosis? A systematic review. *Cardiovascular Research* 99:242-250.
- [10] Mohamied, Y., Rowland, E.M., Bailey, E.L., *et al.*, 2015. Change of direction in the biomechanics of atherosclerosis. *Annals of Biomedical Engineering* 43:16-25.
- [11] Morbiducci, U., Gallo, D., Cristofanelli, S., *et al.*, 2015. A rational approach to defining principal axes of multidirectional wall shear stress in realistic vascular geometries, with application to the study of the influence of helical flow on wall shear stress directionality in aorta. *Journal of Biomechanics* 48:899-906.
- [12] Arzani, A., Shadden, S.C., 2016. Characterizations and correlations of wall shear stress in aneurysmal flow. *Journal of Biomechanical Engineering-Transactions of the Asme* 138:10.
- [13] Mohamied, Y., Sherwin, S.J., Weinberg, P.D., 2017. Understanding the fluid mechanics behind transverse wall shear stress. *Journal of Biomechanics* 50:102-109.

- [14] van Ooij, P., Potters, W.V., Nederveen, A.J., *et al.*, 2015. A methodology to detect abnormal relative wall shear stress on the full surface of the thoracic aorta using four-dimensional flow mri. *Magnetic Resonance in Medicine* 73:1216-1227.
- [15] Biegling, E.T., Frydrychowicz, A., Wentland, A., *et al.*, 2011. In vivo three-dimensional mr wall shear stress estimation in ascending aortic dilatation. *Journal of Magnetic Resonance Imaging* 33:589-597.
- [16] Boussel, L., Rayz, V., Martin, A., *et al.*, 2009. Phase-contrast magnetic resonance imaging measurements in intracranial aneurysms in vivo of flow patterns, velocity fields, and wall shear stress: Comparison with computational fluid dynamics. *Magnetic Resonance in Medicine* 61:409-417.
- [17] Oyre, S., Ringgaard, S., Kozerke, S., *et al.*, 1998. Accurate noninvasive quantitation of blood flow, cross-sectional lumen vessel area and wall shear stress by three-dimensional paraboloid modeling of magnetic resonance imaging velocity data. *Journal of the American College of Cardiology* 32:128-134.
- [18] Isoda, H., Ohkura, Y., Kosugi, T., *et al.*, 2010. Comparison of hemodynamics of intracranial aneurysms between mr fluid dynamics using 3d cine phase-contrast mri and mr-based computational fluid dynamics. *Neuroradiology* 52:913-920.
- [19] Frydrychowicz, A., Stalder, A.F., Russe, M.F., *et al.*, 2009. Three-dimensional analysis of segmental wall shear stress in the aorta by flow-sensitive four-dimensional-mri. *Journal of Magnetic Resonance Imaging* 30:77-84.
- [20] Harloff, A., Nussbaumer, A., Bauer, S., *et al.*, 2010. In vivo assessment of wall shear stress in the atherosclerotic aorta using flow-sensitive 4d mri. *Magnetic Resonance in Medicine* 63:1529-1536.
- [21] Stalder, A.F., Russe, M.F., Frydrychowicz, A., *et al.*, 2008. Quantitative 2d and 3d phase contrast mri: Optimized analysis of blood flow and vessel wall parameters. *Magnetic Resonance in Medicine* 60:1218-1231.
- [22] Petersson, S., Dyverfeldt, P., Ebbers, T., 2012. Assessment of the accuracy of mri wall shear stress estimation using numerical simulations. *Journal of Magnetic Resonance Imaging* 36:128-138.
- [23] Brunette, J., Mongrain, R., Laurier, J., *et al.*, 2008. 3d flow study in a mildly stenotic coronary artery phantom using a whole volume piv method. *Medical Engineering & Physics* 30:1193-1200.
- [24] Pielhop, K., Klaas, M., Schroder, W., 2012. Analysis of the unsteady flow in an elastic stenotic vessel. *European Journal of Mechanics B-Fluids* 35:102-110.

- [25] Buchmann, N., Jermy, M., Nguyen, C., 2009. Experimental investigation of carotid artery haemodynamics in an anatomically realistic model. *International Journal of Experimental and Computational Biomechanics* 1:172-192.
- [26] Buchmann, N.A., Atkinson, C., Jeremy, M.C., *et al.*, 2011. Tomographic particle image velocimetry investigation of the flow in a modeled human carotid artery bifurcation. *Experiments in Fluids* 50:1131-1151.
- [27] Kefayati, S., Milner, J.S., Holdsworth, D.W., *et al.*, 2014. In vitro shear stress measurements using particle image velocimetry in a family of carotid artery models: Effect of stenosis severity, plaque eccentricity, and ulceration. *Plos One* 9:19.
- [28] Huh, H.K., Ha, H., Lee, S.J., 2015. Effect of non-newtonian viscosity on the fluid-dynamic characteristics in stenotic vessels. *Experiments in Fluids* 56:12.
- [29] Chen, J., Lu, X.Y., 2004. Numerical investigation of the non-newtonian blood flow in a bifurcation model with a non-planar branch. *Journal of Biomechanics* 37:1899-1911.
- [30] Chen, J., Lu, X.Y., 2006. Numerical investigation of the non-newtonian pulsatile blood flow in a bifurcation model with a non-planar branch. *Journal of Biomechanics* 39:818-832.
- [31] Fortais, A., de Bruyn, J.R., Poepping, T.L., 2015. Non-newtonian blood-mimicking fluid for particle image velocimetry. In Proceedings of the 25th Canadian Congress of Applied Mechanics. London, Canada. pp. 129-132.
- [32] Smith, R.F., Rutt, B.K., Holdsworth, D.W., 1999. Anthropomorphic carotid bifurcation phantom for mri applications. *Jmri-Journal of Magnetic Resonance Imaging* 10:533-544.
- [33] Poepping, T.L., Nikolov, H.N., Rankin, R.N., *et al.*, 2002. An in vitro system for doppler ultrasound flow studies in the stenosed carotid artery bifurcation. *Ultrasound in Medicine and Biology* 28:495-506.
- [34] Kefayati, S., Poepping, T.L., 2013. Transitional flow analysis in the carotid artery bifurcation by proper orthogonal decomposition and particle image velocimetry. *Medical Engineering & Physics* 35:898-909.
- [35] Kefayati, S., Holdsworth, D.W., Poepping, T.L., 2014. Turbulence intensity measurements using particle image velocimetry in diseased carotid artery models: Effect of stenosis severity, plaque eccentricity, and ulceration. *Journal of Biomechanics* 47:253-263.
- [36] Smith, R.F., Rutt, B.K., Fox, A.J., *et al.*, 1996. Geometric characterization of stenosed human carotid arteries. *Academic Radiology* 3:898-911.

- [37] Fox, A.J., 1993. How to measure carotid stenosis. *Radiology* 186:316-318.
- [38] Holdsworth, D.W., Norley, C.J.D., Frayne, R., *et al.*, 1999. Characterization of common carotid artery blood-flow waveforms in normal human subjects. *Physiological Measurement* 20:219-240.
- [39] Yousif, M.Y., Holdsworth, D.W., Poepping, T.L., 2011. A blood-mimicking fluid for particle image velocimetry with silicone vascular models. *Experiments in Fluids* 50:769-774.
- [40] Antonova, N., Zvetkova, E., Ivanov, I., *et al.*, 2008. Hemorheological changes and characteristic parameters derived from whole blood viscometry in chronic heroin addicts. *Clinical Hemorheology and Microcirculation* 39:53-61.
- [41] Bor-Kucukatay, M., Keskin, A., Akdam, H., *et al.*, 2008. Effect of thrombocytapheresis on blood rheology in healthy donors: Role of nitric oxide. *Transfusion and Apheresis Science* 39:101-108.
- [42] Carrera, L.I., Etchepare, R., D'Arrigo, M., *et al.*, 2008. Hemorheologic changes in type 2 diabetic patients with microangiopathic skin lesions. A linear discriminant categorizing analysis. *Journal of Diabetes and Its Complications* 22:132-136.
- [43] Fehr, M., Galliard-Grigioni, K.S., Reinhart, W.H., 2008. Influence of acute alcohol exposure on hemorheological parameters and platelet function in vivo and in vitro. *Clinical Hemorheology and Microcirculation* 39:351-358.
- [44] Galduroz, J.C.F., Antunes, H.K., Santos, R.F., 2007. Gender- and age-related variations in blood viscosity in normal volunteers: A study of the effects of extract of allium sativum and ginkgo biloba. *Phytomedicine* 14:447-451.
- [45] Vaya, A., Murado, J., Santaolaria, M., *et al.*, 2008. Haemorheological changes in patients with systemic lupus erythematosus do not seem to be related to thrombotic events. *Clinical Hemorheology and Microcirculation* 38:23-29.
- [46] Antiga, L., Piccinelli, M., Botti, L., *et al.*, 2008. An image-based modeling framework for patient-specific computational hemodynamics. *Medical & Biological Engineering & Computing* 46:1097-1112.
- [47] Potters, W.V., van Ooij, P., Marquering, H., *et al.*, 2015. Volumetric arterial wall shear stress calculation based on cine phase contrast mri. *Journal of Magnetic Resonance Imaging* 41:505-516.
- [48] Lee, S.W., Antiga, L., Spence, J.D., *et al.*, 2008. Geometry of the carotid bifurcation predicts its exposure to disturbed flow. *Stroke* 39:2341-2347.

- [49] Lee, S.W., Antiga, L., Steinman, D.A., 2009. Correlations among indicators of disturbed flow at the normal carotid bifurcation. *Journal of Biomechanical Engineering-Transactions of the Asme* 131:7.
- [50] Gallo, D., Steinman, D.A., Bijari, P.B., *et al.*, 2012. Helical flow in carotid bifurcation as surrogate marker of exposure to disturbed shear. *Journal of Biomechanics* 45:2398-2404.
- [51] Wong, E.Y., Nikolov, H.N., Thorne, M.L., *et al.*, 2009. Clinical doppler ultrasound for the assessment of plaque ulceration in the stenosed carotid bifurcation by detection of distal turbulence intensity: A matched model study. *European Radiology* 19:2739-2749.
- [52] Wong, E.Y., Nikolov, H.N., Rankin, R.N., *et al.*, 2013. Evaluation of distal turbulence intensity for the detection of both plaque ulceration and stenosis grade in the carotid bifurcation using clinical doppler ultrasound. *European Radiology* 23:1720-1728.
- [53] Wieneke, B., 2015. Piv uncertainty quantification from correlation statistics. *Measurement Science and Technology* 26:10.
- [54] Sciacchitano, A., Wieneke, B., 2016. Piv uncertainty propagation. *Measurement Science and Technology* 27:16.
- [55] Wilson, B.M., Smith, B.L., 2013. Taylor-series and monte-carlo-method uncertainty estimation of the width of a probability distribution based on varying bias and random error. *Measurement Science and Technology* 24:11.
- [56] Tu, C., Deville, M., 1996. Pulsatile flow of non-newtonian fluids through arterial stenoses. *Journal of Biomechanics* 29:899-908.
- [57] Deplano, V., Knapp, Y., Bailly, L., *et al.*, 2014. Flow of a blood analogue fluid in a compliant abdominal aortic aneurysm model: Experimental modelling. *Journal of Biomechanics* 47:1262-1269.
- [58] Ballyk, P.D., Steinman, D.A., Ethier, C.R., 1994. Simulation of non-newtonian blood-flow in an end-to-side anastomosis. *Biorheology* 31:565-586.
- [59] Luo, X.Y., Kuang, Z.B., 1992. Non-newtonian flow patterns associated with an arterial-stenosis. *Journal of Biomechanical Engineering-Transactions of the Asme* 114:512-514.
- [60] Molla, M.M., Paul, M.C., 2012. Les of non-newtonian physiological blood flow in a model of arterial stenosis. *Medical Engineering & Physics* 34:1079-1087.

- [61] Walker, A.M., Johnston, C.R., Rival, D.E., 2012. The quantification of hemodynamic parameters downstream of a gianturco zenith stent wire using newtonian and non-newtonian analog fluids in a pulsatile flow environment. *Journal of Biomechanical Engineering-Transactions of the Asme* 134:10.
- [62] Caballero, A.D., Lain, S., 2015. Numerical simulation of non-newtonian blood flow dynamics in human thoracic aorta. *Computer Methods in Biomechanics and Biomedical Engineering* 18:1200-1216.
- [63] Evju, O., Valen-Sendstad, K., Mardal, K.A., 2013. A study of wall shear stress in 12 aneurysms with respect to different viscosity models and flow conditions. *Journal of Biomechanics* 46:2802-2808.
- [64] Johnston, B.M., Johnston, P.R., Corney, S., *et al.*, 2004. Non-newtonian blood flow in human right coronary arteries: Steady state simulations. *Journal of Biomechanics* 37:709-720.
- [65] Johnston, B.M., Johnston, P.R., Corney, S., *et al.*, 2006. Non-newtonian blood flow in human right coronary arteries: Transient simulations. *Journal of Biomechanics* 39:1116-1128.
- [66] Morbiducci, U., Gallo, D., Massai, D., *et al.*, 2011. On the importance of blood rheology for bulk flow in hemodynamic models of the carotid bifurcation. *Journal of Biomechanics* 44:2427-2438.
- [67] Lee, S.W., Steinman, D.A., 2007. On the relative importance of rheology for image-based cfd models of the carotid bifurcation. *Journal of Biomechanical Engineering-Transactions of the Asme* 129:273-278.
- [68] Razavi, A., Shirani, E., Sadeghi, M.R., 2011. Numerical simulation of blood pulsatile flow in a stenosed carotid artery using different rheological models. *Journal of Biomechanics* 44:2021-2030.
- [69] Gallo, D., Steinman, D.A., Morbiducci, U., 2016. Insights into the co-localization of magnitude-based versus direction-based indicators of disturbed shear at the carotid bifurcation. *Journal of Biomechanics* 49:2413-2419.
- [70] Kabinejadian, F., Ghista, D.N., 2012. Compliant model of a coupled sequential coronary arterial bypass graft: Effects of vessel wall elasticity and non-newtonian rheology on blood flow regime and hemodynamic parameters distribution. *Medical Engineering & Physics* 34:860-872.
- [71] Fatemi, R.S., Rittgers, S.E., 1994. Derivation of shear rates from near-wall lda measurements under steady and pulsatile flow conditions. *Journal of Biomechanical Engineering-Transactions of the Asme* 116:361-368.

- [72] Steinman, D.A., Poepping, T.L., Tambasco, M., *et al.*, 2000. Flow patterns at the stenosed carotid bifurcation: Effect of concentric versus eccentric stenosis. *Annals of Biomedical Engineering* 28:415-423.

Chapter 3

3 Effects of waveform pulsatility on shear stress and flow disturbances in carotid artery models using particle image velocimetry

3.1 Introduction

Atherosclerosis at the carotid bifurcation - characterized by thickening and stiffening of the vascular wall and the development of lesions and plaque - is a common cause of ischemic stroke due to vessel narrowing and subsequent athero- or thromboembolism. Hemodynamic factors play an important role in the initiation and progression of atherosclerosis. Arterial wall shear stress (WSS) is a key regulator of endothelial cell function and can elicit both atherosusceptible and atheroprotective responses from the endothelium. In particular, a disturbed flow environment – characterized by low and multidirectional oscillatory wall shear stress – appears to promote atherogenesis. Intimal thickening has been shown to develop primarily in regions of low wall shear stress, oscillating shear, flow reversal, and departure from unidirectional flow [1-3]. Conversely, endothelial cells in regions with non-disturbed flow and moderate unidirectional shear stress align axially and exhibit atheroprotective genes [2; 4].

In addition to local geometry, systemic vascular disease affects impedance and thus impacts the pulsatility of the flow waveform [5-7]. Waveform pulsatility is impacted by various factors – including age, diabetes and hypertension due to vessel stiffening, and loss of vasculature due to disease or cerebral infarction resulting in changes to peripheral resistance. Thus, there is a large variation in flow waveforms between individuals and between arterial sites of a single individual. Characterizing the effect of the local waveform shape on local hemodynamics may provide insight into how waveform pulsatility is related to local and systemic cerebrovascular disease. Pulsatility can be replicated by controlling boundary conditions, either physically for in vitro models or numerically for computational fluid dynamics.

Computational fluid dynamics (CFD) is the most common method of assessing hemodynamics within arterial models. In general, patient-specific inlet and outlet flow waveforms are not available and assumptions need to be made regarding the boundary conditions used for simulations. Studies have compared the effects of patient-specific versus idealized boundary conditions on local wall shear stress patterns in aneurysm models found differences on the order of 30% [8] and up to 69% [9]. Geers et al. [10] showed that steady flow simulations could predict the time-averaged wall shear stress (TAWSS) when compared to pulsatile simulations but underestimated the WSS at peak systole even when using a steady simulation with the peak flow rate. Xiang et al. [11] found that in a study of intracranial aneurysms with various inlet waveform conditions, a strong correlation was observed between pulsatility and mean oscillatory shear index (OSI) magnitude. Moreover, steady flow simulations cannot predict flow disturbances and wall shear oscillations. While CFD models allow patient-specific geometries to be investigated, pulsatile flow simulations can be time-consuming and often cannot easily model turbulence and disturbed flow.

The objectives of this work are: 1.) to determine the effect of flow rate pulsatility on the multidirectional nature of flow by studying both WSS metrics and turbulence intensity (TI) in an in-vitro experimental model of the carotid bifurcation 2.) to determine if correlations exist between hemodynamic risk parameters (OSI and TI) and the waveform pulsatility characteristics that are more readily measured clinically. In this study, we employ the use of a particle image velocimetry (PIV) system, in conjunction with a computer controlled pulsatile flow pump to measure three-dimensional velocity fields within idealized carotid artery models of varying stenosis and under three different inlet flow conditions. In addition, by combining volumetric velocity data with wall location information from computed tomography (CT) scans, three-dimensional wall shear stress magnitude and direction could be calculated. In this manner we can independently assess the effect of waveform shape parameters on velocity maps, variability in WSS direction and magnitude, as well as disturbed flow metrics, which are difficult to obtain using computational models.

3.2 Methods

Carotid artery geometries used in the present study were based on average representations of carotid bifurcations with varying levels of ICA stenosis previously derived from angiography data [12]. PIV-compatible phantom models were fabricated from polydimethylsiloxane (PDMS) using a lost-core casting technique as previously described [13; 14]. Volumetric velocity data were collected, as described below, for a stenosed geometry with a 50% cross-sectional area reduction of the internal carotid artery (based on NASCET criteria [15]) and eccentric plaque symmetry, as shown in Figure 3.1a. In addition, central plane velocity data were acquired for two additional geometries containing a 30% and a 70% eccentric stenosis of the ICA respectively. Micro-computed tomography scans of the phantoms were used to extract accurate vessel boundary information. A coarse surface mesh was obtained via level-set segmentation using the Vascular Modeling Toolkit (VMTK) [16].

The arrangement of the stereoscopic PIV system components (LaVision) with respect to the phantom model is shown in Figure 3.1b. A continuous wave Nd:YAG laser (532 nm, 5.5W) illuminates an approximately 1 mm thick horizontal (x-y) slice of the model. For the purpose of volumetric acquisition, the phantom is mounted on a translational stage and repositioned vertically in 0.5 mm increments. Two high-speed CMOS cameras (1024x1024 pixels), equipped with long pass filters and Scheimpflug adapters, are mounted above the phantom, each at 35 degrees viewing angle. A PDMS prism is placed above the test section of the phantom to ensure normal viewing angle at the air-PDMS interface.

PIV images were collected and processed using commercial software (DaVis 7.2, LaVision). Double-frame particle images were acquired at a temporal resolution of 100 Hz for 870 ms of the total 920 ms cardiac cycle. Velocity vectors were calculated using a standard fast Fourier transform based cross-correlation algorithm, incorporating decreasing window size from 64x64 to 16x16 pixels with 50% overlap and applying Gaussian weighting and high accuracy Whittaker reconstruction for final passes. The parameters

resulted in a test-section extending approximately 40 mm axially at the bifurcation and with an in-plane velocity vector spatial resolution (x and y directions) of 0.3 mm.

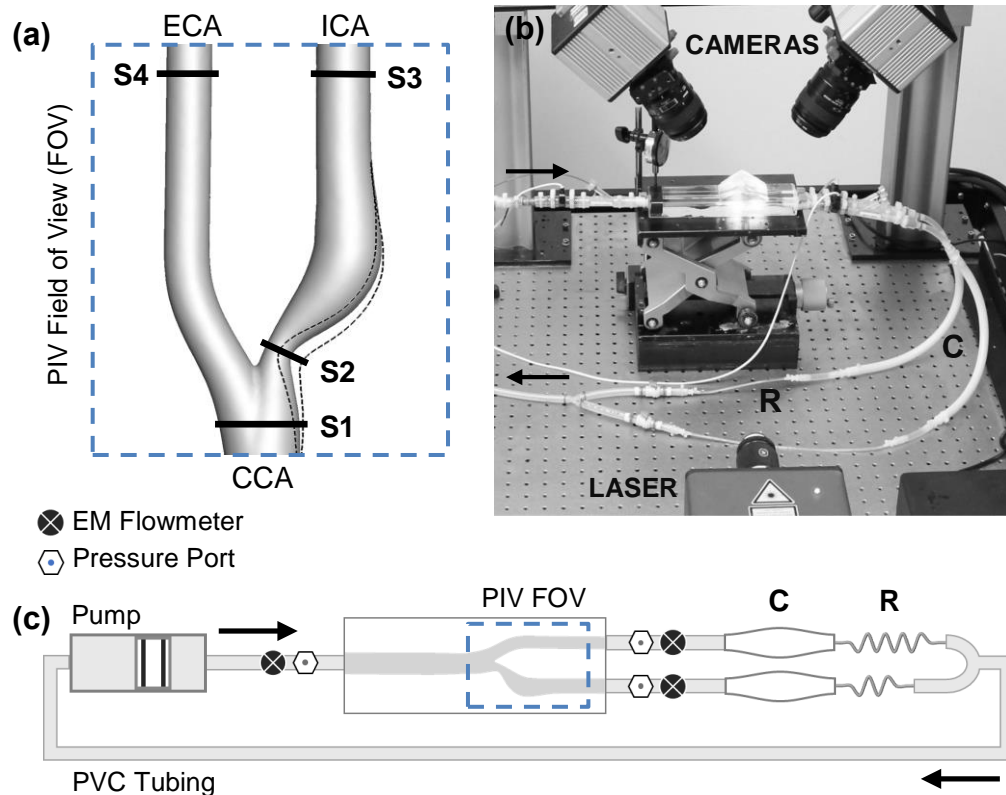


Figure 3.1: a) Phantom geometry with 50% eccentric stenosis. Dashed lines indicate the boundaries of 30% and 70% stenosed geometries. CCA: common carotid artery, ICA: internal carotid artery, ECA: external carotid artery; b) Photo of the experimental setup. Arrows indicate flow direction from and to pump; c) Schematic diagram of flow circuit (not to scale) including compliant (C) and resistive (R) elements. Direction of flow indicated by arrows.

The flow loop setup is depicted in the schematic diagram in Figure 3.1c (not to scale) consisting of a programmable computer-controlled volumetric pump, a carotid artery phantom, and downstream compliant and resistive elements constructed from flexible tubing and small inner-diameter tubing, respectively. A refractive-index matched blood-mimicking fluid [17] seeded with 15 μm fluorescent tracer particles was applied as the working fluid, with a constant Newtonian viscosity for simplicity. Inlet and outlet boundary

conditions were monitored using electromagnetic flowmeters (Carolina Medical Inc) and a catheter deployed pressure probe (Millar). Flowmeters and pressure catheter ports were inserted upstream of the phantom CCA inlet and downstream of both the ICA and ECA outlets, as indicated in Figure 3.1c. The approximate location of flow and pressure measurements from the bifurcation apex of the phantom geometry were 25 cm proximal and 15 cm distal for the CCA and ICA/ECA respectively. In addition, inlet and outlet velocity waveforms were extracted from experimental PIV data by taking the peak velocity magnitude from a profile through the central plane, reflective of what would be represented by the peak velocity envelope of a doppler ultrasound spectrogram. Velocity waveforms were examined at the sections indicated in Figure 3.1a, with S1 located at -6 mm and S3/S4 located at 32 mm from the bifurcation apex. S2 is a slice taken orthogonal to the vessel centerline at the narrowest stenotic diameter.

Flow Rate Waveforms

The effect of the flow rate waveform shape on hemodynamics was investigated by studying three idealized CCA inlet flow waveforms. These include: 1.) a high pulsatility waveform applied in Chapter 2 and extensively in previous US and PIV experimental studies [18-21] that was previously derived from the carotid arteries of a cohort of 17 young healthy volunteers measured using pulsed Doppler ultrasound and an ECG timing technique [22]; 2.) a low pulsatility waveform derived from retrospectively gated phase-contrast magnetic resonance imaging (PC-MRI) of the carotid bifurcations of 94 older adults applying a similar timing synchronization [23]; 3.) a waveform with intermediate pulsatility derived from a lumped parameter model, reflecting the effect of a reduction in downstream systemic compliance on the above high pulsatility waveform [24]. From here, the three waveforms will be referred to as the high PI, low PI and intermediate PI waveforms respectively and results will be displayed in order of decreasing pulsatility from left to right. Inlet and outlet waveforms for flow, pressure and velocity as measured for a 50% stenosed geometry are shown in Figure 3.2.

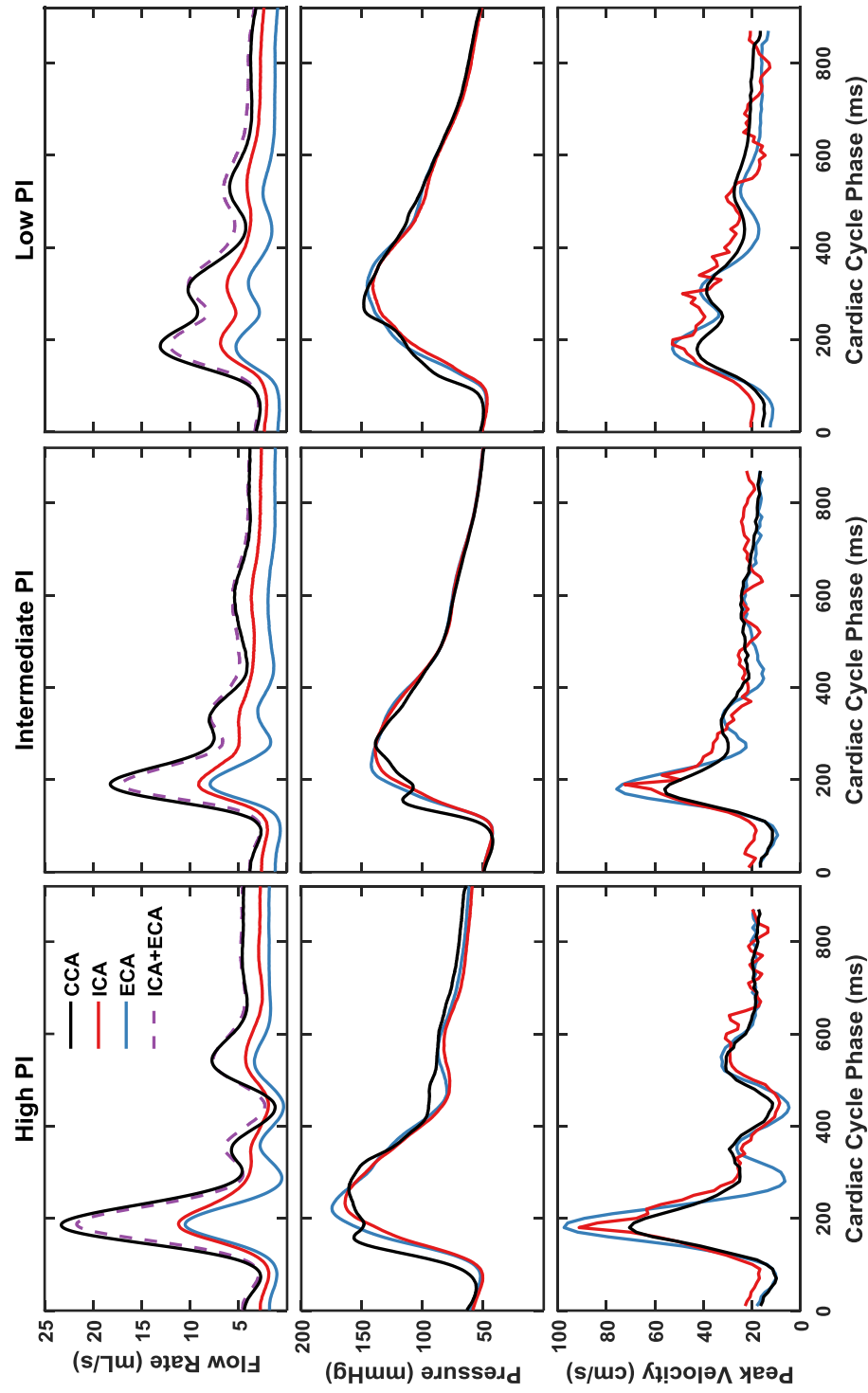


Figure 3.2: Volumetric flow, pressure, and velocity waveforms for the three cases of high, intermediate, and low pulsatility index (PI) for the 50% stenosed model. Flow and pressure waveforms were measured via electromagnetic flowmeters and pressure transducer at the inlets and outlets of the phantom at locations indicated in Figure 3.1c. Velocity waveforms were extracted from PIV data at sections S1, S3 and S4 shown in Figure 3.1a for CCA, ICA, and ECA respectively.

Data Analysis

Flow and velocity waveform shapes were characterized using common waveform descriptors: the pulsatility index (PI) and the resistive index (RI) defined as

$$PI = \frac{\Phi_{MAX} - \Phi_{MIN}}{\Phi_{MEAN}} \quad (3.1)$$

$$RI = \frac{\Phi_{MAX} - \Phi_{MIN}}{\Phi_{MAX}} \quad (3.2)$$

where Φ refers to either the flow rate Q or the peak velocity U . The values of waveform descriptors measured at the CCA inlet and ICA and ECA outlets for both flow and velocity waveforms for the 50% stenosed geometry are summarized in Table 3.1.

Velocity data were phase-averaged over $N = 15$ cycles (based on Kefayati et al. [18]) and the turbulence intensity (TI) metric was applied to assess the level of flow disturbances under varying inlet waveform conditions. TI was defined in this case as the RMS of the cycle-to-cycle velocity vector component fluctuations:

$$TI(t) = \sqrt{(TI_x(t))^2 + (TI_y(t))^2 + (TI_z(t))^2} \quad (3.3)$$

$$TI_i(t) = \sqrt{\frac{\sum_{n=1}^N u'_i(t, n)u'_i(t, n)}{N - 1}}, i = x, y, z \quad (3.4)$$

At each cardiac cycle phase, a representative TI value was extracted by taking a spatial average over the ICA central plane extending radially wall-to-wall radially and axially to 30 mm from the bifurcation apex, denoted ICA-TI.

The segmented CT geometries were registered with the corresponding velocity vector data for the volumetric cases (50% stenosis) and the WSS was calculated, as previously described in Chapter 2, by interpolating the velocity data along the inward normal at each vessel wall location. Commonly used integrated shear parameters, time-averaged wall

shear stress (TAWSS) and oscillatory shear index (OSI) were computed. For TAWSS an upper limit threshold was found from the 20th percentile of TAWSS values for the high PI waveform case. The percentage of surface area exposed to ‘low’ shear, defined as values below the 20th percentile threshold, was denoted TAWSS₂₀. For OSI, the percentage of surface area exposed to values exceeding the 80th percentile threshold of OSI (again found from the high PI waveform case) was computed for each model, denoted OSI₈₀.

Table 3.1: Waveform properties for the 50% stenosed model. The pulsatility and resistive index were calculated from both flow and velocity waveforms, indicated by Q and U respectively. Reynolds numbers (Re) were calculated from velocity at the narrowest stenosis diameter.

Waveform Model	High PI		Intermediate PI		Low PI	
Peak Flow Rate (mL/s)						
CCA	23.3 ± 0.1		18.2 ± 0.1		13.08 ± 0.01	
ICA	11.20 ± 0.07		9.1 ± 0.2		6.87 ± 0.07	
ECA	10.51 ± 0.07		7.95 ± 0.05		5.27 ± 0.03	
Mean Flow Rate (mL/s)						
CCA	6.391 ± 0.008		6.01 ± 0.02		5.79 ± 0.02	
ICA	3.79 ± 0.02		3.84 ± 0.02		3.85 ± 0.01	
ECA	2.53 ± 0.02		2.11 ± 0.01		2.11 ± 0.01	
Peak Velocity (m/s)						
CCA (at S1)	0.705 ± 0.007		0.560 ± 0.008		0.426 ± 0.006	
ICA (at S3)	0.9 ± 0.1		0.73 ± 0.07		0.53 ± 0.08	
ECA (at S4)	0.97 ± 0.02		0.76 ± 0.01		0.527 ± 0.006	
Mean Velocity (m/s)						
CCA (at S1)	0.252 ± 0.002		0.247 ± 0.002		0.2574 ± 0.0005	
ICA (at S3)	0.268 ± 0.005		0.269 ± 0.005		0.276 ± 0.005	
ECA (at S4)	0.252 ± 0.002		0.244 ± 0.002		0.2421 ± 0.0005	
Peak Re (at S2)	1616		1317		1006	
Mean Re (at S2)	541		540		564	
Pulsatility Index						
	Q	U	Q	U	Q	U
CCA	3.45	2.40	2.59	1.80	1.78	1.08
ICA	2.46	3.09	1.85	2.12	1.24	1.46
ECA	4.02	3.69	3.43	2.72	2.12	1.71
Resistive Index						
CCA	0.95	0.86	0.85	0.79	0.79	0.65
ICA	0.83	0.91	0.78	0.78	0.70	0.76
ECA	0.97	0.95	0.91	0.88	0.85	0.78

3.3 Results

Figure 3.3 shows phase-averaged velocity maps at the time point of peak systole for the three waveforms applied to the 50% stenosed geometry. The flow pattern consists of a high velocity jet emerging from the throat of the stenosis, crossing the vessel lumen and impinging on the outer ICA wall, forming two recirculation regions on either side of the jet. The jet impingement site at the outer wall, located approximately 20 mm distal to the bifurcation apex on average, gets shifted more proximally for high flow rates. Thus, the impingement zone fluctuates more with higher pulsatility, leading to expansion and contraction of the recirculation region and oscillatory shear at the vessel wall. The maximum systolic velocities found in the jet region are 1.98, 1.65, and 1.25 m/s for the high, intermediate, and low PI waveforms, respectively. The velocities within the larger recirculation zone at the outer wall of the vessel are comparatively low for all waveforms, dropping below 0.10 m/s.

Downstream flow disturbances are quantified in Figure 3.4, where 3D and central plane turbulence intensity maps in the ICA branch are displayed for the three inlet waveforms and the 50% stenosed geometry at the time point of maximum ICA-TI for each case. Absolute maximum turbulence intensity values found in the central plane were 69, 54, and 36 cm/s for the high, intermediate and low PI waveforms respectively. Like the jet impingement site, the region of maximum turbulence occurred further upstream with increasing PI. Similarly, for constant flow studies, the maximum turbulence region is more proximal for higher flow rates. Peak TI occurs after peak systole during the flow deceleration phase, and additional local maxima of TI can be found at other instances of flow deceleration, which can be seen in the plot of ICA-TI versus cardiac cycle phase shown in Figure 3.5. For reference, temporally and spatially averaged background TI values in the CCA across all waveforms and geometries were approximately 1.5 cm/s.

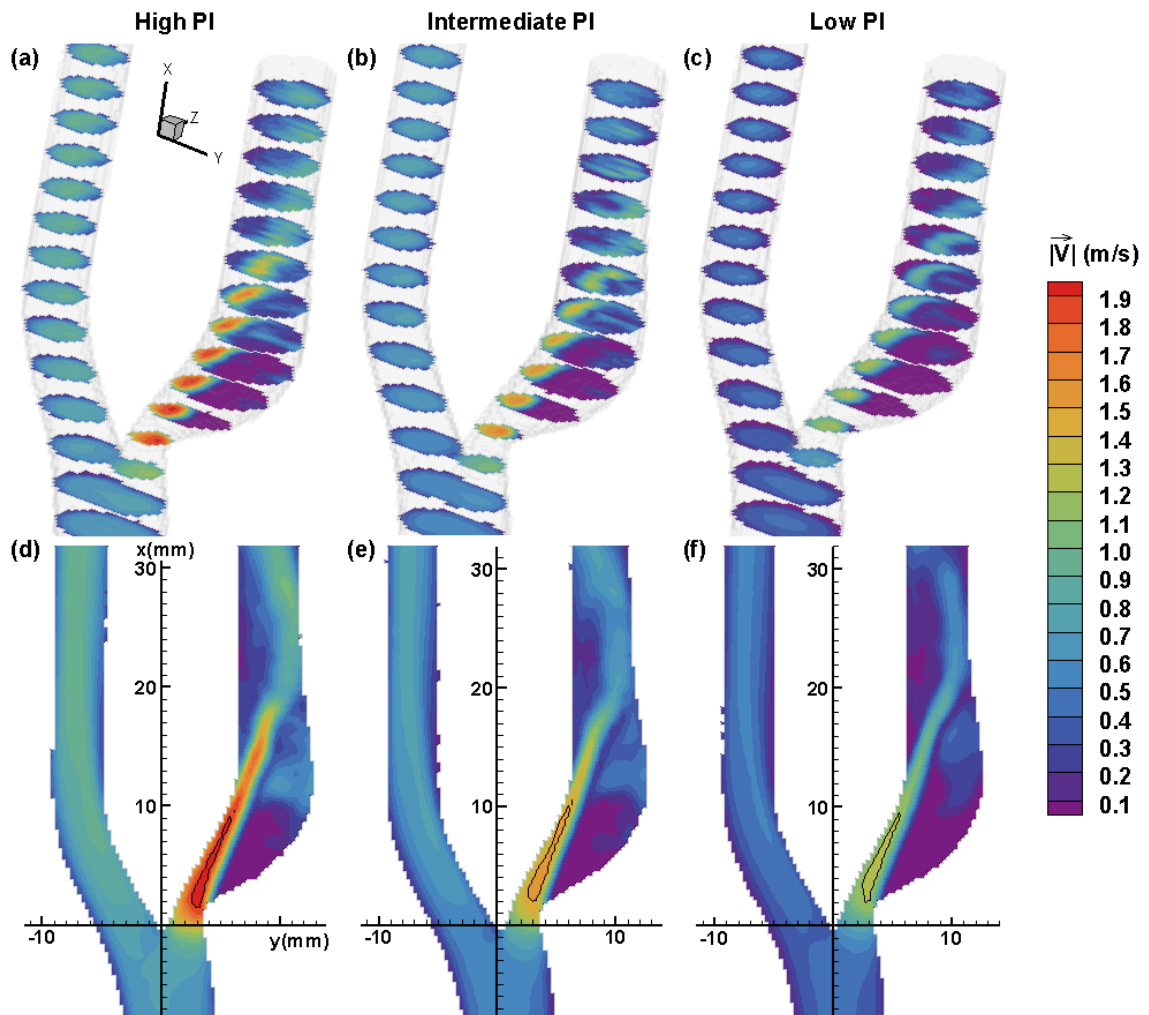


Figure 3.3: Phase-averaged velocity magnitude at peak systole for a 50% stenosed model with high (a,d), intermediate (b,e), and low (c,f) PI waveforms applied. A volumetric representation with transverse slices at 6 mm increments is shown in the top row (a-c); central-plane maps are shown in the bottom row (d-f). Contour lines indicate the highest contour level reached: 1.9, 1.5, and 1.2 m/s for the high, intermediate, and low PI cases, respectively.

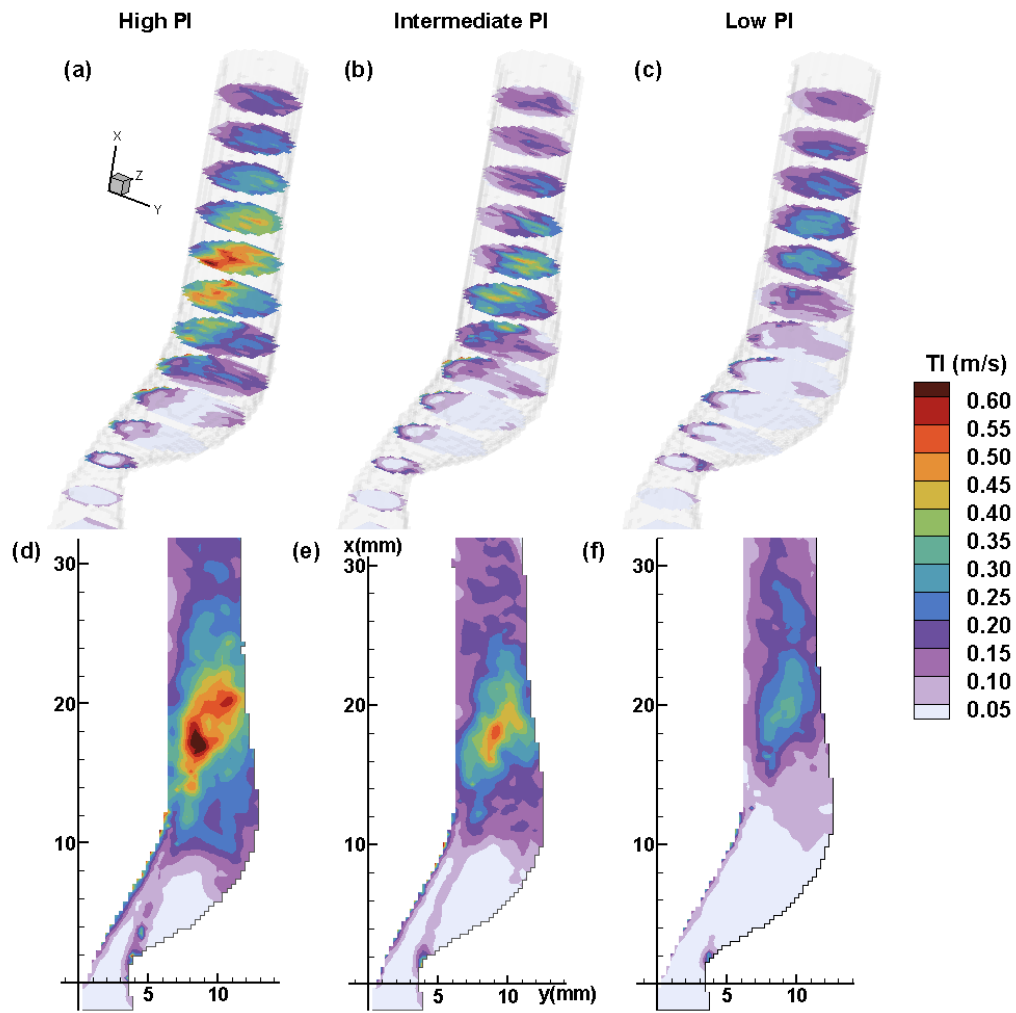


Figure 3.4: Turbulence intensity maps at the time point of maximum ICA-averaged TI in the 50% stenosed model with high (a,d), intermediate (b,e), and low (c,f) PI waveforms applied. A volumetric representation with transverse slices at 6 mm increments is shown in the top row (a-c); central-plane maps are shown in the bottom row (d-f).

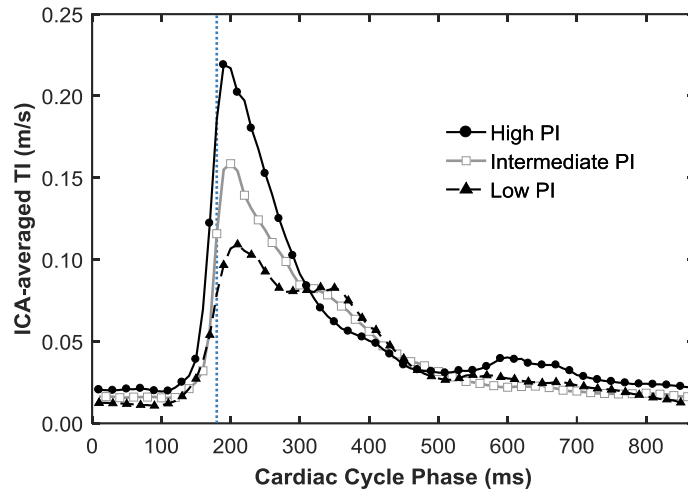


Figure 3.5: ICA-averaged TI versus cardiac cycle phase for the three inlet waveforms applied in the 50% stenosed model, calculated from central-plane TI maps. The dotted blue line indicates the time of peak systole, for phase reference.

Figure 3.6 demonstrates the combined effect of waveform pulsatility and stenosis severity on the turbulence intensity in the ICA downstream of the stenosis. The peak ICA-TI reached in each model is linearly correlated with the PI of both the ICA and CCA velocity waveforms, as shown in Figure 3.6a. Decreasing from high to low PI results in a 65%, 50% and 40% decrease in peak ICA-TI in the 30, 50 and 70% stenosis models, respectively. The effect on PI by the stenosis severity and the resulting imposed resistance can also be observed in Figure 3.6a. For high grade stenosis, the PI of the velocity waveform decreases between the CCA and ICA, due to the increased resistance imposed by the stenosis itself. The converse is true for lower stenosis grades, where the dominant source of resistance is the inline downstream resistors (mimicking peripheral resistance). Peak ICA-TI increases with the peak velocity across the stenosis, as shown in Figure 3.6b. Similarly, the cycle-mean ICA-TI increases with the cycle-mean velocity across the stenosis, as shown in Figure 3.6c. For a single stenosis severity, all three inlet waveforms produce approximately equal cycle-mean turbulence intensity. For comparison, figure 3.6c also includes data points from constant flow experiments with CCA inlet flow rates of 6, 8 and 10 mL/s shown

as crosses, which follow the linear trend but were not used in the fit calculation, keeping in mind all three pulsatile waveforms have an average CCA inlet flow rate of 6 mL/s.

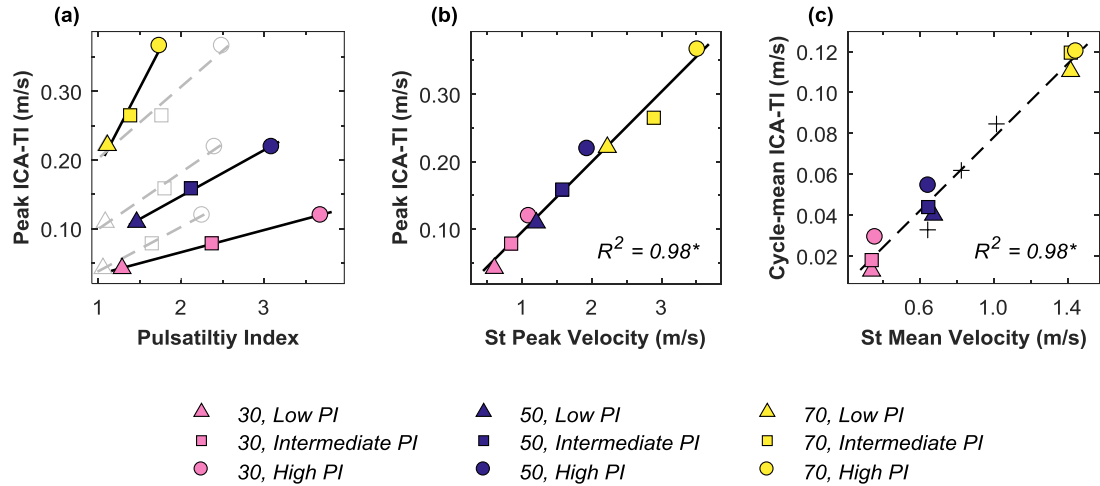


Figure 3.6: Trends in ICA-averaged TI for 30, 50, and 70% stenosed models and three inlet waveforms. a) Peak ICA-averaged TI as a function of ICA velocity waveform PI (coloured) and CCA velocity waveform PI (grey markers + dashed line). b) Peak ICA-averaged TI versus peak stenosis velocity measured at section S2 indicated in Figure 3.1a. c) Cycle mean ICA-averaged TI versus cycle mean stenosis velocity measured at section S2. For comparison, ICA-averaged TI in a 50% stenosed geometry with constant CCA-inlet flow rates of 6, 8, and 10 mL/s are also shown (crosses). $St = Stenosis$.

Instantaneous 3D WSS magnitude maps are shown in Figure 3.7 for the 50% stenosed geometry. In each frame, the vessel is shown in two orientations, revealing the inner and outer walls of the ICA on the left and right respectively. The maximum WSS values are reached within the stenosis throat and along the ICA inner wall, equaling 42, 33 and 26 Pa for the high, intermediate and low PI waveforms, respectively. The instantaneous WSS along the inner wall is generally unidirectional and scales with waveform amplitude. The low PI waveform has a larger secondary peak velocity resulting in higher WSS values post-peak systole. At diastole, the three cases have similar WSS patterns and magnitudes. Time-averaged wall shear parameter maps are shown in Figure 3.8. TAWSS patterns are similar across the three waveforms, shown in Figure 3.8a-c, as expected owing to the same mean flow rate, however some variation in the ICA is evident.

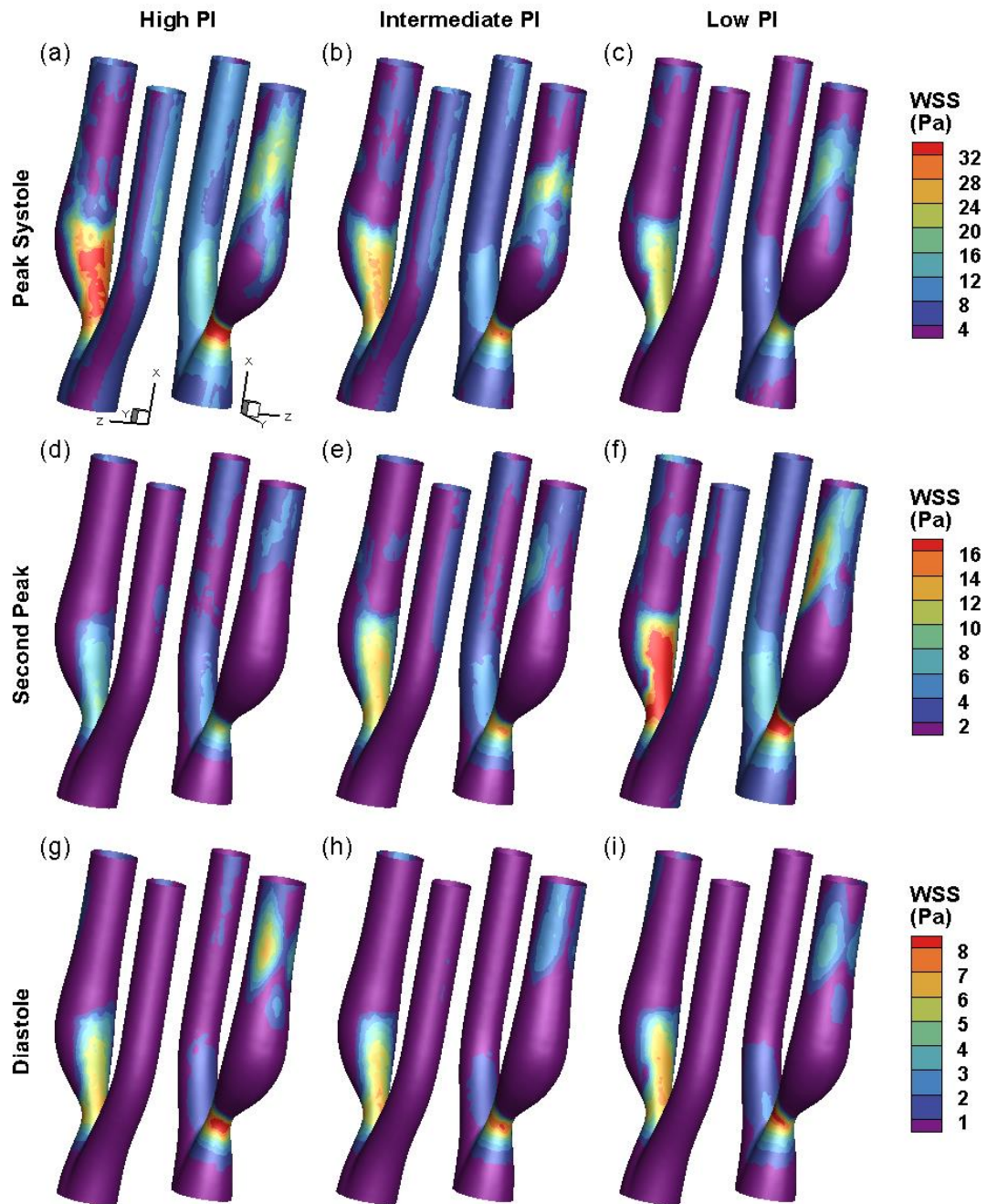


Figure 3.7: Contours of WSS magnitude for the 50% stenosed model and the high (left column), intermediate (middle) and low (right) PI waveforms. Two orientations are shown in each frame, displaying the inner ICA wall on the left and outer ICA wall on the right. (a-c) at peak systole ($t = 180$ ms); (d-f) at second flow peak ($t = 350$ ms); (g-i) mid diastole ($t = 830$ ms). Note different individual contour levels implemented for each row.

OSI magnitude maps are shown in Figure 3.8d-f, overlaid with a sparse sample of vectors representing the direction only of the cycle mean WSS vector. Two regions of high OSI are evident in each geometry, and are found to demarcate the recirculation regions, due to the shifting of the boundaries of these regions with pulsatile flow. One dimensional plots of OSI magnitude versus distance along the ICA inner and outer walls at the central plane of symmetry are shown in Figure 3.9. The extent of the recirculation region is evidently larger for lower PI waveforms. Also, OSI magnitudes within the ICA outer wall recirculation region increase with decreasing PI, whereas with higher PI, the WSS in this region is mostly unidirectional and reversed.

Bar plots of $TAWSS_{20}$ and OSI_{80} are shown in Figure 3.10, indicating that a higher PI waveform results in less surface area exposed to low magnitude WSS, but the highest exposure to oscillatory shear. The intermediate PI waveform has the highest SA exposed to both low TAWSS and high OSI, as indicated by the blue bars in Figure 3.10b. OSI_{80} increases approximately linearly with inlet waveform pulsatility metrics PI and RI, and peak stenosis velocity (similar to TI) as shown in Figure 3.11.

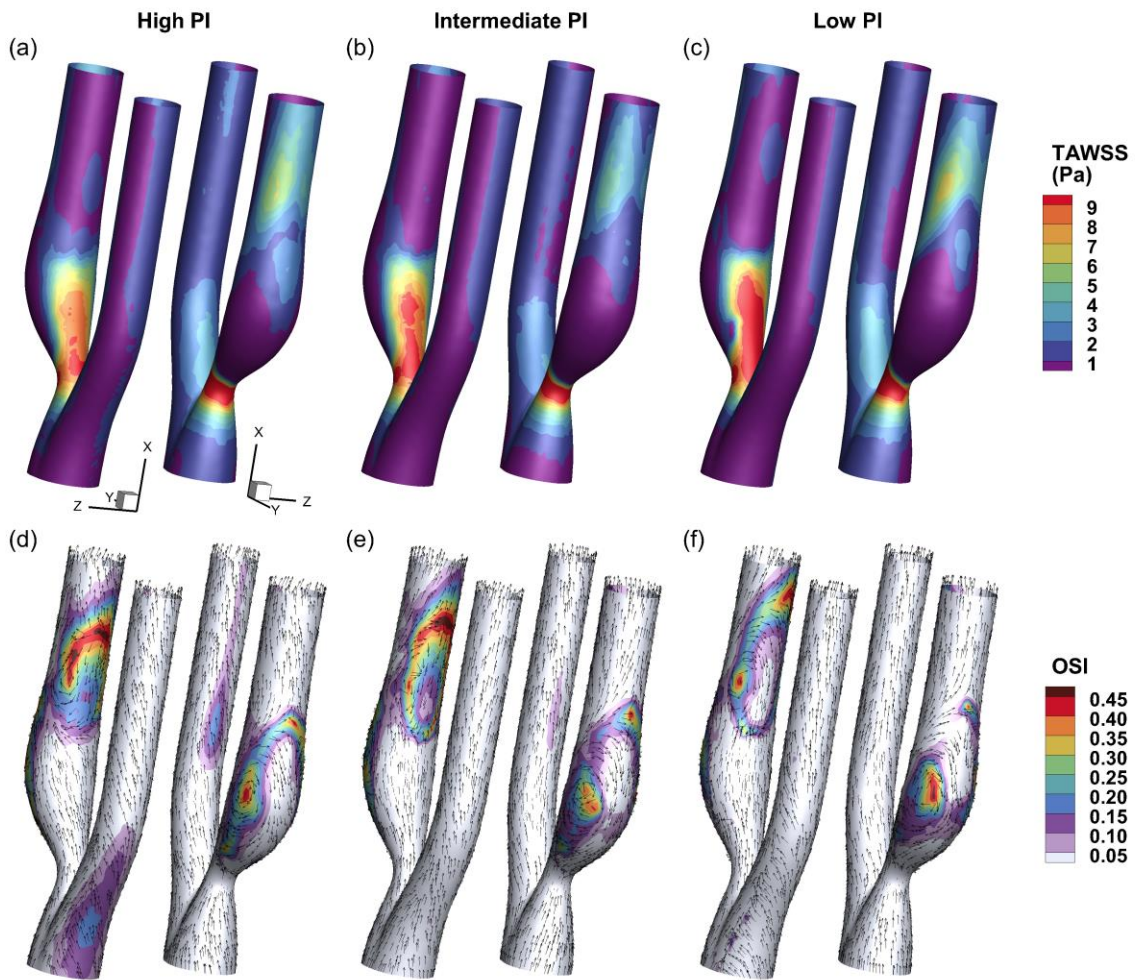


Figure 3.8: Time-averaged shear metrics for the 50% stenosed model with high (a,e), intermediate (b,f) and low (c,g) PI waveforms. Two orientations are shown in each frame, displaying the inner (left) and outer (right) walls of the ICA. (Top row, a-c) Contour maps of TAWSS. (Bottom row, d-f) Contour maps of OSI overlaid with a sparse sample of unit vectors indicating the direction of the mean WSS vector.

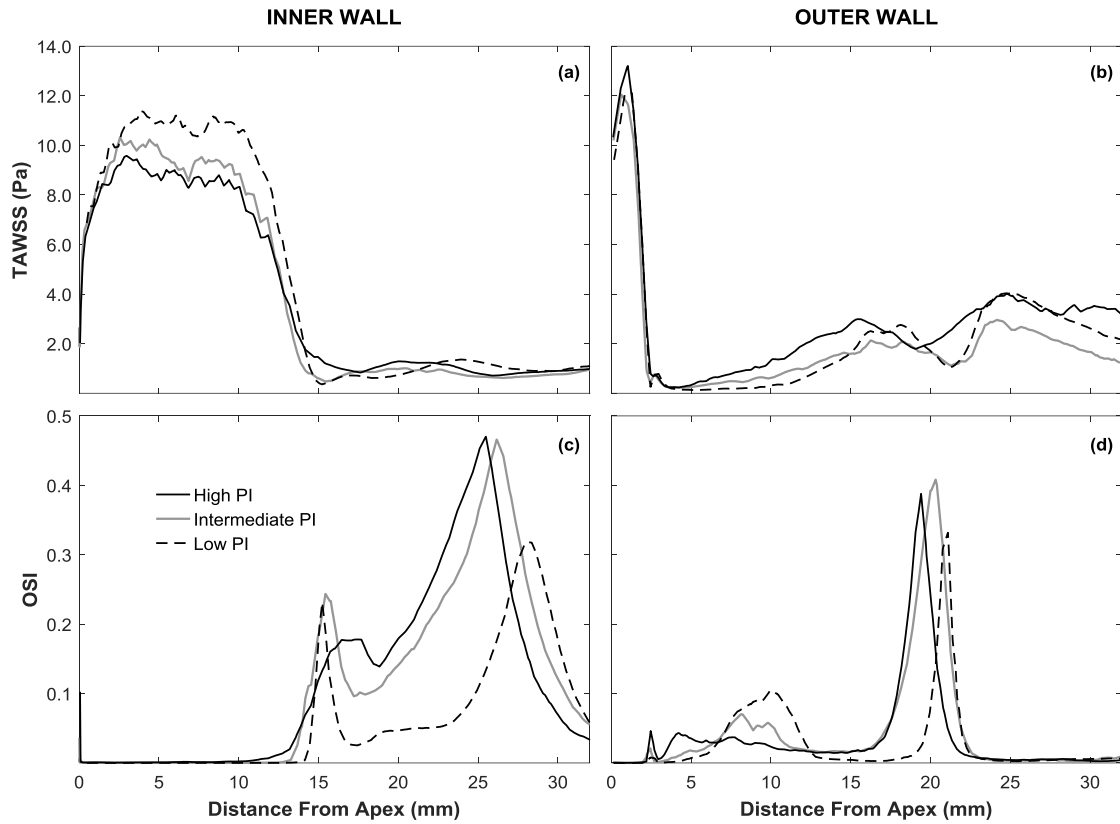


Figure 3.10: TAWSS (a,b) and OSI (c,d) magnitude profiles extracted along the inner (left column) and outer (right column) walls of the ICA along the plane of symmetry.

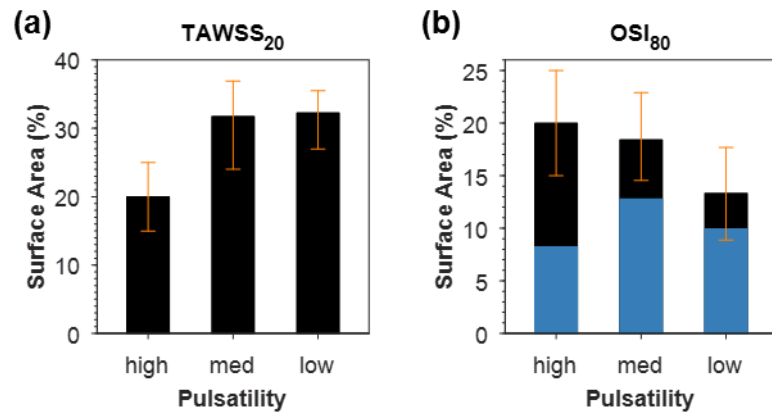


Figure 3.9: Relative ICA surface area exposed to a) TAWSS below the 20th percentile threshold and b) OSI above the 80th percentile threshold. Threshold values calculated from parameter distributions for the 50% stenosed model with high PI waveform. Error bars indicate the area exposed when +/- 5 percentile thresholds were applied. SA exposed to *both* low TAWSS and high OSI is indicated by blue shading.

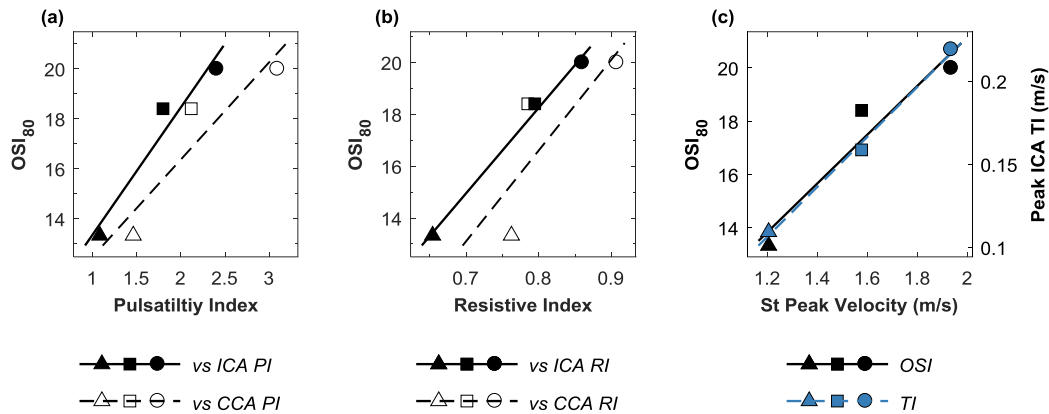


Figure 3.11: Correlation between surface area exposed to high OSI (OSI₈₀) and waveform descriptors. a) OSI₈₀ vs CCA velocity waveform PI (filled markers, solid line) and vs ICA velocity waveform PI (open markers, dashed line). b) OSI₈₀ vs CCA velocity waveform RI (closed markers, solid line) and vs ICA velocity waveform RI (open markers, dashed line). c) OSI₈₀ (black) and peak ICA-averaged TI (blue) vs peak stenosis velocity.

3.4 Discussion

Increasing cardiac (flow rate waveform) pulsatility leads to more multi-directional – and potentially atheroprone – wall shear stress. In particular a direct correlation between the amount of surface area exposed to high OSI levels and the waveform pulsatility index and resistive index was observed, indicating that increased PI results in more disturbed shear stress. This is consistent with a previous study in straight vessels in which OSI was shown to correlate with PI [25]. Similarly, Xiang et al. found a strong correlation between mean OSI over an aneurysm surface and the PI of the inlet waveform used in CFD simulations [11]. In a CFD study of intracranial aneurysms, the vortex formation and flow patterns were found to be largely impacted by PI (rather than Reynolds number or Womersley number), and high PI waveforms with retrograde flow were associated with larger regions of high OSI [26]. Together these results imply that accurate waveform amplitude as well as mean flow rate are required to calculate OSI. The present study also demonstrates that, even when the local geometry remains unchanged, the exposure of a vascular segment to

oscillatory shear stress can evolve over time as the waveform varies, for instance, by systemic changes in impedance [24] such as hypertension, by variations in pressure and flow due to isolated events or activities such as exercise [27], or simply by cardiac cycle variability.

Flow disturbances have implications for increased platelet aggregation and turbulence is associated with increased thrombus formation [28]. Sutura et al. [29] showed that the amount of platelet aggregation was increased with pulsed exposure to shear compared to steady exposure with equivalent cumulative shearing time, and that platelet aggregation was proportional to the amplitude of the shear pulse, suggesting increased pulsatility may result in increased platelet aggregation. Flow disturbances, as quantified here by peak turbulence intensity within the ICA branch, were shown to increase with both the PI of the inlet waveform and the stenosis severity. An increase in PI for a lesser stenosed geometry brings its peak TI into the range of the next stenosis severity grade, as seen in Figure 3.6. For example, a 30% stenosis geometry with a high PI waveform exhibits the same peak ICA TI as a 50% stenosis geometry with a low PI waveform. A similar effect was observed in previous experimental studies of other factors such as plaque eccentricity, plaque ulceration and the implementation of a non-Newtonian fluid in Chapter 2 [18; 21]. Risk diagnosis based on grouping according to stenosis severity alone, as prescribed by NASCET and ECST, does not account for the possible implications of flow waveform variation on the local hemodynamics.

Low and oscillatory WSS has been associated with the platelet adhesion to the vessel wall and the development of atherosclerotic lesions. Regions experiencing low wall shear stress, quantified here by the TAWSS₂₀ parameter, is reduced with higher PI, even though the qualitative TAWSS pattern is similar for all PIs. A similar effect was observed by Corbett et al. [30] in an experimental and numerical study of flow at a step transition, where the persistent stagnation length, indicating wall shear stress consistently less than 0.1 Pa throughout the cardiac cycle, decreased with both pulsatility index and mean inlet velocity. In addition, stagnation near the reattachment point was eliminated with pulsatile flow

compared to steady flow, and particle buildup in the step corner was shown to be significantly reduced with pulsatility. The work by Corbett would suggest that pulsatility may be protective in that particles trapped in low shear regions get washed out during the systolic portion of the following cardiac cycle.

The axial extent (length) of recirculation regions increased with decreasing pulsatility. Regions of high OSI coincide with a convergence or divergence of the time-averaged WSS vector, shown in Figure 3.8, and thus also appear at the boundary of recirculation. Similarly, Karri and Vlachos showed in a simplified stenosis model, that regions of high OSI coincided with the mean reattachment site and recirculation length decreased with increasing PI [31]. While increased jet velocities are associated with the presence of flow disturbances and vortex shedding, they cause the flow reattachment point to shift proximal or upstream resulting in shorter mean recirculation lengths for higher amplitude waveforms, as shown here and by others [31; 32].

Several computational studies have investigated the effect of assumed or steady versus patient specific inlet flow conditions in aneurysm geometries. Geers et al. [10] found that steady flow simulations using the mean inlet flow rate could predict the TAWSS reasonably well, but steady flow simulations using peak systolic flow rate underestimated peak WSS compared to pulsatile simulations. Simulations comparing boundary conditions found that qualitative patterns of WSS and OSI could be captured using idealized (population averaged) waveforms, but the exposure to OSI using a thresholding method (as applied here) was dependent on patient specific waveform shape [33] and relative differences in mean WSS and OSI exceeded 30% [8].

In the present study a Newtonian blood mimicking fluid and rigid walls were applied. While blood is known to exhibit non-Newtonian shear thinning behaviour several studies have found that a Newtonian assumption works reasonably well on the scale of large arteries [34]. In the work in Chapter 2 with identical models, differences in hemodynamics were observed between non-Newtonian and Newtonian blood analogue fluids. However,

the present study allowed the relative contribution of pulsatility to hemodynamics to be investigated independent of other variables.

Previous computational work showed that a change in pulsatility could be achieved through a change in systemic impedance [24]. However, in the present study different PIs were obtained through direct change in the pump output while using identical downstream resistance and compliance components in the flow loop. The mean inlet flow rate was held constant and the diastolic flow rate was comparable for the three inlet waveforms applied here, such that an increase in pulsatility is effectively equivalent to an increase in waveform amplitude. Further investigation would be required to determine if the correlation between OSI and PI is dependent upon mean flow rate, cycle length, or retrograde (negative) flow.

3.5 References

- [1] Zarins, C.K., Giddens, D.P., Bharadvaj, B.K., *et al.*, 1983. Carotid bifurcation atherosclerosis quantitative correlation of plaque localization with flow velocity profiles and wall shear-stress. *Circulation Research* 53:502-514.
- [2] Wentzel, J.J., Chatzizisis, Y.S., Gijzen, F.J.H., *et al.*, 2012. Endothelial shear stress in the evolution of coronary atherosclerotic plaque and vascular remodelling: Current understanding and remaining questions. *Cardiovascular Research* 96:234-243.
- [3] Caro, C.G., Fitzgerald, J.M., Schroter, R.C., 1971. Atheroma and arterial wall shear - observation, correlation and proposal of a shear dependent mass transfer mechanism for atherogenesis. *Proceedings of the Royal Society Series B-Biological Sciences* 177:109-+.
- [4] Davies, P.F., 2009. Hemodynamic shear stress and the endothelium in cardiovascular pathophysiology. *Nature Clinical Practice Cardiovascular Medicine* 6:16-26.
- [5] Park, K.Y., Chung, P.W., Kim, Y.B., *et al.*, 2013. Increased pulsatility index is associated with intracranial arterial calcification. *European Neurology* 69:83-88.
- [6] Kidwell, C.S., El-Saden, S., Livshits, Z., *et al.*, 2001. Transcranial doppler pulsatility indices as a measure of diffuse small-vessel disease. *Journal of Neuroimaging* 11:229-235.

- [7] Lee, K.Y., Sohn, Y.H., Baik, J.S., *et al.*, 2000. Arterial pulsatility as an index of cerebral microangiopathy in diabetes. *Stroke* 31:1111-1115.
- [8] Karmonik, C., Yen, C., Diaz, O., *et al.*, 2010. Temporal variations of wall shear stress parameters in intracranial aneurysms-importance of patient-specific inflow waveforms for cfd calculations. *Acta Neurochirurgica* 152:1391-1398.
- [9] Marzo, A., Singh, P., Larrabide, I., *et al.*, 2011. Computational hemodynamics in cerebral aneurysms: The effects of modeled versus measured boundary conditions. *Annals of Biomedical Engineering* 39:884-896.
- [10] Geers, A.J., Larrabide, I., Morales, H.G., *et al.*, 2014. Approximating hemodynamics of cerebral aneurysms with steady flow simulations. *Journal of Biomechanics* 47:178-185.
- [11] Xiang, J., Siddiqui, A.H., Meng, H., 2014. The effect of inlet waveforms on computational hemodynamics of patient-specific intracranial aneurysms. *Journal of Biomechanics* 47:3882-3890.
- [12] Smith, R.F., Rutt, B.K., Fox, A.J., *et al.*, 1996. Geometric characterization of stenosed human carotid arteries. *Academic Radiology* 3:898-911.
- [13] Smith, R.F., Rutt, B.K., Holdsworth, D.W., 1999. Anthropomorphic carotid bifurcation phantom for mri applications. *Jmri-Journal of Magnetic Resonance Imaging* 10:533-544.
- [14] Poepping, T.L., Nikolov, H.N., Thorne, M.L., *et al.*, 2004. A thin-walled carotid vessel phantom for doppler ultrasound flow studies. *Ultrasound in Medicine and Biology* 30:1067-1078.
- [15] Fox, A.J., 1993. How to measure carotid stenosis. *Radiology* 186:316-318.
- [16] Antiga, L., Piccinelli, M., Botti, L., *et al.*, 2008. An image-based modeling framework for patient-specific computational hemodynamics. *Medical & Biological Engineering & Computing* 46:1097-1112.
- [17] Yousif, M.Y., Holdsworth, D.W., Poepping, T.L., 2011. A blood-mimicking fluid for particle image velocimetry with silicone vascular models. *Experiments in Fluids* 50:769-774.
- [18] Kefayati, S., Holdsworth, D.W., Poepping, T.L., 2014. Turbulence intensity measurements using particle image velocimetry in diseased carotid artery models: Effect of stenosis severity, plaque eccentricity, and ulceration. *Journal of Biomechanics* 47:253-263.

- [19] Kefayati, S., Milner, J.S., Holdsworth, D.W., *et al.*, 2014. In vitro shear stress measurements using particle image velocimetry in a family of carotid artery models: Effect of stenosis severity, plaque eccentricity, and ulceration. *Plos One* 9:19.
- [20] Wong, E.Y., Nikolov, H.N., Thorne, M.L., *et al.*, 2009. Clinical doppler ultrasound for the assessment of plaque ulceration in the stenosed carotid bifurcation by detection of distal turbulence intensity: A matched model study. *European Radiology* 19:2739-2749.
- [21] Wong, E.Y., Nikolov, H.N., Rankin, R.N., *et al.*, 2013. Evaluation of distal turbulence intensity for the detection of both plaque ulceration and stenosis grade in the carotid bifurcation using clinical doppler ultrasound. *European Radiology* 23:1720-1728.
- [22] Holdsworth, D.W., Norley, C.J.D., Frayne, R., *et al.*, 1999. Characterization of common carotid artery blood-flow waveforms in normal human subjects. *Physiological Measurement* 20:219-240.
- [23] Hoi, Y., Wasserman, B.A., Xie, Y.Y.J., *et al.*, 2010. Characterization of volumetric flow rate waveforms at the carotid bifurcations of older adults. *Physiological Measurement* 31:291-302.
- [24] Onaizah, O., Poepping, T.L., Zamir, M., 2017. A model of blood supply to the brain via the carotid arteries: Effects of obstructive vs. Sclerotic changes. *Medical Engineering & Physics* 49:121-130.
- [25] Avrahami, I., Kersh, D., Liberzon, A., 2016. Pulsatility index as a diagnostic parameter of reciprocating wall shear stress parameters in physiological pulsating waveforms. *Plos One* 11:16.
- [26] Le, T.B., Borazjani, I., Sotiropoulos, F., 2010. Pulsatile flow effects on the hemodynamics of intracranial aneurysms. *Journal of Biomechanical Engineering-Transactions of the Asme* 132:11.
- [27] Babcock, M.C., Lefferts, W.K., Hughes, W.E., *et al.*, 2015. Acute effect of high-intensity cycling exercise on carotid artery hemodynamic pulsatility. *European Journal of Applied Physiology* 115:1037-1045.
- [28] Stein, P.D., Sabbah, H.N., 1974. Measured turbulence and its effect on thrombus formation. *Circulation Research* 35:608-614.
- [29] Suter, S.P., Nowak, M.D., Joist, J.H., *et al.*, 1988. A programmable, computer-controlled cone plate viscometer for the application of pulsatile shear-stress to platelet suspensions. *Biorheology* 25:449-459.

- [30] Corbett, S.C., Ajdari, A., Coskun, A.U., *et al.*, 2010. Effect of pulsatile blood flow on thrombosis potential with a step wall transition. *Asaio Journal* 56:290-295.
- [31] Karri, S., Vlachos, P.P., 2010. Time-resolved dpiv investigation of pulsatile flow in symmetric stenotic arteries effects of phase angle. *Journal of Biomechanical Engineering-Transactions of the Asme* 132:11.
- [32] Ojha, M., Cobbold, R.S.C., Johnston, K.W., *et al.*, 1989. Pulsatile flow through constricted tubes - an experimental investigation using photochromic tracer methods. *Journal of Fluid Mechanics* 203:173-197.
- [33] Hoi, Y., Wasserman, B.A., Lakatta, E.G., *et al.*, 2010. Carotid bifurcation hemodynamics in older adults: Effect of measured versus assumed flow waveform. *Journal of Biomechanical Engineering-Transactions of the Asme* 132:6.
- [34] Morbiducci, U., Gallo, D., Massai, D., *et al.*, 2011. On the importance of blood rheology for bulk flow in hemodynamic models of the carotid bifurcation. *Journal of Biomechanics* 44:2427-2438.

Chapter 4

4 Modeling the Effects of vascular stiffening: An in vitro study of carotid artery hemodynamics using particle image velocimetry

4.1 Introduction

Atherosclerosis, and subsequent thrombosis and plaque rupture, is a major cause of cerebrovascular events. The carotid artery bifurcation is a common site of atherosclerosis, and the carotid artery is often the origin of thrombotic plaques that eventually lead to ischemic strokes. The focal distribution of atherosclerosis in the arterial tree, developing primarily at curvatures and bifurcations, suggests a hemodynamically driven mechanism for the development of vascular disease [1-3]. More specifically low and oscillatory wall shear stress (WSS) is associated with the early development of lesions and plaque growth [3] by inhibiting the protective function of the endothelium [4]. The progression of atherosclerosis contributes to local geometrical and structural changes that further impact the hemodynamics, creating localized areas of complex or disturbed flow.

Arterial stiffness is intricately connected with atherosclerosis, due to changes in the mechanical properties of the vessel wall with plaque development [5], and arterial stiffness has emerged as a diagnostic indicator of vascular disease. Reduced compliance is an independent predictor of cerebrovascular events [6] where compliance decreases with aging, diabetes, hypertension and other associated risk factors [7]. In addition, systemic vessel stiffening manifests in changes to flow and pressure waveform shapes seen in vivo [8; 9] and in vitro [10], expected to impact local hemodynamics. While the association between arterial stiffness and atherosclerosis is well established, the effect of local vessel compliance on WSS, and other hemodynamic parameters thought to impact the progression of atherosclerosis, is still debated.

It is difficult to measure hemodynamics in vivo with sufficient accuracy for WSS computation, thus experimental and numerical modeling techniques are typically

employed. Computational fluid dynamics (CFD) or in-vitro experimental particle image velocimetry (PIV) are widely used to study hemodynamics. Simulations of rigid vessels have demonstrated that geometry is the most impactful factor on hemodynamics, followed by flow pulsatility and then additional factors like blood rheology. However, vessel compliance is neglected in the majority of these studies. More recently, fluid-structure interaction (FSI) has allowed wall motion and compliance to be incorporated into numerical simulations and has been applied in attempts to more accurately model hemodynamics in various parts of the arterial tree. Incorporating compliance into experimental PIV studies remains challenging. Some studies have evaluated flow and WSS in elastic vessel replicas using PIV [11; 12]. However, limited experimental and numerical studies have conducted matched-model comparisons between rigid and elastic vessels [13; 14]. From these, the importance of compliance in modeling hemodynamics, including WSS and turbulence, has not been conclusively determined.

In this study we carry out a matched-model comparison of flow disturbances and WSS variation in two idealized models – rigid and compliant versions – of a carotid bifurcation with 50% eccentric stenosis using stereoscopic PIV in conjunction with an in-vitro flow facility. The rigid and compliant phantoms are life-sized with suitable blood-mimicking viscosity eliminating the need for flow scaling. Wall location information over time is obtained from a retrospectively gated computed tomography technique and applied to calculate WSS in the thin-walled compliant model. This is compared to the calculation performed using a static vessel wall, as well as to flow and WSS data obtained in a rigid phantom for comparison.

4.2 Methods

4.2.1 Experimental Flow Set-up

Optically transparent, life-sized, PIV-compatible flow phantoms used in this study were fabricated from silicone elastomer (Sylgard® 184, Dow Corning Canada, Inc.; refractive index 1.41–1.43) using a lost metal core casting technique, previously described for ultrasound and MRI applications [15; 16]. Two versions were constructed, depicted in

Figure 4.1a: 1) an approximately rigid model with lumen geometry cast in a block of silicone, and 2) a semi-compliant model with 1 mm thick silicone walls mounted in a transparent box, referred to as the block and thin-walled models, respectively. The chosen geometry for the present study has an 8mm CCA inlet diameter and a 50% eccentric stenosis of the internal carotid artery based on previous in-vivo characterization [17]. The thin-walled model was loosely tensioned such that there were no geometrical discrepancies between the models.

The flow set-up is depicted in Figure 4.1b. A physiological flow-waveform was generated by a computer-controlled pump (CompuFlow 1000, Shelley Medical Imaging Technologies, London ON Canada). The idealized carotid flow waveform was based on in-vivo ultrasound measurements derived from young adults with a peak flow-rate of 26.3 mL/s, average volume flow-rate of 6.0 mL/s and cardiac cycle period of 920 ms [18]. Flow and pressure were monitored at the phantom inlet and outlets using electromagnetic flowmeters (Caroline Medical Electronics, East Bend NC, USA) and a Millar Mikro-tip pressure transducer catheter. The locations of the flow and pressure measurements were approximately 25 cm proximal to the bifurcation apex for the CCA and 15 cm distal to the apex for the ICA and ECA. Measured flow and pressure waveforms at the CCA inlet and ICA outlet for both phantom models are shown in Figure 4.2a-d. A set of downstream flow resistors, connected to the ICA and ECA outlets were used to achieve an approximate flow division of 60:40, as applied in other experiments [8; 19-22] based on literature values [8]. The working fluid was a refractive-index matched Newtonian solution composed of water, glycerol, and sodium iodide, with appropriate dynamic viscosity of 4.31 ± 0.03 cP, and density of 1.244 g/mL, as previously characterized [23]. The resulting Womersley number was equal to 5.62. The circulating fluid was seeded with 15 μm fluorescent Rhodamine B-encapsulated polystyrene tracer particles. The thin-walled model was also submerged in the (un-seeded) refractive-index matched blood-mimicking fluid to minimize optical

distortion and to prevent vessel collapse and ensure it remained level throughout the experiment.

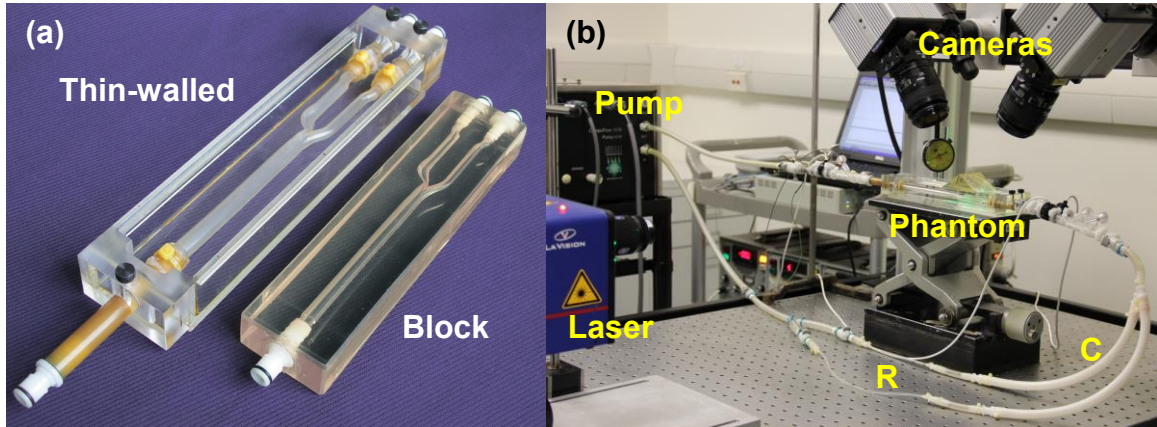


Figure 4.1: a) Thin-walled and block phantom models. b) Photo of the experimental setup. R and C indicate downstream resistive and compliant elements, respectively.

4.2.2 PIV Experiments

Experimental particle image velocimetry data were collected using a stereoscopic PIV system (LaVision Inc. Ypsilanti MI, USA), used in previous experiments. The flow was illuminated by a diode-pumped continuous-wave Nd-YAG laser (LSR-532-TM-5000-10, 532 nm, 5.5 W, LaserGlow.com Ltd., Toronto) equipped with two cylindrical divergent lenses to form an approximate 1 mm thick laser sheet. Two high-speed CMOS cameras with sensor matrix size 1024x1024 pixels and 60mm Nikon lenses, were arranged in stereoscopic configuration (opening angle 90°) and equipped with Scheimpflug adapters as well as 550 nm long-pass filters to isolate light from tracer particles. Orthogonal viewing was maintained using a silicone prism placed over the region of interest of the phantom. Image acquisition was triggered at the start of each waveform cycle by an ECG-simulation pulse from the pump. Double frame PIV images were recorded at 100 Hz, for the first 870 ms of the 920 ms cardiac cycle. Scans were repeated for multiple planes at 0.5 mm increments for 3.5 mm above and 3.5 mm below the central plane of symmetry of the

phantom lumen to allow a 3D three-component velocity data set to be constructed. For each plane, 15 cardiac cycles were collected and processed, previously shown to adequately capture the turbulent fluctuations [20].

PIV data were processed using commercial software (DaVis 7.2, LaVision). A combined RMS image was generated from the individual particle images and applied as a mask for velocity vector calculation. In the case of the thin-vessel phantom, the RMS image was generated from phase synchronized images to preserve possible wall-motion. Images were preprocessed with a high-pass filter to remove background noise. Particle images were evaluated using a multi-pass fast-Fourier transform based cross-correlation algorithm with decreasing window size from 64x64 pixels to 16x16 pixels and 50% window overlap. A Gaussian-weighting scheme and high-accuracy Whittaker reconstruction were applied for the final passes. The velocity data were post-processed with a median filter and smoothed once using a 1x3 smoothing kernel. The processing resulted in a final velocity vector field with approximately 0.30 mm in-plane resolution. CCA and ICA velocity waveforms were extracted from the measured central plane PIV data at the extremities of the phantom within the field of view, displayed in Figure 4.2e-f.

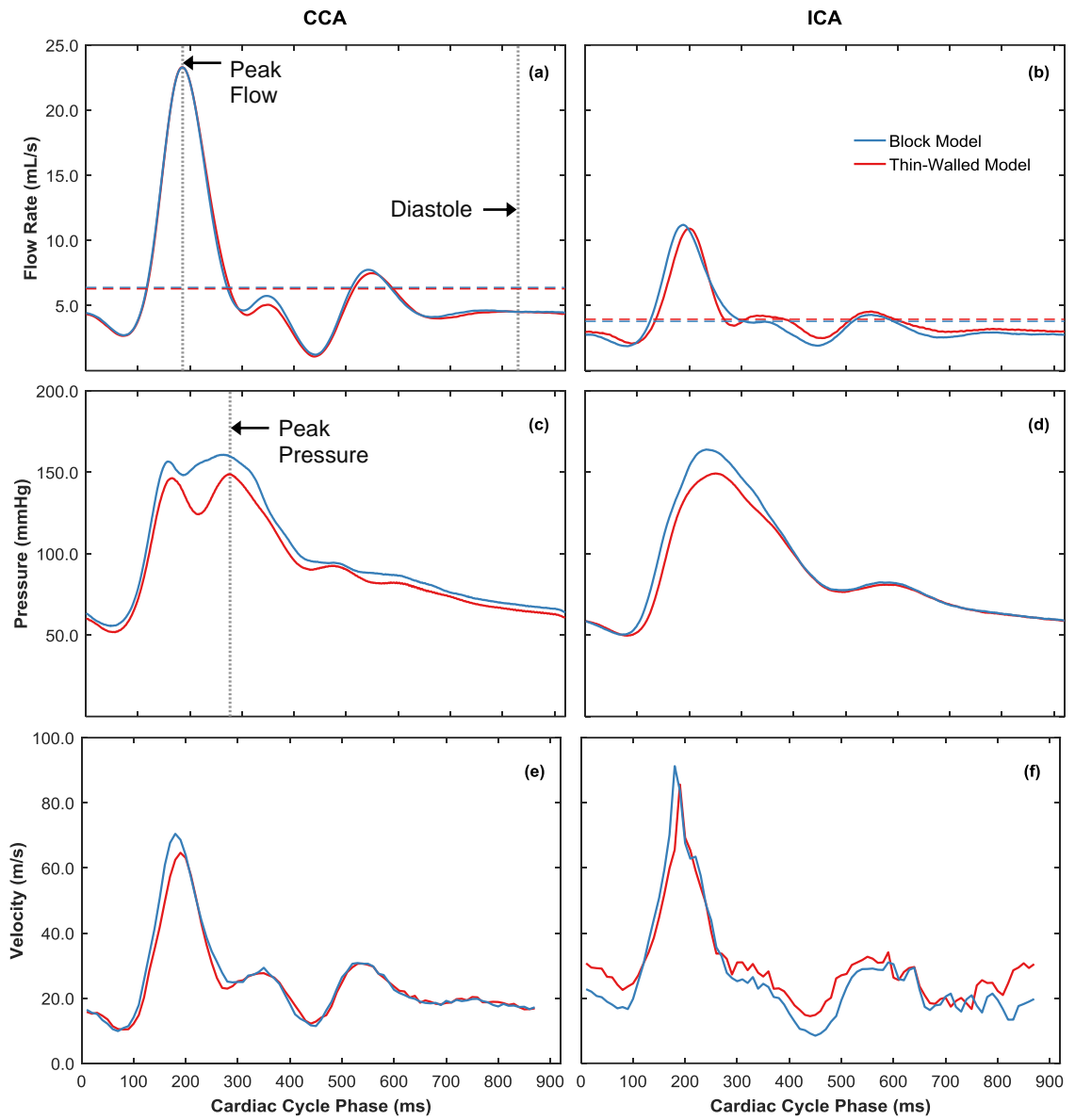


Figure 4.2: Flow (top row, a-b), pressure (middle, c-d) and velocity (bottom, e-f) waveforms measured at the CCA inlet and ICA outlet for block (blue) and thin-walled (red) phantom models. Grey dotted vertical lines indicate time points of peak flow ($t = 180$ ms) peak pressure (approximately $t = 290$ ms) and mid-diastole ($t = 830$ ms).

4.2.3 Micro Computed Tomography Experiments

Anatomical scans of both block and thin-walled models were obtained using a volumetric cone-beam micro-computed tomography scanner (Locus Ultra, General Electric Healthcare, London, ON, Canada). Scans of the pressurized phantoms were acquired at static pressure increments of 40 mmHg, held during the micro-CT collection using a clamped pressure manometer. The spatial resolution of the reconstructed CT images was 154 μm .

For the thin-walled phantom, a dynamic retrospectively-gated CT protocol was also implemented to extract temporal wall location information over the cardiac cycle [24; 25]. The flow set-up was identical to that used in PIV experiments, described above, with the pump ECG signal used to synchronize the data. The micro-CT scanner consists of a flat-panel detector and x-ray tube, mounted on a slip-ring gantry that rotates continuously during acquisition. Projection images of the moving phantom are acquired over many cardiac cycles from multiple complete rotations of the gantry. The data are sorted post-acquisition via a least-error technique, in which all projection angles are filled for a particular cardiac phase from the available projection data occurring closest to the phase of interest. The dynamic CT reconstruction method provided volumetric CT images every 46 ms.

Micro CT surfaces were segmented from the reconstructed CT images using a level-set segmentation algorithm in the Vascular Modeling Toolkit (VMTK) [26]. The segmented model surfaces were subsequently smoothed and remeshed in VMTK. The micro-CT surfaces were registered to velocity vector data using an iterative closest point algorithm with the outermost (boundary) velocity data, implemented in VMTK. The remainder of the data processing was completed in Matlab.

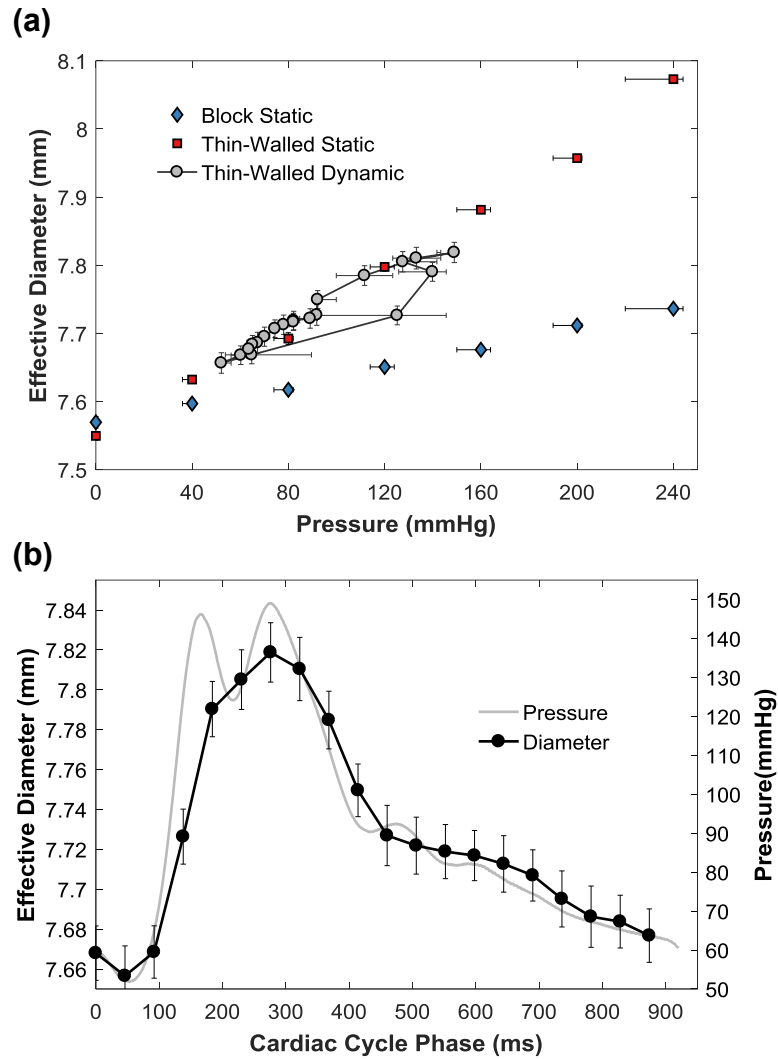


Figure 4.3: a) CCA diameter vs static pressure for the block (blue, diamond) and thin-walled (red, square) phantom models. CCA diameter vs dynamic pressure over the cardiac cycle for the thin-walled phantom (grey, circle) displays a hysteresis, with lower distension when pressure is increasing. b) CCA diameter vs cardiac cycle phase for the thin-walled phantom, plotted against CCA inlet pressure, for reference.

4.2.4 Data Postprocessing

Vessel Compliance

Vessel distension was measured for all static and dynamic CT images by implementing an edge-detection algorithm on 2D transverse slices through the volumetric CT images and calculating the effective vessel diameter from the observed lumen area. The measurement was averaged over 5 transverse slices in the CCA 10 mm proximal to the bifurcation apex. The vessel distensibility coefficient and Peterson's elastic modulus were computed from the static pressure CT scans for both phantoms using:

$$d = \frac{\Delta A/A_0}{\Delta P} = \frac{(D^2 - D_0^2)}{D_0^2 \Delta P} \quad (4.1)$$

$$E_p = \frac{D_0 \Delta P}{\Delta D} \quad (4.2)$$

where D_0 refers to the unstretched diameter at zero pressure, and the ratio $\Delta D/\Delta P$ is determined from the slope of the best-fit line through the data. Fig. 3 shows the CCA distension of the thin-walled phantom versus phase, as well as the distension versus pressure curves for the block and thin-walled models. Distension versus pressure plotted for the dynamic case shows a hysteresis, with a smaller vessel diameter during acceleration compared to deceleration phases, indicating viscoelasticity of silicone. Measurements of compliance are summarized in Table 4.1, along with systolic and diastolic diameter and relative diameter change for the thin-walled dynamic case.

Table 4.1: Mechanical properties of carotid artery phantoms

Parameter	Block	Thin-Walled
Distensibility Coefficient ($\times 10^{-3}$ kPa $^{-1}$)	1.41	4.43
Peterson's modulus, E_p ($\times 10^5$ Pa)	14.3	4.67
Wall Thickness (mm)	-	~ 1 mm
Diastolic Diameter (mm)	-	7.66*
Systolic Diameter (mm)	-	7.82*
Relative diameter change (%)	-	2.12*

*measured from dynamic CT experiments

Turbulence Intensity

Velocity maps were first ensemble averaged at each phase of the cardiac cycle and the phase-averaged flow, $U_i(t)$ was separated from non-coherent fluctuations using a Reynolds decomposition method [27]

$$U_i(t) = \frac{1}{N} \sum_{n=1}^N u_i(t, n), \quad i = x, y, z \quad (4.3)$$

$$u'_i(t, n) = u_i(t, n) - U_i(t) \quad (4.4)$$

where N represents the number of total cardiac cycles (N=15). The total turbulence intensity (TI) at each spatial location can be estimated from

$$TI_i(t) = \sqrt{\frac{\sum_{n=1}^N u'_i(t, n)u'_i(t, n)}{N - 1}} \quad (4.5)$$

$$TI(t) = \sqrt{(TI_x(t))^2 + (TI_y(t))^2 + (TI_z(t))^2} \quad (4.6)$$

to compare the turbulence over time, the spatial mean of TI was computed over the ICA branch within the central plane at each cardiac cycle phase.

Wall Shear Stress

Wall shear stress (WSS) was calculated using a combination of velocity vector data from PIV and segmented surface data from micro-CT, allowing both magnitude and direction of WSS vectors to be computed. The method is described in detail in Chapters 1 and 2. Starting from a single surface point, three-component velocities were interpolated from the surrounding velocity data at equally spaced (0.3 mm) increments along the inward normal from the surface using a cubic polynomial interpolation scheme. Assigning zero velocity at the surface, a cubic fit was applied to each velocity component, and velocity gradients

were calculated from the slope of the fit at the wall location. The local traction vector could then be calculated as the product of the normal vector with the shear stress tensor

$$\mathbf{t} = \hat{\mathbf{n}} \cdot \boldsymbol{\tau} \quad (4.7)$$

We isolate the forces acting tangential to the wall plane using

$$\boldsymbol{\tau}_w = \mathbf{t} - (\mathbf{t} \cdot \hat{\mathbf{n}})\hat{\mathbf{n}} \quad (4.8)$$

which we the wall shear stress vector.

For the block model, WSS was calculated at all time points using the surface generated from the static pressure CT scan at 80 mmHg, being the closest to the average cardiac cycle pressure in the model. For the thin-walled model, WSS was calculated twice: 1) neglecting wall motion, using the surface segmented from the static pressure CT scan at 80 mmHg registered with the thin-walled velocity data and 2) accounting for wall motion by using surfaces segmented from dynamic CT and the thin-walled velocity data. In the latter case, the closest WSS surface was chosen for each phase of the PIV dataset. Time-integrated WSS metrics of TAWSS, OSI and transWSS (previously described in Chapter 1) were calculated for both block and thin-walled models. For the thin-walled phantom with dynamic CT, the instantaneous WSS data was translated onto the minimum pressure dynamic surface (occurring at $t = 46$ ms) using vmtk for the calculation of time-integrated metrics.

Quantification of ICA surface area exposure to key metrics such as low or high WSS magnitude or high oscillatory WSS was achieved by applying a thresholding method [28]. Threshold values were selected from the block model parameter distributions using the 80th percentile values (i.e. 80% of the ICA surface area exposed) of OSI and transWSS and the 20th and 80th percentile values of TAWSS (for low and high WSS respectively). The threshold was then applied to WSS parameter maps to determine the cumulative area of ICA surface elements above (denoted OSI_{80} , $transWSS_{80}$, and $TAWSS_{80}$) or below

(denoted $TAWSS_{20}$) the threshold and normalized by the total surface area to compare exposure between models.

4.3 Results

A comparison of block and thin-walled central plane, phase averaged velocity is shown in Figure 4.4 for three timepoints corresponding to peak flow ($t = 180$ ms), peak pressure ($t = 290$ ms) and diastole ($t = 830$ ms). Velocity magnitude contours are displayed overlaid with central plane projected velocity vectors to indicate the direction of flow. The flow pattern is similar for both block and thin-walled models, consisting of a high velocity jet emerging from the stenosis into the ICA along the inner wall, crossing the lumen, and impinging on the outer wall. A large primary recirculation region is created between the outer wall of the vessel and the high velocity jet. Downstream of the impingement site, rebounding flow travels back toward the inner wall creating a small secondary region of reversed flow. At peak flow rate, the maximum velocity in the jet region is slightly higher (6.2% difference) and more reversed flow is observed in the large recirculation region for the block compared to thin-walled model. At peak pressure (and subsequent phases), the thin-walled model exhibits higher jet velocity (14.5% difference at $t = 300$ ms) and increased width and extent of the jet compared to the block model. Centerline projected phase averaged velocity profiles extracted from the central plane are shown in Figure 4.5 at two axial locations along the centerline, $S1 = 8$ mm and $S2 = 30$ mm. A sparse sample of error bars indicate the standard deviation in the velocity, representative of the turbulence intensity, which is higher downstream at $S2$ compared to $S1$ and very low prior to systole ($t = 160$ ms).

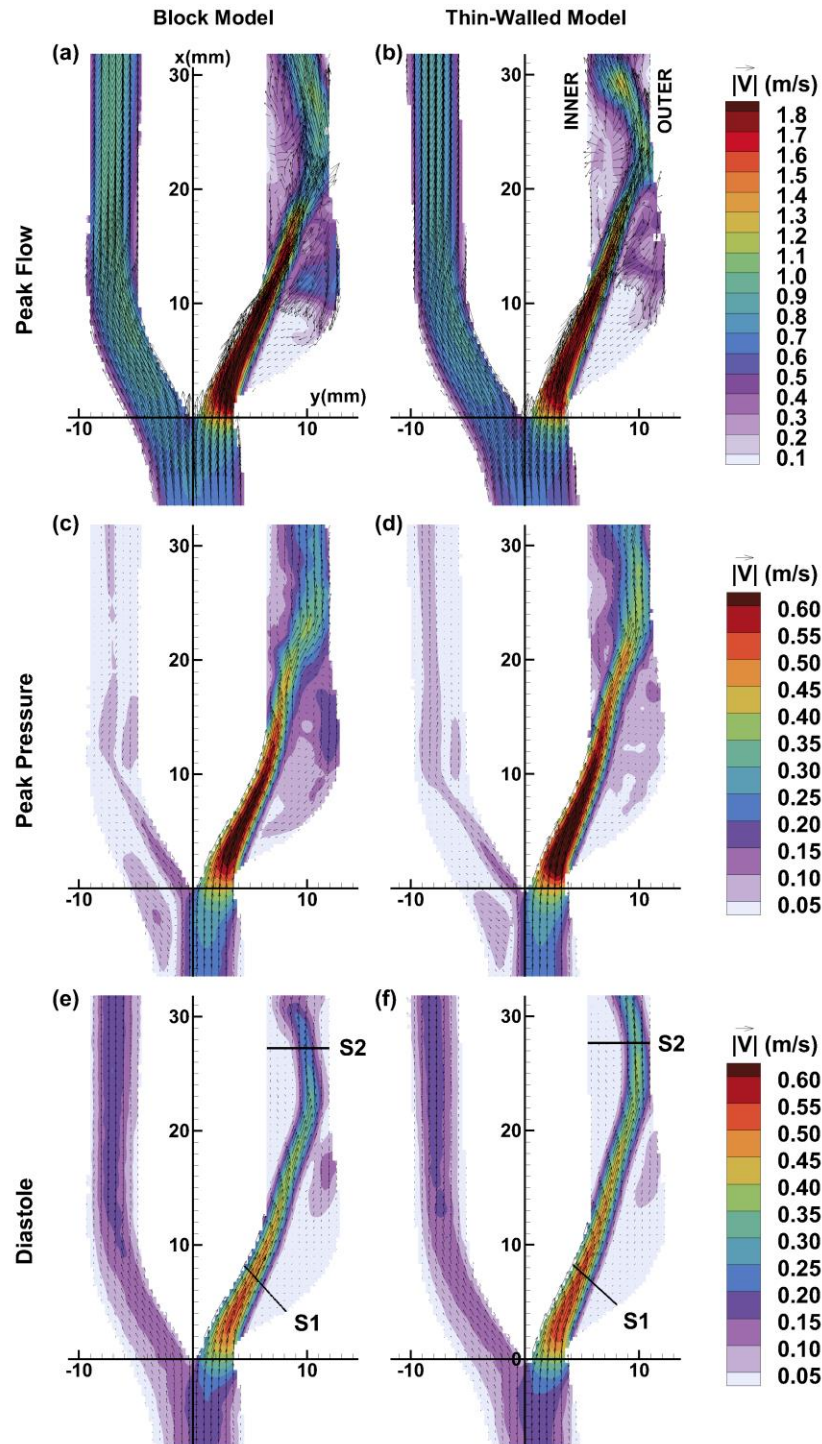


Figure 4.4: Phase-averaged velocity vector maps superimposed on contours of phase-averaged velocity magnitude at time points of peak flow (top row, a-b), peak pressure (middle, c-d) and diastole (bottom, e-f). Note different individual color bars for each row. Slices S1 and S2 on panels e-f indicate cross-sections where velocity profiles were extracted.

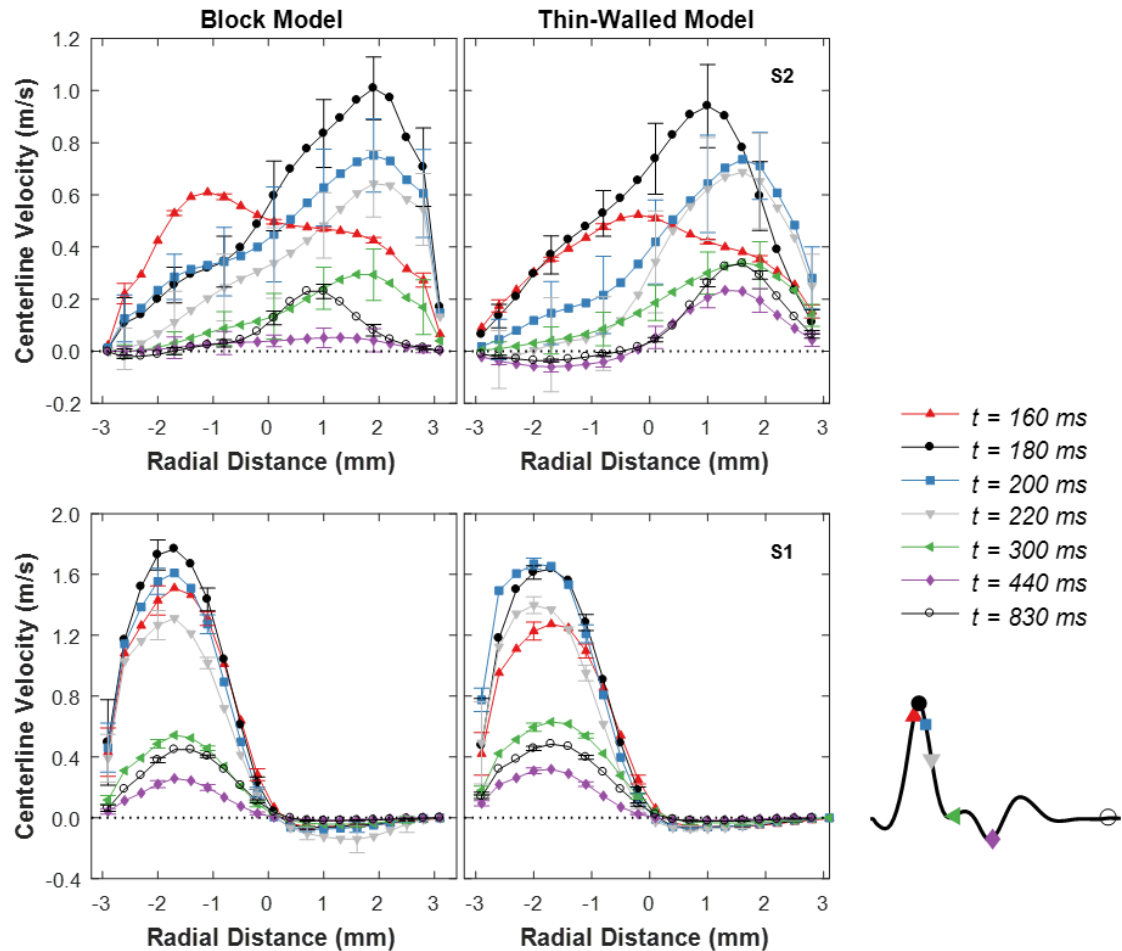


Figure 4.5: Temporal phase-averaged centerline-projected velocity profiles extracted from the central plane ICA at slices S1 (bottom row) and S2 (top row) indicated in Figure 4.4e-f. Sparse error bars represent standard deviation over 15 collected cardiac cycles.

Figure 4.6 shows the temporal evolution of central plane TI maps for the ICA branch, for timepoints beginning just before peak systole and continuing into the deceleration phase. The block model exhibits maximum TI just after peak systole ($t = 190$ ms) while the thin-walled model reaches maximum TI at a later time ($t = 220$ ms). High TI regions are shifted slightly downstream in the thin-walled model and the spatial extent of elevated TI in the ICA is reduced. Spatially averaged TI over the ICA central plane versus phase is plotted in Figure 4.7. In general, maximum ICA-averaged TI is 17% higher in the block model and

consistently higher compared to the thin-walled model. The cumulative difference in TI between block and thin-walled model when averaged both temporally and spatially over the central plane is 21%.

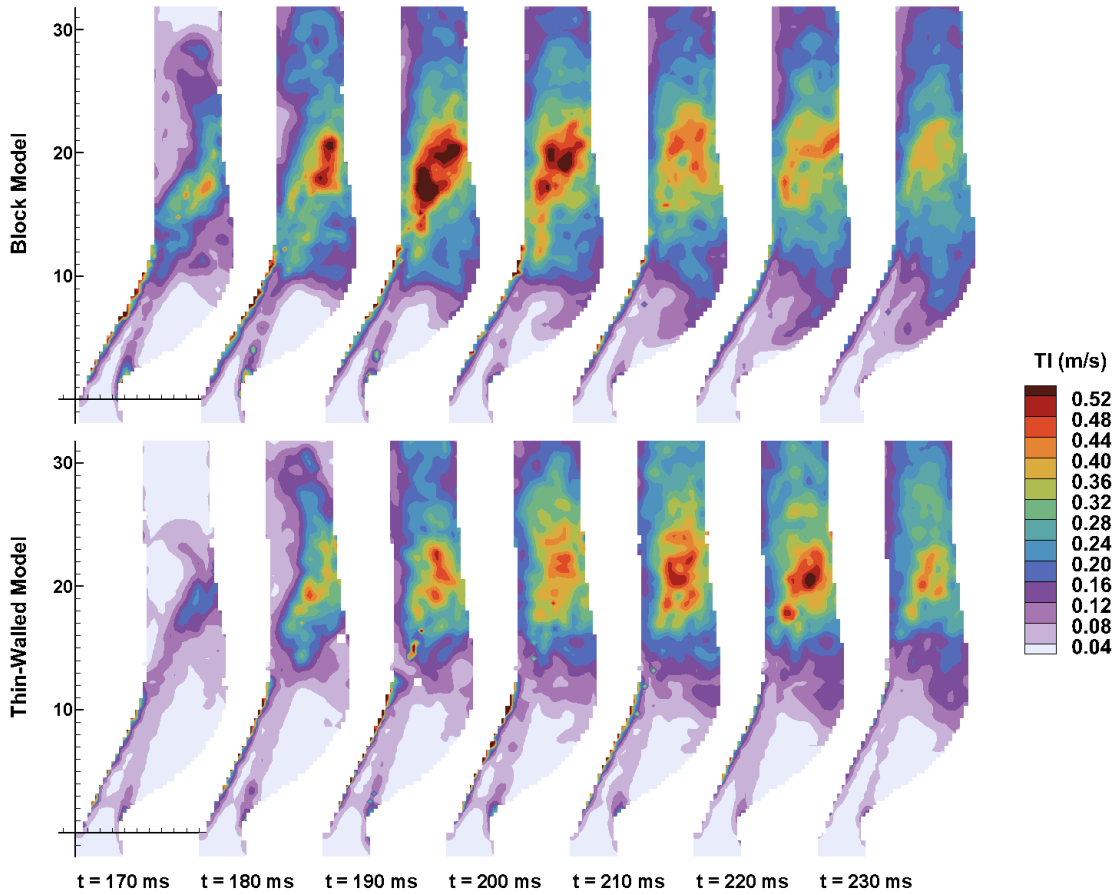


Figure 4.6: Temporal evolution of central plane turbulence intensity in the ICA branch spanning time points from before peak systole through flow deceleration, as indicated.

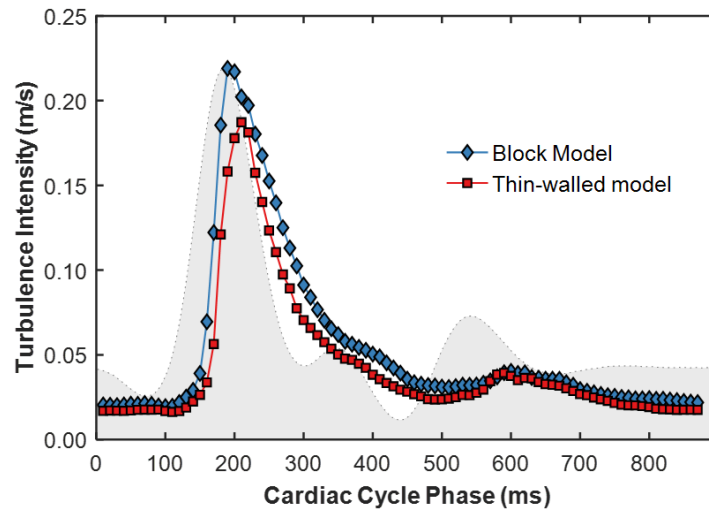


Figure 4.7: ICA-averaged turbulence intensity vs cardiac cycle phase for the block (blue, diamond) and thin-walled (red, square) phantom models, extracted from central plane TI maps. A scaled CCA inlet flow-rate waveform is shown in the background for reference.

Three-dimensional surface maps of WSS parameters are shown in Figure 4.8 for the block and thin-walled models with static CT and the thin-walled model calculated with dynamic CT wall information. In each frame the vessel is displayed in two orientations, exposing the inner and outer walls of the ICA respectively. TAWSS is shown in Figure 4.8a-c. The maximum TAWSS occurs at the stenosis throat with values of 13.3 Pa and 12.3 Pa for block and thin-walled models, respectively. Higher TAWSS was found at the ICA inner wall region for the thin-walled model compared to block model, due to prolonged higher ICA velocities following the peak pressure phase. OSI contour maps overlaid with a sparse sample of unit vectors indicating the direction of the mean WSS vector are shown in Figure 4.8d-f. Elevated OSI appears in a ring-like pattern at the boundary of recirculation regions. TransWSS contour maps are shown in Figure 4.8g-i. The highest transWSS occurs at the boundary of the large recirculation adjacent to the flow impingement site on the outer ICA wall. WSS parameters calculated using static and dynamic walls showed small differences (2.8% in TAWSS, 6.2% in OSI and 5.0% in transWSS averaged over ICA).

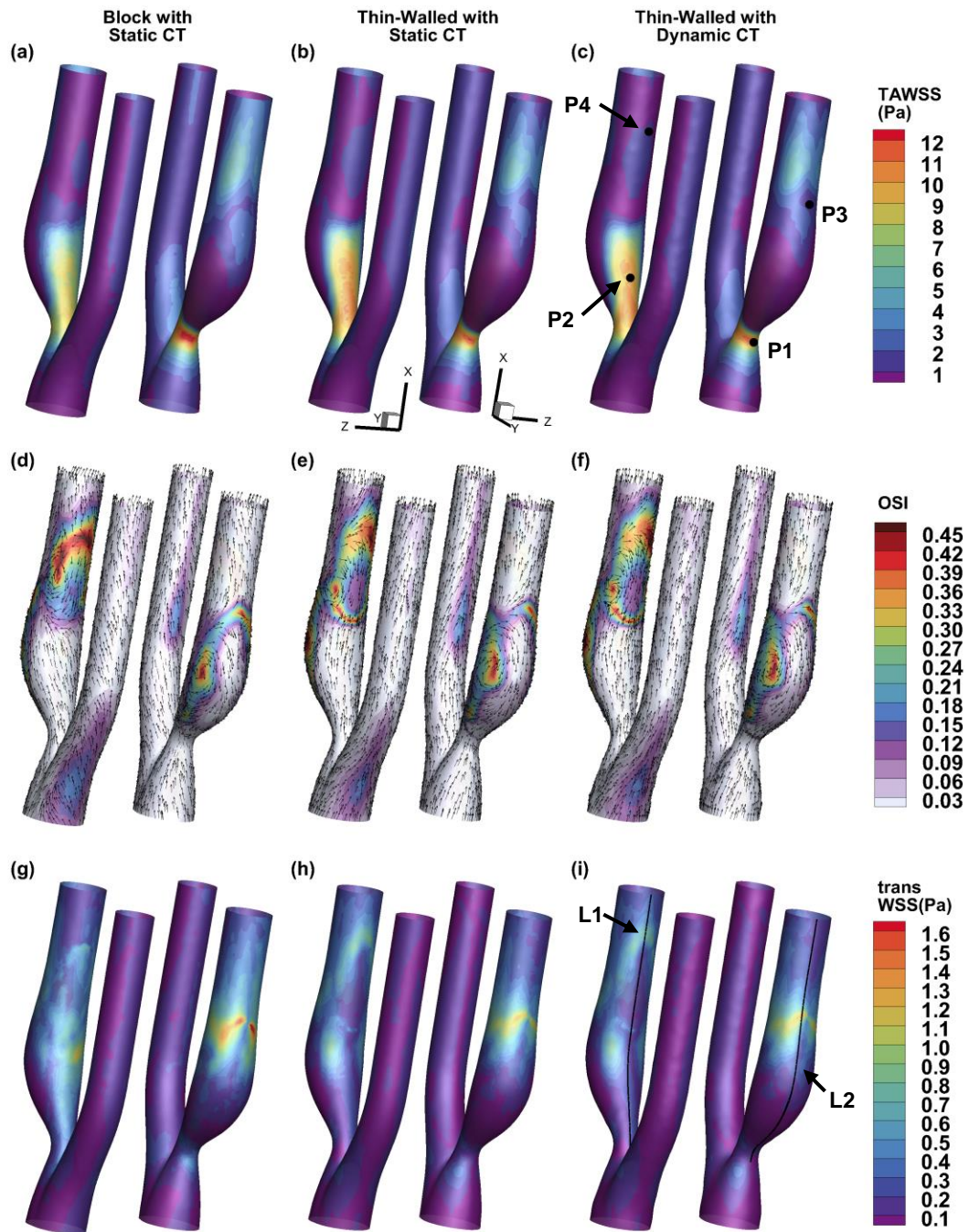


Figure 4.8: Time-averaged WSS metrics calculated for block (left) and thin-walled (middle) phantoms with static CT surfaces, and thin-walled phantom applying dynamic CT surfaces (right). Two orientations are shown in each frame, displaying the inner and outer walls of the ICA. (Top row, a-c) Contour maps of TAWSS. (middle row, d-f) Contour maps of OSI overlaid with a sparse sample of unit vectors indicating the direction of the mean WSS vector. (Bottom row, g-i) Contour maps of transWSS.

A comparison of the WSS parameters extracted along the central plane lines L1 and L2 (as indicated in Figure 4.8i) is presented in Figure 4.9. While higher TAWSS is observed for the thin-walled model compared to the block along the inner wall of the ICA, lower TAWSS is found along the outer wall recirculation region from approximately 2 mm to 20 mm. Locations of maximum OSI, highlighted by the vertical dotted lines, occur at the boundaries of recirculation zones and also tend to co-localize with reduced TAWSS. Based on the OSI peaks in Figure 4.9c-d, the inner and outer wall recirculation zones are approximately 3.3 mm and 1.2 mm longer, respectively, in the thin-walled model compared to the block (0.6 ID and 0.2 ID, expressed relative to ICA inner diameter). Locations of maximum transWSS generally co-localize with maximum OSI, as shown in Figure 4.9e-f. However, the block model exhibits a larger transWSS component in the inner wall jet region, despite the thin-walled model having higher TAWSS here. This implies small transverse oscillations of the large magnitude WSS vector in the jet region (not captured by OSI which is normalized by vector magnitude) are more prominent for the block phantom, and possibly damped by the local compliance in the thin-walled model.

Figure 4.10 shows the temporal evolution of the axial WSS component over the cardiac cycle at locations P1 to P4 (indicated in Figure 4.8c). At P1 and P2, corresponding to the outer stenosis throat and mid-jet inner wall respectively, moderate to high magnitude axial WSS component is directed forward (positive) throughout the cardiac cycle, therefore the OSI is effectively zero. The block and thin-walled WSS magnitudes at P1 agree well, with the exception of a slight phase delay in the thin-walled model during the acceleration phase and peak systole. At P2, the WSS magnitude is higher for the thin-walled model for all time points following the peak pressure until the flow acceleration phase of the next cycle begins. At P3, corresponding to the outer wall jet impingement point, the axial WSS changes direction with large forward components aligning with peaks in the inlet flow rate (block OSI = 0.35, thin-walled OSI = 0.17). This is reflective of the axial shift in the jet impingement location as the pulsatile flow-rate evolves over time. At P4, corresponding to the maximum OSI location at the ICA inner wall, the relatively low magnitude WSS changes direction in a less organized manner (block OSI = 0.47, thin-walled OSI = 0.38).

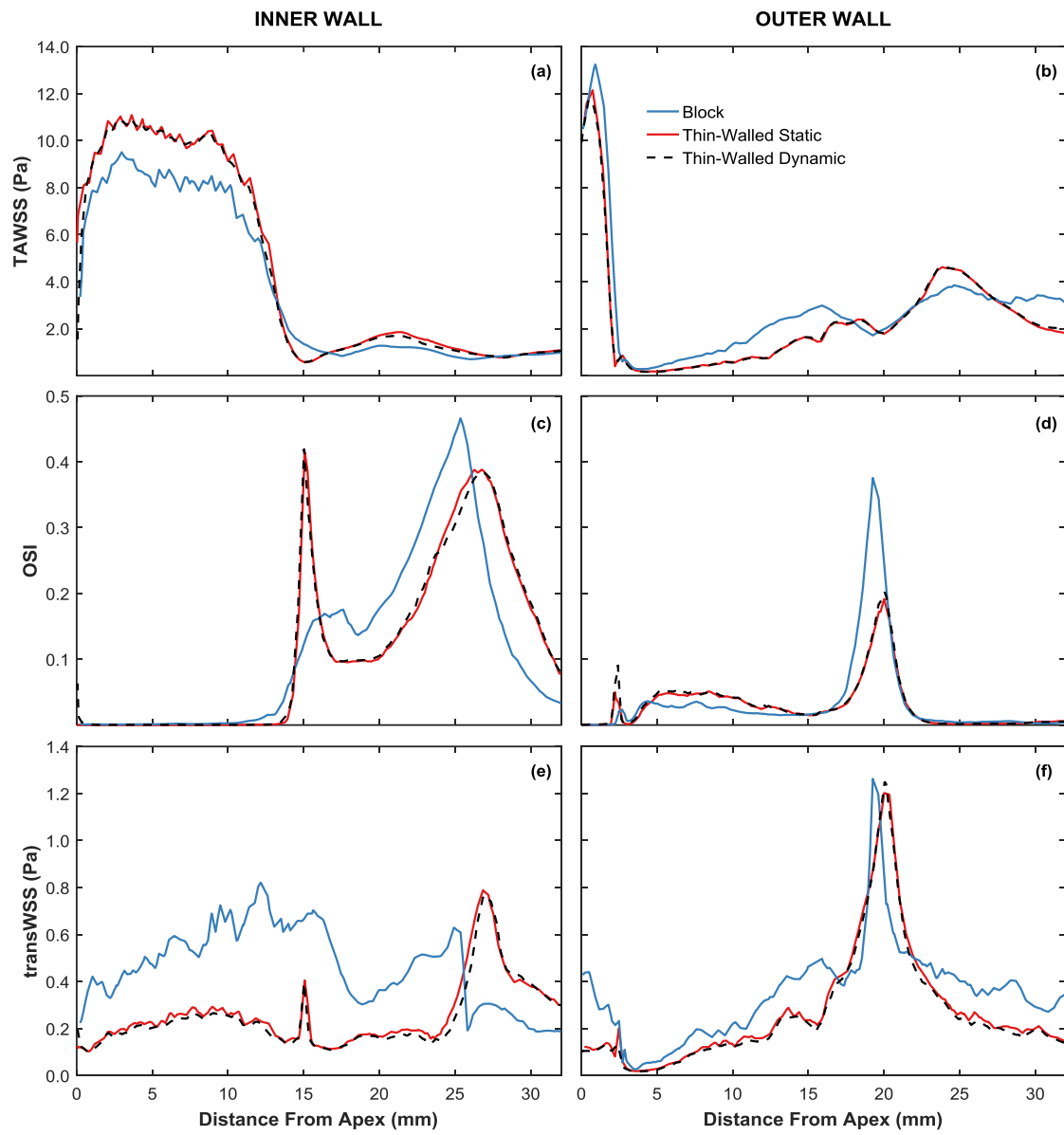


Figure 4.9: Axial profiles of TAWSS (a,b), OSI (c,d) and transWSS (e,f) magnitude extracted along the inner (left column) and outer (right column) walls of the ICA, at lines L1 and L2 indicated in Figure 4.8i.

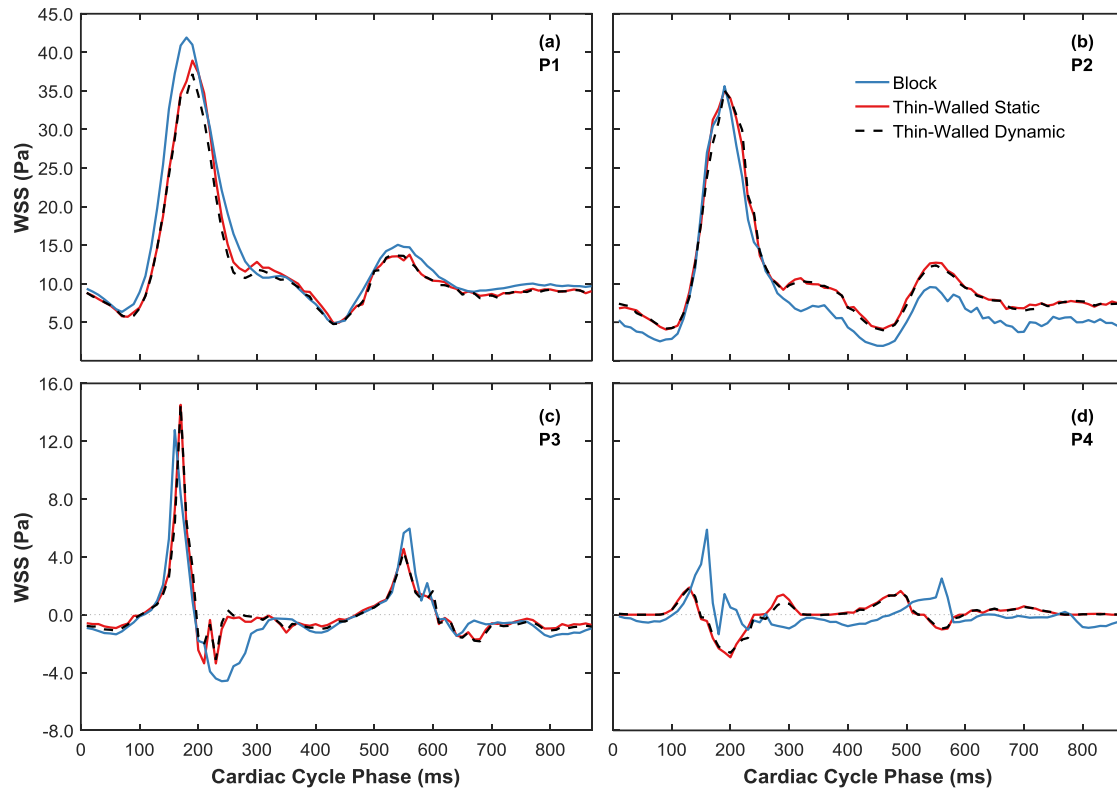


Figure 4.10: Axial-projected WSS magnitude vs cardiac cycle phase at specific points indicated by P1-P4 in Figure 4.9c. a) Outer wall stenosis throat; b) Inner wall mid-jet; c) Outer wall jet impingement; d) Inner wall high OSI region.

Figure 4.11 compares the surface area exposed to key WSS parameters, with error bars reflecting the threshold sensitivity, by indicating the normalized surface area obtained for 75th and 85th percentile thresholds (15th and 25th for TAWSS₂₀). Although TAWSS distributions are similar, TAWSS₂₀ is slightly higher for the thin-walled model compared to the block model, likely due to lower overall velocities and WSS in the primary recirculation region. OSI₈₀ is higher for the thin-walled model compared to the block model, reflective of the larger elevated OSI region at the downstream inner ICA. TransWSS exposure is higher in the block model, suggesting compliance may provide a

damping effect on transverse oscillations. Exposure to high shear stress magnitude is similar among block and thin-walled models, isolated to the jet region and mostly dependent on vessel geometry. The use of the static CT geometry, as opposed to dynamic vessel walls, leads to overestimating the overall WSS by neglecting vessel dilations. Thus, the thin-walled dynamic model predicts slightly greater TAWSS₂₀ and OSI₈₀ and slightly reduced transWSS₈₀ compared to the static model.

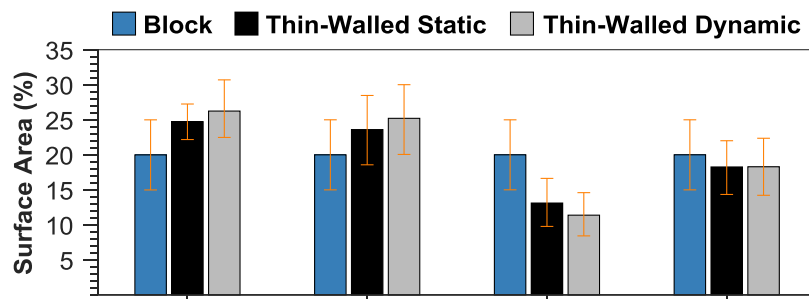


Figure 4.11: Relative ICA surface area exposure to TAWSS below the 20th percentile threshold and OSI, transWSS and TAWSS above the 80th percentile threshold. Threshold values were calculated from parameter distributions for the block phantom model. Error bars represent threshold sensitivity, indicating the area exposed for +/- 5 percentile thresholds.

4.4 Discussion

This study demonstrated that an increase in the volumetric capacity of the semi-compliant vessel upstream of the bifurcation resulted in changes to the downstream ICA hemodynamics, compared to the more stiff model. The volume uptake of the thin-walled vessel during systolic acceleration results in increased cross-sectional area and diameter, thus the thin-walled phantom saw a lower maximum velocity compared to the rigid model under identical inlet flow conditions. Geoghegan et al. [29] observed a similar effect in an experimental PIV study of straight models of the CCA. In computational studies comparing rigid and compliant healthy (non-stenosed) carotid bifurcation models, others observed reduced flow separation and recirculation and a decrease of flow velocities in the carotid

sinus [30]. This is similar to the present observation of reduced velocity magnitude in the primary recirculation at the outer ICA wall for the thin-walled compared to the block model.

Overall, wall shear stress distributions were found to depend on both location and phase, in addition to wall mechanics. An increase in WSS at the inner wall of the ICA was observed in the thin-walled model following peak pressure due to the subsequent contraction of the vessel after peak dilation resulting in higher TAWSS. Torii et al. [13] also observed that FSI predicted higher WSS after peak pressure compared to a rigid wall assumption in a stenosed right coronary artery. Overall, a larger region of low TAWSS was measured in the thin-walled model compared to the block model, which is in line with the predictions of many numerical studies in arterial geometries that predicted rigid walls to overestimate the WSS [14; 30-35]. Kim et al. [14] observed up to 10% reduction in regional TAWSS due to compliance in a femoral artery bifurcation model and Perktold and Rappitsch [30] observed up to 25% reduction in WSS magnitude due to compliance in healthy carotid bifurcation models.

Increased spatial coverage of high OSI was found for the thin-walled model compared to the block model. Several studies have demonstrated that compliance results in increased OSI [13; 14; 33; 34] Younis et al. [33] observed that the region of highly oscillatory flow in the carotid bulb observed in a rigid model separated into two regions when compliance was accounted for. This reflects an opening (increased extent) of the recirculation region with compliance, as observed here at the downstream ICA inner wall. Conversely, compliance resulted in reduced transWSS, suggesting that compliance may have a dampening effect on the transverse oscillations of high shear flow regions. No previous numerical or experimental studies have compared transWSS in matched-geometry compliant and rigid vessels.

Few studies have conducted FSI simulations in carotid bifurcation geometries and only healthy carotids have been considered [30; 33; 35; 36]. However, the present study demonstrated that the cumulative level of TI downstream of the stenosis was 21% lower in

the more distensible phantom, suggesting that bulk flow disturbances, as opposed to wall parameters, may be more dependent on vessel compliance. These types of flow disturbances only arise in more complex geometries (such as in the presence of stenosis).

Computational studies observing combinations of factors on hemodynamics have suggested that the effects of wall compliance are minor in comparison to other factors such as pulsatility [37], geometry, and rheological properties. Previous work in our models measured relative differences in cumulative TI on the order of 60% due to reduced stenosis severity (Chapter 2), 7.7% due to rheology (Chapter 2) and 21% due to reduced pulsatility (Chapter 3). In this context, the effects of compliance are not negligible when considering bulk flow disturbances.

The present study is limited by the stiffness of the thin-walled vessel, having a Peterson's modulus much larger than observed in vivo for healthy individuals. Boesen et al. [5] recently reviewed measurements of carotid artery elasticity in the literature. While a large range of elasticity was observed, the distensibility coefficient found in carotid plaque regions was as low as $8.8 \times 10^{-3} \text{ kPa}^{-1}$ [38] compared to $54.4 \times 10^{-3} \text{ kPa}^{-1}$ in the adjacent normal carotid. Recent measurements of carotid artery stiffness in young and old individuals by Rosenberg et al. [39] measured E_p values of $0.485 \times 10^5 \text{ Pa}$ and $1.11 \times 10^5 \text{ Pa}$ in the two groups, respectively. Comparisons of the phantom compliance measurements (Table 4.1) with the literature values indicates that the thin-walled phantom, at best and still with some reservation, could model a highly diseased, aged carotid artery, based on its mechanical parameters. None-the-less, the results provide a comparison of different compliances in a matched stenosed carotid bifurcation geometry, which has not previously been investigated.

A more compliant vessel may be achieved either by altering the Young's elastic modulus of the wall material or by increasing the ratio of luminal diameter to wall-thickness. Sylgard 184 is commonly used for PIV phantom fabrication due to its excellent optical properties. The elastic modulus may be tuned by altering the ratio of silicone base polymer to curing agent and was also found to be dependent on curing temperature [40; 41].

Palchesko et al. [42] demonstrated that various mixing ratios of Sylgard 184 and Sylgard 527 produced silicone substrates for cell studies with a range of elastic moduli, however the feasibility of these materials for PIV phantom fabrication has not yet been studied. In previous PIV studies, researchers were able to achieve greater compliance by scaling life-sized models, increasing the luminal diameter while keeping the wall thickness on the order of 1 mm [12; 29; 40; 41; 43]. For instance, Burgmann et al. [40] observed 0.091% distension per mmHg in a straight vessel with 24 mm diameter and 1.5 mm wall thickness (compared to 0.022%/mmHg of the thin-walled phantom here). Pielhop et al. [12] measured distensibility coefficients up to $21.92 \times 10^{-3} \text{ kPa}^{-1}$ and up to 6% vessel diameter change for straight PDMS vessel with 0.9 mm wall thickness and 24 mm diameter. Achieving a thinner wall with the lost-core casting technique and for a small vessel size is difficult due to the possibility of variance in wall thickness and propensity to vessel rupture under high shear stresses seen in the present experiment. The benefit of the current method however, is that the model is life sized and thus physiologically matched waveforms, fluid etc. may be used, eliminating need for dynamic similarity scaling.

4.5 Conclusion

We have demonstrated that increased vessel elasticity results in reduced maximum flow velocity and downstream TI. Increased surface area exposure to low TAWSS and high OSI, and reduced exposure to transWSS were also observed with an increase in vessel compliance. Tracking wall motions was shown to be negligible for the case where the wall moves a very small amount, as in the current study. It is important to note that this result does not imply that FSI should be ignored in computational studies. Differences in flow and turbulence observed between the two models implies that bulk flow features are affected by compliance and volume expansion/uptake of fluid over the length of vessel segment, including upstream of the bifurcation, not just in the flow measurement section.

4.6 References

- [1] Caro, C.G., Fitzgera.Jm, Schroter, R.C., 1971. Atheroma and arterial wall shear - observation, correlation and proposal of a shear dependent mass transfer

- mechanism for atherogenesis. *Proceedings of the Royal Society Series B-Biological Sciences* 177:109-+.
- [2] Gnasso, A., Irace, C., Carallo, C., *et al.*, 1997. In vivo association between low wall shear stress and plaque in subjects with asymmetrical carotid atherosclerosis. *Stroke* 28:993-998.
- [3] Zarins, C.K., Giddens, D.P., Bharadvaj, B.K., *et al.*, 1983. Carotid bifurcation atherosclerosis quantitative correlation of plaque localization with flow velocity profiles and wall shear-stress. *Circulation Research* 53:502-514.
- [4] Davies, P.F., 1995. Flow-mediated endothelial mechanotransduction. *Physiological Reviews* 75:519-560.
- [5] Boesen, M.E., Singh, D., Menon, B.K., *et al.*, 2015. A systematic literature review of the effect of carotid atherosclerosis on local vessel stiffness and elasticity. *Atherosclerosis* 243:211-222.
- [6] Sugioka, K., Sciacca, R.R., Hozumi, T., *et al.*, 2002. Impact of aortic stiffness on the risk of ischemic stroke in elder patients. *Journal of the American College of Cardiology* 39:196A-196A.
- [7] Cheng, K.S., Baker, C.R., Hamilton, G., *et al.*, 2002. Arterial elastic properties and cardiovascular risk/event. *European Journal of Vascular and Endovascular Surgery* 24:383-397.
- [8] Hoi, Y., Wasserman, B.A., Xie, Y.Y.J., *et al.*, 2010. Characterization of volumetric flow rate waveforms at the carotid bifurcations of older adults. *Physiological Measurement* 31:291-302.
- [9] Hirata, K., Yaginuma, T., O'Rourke, M.F., *et al.*, 2006. Age-related changes in carotid artery flow and pressure pulses - possible implications for cerebral microvascular disease. *Stroke* 37:2552-2556.
- [10] Onaizah, O., Poepping, T.L., Zamir, M., 2017. A model of blood supply to the brain via the carotid arteries: Effects of obstructive vs. Sclerotic changes. *Medical Engineering & Physics* 49:121-130.
- [11] Geoghegan, P.H., Buchmann, N.A., Soria, J., *et al.*, 2013. Time-resolved piv measurements of the flow field in a stenosed, compliant arterial model. *Experiments in Fluids* 54:19.
- [12] Pielhop, K., Klaas, M., Schroder, W., 2015. Experimental analysis of the fluid-structure interaction in finite-length straight elastic vessels. *European Journal of Mechanics B-Fluids* 50:71-88.

- [13] Torii, R., Wood, N.B., Hadjiloizou, N., *et al.*, 2009. Fluid-structure interaction analysis of a patient-specific right coronary artery with physiological velocity and pressure waveforms. *Communications in Numerical Methods in Engineering* 25:565-580.
- [14] Kim, Y.H., Kim, J.E., Ito, Y., *et al.*, 2008. Hemodynamic analysis of a compliant femoral artery bifurcation model using a fluid structure interaction framework. *Annals of Biomedical Engineering* 36:1753-1763.
- [15] Smith, R.F., Rutt, B.K., Holdsworth, D.W., 1999. Anthropomorphic carotid bifurcation phantom for mri applications. *Jmri-Journal of Magnetic Resonance Imaging* 10:533-544.
- [16] Poepping, T.L., Nikolov, H.N., Thorne, M.L., *et al.*, 2004. A thin-walled carotid vessel phantom for doppler ultrasound flow studies. *Ultrasound in Medicine and Biology* 30:1067-1078.
- [17] Smith, R.F., Rutt, B.K., Fox, A.J., *et al.*, 1996. Geometric characterization of stenosed human carotid arteries. *Academic Radiology* 3:898-911.
- [18] Holdsworth, D.W., Norley, C.J.D., Frayne, R., *et al.*, 1999. Characterization of common carotid artery blood-flow waveforms in normal human subjects. *Physiological Measurement* 20:219-240.
- [19] Kefayati, S., Poepping, T.L., 2013. Transitional flow analysis in the carotid artery bifurcation by proper orthogonal decomposition and particle image velocimetry. *Medical Engineering & Physics* 35:898-909.
- [20] Kefayati, S., Holdsworth, D.W., Poepping, T.L., 2014. Turbulence intensity measurements using particle image velocimetry in diseased carotid artery models: Effect of stenosis severity, plaque eccentricity, and ulceration. *Journal of Biomechanics* 47:253-263.
- [21] Kefayati, S., Milner, J.S., Holdsworth, D.W., *et al.*, 2014. In vitro shear stress measurements using particle image velocimetry in a family of carotid artery models: Effect of stenosis severity, plaque eccentricity, and ulceration. *Plos One* 9:19.
- [22] Poepping, T.L., Nikolov, H.N., Rankin, R.N., *et al.*, 2002. An in vitro system for doppler ultrasound flow studies in the stenosed carotid artery bifurcation. *Ultrasound in Medicine and Biology* 28:495-506.
- [23] Yousif, M.Y., Holdsworth, D.W., Poepping, T.L., 2011. A blood-mimicking fluid for particle image velocimetry with silicone vascular models. *Experiments in Fluids* 50:769-774.

- [24] Armitage, S.E.J., Pollmann, S.I., Detombe, S.A., *et al.*, 2012. Least-error projection sorting to optimize retrospectively gated cardiac micro-ct of free-breathing mice. *Medical Physics* 39:1452-1461.
- [25] Drangova, M., Ford, N.L., Detombe, S.A., *et al.*, 2007. Fast retrospectively gated quantitative four-dimensional (4d) cardiac micro computed tomography imaging of free-breathing mice. *Investigative Radiology* 42:85-94.
- [26] Antiga, L., Piccinelli, M., Botti, L., *et al.*, 2008. An image-based modeling framework for patient-specific computational hemodynamics. *Medical & Biological Engineering & Computing* 46:1097-1112.
- [27] Reynolds, W.C., Hussain, A.K.M., 1972. Mechanics of an organized wave in turbulent shear-flow .3. Theoretical models and comparisons with experiments. *Journal of Fluid Mechanics* 54:263-&.
- [28] Lee, S.W., Antiga, L., Spence, J.D., *et al.*, 2008. Geometry of the carotid bifurcation predicts its exposure to disturbed flow. *Stroke* 39:2341-2347.
- [29] Geoghegan, P.H., Jermy, M.C., Nobes, D.S., 2017. A piv comparison of the flow field and wall shear stress in rigid and compliant models of healthy carotid arteries. *Journal of Mechanics in Medicine and Biology* 17:16.
- [30] Perktold, K., Rappitsch, G., 1995. Computer-simulation of local blood-flow and vessel mechanics in a compliant carotid-artery bifurcation model. *Journal of Biomechanics* 28:845-856.
- [31] Brown, A.G., Shi, Y.B., Marzo, A., *et al.*, 2012. Accuracy vs. Computational time: Translating aortic simulations to the clinic. *Journal of Biomechanics* 45:516-523.
- [32] Swillens, A., Degroote, J., Vierendeels, J., *et al.*, 2010. A simulation environment for validating ultrasonic blood flow and vessel wall imaging based on fluid-structure interaction simulations: Ultrasonic assessment of arterial distension and wall shear rate. *Medical Physics* 37:4318-4330.
- [33] Younis, H.F., Kaazempur-Mofrad, M.R., Chan, R.C., *et al.*, 2004. Hemodynamics and wall mechanics in human carotid bifurcation and its consequences for atherogenesis: Investigation of inter-individual variation. *Biomechanics and Modeling in Mechanobiology* 3:17-32.
- [34] Kabinejadian, F., Ghista, D.N., 2012. Compliant model of a coupled sequential coronary arterial bypass graft: Effects of vessel wall elasticity and non-newtonian rheology on blood flow regime and hemodynamic parameters distribution. *Medical Engineering & Physics* 34:860-872.

- [35] Karner, G., Perktold, K., Hofer, M., *et al.*, 1999. Flow characteristics in an anatomically realistic compliant carotid artery bifurcation model. *Comput Methods Biomech Biomed Engin* 2:171-185.
- [36] Vavourakis, V., Papaharilaou, Y., Ekaterinaris, J.A., 2011. Coupled fluid-structure interaction hemodynamics in a zero-pressure state corrected arterial geometry. *Journal of Biomechanics* 44:2453-2460.
- [37] Thon, M.P., Hemmler, A., Glinzer, A., *et al.*, 2018. A multiphysics approach for modeling early atherosclerosis. *Biomechanics and Modeling in Mechanobiology* 17:617-644.
- [38] Sadat, U., Usman, A., Howarth, S.P.S., *et al.*, 2014. Carotid artery stiffness in patients with symptomatic carotid artery disease with contralateral asymptomatic carotid artery disease and in patients with bilateral asymptomatic carotid artery disease: A cine phase-contrast carotid mr study. *Journal of Stroke & Cerebrovascular Diseases* 23:743-748.
- [39] Rosenberg, A.J., Lane-Cordova, A.D., Wee, S.O., *et al.*, 2018. Healthy aging and carotid performance: Strain measures and beta-stiffness index. *Hypertension Research* 41:748-755.
- [40] Burgmann, S., Grosse, S., Schroder, W., *et al.*, 2009. A refractive index-matched facility for fluid-structure interaction studies of pulsatile and oscillating flow in elastic vessels of adjustable compliance. *Experiments in Fluids* 47:865-881.
- [41] Geoghegan, P.H., Buchmann, N.A., Spence, C.J.T., *et al.*, 2012. Fabrication of rigid and flexible refractive-index-matched flow phantoms for flow visualisation and optical flow measurements. *Experiments in Fluids* 52:1331-1347.
- [42] Palchesko, R.N., Zhang, L., Sun, Y., *et al.*, 2012. Development of polydimethylsiloxane substrates with tunable elastic modulus to study cell mechanobiology in muscle and nerve. *Plos One* 7:13.
- [43] Pielhop, K., Klaas, M., Schroder, W., 2012. Analysis of the unsteady flow in an elastic stenotic vessel. *European Journal of Mechanics B-Fluids* 35:102-110.

Chapter 5

5 Summary and Future Work

5.1 Research Summary and Conclusions

5.1.1 Summary of Chapter 2

Chapter 2 described an in-vitro PIV study examining the combined impact of progression of stenosis severity and non-Newtonian rheology on disturbed flow and WSS in the carotid bifurcation. This was accomplished by using two different blood-mimicking fluids demonstrating Newtonian and shear-thinning non-Newtonian behaviours and a set of idealized carotid bifurcation models with eccentric stenosis of the internal carotid artery of 30, 50 and 70%. A comparison of the phase averaged velocity maps revealed that comparable maximum velocities were reached for N-fluid and nN-fluid, however blunting of velocity profiles resulted in higher velocity gradients at the wall for nN-fluid compared to N-fluid. The turbulence intensity metric was applied as a measure of bulk flow disturbances downstream of the stenosis. The cumulative level of TI averaged spatially over a selected downstream region of interest and temporally over the cardiac cycle demonstrated that disturbed flow is reduced in the case of nN-fluid. Steeper velocity gradients, as well as shear-thickening effect at low shear rates, contributed to higher WSS magnitude (including time-averaged WSS) in nN-fluid models. Three dimensional OSI patterns elucidated flow features resulting in increased variation in WSS: flow impingement, merging of counter-directed near wall flow, and wall-adjacent vortices. Comparing the OSI distributions across all models revealed that the overall level and spatial coverage of OSI is reduced with nN-fluid models. The transverse WSS parameter is another possible marker of WSS variation. Highest levels of transWSS were concentrated around the jet impingement location, and transWSS increased with both increased stenosis and nN-fluid models. TransWSS normalized by TAWSS and OSI patterns were shown to be qualitatively similar, indicating that a component of transWSS scales with the overall magnitude of WSS. Overall, the effects of non-Newtonian fluid are interrelated with the degree of stenosis severity, with differences in exposure to shear

parameters between fluid models exacerbated with higher stenosis severity compared to low-moderate constrictions. Therefore, studies of healthy or mildly stenosed geometries finding negligible differences between viscosity models may provide incomplete information regarding fluid model assumptions. In addition, a detailed analysis of the velocity and WSS uncertainties was conducted for the intermediate stenosis case (50%) and Newtonian blood analogue fluid. This work is under final review for publication in *Medical Engineering and Physics*.

5.1.2 Summary of Chapter 3

In Chapter 3, the flow and WSS measurement technique used in Chapter 2 was applied to investigate the effects of waveform pulsatility, accomplished by studying three inlet flow waveforms with varying level of pulsatility index. Volumetric PIV data were acquired for a 50% stenosed model, with additional central plane acquisition only collected for 30% and 70% models, using the conventional Newtonian blood analogue fluid. Waveform pulsatility directly contributes to elevated oscillatory shear stress due to the fluctuation of the jet impingement site with changing inlet velocity and subsequent expansion and contraction of the recirculation zones. For higher flow rates, the jet impingement was pulled more proximally, leading to decreased mean recirculation zone size with increasing waveform PI (and constant mean flow rate). The location of maximum TI, corresponding to the region of flow separation, also shifted more proximal with increasing pulsatility. A linear relationship was observed between peak ICA-averaged TI and the peak velocity measured through the narrowest part of the ICA stenosis. It was also observed that, in terms of turbulence intensity as a measure of disturbed flow and potential indicator of risk, the level was dependent on not only the degree of stenosis but also on the PI, or possibly just the amplitude of the inlet waveform, identifying a potential confounding factor which should be considered in clinical risk assessment. The stenosis peak velocity (Reynolds number) may be a more appropriate variable than PI for comparing flow variations across different geometries/subjects, since it accounts for both the degree of restriction and the amplitude of the flow waveform. Differences in TI with PI were less pronounced for 70% stenosis, similar to less pronounced effects of non-Newtonian viscosity also seen in 70%

stenosed models. TAWSS distributions were similar for the three waveform cases, reflective of the matched mean inlet flow rate. Surface area exposure to low shear, however, increased with decreasing PI, due to an enlarged primary recirculation region leading to more low velocities at the outer wall. The OSI surface exposure and the peak TI scaled similarly with PI and peak stenosis velocity, suggesting that TI may be an appropriate bulk flow surrogate indicator for OSI or WSS variation. Further co-localization studies with additional variables will be necessary to confirm this result. This work is in preparation for submission to the *Journal of Biomechanics*.

5.1.3 Summary of Chapter 4

In Chapter 4, the effect of local compliance on hemodynamics was investigated by incorporating a thin-walled carotid artery phantom with a 50% eccentric stenosis of the ICA and comparing to the matched geometry with effectively rigid walls, already studied in Chapters 2 and 3. The study was limited to the Newtonian blood-mimicking fluid and high PI waveform. The Peterson's elastic modulus of the block model, evaluated from computed tomography scans of the phantoms under static pressure, was an order of magnitude higher (stiffer) than the thin-walled model. Differences in flow and WSS patterns downstream of the stenosis between the block and thin-walled model could be attributed to the increased volumetric capacity of the compliant CCA upstream. Post-peak pressure, the thin-walled model exhibited higher velocities and inner wall WSS compared to the block model downstream of the stenosis, despite reaching similar values during flow acceleration, albeit a slightly reduced peak velocity. The upstream compliance of the vessel resulted in dampening of the flow pulsatility transferred to the downstream ICA. Peak ICA-averaged turbulence was reduced for the thin-walled model compared to the block model. Surface area exposure to low TAWSS and high OSI were both increased for the thin-walled model, however, the level of exposure to transWSS was reduced. A dynamic CT protocol was used to track the vessel wall position of the thin-walled model over the cardiac cycle, providing a novel technique for assessing the effect of wall location variation on WSS metrics. The analysis revealed that for small changes in wall position over the cardiac cycle, an average or representative surface could be used to calculate the WSS from measured

velocity data. Comparing to the results obtained in Chapter 2 and 3 (See section 5.1.4), Chapter 4 concluded that in the presence of a stenosis, the effects of local compliance are not negligible, resulting in deflection of high velocity jet, and altering recirculation lengths and thus differences to both TI and OSI distributions. This work is in preparation for submission to the *Journal of Biomechanics*.

5.1.4 Quantitative Comparison of Results

To compare the relative impact of model parameters – geometry, rheology, flow pulsatility, and local compliance – on the resulting hemodynamics, this section presents a comprehensive summary of flow and WSS metrics measured in Chapters 2, 3 and 4. The model with 50% stenosed geometry, block phantom construction, Newtonian blood analogue fluid and highly pulsatile inlet waveform was chosen as the reference case, as in previous chapters. The varying flow set-up components for the remaining models are summarized in Table 5.1a the values of flow and WSS parameters are compared in Table 5.1b, and the relative percent difference with respect to the reference case is presented in Table 5.1c.

Several of the hemodynamic parameters, such as maximum WSS, maximum TAWSS and maximum and mean ICA-averaged TI scale with the peak velocity. In most of these cases, the dominant factor is the geometry, contributing differences on the order of 100% when increasing from moderate to severe stenosis. The area exposed to low WSS, reflected by the TAWSS₂₀ parameter, was increased by a reduction in stenosis severity (less lumen narrowing), decrease in pulsatility and increase in elasticity. Interestingly, TAWSS₂₀ was comparable between moderately and severely stenosed models. All models experienced the full range of OSI values (maximum OSI of 0.485-0.495), thus OSI level alone is not necessarily a good comparative risk parameter. The relative differences in parameters of OSI₈₀ and ICA-averaged OSI due to viscosity, waveform amplitude and compliance are of the same order or greater than those observed due to stenosis severity. The relative differences in transWSS₈₀ are large (>50%) for all models except with the thin-walled phantom construction, however, the relative differences in normalized transWSS are

comparable to differences in OSI. Interestingly, the differences observed in WSS metrics from incorporating non-Newtonian fluid seem to be countered by opposite effects due to compliance. However, both non-Newtonian fluid and compliance result in a decrease to turbulence intensity.

Both elevated turbulence intensity and increased WSS are associated with increased risk of thrombosis and elevated risk of stroke in vivo. While the degree of stenosis has a dominant effect on both the peak and cumulative turbulence intensity, comparable differences in TI were also observed due to reduced PI, as demonstrated in Table 5.1. Thus, the degree of vessel narrowing alone may not be sufficient to stratify risk, as the peak TI reached is also dependent on the peak inlet flow rate and resulting Reynolds' number. Overlap in the measured peak TI for different degrees of stenosis was demonstrated in Chapter 3 based on the amplitude of the flow waveform: a 50% stenosed model with highly pulsatile waveform exhibited similar turbulence intensities to a more severe 70% stenosis with a reduced flow pulsatility, at the same mean inlet flow rate. Similar results were observed between mild and moderate stenosis.

Present work demonstrated that flow and WSS parameters in the studied eccentric models depend largely on the jet pattern, and the motion of the jet over the cardiac cycle due to pulsatility. Increased flow velocities through the stenosis contributed to the location of the jet impingement site, which was found to shift upstream at higher flow rates. Shifting of the jet with pulsatility contributed to elevated OSI at approximate impingement locations. An elevated peak velocity also resulted in a proximally shifted region of elevated TI. While low shear area decreases when increasing from mild to moderate/severe stenosis, the presence of highly activated platelets in the latter cases may result in very concentrated deposition of material at the smaller atheroprone sites. Future work should incorporate particle tracking (versus particle imaging) to investigate the shear histories of particles that become trapped in recirculation regions where both velocities and wall shear stress are low potentially promoting aggregation and adhesion of formed thrombi.

Table 5.1: Overall comparison of hemodynamics parameters across all models. a) Overview of flow components applied for each model. b) Absolute values of hemodynamic parameters. c) Percent difference in hemodynamic parameters relative to the reference model.

(a) Flow Components	Reference		Geometry		Rheology		Pulsatility		Compliance	
	50% Ecc	Block	30% Ecc	70% Ecc	50% Ecc	Block	50% Ecc	Block	50% Ecc	Block
Phantom Geometry	50% Ecc	Block	30% Ecc	70% Ecc	50% Ecc	Block	50% Ecc	Block	50% Ecc	Block
Phantom Construction	High PI	N-fluid	High PI	N-fluid	High PI	nN-fluid	High PI	nN-fluid	High PI	nN-fluid
Flow Waveform	High PI	N-fluid	High PI	N-fluid	High PI	nN-fluid	High PI	nN-fluid	High PI	nN-fluid
Blood Analogue Fluid	High PI	N-fluid	High PI	N-fluid	High PI	nN-fluid	High PI	nN-fluid	High PI	nN-fluid
(b) Parameter Values	Reference	30% Ecc	70% Ecc	70% Ecc	nN-fluid	nN-fluid	Med PI	Low PI	Low PI	Thin-Walled
Stenosis Cross-Section Area (mm ²)	6.58	13.05	2.43	2.43	6.58	6.58	6.58	6.58	6.58	6.47
Stenosis Effective Diameter (mm)	2.90	4.08	1.76	1.76	2.90	2.90	2.90	2.90	2.90	2.87
Peak Stenosis Reynolds Number	1616	1291	1784	1784	1606	1317	1006	1006	1006	1540
Mean Stenosis Reynolds Number	541	423	734	734	526	540	564	564	564	544
Peak Stenosis Velocity (m/s)	1.93	1.10	3.52	3.52	1.91	1.58	1.20	1.20	1.20	1.81
Maximum ICA-averaged TI (m/s)	0.219	0.119	0.366	0.366	0.198	0.159	0.109	0.109	0.109	0.187
Mean ICA-averaged TI (m/s)	0.0545	0.0292	0.120	0.120	0.0504	0.0439	0.0400	0.0400	0.0400	0.0439
Maximum WSS (Pa)	41.9	20.7	88.2	88.2	45.9	33.3	25.9	25.9	25.9	41.5
Maximum TAWSS (Pa)	13.2	5.03	31.7	31.7	13.8	12.3	12.5	12.5	12.5	12.3
ICA-averaged TAWSS (Pa)	2.43	1.30	4.18	4.18	2.84	2.12	2.41	2.41	2.41	2.28
ICA-averaged OSI	0.0865	0.0879	0.0976	0.0976	0.0770	0.0838	0.0636	0.0636	0.0636	0.0949
ICA-averaged transWSS (Pa)	0.346	0.215	0.527	0.527	0.446	0.230	0.215	0.215	0.215	0.277
TA WSS ₈₀	20*	3.32	29.06	29.06	18.85	16.56	20.30	20.30	20.30	17.55
TA WSS ₂₀	20*	30.24	19.52	19.52	14.18	31.73	32.26	32.26	32.26	25.70
OSI ₈₀	20*	21.13	23.36	23.36	15.95	18.40	13.33	13.33	13.33	23.65
transWSS ₈₀	20*	6.15	36.72	36.72	31.32	5.81	5.65	5.65	5.65	12.78
Normalized transWSS ₈₀	20*	21.28	24.83	24.83	18.27	18.69	17.81	17.81	17.81	23.09

*Threshold values are calculated from the reference model.

Table 5.1: Continued

(c) Percent Relative Differences	30% Ecc	70% Ecc	nN-fluid	Med PI	Low PI	Thin-Walled
Peak Stenosis Velocity	-43	82	-1.2	-19	-38	-6.2
Maximum ICA-averaged TI	-45	67	-10	-28	-50	-15
Mean ICA-averaged TI	-46	120	-7.4	-19	-27	-19
Maximum WSS	-51	111	9.6	-21	-38	-0.9
Maximum TAWSS	-62	140	4.5	-7.2	-5.0	-6.9
ICA-averaged TAWSS	-46	72	17	-12	-0.7	-6.1
ICA-averaged OSI	1.5	13	-11	-3.1	-26	9.7
ICA-averaged transWSS	-38	52	29	-33	-38	-20
TAWSS ₈₀	-83	45	-5.8	-17	1.5	-12
TAWSS ₂₀	51	-2.3	-29	59	61	29
OSI ₈₀	5.7	17	-20	-8.0	-33	18
transWSS ₈₀	-69	84	57	-71	-72	-36
Normalized transWSS ₈₀	6.4	24	-8.7	-6.5	-11	15

It is important to note that the model parameters, considered independently in the present in-vitro study, are highly interrelated with one another in vivo. For instance, an increase in stenosis severity due to development of plaque often leads to a focal reduction in elasticity. The local and systemic compliance in-vivo impacts the impedance resulting in changes to waveform shape and, as previously demonstrated, changes in pulsatility can be highly significant. The present results suggest that the combined effect of viscosity, pulsatility, and compliance, if studied in combination, could exceed that due to geometry changes alone. Future studies should examine possible compound effects of studying the effects of multiple parameters at once.

Waveform effects are often thought to play a secondary role to geometrical accuracy when it comes to numerical modeling, followed by compliance and non-Newtonian rheology which are often considered to have comparably negligible effects. The impact of geometry in the form of stenosis severity was the dominant determinant of velocity and WSS magnitude here. However, the present work suggests that for parameters associated with atherosclerosis progression (low TAWSS, high OSI, high transWSS) and risk of thrombosis (TI), the effect of geometry is not clearly dominant. The impact of Newtonian viscosity assumptions, waveform shape and vessel elasticity could still incur measurable errors in the predictions of disturbed flow metrics and thus subsequent risk predictions.

5.2 Future Directions

5.2.1 Further PIV Studies

5.2.1.1 Healthy and concentric plaque geometries

The work presented in Chapters 2-4 focused on more common eccentric (asymmetric) plaque geometries, shown in previous studies to pose greater risk based on elevated levels of WSS and elevated TI compared to models with symmetric plaque geometry [1; 2]. However, those studies only observed WSS magnitude and not directional changes, therefore OSI and transWSS were not investigated.

Concentric stenosed model flow patterns are characterized by helical swirling motion and counter-rotating dean vortices in the ICA downstream of the stenosis [3]. The opposing flow patterns at the vessel inner wall where vortices from either side meet at the plane of symmetry would produce increased levels of OSI at these locations, based on the results presented in this thesis. A much larger extent of reversed flow at the inner wall is also observed. Conversely, the outer wall recirculation region for concentric stenosed models is much smaller than for the eccentric counterpart, therefore we would expect a significant decrease in the size of the outer wall OSI region. In addition, the helical flow patterns produced in concentric models might contribute to elevated transWSS compared to the eccentrically stenosed models studied here.

In healthy, non-stenosed carotid artery models, the flow patterns are quite different than observed in stenosed models, due to overall lower velocities and the absence of a high velocity jet. The highest WSS values are found at the flow divider wall in both the ICA and ECA. A large recirculation is typically found at the outer wall expansion region corresponding to the carotid bulb, resulting in low shear stress and high OSI, confirmed by previous experimental and numerical models [2; 4-6]. In a numerical study of healthy carotid bifurcation geometries, Gallo et al. [4] found that elevated transWSS was mostly concentrated to the region surrounding the bifurcation apex, at the flow divider wall. Incorporating a healthy geometry in the current dataset would provide insight into the differing hemodynamics related to the pathology of atherogenesis (initiation of plaque development) versus the progression of plaque and risk of thrombosis in stenosed models.

Flow phantoms could also be extended to include patient-specific geometries including tortuosity, surface roughness, and ulcerations as opposed to the idealized smooth surface geometries observed here. A much more complex pattern of recirculation regions and vorticity may be observed in rough, highly diseased, patient-specific geometries [7; 8], thus more regions of elevated OSI and TI might be expected. Moreover, Lee et al. [9] observed that vessel tortuosity was negatively correlated with flow disturbances in normal vessel models, measured as surface area exposure to low shear magnitude and high OSI.

Finally, the methodology applied here for carotid bifurcation models could readily be applied for studying other large arteries with important clinical implications (e.g. aneurysms).

5.2.1.2 Additional waveform features and cardiac variability

The work in Chapter 3 showed that both TI and OSI were correlated with the peak velocity through the stenosis which scales with the PI of the waveform. However, the three inlet flow waveform shapes studied were adjusted to have the same mean flow rate. Additional waveforms would need to be studied to separate the effect of flow pulsatility from that due to the maximum or mean flow rate. Increased exposure to OSI is directly related to pulsatile flow which causes variation in flow impingement site and recirculation size over the cardiac cycle, however its relationship to peak flow rate alone is unclear. TI, on the other hand, is known to depend mostly upon Reynolds number. Previous PIV studies of transition to turbulence in pipe flow demonstrated that the onset of transition is dependent on the flow acceleration rate and the duration of the deceleration phase of the pulsatile flow cycle [10], although differences in cumulative TI (over space and time) were negligible for differing waveform shapes and depended solely on mean Reynolds number.

Variability in flow and WSS in-vivo can be attributed to either pulsatility of the waveform, inherent velocity fluctuations (turbulence), or cycle-to-cycle variability due to variations in cardiac output. In order to further strengthen the clinical implications of the present results, an extension would be to investigate the effect of cardiac variability on flow disturbances. Given the dependence of OSI distribution on the high velocity jet and recirculation size, it is expected that small changes in peak and minimum flow rate from cycle-to-cycle variability would result in increased exposure to WSS directional oscillations over many cycles. To observe changes in OSI due to cardiac variability, WSS would need to be measured individually for each cardiac cycle, as opposed to being derived from phase-averaged velocity data as in the work presented. This requires instantaneous volumetric acquisition, not possible with stereoscopic PIV, which requires the stacking of separately acquired slices of data. Other PIV setups (for instance additional cameras

enabling 3D tomographic reconstruction) could enable instantaneous volumetric acquisition for the application of cardiac variability studies.

5.2.1.3 Vorticity and helical flow

In the present work, both vorticity and helical flow metrics have not been calculated. Previous in-vitro studies in the same geometries observed here demonstrated, via the swirl-strength metric, the shedding of counter-rotating vortices from the interface between the high velocity jet region and the adjacent recirculation zones, beginning during flow acceleration and continuing into the deceleration phase [2]. Those studies were confined to rigid models of varying stenosis severity, and the effect of fluid viscosity, compliance, or pulsatility on vorticity or swirl strength has not yet been observed. Helicity, describing flow with a corkscrew like pattern, is calculated as the product of the velocity and vorticity fields, and may have an atheroprotective effect in large arteries. Several in-vitro and in-silico models have observed various metrics of helicity and found that swirling flow resulted in reduced platelet adhesion to the vessel wall [11], reduced recirculation lengths and flow stagnation, overall increase in WSS magnitude, decrease in area exposed to low shear magnitude and reduction in OSI [12-17]. Given the relationship between helical flow and suppression of flow disturbances, it would be interesting to quantify helical flow metrics under the varying flow conditions observed in this work.

5.2.1.4 Co-localization of hemodynamic parameters

Several parameters have been suggested in-vitro and in silico for analyzing WSS variations. The work in this thesis only focuses on the TAWSS, OSI and transWSS in terms of WSS parameters, in addition to TI for studying bulk flow disturbances. Additional metrics include temporal and spatial gradient based metrics [18], axial and circumferential decomposition of the WSS vector [13; 18], as well as frequency-based indicators [19], and turbulent WSS formulations [20]. However, many redundancies exist between the different WSS metrics. Co-localization studies attempt to reveal correlations between WSS metrics either by comparing the spatial distributions of metrics over model surfaces, or by comparing risk stratification by global risk indicators (for instance, OSI_{80} or $TAWSS_{20}$).

Co-localization studies are also useful in determining correlations between difficult to measure parameters known to influence disease progression (ie. OSI) and surrogate measures more easily quantified in vivo, such as helical flow [17]. In computational studies of the healthy carotid bifurcation, TAWSS was found to be inversely correlated with OSI, with both low shear magnitude and high OSI concentrated to the carotid bulb region [4; 9]. Gallo et al. [4] observed that transWSS did not correlate with other metrics of disturbed flow in healthy carotid bifurcations and was instead concentrated at the flow divider, a region typically spared of plaques. Interestingly, Andersson et al. [20] observed that turbulent kinetic energy was not correlated with the conventional OSI metric but that TI was weakly correlated with the normalized transWSS and contributions to WSS from turbulent velocity fluctuations.

The dataset presented in Chapters 2-4 would be ideally suited for investigating the co-localization of various wall and bulk flow metrics, as it incorporates different modeling conditions which are not included in CFD co-localization studies performed under rigid wall and Newtonian fluid assumptions.

5.2.2 Microfluidics and “Lab-on-a-chip” studies

As discussed in Chapter 1, the process of atherosclerosis development begins at the cellular level. The mechanisms by which hemodynamic stimuli influence endothelial cell (EC) mechanotransduction, and hence the relative importance of the various multidirectional shear metrics (such as conventional OSI versus multidirectional metrics like transWSS) are a growing topic of research. In vitro cell studies within microfluidic devices (MFDs) are well-suited for studying adaptive changes in EC signaling when exposed to precisely controlled and monitored shear stress environments. The advantages of microfluidic systems for vascular cell studies over macroscopic methods (for instance cone-and-plate viscometers or parallel-plate devices) include reduced consumption of reagents and materials and throughput enhancement, allowing the ability to generate a large dynamic range of shear rates in small diameters at relatively low flow rates in a single device by varying inlet conditions [21].

Future work will focus on studying early endothelial cell signaling processes in response to different forms of flow-induced shear stress variations using a microfluidic shear-stimulation platform. By implementing carefully chosen device designs and varying flow inputs, a range of steady and transient flows can be generated encompassing both axial and transverse shear stress fluctuations. Flow conditions within the MFD can be accurately quantified *a priori* using numerical simulations and in vitro using the gold-standard micro-particle image velocimetry from which 2D reference maps of flow metrics can be derived for comparison during real time monitoring of cellular responses. Live cell microscopy applied to MFDs seeded with human aortic endothelial cells under flow stimuli will be used to measure elevations in various molecules involved in EC sensing and signaling in response to shear stress, as well as cytoskeletal remodeling. The real-time observation of EC responses (seconds to minutes) to multidirectional flow and shear stress disturbances on the microscopic level will help to elucidate the physiological implications of disturbed flow metrics, guiding the focus of future macroscopic hemodynamic studies.

5.3 References

- [1] Kefayati, S., Holdsworth, D.W., Poepping, T.L., 2014. Turbulence intensity measurements using particle image velocimetry in diseased carotid artery models: Effect of stenosis severity, plaque eccentricity, and ulceration. *Journal of Biomechanics* 47:253-263.
- [2] Kefayati, S., Milner, J.S., Holdsworth, D.W., *et al.*, 2014. In vitro shear stress measurements using particle image velocimetry in a family of carotid artery models: Effect of stenosis severity, plaque eccentricity, and ulceration. *Plos One* 9:19.
- [3] Kefayati, S., Poepping, T.L., 2013. Transitional flow analysis in the carotid artery bifurcation by proper orthogonal decomposition and particle image velocimetry. *Medical Engineering & Physics* 35:898-909.
- [4] Gallo, D., Steinman, D.A., Morbiducci, U., 2016. Insights into the co-localization of magnitude-based versus direction-based indicators of disturbed shear at the carotid bifurcation. *Journal of Biomechanics* 49:2413-2419.
- [5] Steinman, D.A., 2002. Image-based computational fluid dynamics modeling in realistic arterial geometries. *Annals of Biomedical Engineering* 30:483-497.

- [6] Lee, S.W., Antiga, L., Steinman, D.A., 2009. Correlations among indicators of disturbed flow at the normal carotid bifurcation. *Journal of Biomechanical Engineering-Transactions of the Asme* 131:7.
- [7] Stroud, J.S., Berger, S.A., Saloner, D., 2002. Numerical analysis of flow through a severely stenotic carotid artery bifurcation. *Journal of Biomechanical Engineering-Transactions of the Asme* 124:9-20.
- [8] Bale-Glickman, J., Selby, K., Saloner, D., *et al.*, 2003. Experimental flow studies in exact-replica phantoms of atherosclerotic carotid bifurcations under steady input conditions. *Journal of Biomechanical Engineering-Transactions of the Asme* 125:38-48.
- [9] Lee, S.W., Antiga, L., Spence, J.D., *et al.*, 2008. Geometry of the carotid bifurcation predicts its exposure to disturbed flow. *Stroke* 39:2341-2347.
- [10] Brindise, M.C., Vlachos, P.P., 2018. Pulsatile pipe flow transition: Flow waveform effects. *Physics of Fluids* 30:13.
- [11] Zhan, F., Fan, Y.B., Deng, X.Y., 2010. Swirling flow created in a glass tube suppressed platelet adhesion to the surface of the tube: Its implication in the design of small-caliber arterial grafts. *Thrombosis Research* 125:413-418.
- [12] Morbiducci, U., Ponzini, R., Grigioni, M., *et al.*, 2007. Helical flow as fluid dynamic signature for atherogenesis risk in aortocoronary bypass. A numeric study. *Journal of Biomechanics* 40:519-534.
- [13] Morbiducci, U., Gallo, D., Cristofanelli, S., *et al.*, 2015. A rational approach to defining principal axes of multidirectional wall shear stress in realistic vascular geometries, with application to the study of the influence of helical flow on wall shear stress directionality in aorta. *Journal of Biomechanics* 48:899-906.
- [14] Liu, X., Sun, A.Q., Fan, Y.B., *et al.*, 2015. Physiological significance of helical flow in the arterial system and its potential clinical applications. *Annals of Biomedical Engineering* 43:3-15.
- [15] Chen, Z.S., Fan, Y.B., Deng, X.Y., *et al.*, 2009. Swirling flow can suppress flow disturbances in endovascular stents: A numerical study. *Asaio Journal* 55:543-549.
- [16] Ha, H., Kim, G.B., Kweon, J., *et al.*, 2016. Hemodynamic measurement using four-dimensional phase-contrast mri: Quantification of hemodynamic parameters and clinical applications. *Korean Journal of Radiology* 17:445-462.
- [17] Gallo, D., Steinman, D.A., Bijari, P.B., *et al.*, 2012. Helical flow in carotid bifurcation as surrogate marker of exposure to disturbed shear. *Journal of Biomechanics* 45:2398-2404.

- [18] Arzani, A., Shadden, S.C., 2016. Characterizations and correlations of wall shear stress in aneurysmal flow. *Journal of Biomechanical Engineering-Transactions of the Asme* 138:10.
- [19] Himburg, H.A., Friedman, M.H., 2006. Correspondence of low mean shear and high harmonic content in the porcine iliac arteries. *Journal of Biomechanical Engineering-Transactions of the Asme* 128:852-856.
- [20] Andersson, M., Lantz, J., Ebbers, T., *et al.*, 2017. Multidirectional wss disturbances in stenotic turbulent flows: A pre- and post-intervention study in an aortic coarctation. *Journal of Biomechanics* 51:8-16.
- [21] Wong, K.H.K., Chan, J.M., Kamm, R.D., *et al.*, 2012. Microfluidic models of vascular functions. *Annual Review of Biomedical Engineering* 14:205-230.

Appendix A

Supplementary Figures to Chapter 2

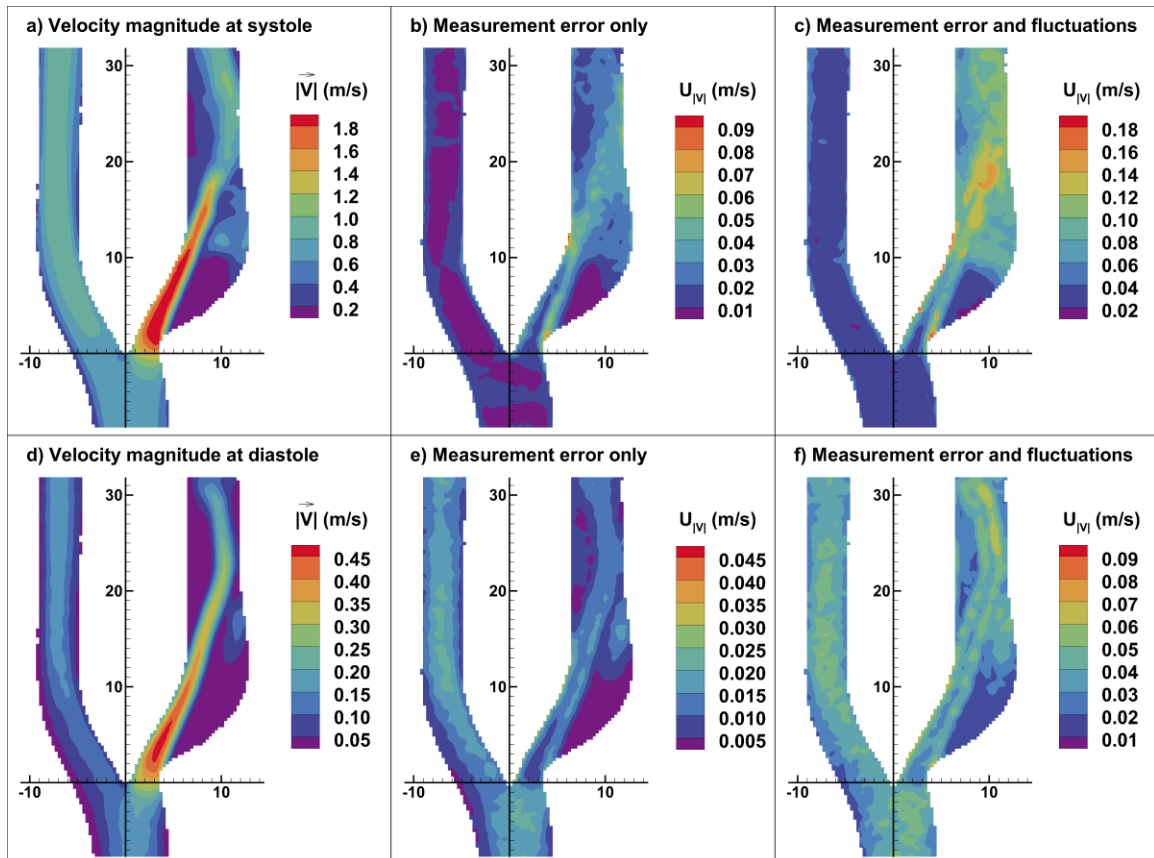


Figure A.1: Central-plane instantaneous ensemble-averaged velocity maps for the 50% eccentric geometry (a, d) followed by corresponding maps of uncertainty in the velocity propagated from measurement errors only (b, e) and uncertainty propagated from combined measurement errors and flow fluctuations (c, f). The time point of peak systole is shown in the top row (a-c) and diastole in the bottom row (d-f).

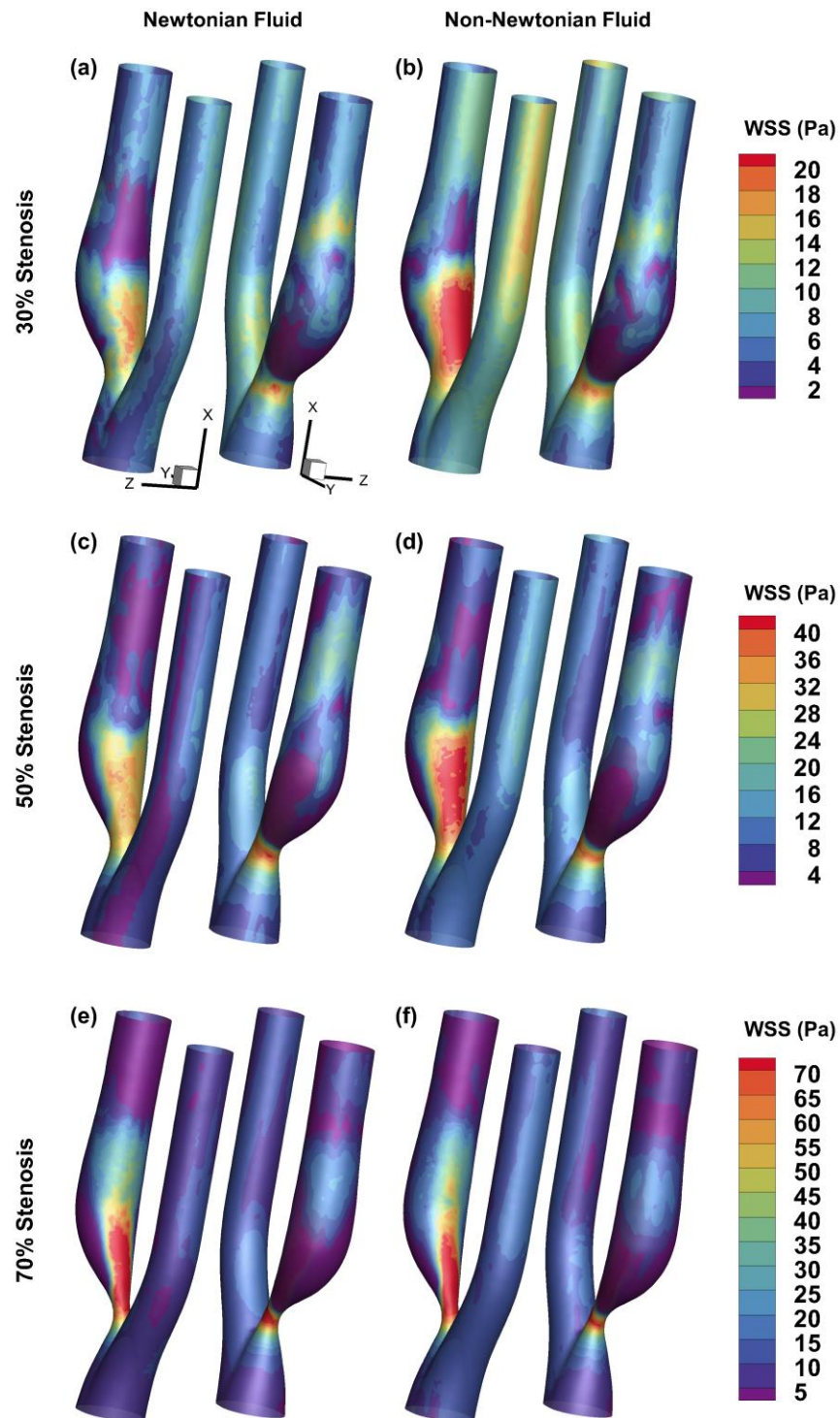


Figure A.2: Contours of instantaneous WSS at peak systole. Each model is shown in two orientations, exposing the inner and outer walls of the ICA on the left and right, respectively. Note that each row of models has an individual color bar.

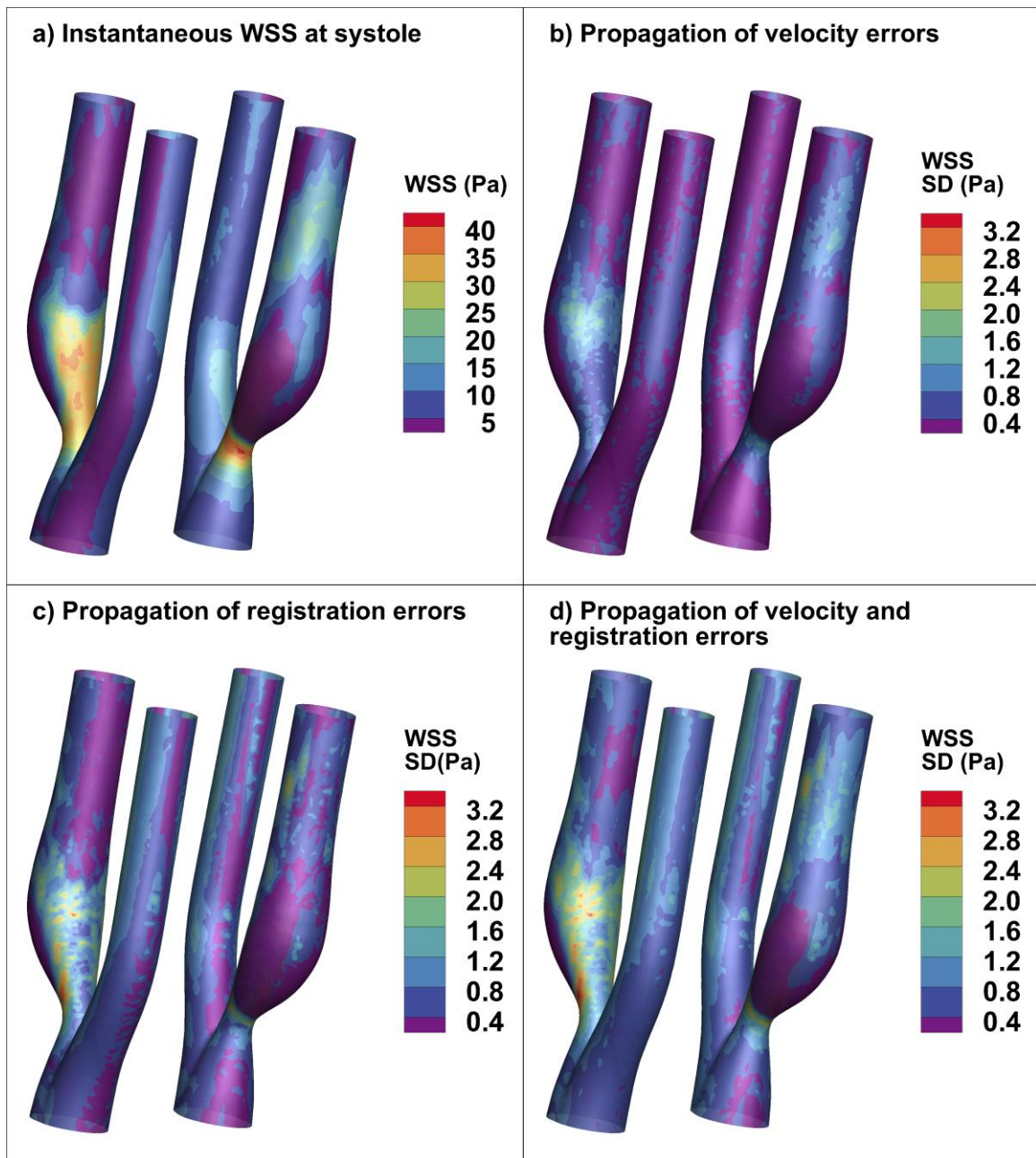


Figure A.3: Contours of instantaneous WSS magnitude at peak systole for the 50% eccentric geometry along with corresponding maps of WSS uncertainty estimated from simulations.

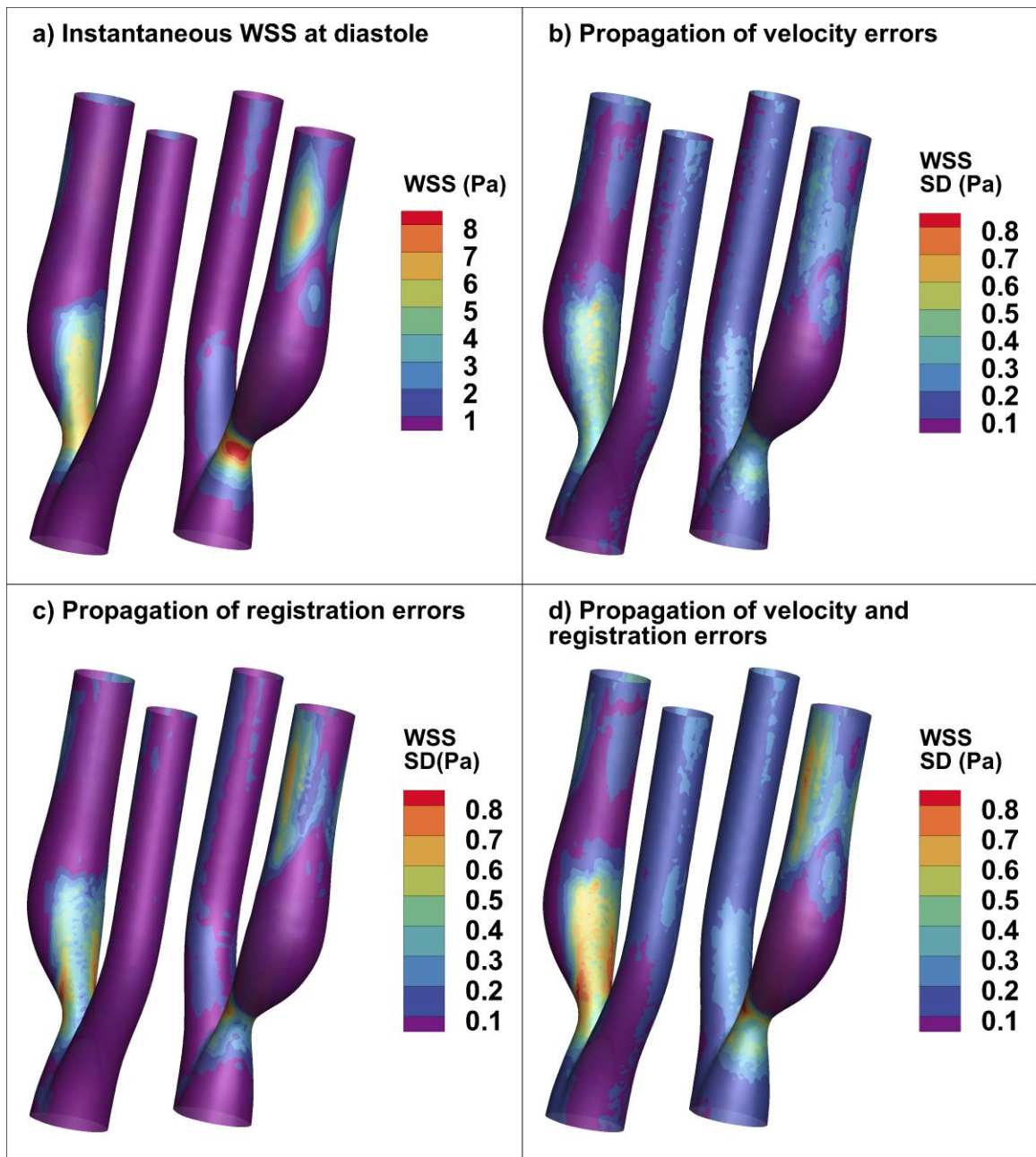


Figure A.4: Contours of instantaneous WSS magnitude at diastole for the 50% eccentric geometry along with corresponding maps of WSS uncertainty estimated from simulations.

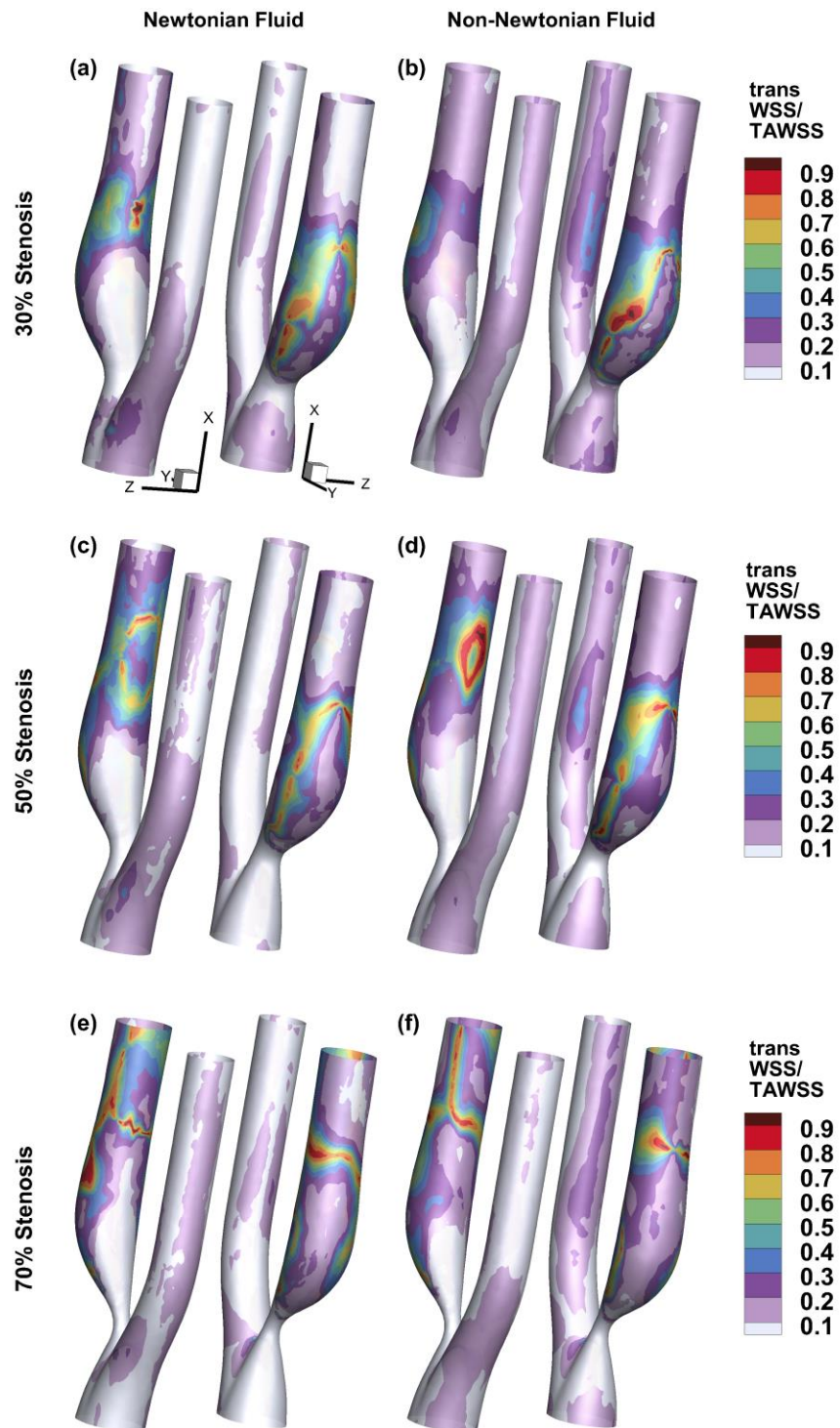


Figure A.5: Contours of transWSS normalized by the site-specific TAWSS. Each model is shown in two orientations, exposing the inner and outer walls of the ICA on the left and right, respectively.

Appendix B

Supplementary Data to Chapter 3

30% stenosed model

Table B.1: Waveform properties for the 30% stenosed model. The pulsatility and resistive index were calculated from both flow and velocity waveforms, indicated by Q and U respectively. Reynolds numbers (Re) were calculated from velocity at the narrowest stenosis diameter.

Waveform Model	High PI		Intermediate PI		Low PI	
Peak Flow Rate (mL/s)						
CCA	23.3 ± 0.01		18.1 ± 0.1		13.01 ± 0.09	
ICA	12.2 ± 0.02		9.6 ± 0.1		6.89 ± 0.09	
ECA	10.05 ± 0.09		7.66 ± 0.06		5.03 ± 0.06	
Mean Flow Rate (mL/s)						
CCA	5.83 ± 0.04		6.01 ± 0.03		6.05 ± 0.03	
ICA	3.89 ± 0.01		3.91 ± 0.01		3.91 ± 0.01	
ECA	2.10 ± 0.01		2.029 ± 0.009		2.13 ± 0.01	
Peak Velocity (m/s)						
CCA (at S1)	0.664 ± 0.006		0.517 ± 0.006		0.377 ± 0.003	
ICA (at S3)	1.02 ± 0.05		0.72 ± 0.06		0.43 ± 0.02	
ECA (at S4)	0.92 ± 0.01		0.694 ± 0.007		0.494 ± 0.004	
Mean Velocity (m/s)						
CCA (at S1)	0.245 ± 0.001		0.2364 ± 0.0004		0.2347 ± 0.0003	
ICA (at S3)	0.253 ± 0.003		0.242 ± 0.002		0.230 ± 0.001	
ECA (at S4)	0.232 ± 0.001		0.2367 ± 0.0006		0.2349 ± 0.0004	
Peak Re (at S2)	1291		991		708	
Mean Re (at S2)	423		401		400	
Pulsatility Index						
	Q	U	Q	U	Q	U
CCA	3.92	2.25	2.58	1.64	1.72	1.06
ICA	2.69	3.68	1.93	2.37	1.26	1.29
ECA	4.83	3.89	3.45	2.45	2.03	1.63
Resistive Index						
CCA	0.98	0.83	0.85	0.75	0.80	0.66
ICA	0.86	0.91	0.79	0.80	0.71	0.69
ECA	1.01	0.97	0.91	0.84	0.86	0.78

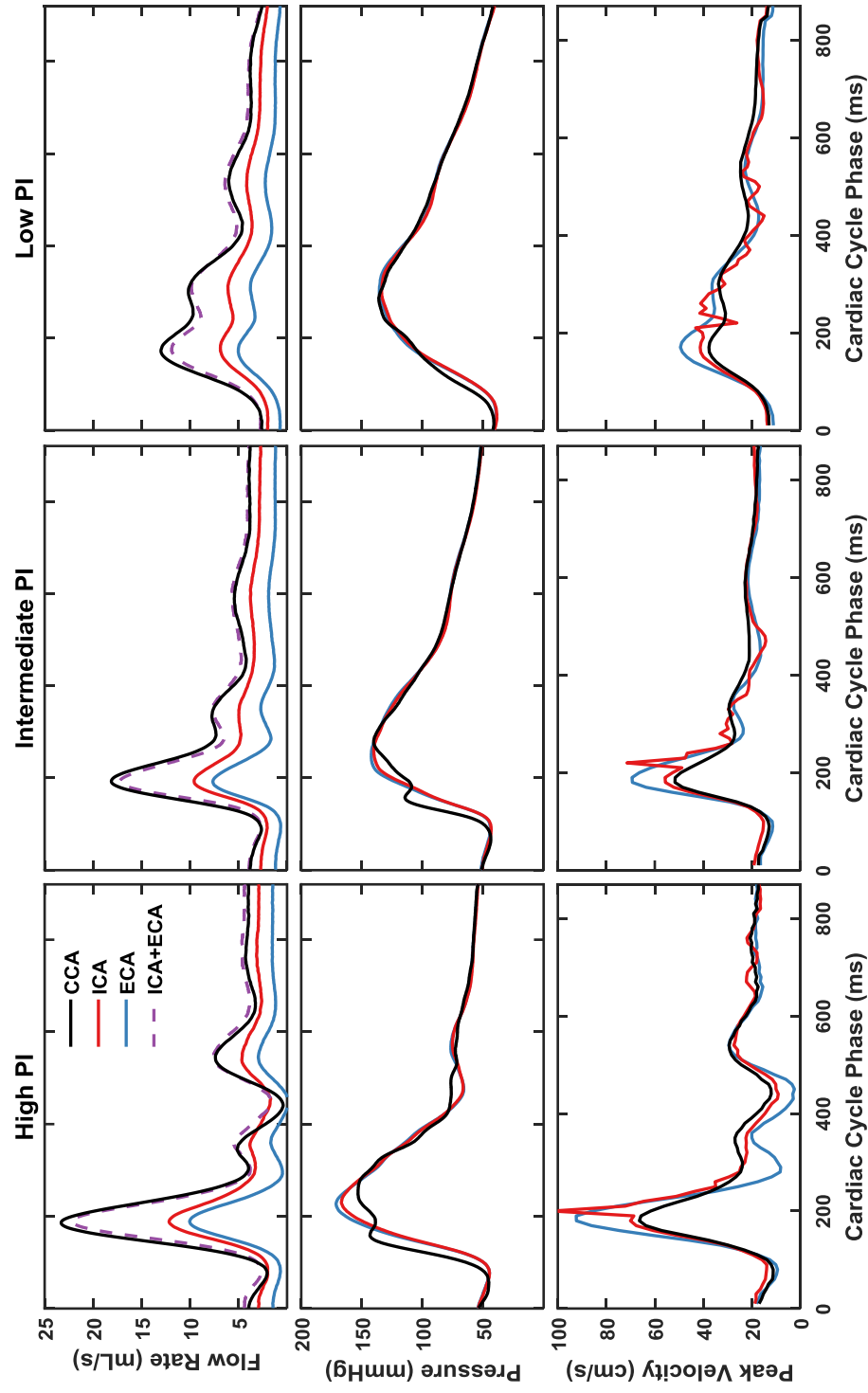


Figure B.1: Volumetric flow, pressure, and velocity waveforms for the three cases of high, intermediate, and low pulsatility index (PI) for the 30% stenosed model. Flow and pressure waveforms were measured via electromagnetic flowmeters and pressure transducer at the inlets and outlets of the phantom at locations. Velocity waveforms were extracted from PIV data at sections S1, S3 and S4 shown in Figure 3.1a for the CCA, ICA, and ECA respectively.

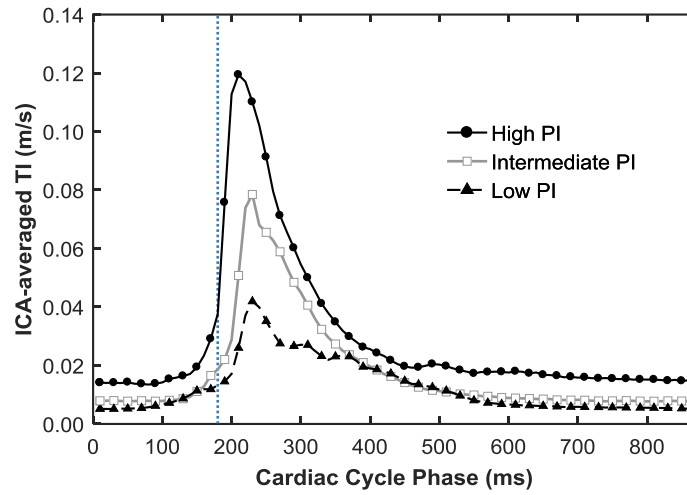


Figure B.2: ICA-averaged TI versus cardiac cycle phase for the three inlet waveforms applied in the 30% stenosed model, calculated from central-plane TI maps. The dotted blue line indicates the time of peak systole, for phase reference.

70% stenosed model

Table B.2: Waveform properties for the 70% stenosed model. The pulsatility and resistive index were calculated from both flow and velocity waveforms, indicated by Q and U respectively. Reynolds numbers (Re) were calculated from velocity at the narrowest stenosis diameter.

Waveform Model	High PI		Intermediate PI		Low PI	
Peak Flow Rate (mL/s)						
CCA	24.0 ± 0.3		17.6 ± 0.1		12.8 ± 0.1	
ICA	10.0 ± 0.4		7.3 ± 0.2		5.8 ± 0.2	
ECA	12.76 ± 0.09		9.37 ± 0.08		5.82 ± 0.06	
Mean Flow Rate (mL/s)						
CCA	6.16 ± 0.03		6.02 ± 0.02		6.01 ± 0.02	
ICA	4.99 ± 0.02		3.95 ± 0.03		3.77 ± 0.01	
ECA	2.24 ± 0.03		2.123 ± 0.006		2.37 ± 0.01	
Peak Velocity (m/s)						
CCA (at S1)	0.720 ± 0.007		0.559 ± 0.007		0.405 ± 0.007	
ICA (at S3)	0.7 ± 0.1		0.6 ± 0.2		0.6 ± 0.1	
ECA (at S4)	1.11 ± 0.03		0.79 ± 0.01		0.54 ± 0.01	
Mean Velocity (m/s)						
CCA (at S1)	0.248 ± 0.001		0.248 ± 0.001		0.251 ± 0.001	
ICA (at S3)	0.33 ± 0.01		0.32 ± 0.01		0.34 ± 0.01	
ECA (at S4)	0.231 ± 0.002		0.220 ± 0.002		0.238 ± 0.002	
Peak Re (at S2)	1784		1466		1128	
Mean Re (at S2)	734		720		719	
Pulsatility Index						
	Q	U	Q	U	Q	U
CCA	3.85	2.49	2.46	1.76	1.70	1.10
ICA	1.40	1.74	1.27	1.38	0.97	1.11
ECA	6.14	4.75	4.11	3.32	2.11	1.92
Resistive Index						
CCA	0.99	0.86	0.84	0.78	0.80	0.68
ICA	0.69	0.81	0.68	0.71	0.63	0.64
ECA	1.08	0.99	0.93	0.92	0.86	0.85

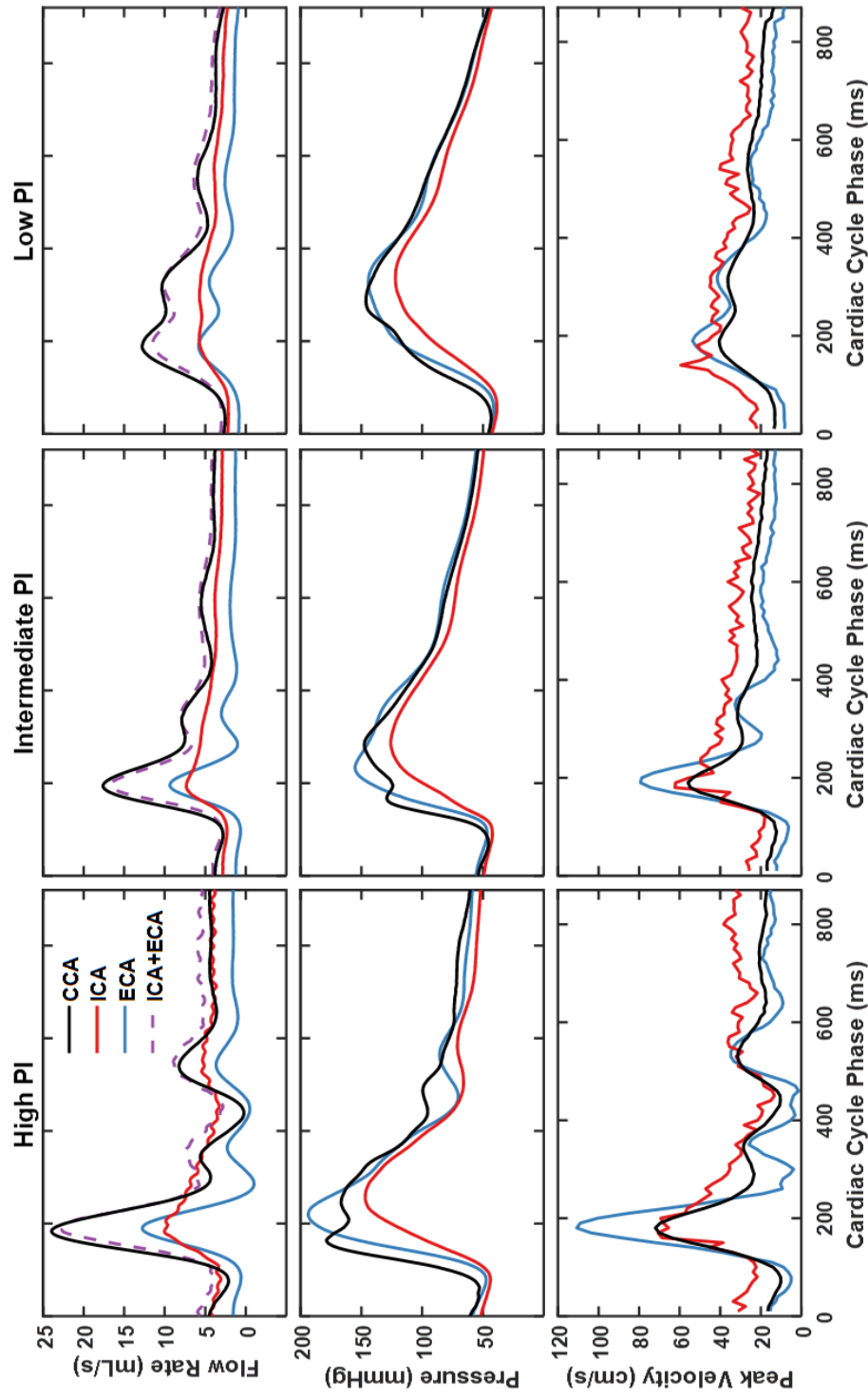


Figure B.3: Volumetric flow, pressure, and velocity waveforms for the three cases of high, intermediate, and low pulsatility index (PI) for the 70% stenosed model. Flow and pressure waveforms were measured via electromagnetic flowmeters and pressure transducer at the inlets and outlets of the phantom at locations. Velocity waveforms were extracted from PIV data at sections S1, S3 and S4 shown in Figure 3.1a for the CCA, ICA, and ECA respectively.

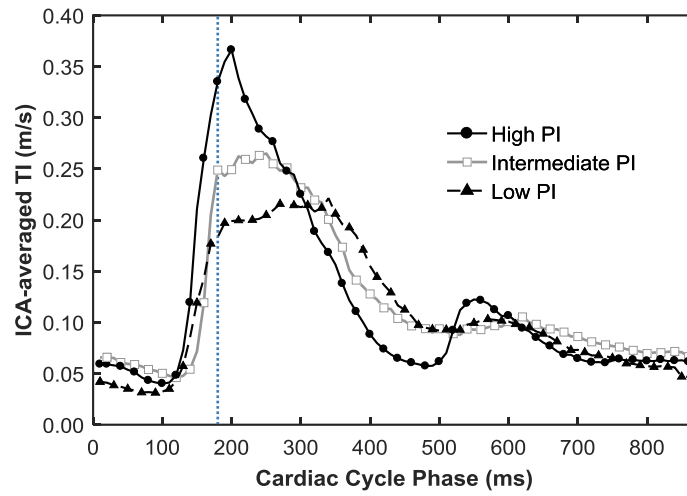


Figure B.4: ICA-averaged TI versus cardiac cycle phase for the three inlet waveforms applied in the 70% stenosed model, calculated from central-plane TI maps. The dotted blue line indicates the time of peak systole, for phase reference.

Curriculum Vitae

AMANDA L. DiCARLO

EDUCATION

- 2011 – 2018 Doctor of Philosophy, Physics
University of Western Ontario, London, Ontario
Department of Physics and Astronomy
- 2007 - 2011 Bachelor of Science, Physics
University of Windsor, Windsor, Ontario
Department of Physics
President's Honour Roll, Dean's List

RESEARCH & TEACHING EXPERIENCE

- 2011 – 2018 Research Assistant
University of Western Ontario, London, ON
Department of Physics and Astronomy
Supervisor Dr. T. L. Poepping
- 2011 – 2017 Teaching Assistant
University of Western Ontario, London, ON
Department of Physics and Astronomy
- 2008 – 2011 Research Assistant
University of Windsor, Windsor, ON
Department of Physics
Supervisor: Dr. J.W. McConkey
- 2008 Research Assistant
University of Windsor, Windsor, ON
Department of Physics
Supervisor: Dr. Roman Maev

AWARDS AND DISTINCTIONS

- 2015 – 2016 Ontario Graduate Scholarship
University of Western Ontario
- 2014 – 2015 Ontario Graduate Scholarship
University of Western Ontario

2012 – 2013	CIHR Master's Award: Frederick Banting and Charles Best Canada Graduate Scholarship University of Western Ontario
2011 – 2013	CIHR Vascular Training Program Fellowship University of Western Ontario
2011 – 2012	Ontario Graduate Scholarship University of Western Ontario
2011	NSERC Undergraduate Student Research Award University of Windsor
2007 – 2010	Outstanding Scholar's Award University of Windsor
2007 – 2010	Dean's Entrance Scholarship University of Windsor
2007 – 2010	Queen Elizabeth II Aiming for the Top Scholarship University of Windsor
2009	NSERC Undergraduate Student Research Award University of Windsor

PUBLICATIONS

Peer-reviewed Journal Articles

DiCarlo A, Holdsworth DW, and Poepping TL *Study of the effect of stenosis severity and non-Newtonian viscosity on multidirectional wall shear stress and flow disturbances in the carotid artery using particle image velocimetry*. 2018. Manuscript submitted for publication.

Kedzierski W, Blejdea E, **DiCarlo A**, and McConkey JW *Electron impact dissociation of N_2O and CO_2 with single particle detection of $O(^1D_2)$* . Chemical Physics Letters. 498(1-3):38-41, 2010.

Kedzierski W, Blejdea E, **DiCarlo A**, and McConkey JW *Metastable oxygen atom detection using rare gas matrices*. Journal of Physics B-Atomic Molecular and Optical Physics. 43(8):085204, 2010.

Refereed Conference Proceedings

DiCarlo A, and Poepping TL *Investigation of flow and turbulence in carotid artery models of varying compliance using particle image velocimetry*. World Congress on Medical Physics and Biomedical Engineering, Toronto, Canada. Springer International Publishing, 51:1743-1746, 2015.

Conference Presentations and Abstracts

DiCarlo A, and Poepping TL *Analysis of flow and oscillating wall shear stress in the carotid bifurcation using particle image velocimetry: Effects of stenosis severity and waveform pulsatility*. 16th Annual Meeting of the Imaging Network of Ontario, Toronto, Canada, Mar. 28-29, 2016.

DiCarlo A, and Poepping TL *In vitro study of the effects of vessel stiffening on carotid artery hemodynamics using particle image velocimetry*. 14th Annual Meeting of the Imaging Network of Ontario, Toronto, Canada, Mar. 30-31, 2016.

DiCarlo A, and Poepping TL *Stereoscopic PIV for wall shear stress studies of pulsatile flow in life-sized carotid artery models*. 11th International Symposium on Particle Image Velocimetry, Santa Barbara, USA, Sept. 14-16, 2015.

Poepping TL, **DiCarlo A**, Onaizah O, and Zamir M *Evaluating flow disturbances in the carotid bifurcation*. 25th Canadian Congress of Applied Mechanics, London, Canada, May 31 – Jun. 4, 2015.

DiCarlo A, Onaizah O, and Poepping TL *Turbulence in the Carotid Bifurcation Measured Using Particle Image Velocimetry*. 13th Annual Meeting of the Imaging Network of Ontario, London, Canada, Mar. 30-31, 2015.

DiCarlo A, and Poepping TL *Investigation of the Effect of Compliance on Hemodynamics in Carotid Artery Bifurcation Models using Particle Image Velocimetry*. 9th London Imaging Discovery Day, London, Canada, Jun. 26, 2014.

DiCarlo A, Kefayati S, and Poepping TL *Effects of Compliance on Flow and Shear Stress in Carotid Artery Phantom Models using Particle Image Velocimetry*. 9th International Symposium on Biomechanics in Vascular Biology and Cardiovascular Disease, Montreal, Canada. Apr. 28-29, 2014.

Kedzierski W, Blejdea E, **DiCarlo A**, Hein JD, and McConkey JW *O(¹D) Production Following Electron Impact on Oxygen-Containing Molecules*. 27th International

Conference on Photonic, Electronic and Atomic Collisions (ICPEAC), Belfast, Ireland, 2011.

McConkey JW, Kedzierski W, Blejdea E, **DiCarlo A**, and Hein JD, *O(¹D) Production Following Electron Impact on Oxygen-Containing Molecules*. 42nd Meeting of the American Physical Society Division of Atomic, Molecular, and Optical Physics, Atlanta, USA, 2011.

Kedzierski W, Blejdea E, **DiCarlo A**, and McConkey JW. *Electron Impact Excitation of O(¹S) and O(¹D) Following Dissociation of Oxygen-Containing Molecules*. 41st Meeting of the American Physical Society Division of Atomic, Molecular, and Optical Physics, Houston, USA, 2010.

Kedzierski W, **DiCarlo A**, and McConkey JW, *Rare Gas Matrix Detector for Molecular Fragmentation Studies*. 8th International Conference on Photonic, Electronic and Atomic Collisions (ICPEAC), Kalamazoo, USA, 2009.

Sadler J, Shapoori K, Malyarenko E, **DiCarlo A**, Dech J, Severin F, and Maev R *Resolving the Location of Acoustic Point Sources Scattered due to the Presence of a Skull Phantom*. 30th International Symposium on Acoustical Imaging. Monterey, USA, 2009.